LINKING LATE MIOCENE-PLIOCENE SEA SURFACE TEMPERATURES, TERRESTRIAL BIOME TRANSITIONS AND INTENSIFICATION OF GLACIATION USING ALKENONE PALEOTHERMOMETRY

by

Alexandrina Tzanova

B.A., Columbia University, New York, NY 10027

M.Sc., Brown University, Providence, RI 02912

A dissertation submitted in partial fulfillment of the requirements for the degree Doctor of Philosophy in the Department of Earth, Environmental and Planetary Sciences at Brown University

PROVIDENCE, RHODE ISLAND

MAY 2015

This dissertation by Alexandrina Tzanova is accepted in its present form by the Department of Earth, Environmental and Planetary Sciences as satisfying the dissertation requirement for the degree of Doctor of Philosophy.

Date_____________ ____
Timothy D. Herbert, Adviser

Recommended to the Graduate Council

Date_____________ ____
Steven Clemens, Reader

Date_____________ ____
Meredith Hastings, Reader

Date_____________ ____
Jan Tullis, Reader

Date_____________ ____
James Wright, Reader

Approved by the Graduate Council

Date_____________ ____
Peter M. Weber
Dean of the Graduate School

Alexandrina Tzanova

Born June 29, 1986

Sofia, Bulgaria

Education

Brown University Providence, RI

PhD Candidate in Department of Earth, Environmental and Planetary Sciences

Dissertation: Prelude to large Northern Hemisphere glacial cycles: Sea surface temperatures from the Late Miocene to the Pliocene (13 – 2.6 Ma)

Thesis Advisor: Timothy D. Herbert

ScM, Geological Sciences, May 2011

Thesis: *The Evolution of Late Miocene (6-12 Ma) Climate as Seen Through a Sea Surface Temperature Perspective*

Sheridan Center for Teaching and Learning at Brown University

Teaching Certificate I (Reflective Teaching), 2011

Columbia University New York, NY

BA, Environmental Science, 2009

Senior Thesis: *Using Cadmium and Molybdenum sediment content from Soledad Basin, Baja California as a high resolution paleoproxy indicator of ENSO*; Mentor: Dr. Jacob Mey and Dr. Lex van Geen, LDEO; Palisades, NY

Publications

Seager, R., **A. Tzanova** and J. Nakamura, 2009: Drought in the Southeastern United States: Causes, Variability over the Last Millennium, and the Potential for Future Hydroclimate Change. *Journal of Climate*, **22**(19): 5021-5045.

Hernández-Molina, J.F., D.A.V. Stow, C.A. Alvarez-Zarikian, G. Acton, A. Bahr, B. Balestra, E. Ducassou, R. Flood, J.A. Flores, S. Furota, P. Grunert, D. Hodell, F. Jimenez-Espejo, J. K. Kim, L. Krissek, J. Kuroda, B. Li, E. Llave, J. Lofi, L. Lourens, M. Miller, F. Nanayama, N. Nishida, C. Richter, C. Roque, H. Pereira, M. F. Sanchez Goñi, F. J. Sierro, A. D. Singh, C. Sloss, Y. Takashimizu, **A. Tzanova**, A. Voelker, T. Williams and C. Xuan, 2014: Onset of Mediterranean Outflow into the North Atlantic. *Science,* **344** (6189): 1244-1250

Grunert, P., **A. Tzanova**, M. Harzhauser, and W.E. Piller, 2014: Mid-Burdigalian Paratethyan alkenone record reveals link between orbital forcing, Antarctic ice-sheet dynamics and European climate at the verge to Miocene Climate Optimum. *Global and Planetary Change,* **123** (Part A): 36-43

Tzanova, A., T. D. Herbert, L. Peterson, (2015): Cooling Mediterranean Sea Surface Temperatures during the Late Miocene provide a climate context for evolutionary transitions in African and Eurasian flora and fauna. *EPSL*, **419**: 71-80

Tzanova, A., T.D. Herbert, (In review): Sea surface temperatures from the Gulf of Cadiz and the Mediterranean in the Pliocene have implications for MOW formation. *Global and Planetary Change*

Tzanova, A., T.D. Herbert, K. Lawrence, (In prep), Global cooling in the Late Miocene accompanies terrestrial biotic shifts

Tzanova, A., T.D. Herbert, (In prep), Late Miocene salinity reconstructions for the Mediterranean Sea based on temperature deconvolution of planktonic $\delta^{18}O$ time series

Professional Presentations

CCSU Geology Department **November 2014**

Organic biomarkers unlock global cooling at the transition to modern flora and fauna 8 Million years ago (Invited)

European Geosciences Union General Assembly **April 2014**

Reconstructing the temperature and salinity of the Mediterranean Sea through the Late Miocene (13 Ma - 6 Ma) prior to the Messinian Salinity Crisis (Oral)

Mediterranean and subtropical Atlantic (Gulf of Cadiz) SST gradient from the Messinian Salinity Crisis to the onset of permanent glaciation in the Northern hemisphere (Poster)

American Geophysical Union Fall Meeting **December 2013**

How the Mediterranean and subtropical Atlantic (Gulf of Cadiz) SST gradient increased in the Pliocene (2.5 – 6 Ma) – implications for regional and global climate (Poster)

Regional Committee on Mediterranean Neogene Stratigraphy Congress **September 2013**

Implications for Mediterranean isolation and climate via SST reconstructions through the Miocene-Pliocene (Oral)

American Geophysical Union Fall Meeting **December 2012**

Staggering Changes in Mediterranean Sea Surface Temperatures Coincide with Global Climate and Evolution Transitions during the Late Miocene – Pliocene (Oral)

American Geophysical Union Fall Meeting **December 2010**

Alkenone-derived Northern Hemisphere SST during the Serravallian to Messinian Stages of the late Miocene (6.3-12.9Ma) reveal cooling prior to northern hemisphere glaciation (Poster)

Research Cruises

R/V JOIDES Resolution Expedition 339 (organic geochemist) **Nov 2011- Jan 2012**

Teaching Experience

Central Connecticut State University New Britain, CT

Adjunct Faculty

- ESCI 125 – Dynamic Earth **Spring 2015**

Brown University Providence, RI

Graduate Teaching Assistant

- GEO 0137 – Principles of Environmental Geochemistry **Fall 2013**
- GEO 0240 – Evolution of a Habitable Planet **Spring 2013**
- GEO 0030 – Climate and Climate Change **Fall 2012**
- GEO 0070 – Introduction to Oceanography **Spring 2012**
- GEO 1240 – Sedimentology and Stratigraphy **Fall 2010**

Columbia University New York New, NY

Undergraduate Teaching Assistant

- EESC V2100 – Earth's Climate System **Fall 2008**

Community Impact Columbia University New York, NY

ESL Instructor

- Teaching English as a Second Language (ESL) to adults **Sept 2005 – May 2009**

Mentoring and Advising

Daniel McGill, senior thesis, BA Brown University, Fall 2013 – Spring 2014

Tess Plant-Thomas, senior thesis, BS Brown University, Fall 2012 – Spring 2013

Maria Rubinsky, senior thesis, BA Brown University, Fall 2011-Spring 2012

Honors, Awards, Professional Affiliations

First Year Graduate Fellowship, Brown University **2009- 2010**

American Geophysical Union **2009-Present**

Geological Society of America **2009-Present**

Sigma Xi (Scientific Research Society) **2011-Present**

Evolving Earth Foundation grant ($2,700) **2011- 2012**

Earth Science Women Network (ESWN) **2013-Present**

IODP Post-expedition Award ($14,998) **2013-2015**

Brown University Dissertation Fellowship **2014-2015**

Community Involvement

Sheridan Center Graduate Student Liaison **2012-2014**

- Coordinating Sheridan Center for Teaching and Learning and Department of Geological Sciences communication, department TA orientation, teaching practicum

Columbia University Alumni Representative Committee **2009-Present**

- Interviewing applicants, representing Columbia University at local college fairs and hosting regional programs for admitted students, so that as many students as possible have the opportunity to learn about the unique Columbia experience firsthand

Science Café Public Outreach **Fall 2010**

- Was invited through Harvard's Science in the News program to do a public outreach event, "Climates Past and Present". I interacted with people who had varying degrees of knowledge and understanding of climate on the topics of my own research, global climate change and general climate questions.

High School Student Mentor

Supervised high school students working in the lab through an American Chemical Society program and HS internship program that matches high-performing students from low-performing schools in Rhode Island with labs at Brown University.

- Amanda Irwin, HS senior internship, Fall 2011-Spring 2012
- Mathias Vialva, HS senior internship, Summer 2011
- Anthony Gutierrez, HS senior internship, Summer 2010

Internships

Lamont Doherty Earth Observatory Columbia University, Palisades, NY **Summer 2008**

Earth Intern; Advisors: Dr. Jacob Mey and Dr. Lex van Geen

- Method development for establishing Mo and Cd as high-resolution paleorpxies of ENSO variability off the coast of Baja California in the Soledad Basin. Data obtained through HR ICP-MS analysis of digested sediment cores

Earth Institute Columbia University New York, NY **Feb 2008- May 2008**

Earth Institute Intern to Dr. Richard Seager

- Exploring drought in the Southeastern US, hydroclimate in the region and the consequences of greenhouse warming in the region, see publications

To my wonderful husband and my parents, for your amazing patience.

ACKNOWLEDGEMENTS

I owe my sincerest thanks to everyone who made this work possible. I could not have done it without you. Thank you.

First, I would like to acknowledge my parents for their unwavering support, love and belief that I could do anything. Their faith in my abilities often exceeded my own and I cannot express how much that helped me. They never questioned my love of rocks and all things natural. They just encouraged me to go as far as I can with it. Thank you for always letting me march to the beat of my own drum: from my decision to attend a professional arts high school to starting out as a French/Art history/Environmental Science major at Columbia College. Thank you for always putting me first. I could not have asked for better parents.

None of this work would have been possible without the help of my extremely patient and supportive husband who was not scared of long-distance. Thank you for braving snow, sleet, rain, car troubles and actuarial exams to drive to Providence and never miss a weekend. Thank you for not letting me quit and for listening to me vent about research in the middle of the night.

At Brown, the list of people who contributed to my success is endless. My adviser, Tim Herbert, has been an inspiration and source of support through my entire graduate career. His ideas, comments and suggestions guided me through projects, teaching and professional development. His home cooked dinners for the entire lab will remain some of my fondest memories from Brown.

My committee, Steve Clemens, Meredith Hastings, Warren Prell and Jan Tullis were invaluable in making this work what it is today. Steve, thank you for always having your door open and being available to discuss research and IODP expeditions with me. Warren, thank you for your insightful feedback and comments and for making me feel welcome at Brown from the day that I first visited the department. Meredith, you have gone out of your way to help me reach my goals with valuable advice and guidance. Jan, you are one of the most expiring and dedicated educators I have ever met. You have been, and will always be, my role model for teaching.

I am very grateful to the entire lab group, past and present. Caitlin Chazen and Rocio Caballero-Gill, you made me feel welcome from day one and I could not have done this without your help, advice and useful discussions. Alice Alpert, I cannot express how happy I am our paths crossed! Many thanks to all the undergraduates who were part of the lab and the research: Angel Mojarro, Maria Rubinsky, Tess Plant-Thomas, Oliver McLellan, Klara Zimmerman and Daniel McGill. Kira Lawrence and Laura Peterson have been amazing examples to follow and have been great collaborators.

I want to express my sincerest gratitude to three extraordinary people: April Martin, Joe Orchardo and Dave Murray. April is one of the kindest, most hardworking people I have met and she guided me through the initial steps of lab work when I first arrived at Brown. Since then, she has gone out of her way to help me and has become a friend who has kept me sane. April, thank you for being there for me and reminding me there is more to life than grad school. Joe and Dave have gone beyond the call of duty to help me troubleshoot lab and field instruments, analyze samples and answer my questions at a moment’s notice. For that, I will always be grateful.

The administrative staff of the department deserves mention as well because they have been so wonderful and efficient. Particularly, I want to recognize Bill Collins and Pat Davey who have both been absolutely invaluable sources of information and support.

My time in Providence would not have been the same without Mariela Bao, Caitlin Chazen, Dorothy Fibiger, Rocio Caballero-Gill, Elizabeth Thomas and Jessica Whiteside. I will always cherish our "girl nights" of good food and great conversation. We made it through the good and the bad, the questionable neighbors, bachelorette parties, weddings and births with a lot of wine and pisco sours.

I also want to thank Yasemin Erboy Ruff and Ilana Somasunderam who are the best friends a girl can ask for. We supported each other through our internship at LDEO in 2008, our senior thesis in 2009 and the two of you have continued to encourage me through graduate school.

Last but not least, I want to acknowledge my grandmother, Jiji and my grandfather, Todor. Through this Jiji has been a ray of sunshine that has always been there for me to listen, laugh, and bring a smile to my face. She has patiently understood that my short and far in between visits are dictated by project deadlines and samples. My grandfather loved me unconditionally and always believed in me. He passed away in 2013. Dedi, I miss you and I wish you could be here to see the end of this chapter.

TABLE OF CONTENTS

CURRICULUM VITAE ……………………………………………………………….iv

ACKNOWLEDGEMENTS …………………………………………………………xi

INTRODUCTION: ALKENONE PALEOTHERMOMETRY IN THE LATE MIOCENE-PLIOCENE MEDITERRANEAN SEA REVEALS THE PROGRESSION OF INTENSIFICATION OF NORTHERN HEMISPHERE GLACIATION…...…….….....1

CHAPTER 1: COOLING MEDITERRANEAN SEA SURFACE TEMPERATURES DURING THE LATE MIOCENE PROVIDE A CLIMATE CONTEXT FOR EVOLUTIONARY TRANSITIONS IN AFRICA AND EURASIA……………………11

Abstract…………………………………………………………………..…12

1.1 Introduction……………………………………………………………..14

1.1.1 Late Miocene Climate and Evolutionary Transitions.……..….…14

1.1.2 Mediterranean perspective on mid-latitude Northern hemisphere climate……………………………………………………………16

1.2 Methods…………………………………………………………………20

1.2.1 Site and sampling strategy…………..…...………………………….20

1.2.2 Alkenone analysis……………………………………………..21

1.3 Results…………………………………………………………………..23

1.3.1 Stability and warmth between 12.9 and ~8 Ma……….……….23

1.3.2 Onset of cooling and increase in variability between ~8 and 6.7 Ma……………………………………………………………..24

1.3.3 Temperature rebound and stability into the onset of the Messinian Salinity Crisis between 6.7 and 6.3 Ma……………………………26

1.3.4 Orbital scale SST variability in the Late Miocene Mediterranean……………………………………………………26

1.4 Discussion…………………………………………………………………28

1.4.1 Sapropel formation in the Late Miocene Mediterranean ..………28

1.4.2 Mediterranean SSTs link aridification and cooling……………...29

1.4.3 Implications for Modeling Late Miocene Climates…...………....33

1.5 Conclusions……………………………………………………………..35

1.6 Acknowledgements……………………………………………………..36

References…………………………………………………………………..37

Figures………………………………………………………………………52

CHAPTER 2: LATE MIOCENE SALINITY RECONSTRUCTIONS FOR THE MEDITERRANEAN SEA BASED ON TEMPERATURE DECONVOLUTION OF PLANKTONIC δ18O TIME SERIES…………………………...……………...58

Abstract…………………………………………………………...…………..59

2.1 Introduction……………………………………………………..…………..60

2.2 Background………………………………………………………...……...64

2.3 Methods…………………………………………………...……………..65

2.4 Results……………………………………………………..……………..69

2.5 Discussion…………………………………………………………...…………72

2.6 Conclusions…………………………………………...………………..81

2.7 Acknowledgements……………………………………………………………..81

References……………………………………………………………………..83

Table 2.1………...…………………………………………………………..98

Figures…………………………………………………………………………100

CHAPTER 3: GLOBAL COOLING IN THE LATE MIOCENE ACCOMPANIES TERRESTRIAL BIOME SHIFTS…………………………………………………...107

Abstract………………………………………………………………………108

3.1 Introduction………………………………………………………………109

3.2 Methods……………..………………………………………………..111

3.3 Results……………………………………………………………...……114

3.3.1 North Atlantic & Mediterranean………………………………..114

3.3.2 North Pacific……………………………………...…….……115

3.3.3 South Atlantic……………………………………………..……116

3.4 Discussion………………………………………………...…………..117

3.5 Conclusions…………………………………………………...………122

3.6 Acknowledgements…………………………………...…………..……124

References……………………………………………………………………125

Figures………………………………………………………………………..136

CHAPTER 4: REGIONAL AND GLOBAL SIGNIFICANCE OF PLIOCENE SEA SURFACE TEMPERATURES FROM THE GULF OF CADIZ (SITE U1387) AND THE MEDITERRANEAN……………………………………………………………..141

Abstract……………………………………………………………………………142

4.1 Introduction………………………………………………………………………144

4.2 Background………………………………………………………………………147

4.3 Methods…………………………………………………………………………...150

4.4 Results……………………………………………………………………………150

4.5 Discussion………………………………………………………………………..152

4.5.1 Site U1387 in the Pliocene framework…………………………152

4.5.2 Site U1387 and the Mediterranean Sea…………………………153

4.5.3 Site U1387 SST, MOW and future applications…………………155

4.6 Conclusions………………………………………………………………………157

4.7 Acknowledgements………………………………………………………………158

References…………………………………………………………………………159

Figures……………………………………………………………………………..169

APPENDICES

Appendix A Monte dei Corvi Alkenone Indices…………………………………………174

Appendix B Alkenone Indices from ODP Sites 883, 884, 887, 907, 982, 1088…….....181

Appendix C Alkenone Indices from IODP Site U1387………………………………194

LIST OF TABLES

2.1 Modern Mediterranean mass balance…...…………...………………………………98

LIST OF FIGURES

1.1 Late Miocene records of global significance spanning the time period covered by the Monte dei Corvi section…..…………..……………………………………..……....52

1.2 Location map of Monte dei Corvi uplifted marine sediments.………………..…....53

1.3 Mediterranean SSTs and C_{37}total values derived from alkenone analyses…………..54

1.4 Orbitally resolved intervals of Late Miocene Mediterranean SST…………………….55

1.5 Late Miocene Mediterranean C_{37}total and average sedimentation rate at Monte dei Corvi……………………………………………..…………..………………....56

1.6 Comparison of Mediterranean SSTs and $\delta^{13}C$ of soil carbonates from Pakistan..……57

2.1 Mediterranean site map ……………………………………...………...……………99

2.2 Late Miocene orbital configuration of eccentricity, precession, planktonic isotope records and SST ………………………...……………………………………..……………100

2.3 High resolution windows of SST and the corresponding $\delta^{18}O$…………………........101

2.4 Published $\delta^{18}O$ and deconvolved $\delta^{18}O_{Med}$ ……………….…………..……………..….102

2.5 Statistical relationship between $\delta^{18}O_{Med}$ and SST ……….……..…………………103

2.6 Orbital configuration of eccentricity and precession, deconvolved $\delta^{18}O_{Med}$, C_{37}total and SST ….…………………….……………………………………..……….…………104

2.7 Late Miocene Mediterranean salinity …………………………………………….....105

2.8 Planktonic and benthic $\delta^{18}O$ from Monte dei Corvi ….……………………………106

3.1 Late Miocene trends in global benthic $\delta^{18}O$ and $\delta^{13}C$……………...…………...……136

3.2 Site map with modern SST..……...……………………………………..……...…137

3.3 Differences between reconstructed Late Miocene sea surface temperatures and modern annual SST at ODP 907, OPD 982, ODP 883/884, ODP 887, MDC and ODP 1088………………………………...…………………………………………...…138

3.4 Reconstructed Late Miocene sea surface temperatures for ODP 907, OPD 982, ODP 883/884, ODP 887, MDC and ODP 1088 with published records from the North Pacific and Arabian Sea. ……………………………………...…………………………139

3.5 Reconstructed Late Miocene C_{37}total for ODP 907, OPD 982, ODP 883/884, ODP 887, MDC and ODP 1088 ……………………………………………………...…140

4.1 A)Site map of IODP Site U1387 and Mediterranean land sections along with modern SST. B) Predominant winds over the Mediterranean region and idealized surface circulation……...………………………..………………………………….………169

4.2 Plot of biostratigraphic datums of Site U1387……………...………………………170

4.3 $U^{K'}_{37}$ SST reconstruction for Site U1387 …...…………...………...…………………..171

4.4 $U^{K'}_{37}$ SST reconstruction for Site U1387, Mediterranean SST, Site U1387 C_{37}total and Mediterranean C_{37}total plotted along insolation at 65°N…………..…………………172

4.5 Difference in Pliocene to modern SST in the Gulf of Cadiz and the Mediterranean Sea……………………………………………………...…………………………173

INTRODUCTION

Alkenone paleothermometry in the Late Miocene-Pliocene Mediterranean Sea reveals the progression of intensification of Northern Hemisphere glaciation

The paleoclimate of the Late Middle Miocene to Pliocene (13 – 2.5 Ma) holds the clues not just to our present, but also to our future climate. During this time, the Earth transitioned from a world with sporadic and relatively small-scale Northern hemisphere glaciation to the large-scale glacial-interglacial cycles that define the Plio-Pleistocene (Lisiecki and Raymo, 2005; Zachos et al., 2001). Furthermore, the terrestrial biomes that we observe and inhabit today trace their origins to this pivotal time, but the interplay between Late Miocene and Pliocene flora and fauna and climate is not well defined. Most of our understanding of the climate progression that accompanied biome transition comes from benthic isotope data, which reflect the temperature and ice volume signature imparted to bottom waters at their high-latitude origins. However, this view leaves out an important component, which is what the climate transition looked like on land in the mid-latitudes where the biome transitions occurred (Pound et al., 2011).

The existing proxy data for this period present a seemingly contradictory view of climate sensitivity and climate forcing during pivotal biome transitions such as expansion of grasslands and the emergence of the Sahara (Cerling et al., 1997; Schuster et al., 2006; Zhang et al., 2014). Benthic isotope data suggest a progressively cooling climate without large or notable, ice-growth episodes prior to 2.7 Ma. The reconstructions of greenhouse gasses imply stable, Last Glacial Maximum to modern (400 ppm) values (Demicco et al., 2003; Vanderburgh et al., 1993; Zhang et al., 2013), which has led some authors to suggest decoupling between warmth and CO_2 during this time (LaRiviere et al., 2012; Pagani et al., 2010). Furthermore, even though temperature records from the period are few, the available ones indicate warming that is far above what we previously suspected

(Huang et al., 2007; LaRiviere et al., 2012). Paradoxically, the clustering in time of succulent plant diversification, grassland expansion, bi-pedalism transitions, paleoflora reconstructions and ice-rafted debris from the high- latitudes contradicts the notion of static climate conditions.

This work focuses on reconciling the apparent contradiction in currently available paleoclimate data for this interval by generating sea surface temperatures (SST) from multiple mid to high latitude sites (ODP Sites 883/884, 887, 907, 982, 1088, U1387 and the Mediterranean Sea). The SSTs bridge the transition into bi-polar glaciation with Late Miocene warmth across a wide range of latitudes. The Mediterranean Sea also links SST to terrestrial floral and faunal evolutionary events because the sea is land-locked and highly sensitive to continental climate. Today, the Mediterranean is a salt source for global thermohaline circulation (Lozier and Stewart, 2008; Voelker et al., 2006), which makes the data from the region not only valuable as a climate reconstruction, but also as evidence of a climate feedback.

The SSTs presented in this work come from alkenone paleothermometry, which allows for continuous, high-resolution records across a wide range of timescales, latitudes and salinities (Herbert, 2003; Prahl and Wakeham, 1988). The main advantage of this approach is that we avoid multi-proxy bias and continuously reconstruct temperature in the same portion of the water column. Alkenone producers are widespread and confined to the photic zone, and their signal is unbiased in a wide range of salinities. However, the isotopic signal recorded in foraminifera carries a salinity component, which makes it problematic for use in the Mediterranean because of the basin's high-salinity variance on both orbital and long-term timescales. However, the Mediterranean presented another hurdle, namely the Late Miocene sedimentary record from this area is buried under thick layers of salt deposited when the Mediterranean desiccated at the end of the Late Miocene. Fortunately, long, continuous sections of sediment are exposed in uplifted marine sequences, which preserve the alkenone signal intact (Beltran et al., 2011; Cleaveland and Herbert, 2009). This work extends the application of the paleothermometer to Late Miocene Mediterranean sections and inserts the climate history of this locale into the framework of global climate change through the Late Miocene and Pliocene.

The SST view of the transition to large glacial cycles is presented in the following order:

In Chapter 1, we present Late Miocene (13 – 6 Ma) Mediterranean SST from the Monte dei Corvi reference section. This work shows SSTs that were as much as 10°C over the modern annual average at the site in the beginning of the study period, followed by a notable cold episode of SST analogous to the modern average at the time of grassland expansion, succulent plant diversification and the emergence of the Sahara. We suggest the Mediterranean reflects mid-latitude continental climate trends, which contributed to biome shift. We propose that the Late Miocene in the area was notably warmer than previously assumed (Montanari et al., 1997) and that warmth was not static. Therefore, the trends in Mediterranean SSTs show correspondence with existing terrestrial and high-latitude ice-rafted debris data, but are inconsistent with stable CO_2 reconstructions. We propose that a strengthening in the equator-pole temperature gradient shifted the extent of the Hadley cell linking cooling, aridification and evolution during the Late Miocene.

Chapter 2 builds on the SST record from Monte dei Corvi and uses the temperature quantification to deconvolve the existing planktonic foraminiferal record from the region (Kouwenhoven et al., 1999; Sprovieri et al., 2003; Turco et al., 2001), isolating isotopic signature of the surface waters. In this chapter we consider the causes of the onset of Mediterranean desiccation associated with the Messinian Salinity Crisis (MSC). The drivers for isolation vary and there is little consensus as to the ultimate trigger (Roveri et al., 2014). The most widely proposed and competing hypotheses for Mediterranean isolation cite glacioeustatic or tectonic control, with geochemical and sedimentary changes attributed to isolation. We conclude that some of the evidence previously attributed to the onset of MSC reflects the strong temperature decrease reconstructed with SST (Chapter 1) and does not correspond to a concurrent surface salinity increase. Mediterranean salinity surpassed Late Miocene mean at 6.7 Ma, which is much later than the ~7.2 Ma onset suggested previously (Roveri et al., 2014). We conclude the most likely cause for the MSC was a combination of tectonic restriction and sea-level decrease due to ice build up at 6.73 Ma (Hodell et al., 1989; Hodell et al., 2001).

Chapter 3 focuses on the notable cold episode at ~7 Ma first reconstructed in the Mediterranean (Chapter 1) and explores the extent of this episode on a global scale. In this work we present SST data spanning 9-5 Ma from sites in the North Pacific (ODP 883/884, 887), North Atlantic (ODP 907, 982), South Atlantic (ODP 1088) and the an orbitally resolved supplement to the Mediterranean record. At all sites we report onset of cooling concurrent with major biome shifts, which supports the conclusions of Chapter 1. We report a shift in the temperature gradient with higher latitude sites cooling relatively more than lower latitude sites. Additionally, we observe a concurrent order of magnitude increase in haptophyte productivity at the time of large biogenic blooms at all of our study sites. We propose that these findings question the validity of the CO_2 reconstructions (Demicco et al., 2003; Pagani et al., 2010; Vanderburgh et al., 1993) because they imply a large perturbation to the global carbon cycle, which CO_2 reconstructions do not show.

Lastly, in Chapter 4 we reconstruct the SST of the Gulf of Cadiz in the Pliocene (6 – 2.6 Ma) to address the initial objective for IODP Expedition 339, which was to link Mediterranean Outflow (MOW) and cooling in the Pliocene (preceding the intensification of large glacial-interglacial cycles). We address MOW variability by comparing the orbitally resolved SST on both sides of Gibraltar over the period from 3.6 – 2.6 Ma and reconstruct the SST gradient between the Mediterranean (Herbert et al., 2015) and the Atlantic waters that feed it. The SSTs are an integral component of the region's heat and water budget that drive the density of MOW. This work validates the application of the alkenone paleothermometer in the Mediterranean and provides a starting point for future studies into MOW flow and density.

References

Beltran, C., Flores, J.A., Sicre, M.A., Baudin, F., Renard, M., de Rafelis, M., 2011. Long chain alkenones in the Early Pliocene Sicilian sediments (Trubi Formation - Punta di Maiata section): Implications for the alkenone paleothermometry. Paleogeogr. Paleoclimatol. Paleoecol. 308, 253-263.

Cerling, T.E., Harris, J.M., MacFadden, B.J., Leakey, M.G., Quade, J., Eisenmann, V., Ehleringer, J.R., 1997. Global vegetation change through the Miocene/Pliocene boundary. Nature 389, 153-158.

Cleaveland, L.C., Herbert, T.D., 2009. Preservation of the alkenone paleotemperature proxy in uplifted marine sequences: A test from the Vrica outcrop, Crotone, Italy. Geology 37, 179-182.

Demicco, R.V., Lowenstein, T.K., Hartdie, L.A., 2003. Atmospheric pCO2 since 60 Ma from records of seawater pH, calcium and primary carbonate mineralogy. Geology 31, 793-796.

Herbert, T., Ng, G., Peterson, L.C., 2015. Evolution of Mediterranean sea surface temperatures 3.5–1.5 Ma: Regional and hemispheric influences. Earth Planet. Sci. Lett. 409, 307-318.

Herbert, T.D., 2003. Alkenone Paleotemperature Determinations, In: Elderfield, H., Turekian, K.K. (Ed.), Treatise in Marine Geochemistry. Elsevier, pp. 391-432.

Hodell, D.A., Benson, R.H., Kennett, J.P., Rakic-El Bied, K., 1989. Stable isotope stratigraphy of latest miocene sequences in northwest Morocco: the Bou Regreg section. Paleoceanography 4, 467-482.

Hodell, D.A., Curtis, J.H., Sierro, F.J., Raymo, M.E., 2001. Correlation of late Miocene to early Pliocene sequences between the Mediterranean and North Atlantic. Paleoceanography 16, 164-178.

Huang, Y.S., Clemens, S.C., Liu, W.G., Wang, Y., Prell, W.L., 2007. Large-scale hydrological change drove the late Miocene C-4 plant expansion in the Himalayan foreland and Arabian Peninsula. Geology 35, 531-534.

Kouwenhoven, T.J., Seidenkrantz, M.S., van der Zwaan, G.J., 1999. Deep-water changes: the near-synchronous disappearance of a group of benthic foraminifera from the Late Miocene Mediterranean. Paleogeogr. Paleoclimatol. Paleoecol. 152, 259-281.

LaRiviere, J., Ravelo, A.C., Crimmins, A., Dekens, P.S., Ford, H.L., Lyle, M., Wara, M.W., 2012. Late Miocene decoupling of oceanic warmth and atmospheric carbon dioxide forcing. Nature 486, 97-100.

Lisiecki, L.E., Raymo, M.E., 2005. A Pliocene-Pleistocene stack of 57 globally distributed benthic delta O-18 records. Paleoceanography 20.

Lozier, M.S., Stewart, N.M., 2008. On the temporally varying northward penetration of Mediterranean Overflow Water and eastward penetration of Labrador Sea water. J. Phys. Oceanogr. 38, 2097-2103.

Montanari, A., Odin, G.S., Coccioni, R., 1997. Miocene Stratigraphy An Integrated Approach. Elsevier Science, The Netherlands.

Pagani, M., Liu, Z.H., LaRiviere, J., Ravelo, A.C., 2010. High Earth-system climate sensitivity determined from Pliocene carbon dioxide concentrations. Nat. Geosci. 3, 27-30.

Pound, M.J., Haywood, A.M., Salzmann, U., Riding, J.B., Lunt, D.J., Hunter, S.J., 2011. A Tortonian (Late Miocene, 11.61-7.25 Ma) global vegetation reconstruction. Paleogeogr. Paleoclimatol. Paleoecol. 300, 29-45.

Prahl, F.G., Wakeham, S.G., 1988. Calibration of unsaturation patterns in long-chain ketone compositions for paleotemperature assessment Nature 330, 367-369.

Roveri, M., Flecker, R., Krijgsman, W., Lofi, J., Lugli, S., Manzi, V., Sierro, F.J., Bertini, A., Carnerlenghi, A., De Lange, G., Govers, R., Hilgen, F.J., Hubscher, C., Meijer, P.T., Stoica, M., 2014. The Messinian Salinity Crisis: Past and future of a great challenge for marine sciences. Mar. Geol. 352, 25-58.

Schuster, M., Duringer, P., Ghienne, J.F., Vignaud, P., Mackaye, H.T., Likius, A., Brunet, M., 2006. The age of the Sahara Desert. Science 311, 821-821.

Sprovieri, M., Sacchi, M., Rohling, E.J., 2003. Climatically influenced interactions between the Mediterranean and the Paratethys during the Tortonian. Paleoceanography 18.

Turco, E., Hilgen, F.J., Lourens, L.J., Shackleton, N.J., Zachariasse, W.J., 2001. Punctuated evolution of global climate cooling during the late Middle to early Late Miocene: High-resolution planktonic foraminiferal and oxygen isotope records from the Mediterranean. Paleoceanography 16, 405-423.

Vanderburgh, J., Visscher, H., Dilcher, D.L., Kurschner, W.M., 1993. Paleoatmospheric signatures in neogene fossil leaves Science 260, 1788-1790.

Voelker, A.H.L., Lebreiro, S.M., Schonfeld, J., Cacho, I., Erlenkeuser, H., Abrantes, F., 2006. Mediterranean outflow strengthening during northern hemisphere coolings: A salt source for the glacial Atlantic? Earth Planet. Sci. Lett. 245, 39-55.

Zachos, J., Pagani, M., Sloan, L., Thomas, E., Billups, K., 2001. Trends, rhythms, and aberrations in global climate 65 Ma to present. Science 292, 686-693.

Zhang, Y.G., Pagani, M., Liu, Z.H., Bohaty, S.M., DeConto, R., 2013. A 40-million-year history of atmospheric CO2. Philos. Trans. R. Soc. A-Math. Phys. Eng. Sci. 371.

Zhang, Z.S., Ramstein, G., Schuster, M., Li, C., Contoux, C., Yan, Q., 2014. Aridification of the Sahara desert caused by Tethys Sea shrinkage during the Late Miocene. Nature 513, 401-+.

CHAPTER 1

Cooling Mediterranean Sea Surface Temperatures during the Late Miocene provide a climate context for evolutionary transitions in Africa and Eurasia

Alexandrina Tzanova[1]

Timothy D. Herbert[1]

Laura Peterson[2]

1. Department of Geological Sciences, Brown University, 324 Brook Street, Providence RI, 02906

2. Environmental Studies Program, Luther College, Decorah, IA 52101

EPSL, 2015

ABSTRACT

During the Late Miocene, grasslands proliferated, succulent plants diversified in the mid-latitudes, and the desert-like conditions appeared in the Sahara. Despite these major environmental changes on land, the coeval deep-sea oxygen isotope record does not provide evidence for significant high latitude cooling or continental ice growth, making it difficult to relate widespread terrestrial environmental change to global mid-latitude climatic changes. A $U^{K'}_{37}$ –derived sea surface temperature (SST) reconstruction spanning 13 to 6 Ma from uplifted hemipelagic sediments in Northern Italy provides the first continuous mid-latitude temperature record with which to compare the evolution of aridity and biotic events at similar latitudes in Northern Africa and Pakistan. Between 13 and 8.8 Ma, Mediterranean SST lay near the upper limit of the alkenone temperature proxy (~28^{o}C), exceeding modern SST at the site by as much as 10^{o}C. Throughout the record, sapropel layers correspond to local SST maxima, suggesting that Late Miocene hydrological conditions in the Mediterranean responded to insolation forcing via mechanisms similar to those documented for the Plio-Pleistocene. Mediterranean SST cooled rapidly beginning at ~8Ma, with an episode of intense cooling to ~19°C between 7.2 Ma and 6.6 Ma, followed by a rebound to ~25^{o}C preceding the Messinian Salinity Crisis at 5.9 Ma. These observations establish, for the first time, a direct relationship between increasing aridity in the Northern Hemisphere mid-latitudes and significant cooling. Evidently, this cooling was not accompanied by significant growth in continental ice volume. The extreme warmth and subsequent cooling of the Mediterranean Sea are not well-represented in current Late Miocene climate models, which our results suggest underestimate regional warmth prior to the Late Miocene cooling. Our record suggests a

decrease in atmospheric CO_2 levels despite the fact that reconstructions do not show this.

1. 1 Introduction

1.1.1 Late Miocene Climate and Evolutionary Transitions

Numerous evolutionary transitions and shifts in continental biomes occurred in the mid-latitudes during the Late Miocene (13 – 6 Ma). This time period pre-dates large bi-polar glacial cycles as shown by the benthic stable isotope record (Zachos et al., 2001), although continental landmasses lay in similar positions to the present day. Terrestrial ecological changes are consistent with increased aridity and possible cooling. Among them, low CO_2 and seasonal aridity adapted C_4 grasslands spread between 8 and 6 Ma (Behrensmeyer et al., 2007; Cerling et al., 1997; Cerling et al., 1993). Aridity-adapted cacti and succulent plants diversified between 10 and 5 Ma (Arakaki et al., 2011). The first dunes in the Sahara date to ~7 Ma (Schuster et al., 2006; Zhang et al., 2014). A similar terrestrial shift towards dryer and possibly colder conditions occurred concurrently along the northern rim of the Mediterranean, where the better suited for colder and drier conditions conifers and herbs proliferated, although the transition to modern assemblages did not conclude until the mid-Pliocene and mid-Pleistocene (Jimenez-Moreno et al., 2008, 2010). *Sahelanthropus tchadensis* and *Orrorin tugensis*, two key transitional evolutionary forms on the road to bipedalism and modern humans, date to 7 and 6 Ma respectively (Brunet, 2010a, b; Hawks, 2012).

The Late Miocene evolutionary transitions may have arisen in response to shifts in environmental parameters such as temperature, aridity, and CO_2. However, the contribution of each to the terrestrial events is unclear. For example, the initial hypothesis for proliferation of grasslands between 8 Ma and 6 Ma (Cerling et al., 1997; Cerling et al., 1993) postulated concurrent decrease in CO_2, cooling, and seasonal aridification.

Paleoclimate reconstructions of paleosol stable isotopes, leaf wax δD, and paleo-dune deposits show an undisputable increase in aridity in India, Pakistan, the Arabian Peninsula (Behrensmeyer et al., 2007; Huang et al., 2007), and Northern Africa (Schuster et al., 2006). Shifts in herpetological assemblages in Europe and the Mediterranean indicate the following precipitation progression: drier than modern conditions between 13 and 11 Ma gave way to a very humid period, which ended at 8 Ma when precipitation was analogous to modern and the last Late Miocene dry excursion occurred at 7.2 Ma (Bohme et al., 2008; Bohme et al., 2011). The hypothesis of CO_2 decrease over the Late Miocene fell out of favor because available reconstructions of Late Miocene CO_2 (Figure 1) range from ~200 - ~400 ppm (Zhang et al., 2013), without suggestion of a strong decrease between 8 and 6 Ma (it should be noted, however, that the resolution of paleo-CO_2 proxy coverage is very sparse for the Late Miocene). Such values remain puzzling in view of the evidence of a generally warm climate during this time and absence of large northern latitude ice sheets (LaRiviere et al., 2012; Pekar, 2008; Zachos et al., 2001). Climate modeling sensitivity studies of tectonics, vegetation feedbacks suggest that vegetation-albedo feedbacks and tectonics can cause regional warmth of as much as 9°C above present values but not global warming of the scale indicated by paleotemperature proxies (Herold et al., 2009; Knorr et al., 2011).

The hypothesis linking declining CO_2 levels to terrestrial ecosystem changes also lacks supporting evidence from paleotemperature and/or ice volume changes. Large permanent ice existed only in the Southern high latitudes (Jansen and Sjoholm, 1991; Mudelsee and Raymo, 2005). At ~14 Ma Antarctica underwent significant ice sheet expansion and a switch from wet-based to cold-based glaciers (Lewis et al., 2008; Lewis et al., 2007), yet the major intensification of Northern Hemisphere Glaciation (NHG) is much later at 2.7 Ma (Zachos et al., 2001). The permanent freezing of the Antarctic continent therefore pre-dates major mid-latitude evolutionary shifts such as succulent plant diversification by as much as 6 Myr. As seen in Figure 1, benthic foraminiferal isotopic records (Cramer et al., 2009; Zachos et al., 2001) do not show major deep-sea cooling and/or sustained ice volume growth between the expansion of ice sheets in Antarctica after ~14 Ma (Holbourn et al., 2005; Kennett, 1977; Zachos et al., 2001) and NHG at ~2.7 Ma. Note, however, that the conventional interpretation of Late Miocene and early Pliocene oxygen isotope data is hard to reconcile with evidence of ice rafted debris (IRD) from Greenland at ~7.3 Ma, coincident with mid-latitude biotic change (St John, 2008; St John and Krissek, 2002). However, an independent sea surface temperature (SST) reconstruction from a continentally sensitive, mid-latitude location like the Mediterranean Sea can reveal the temperature changes that accompanied terrestrial evolutionary data and high-latitude stable isotope trends.

1.1.2 Mediterranean perspective on mid-latitude Northern Hemisphere climate

The Monte dei Corvi section in the Mediterranean (Figure 2) exposes a continuously deposited sequence of uplifted pelagic sediments from a marine setting sensitive to continental climate in the Late Miocene (Hilgen et al., 2003; Husing et al., 2009; Montanari et al., 1997). Outcropping marine sediments in Sicily and this region (Montanari et al., 1997) provide windows into the Mediterranean that have not been recovered by deep sea drilling. The new paleotemperature data we report allows us to investigate trends and variability of Mediterranean temperatures in a variety of contexts. First, the exceptional record of lithological cyclicity and organic-rich sapropel beds allows us to connect temperature changes to the behavior of the hydrological cycle in the circum-Mediterranean region during the Late Miocene. In the Plio-Pleistocene, cyclical sapropel deposition resulted when precessionally-controlled summer insolation over the region increased and the African summer monsoon shifted to the North over the Nile catchment (Lourens et al., 1996; Rossignol-Strick, 1985). As the Nile delivered greater than average quantities of freshwater and nutrients to the Mediterranean, productivity and preservation of organic matter increased (Daux et al., 2006; De Lange et al., 2008; Emeis et al., 1998; Fhlaithearta et al., 2010; Kohler et al., 2010; Meijer and Tuenter, 2007; Rohling and Hilgen, 1991; Rossignol-Strick, 1985). Sapropel layers are found in the upper Miocene sections, pre-dating the Plio-Pleistocene (Di Stefano et al., 2010; Husing et al., 2007) and are apparent in the Monte dei Corvi section, indicative of large, orbitally-paced climate cycles prior to NHG and under a wide range of runoff availability (Bohme et al., 2008; Bohme et al., 2011).

Next, longer-term temperature changes provide an important constraint in interpreting marine and terrestrial biotic events. The Tortonian/Messinian boundary, defined by the first appearance of the planktonic foraminifer *Globorotalia conomiozea* in the Mediterranean, has been interpreted as an influx of colder Atlantic waters into the basin (Hodell et al., 1989; Krijgsman et al., 1997; Montanari et al., 1997). The paleontological events, however, have not been directly calibrated to an unambiguous paleotemperature record. At longer length scales, the proximity of the region to North Africa and Eurasia allows for comparison between Mediterranean SST and terrestrial paleoclimatic data from northern Africa and Eurasia.

Lastly, an improved and independent temperature reconstruction may help to place the Messinian Salinity Crisis (MSC), which dramatically interrupts the marine succession at Monte dei Corvi, into an improved paleoclimatic context (Roveri et al., 2014). The first sign of the approaching crisis at Monte dei Corvi comes from a change from pelagic carbonates and marls to dark sediments in the Euxinic Shale interval at ~6.5 Ma (Husing et al., 2009). The change in sedimentation corresponds to a shift from open marine toward increasingly saline conditions that culminate with MSC evaporites at ~5.9 Ma (Barhoun and Taoufio, 2008; Kouwenhoven et al., 2003). The shift is symptomatic of a potential global sea level decrease and tectonic changes in the corridors connecting the Mediterranean and the Atlantic (Husing et al., 2010; Krijgsman et al., 1999; Perez-Asensio et al., 2012; Rogerson et al., 2012; Roveri et al., 2014; Seidenkrantz et al., 2000). Currently, the individual contributions of global and regional tectonics and climate to timing and progression of isolation of heat exchange between the Mediterranean and Atlantic is still unresolved (Roveri et al., 2014).

We present the first continuous record of Late Miocene Mediterranean SST based on the alkenone biomarker technique, recovered from sampling at Monte dei Corvi. Two studies have recently shown that the alkenone unsaturation ratio appears unaltered during diagenesis and lithification (Beltran et al., 2011; Cleaveland and Herbert, 2009) and is preserved in outcropping marine sediments in Italy. In contrast stable oxygen isotope data cannot resolve regional Mediterranean SST unambiguously, because of the large and underconstrained isotopic component attributable to hydrological variability in the Mediterranean (Di Stefano et al., 2010; Hodell et al., 1989; Kouwenhoven et al., 1999). Burial diagenesis likely compromises the alternative carbonate-based paleotemperature proxy based on Mg/Ca ratios in foraminiferal tests. Therefore, in this setting the alkenone unsaturation index ($U^{K'}_{37}$) provides the least amount of bias in reconstructing SST.

In the modern ocean, $U^{K'}_{37}$ varies with surface water temperatures at the time of haptophyte growth (Herbert, 2003; Prahl and Wakeham, 1988). The index correlates best to mean annual temperature in the modern ocean (Herbert, 2003; Prahl et al., 2010; Prahl and Wakeham, 1988). Alkenone-based SST estimates are not affected by salinity variations in the modern ocean (Herbert, 2003). For these reasons, $U^{K'}_{37}$ has found widespread use in paleotemperature reconstructions of the Plio-Pleistocene ice ages (Herbert, 2003; Lawrence et al., 2010). Our alkenone-based reconstruction of SST spanning ~13 Ma to ~6 Ma, is the first of its kind in the region and one of only a few representations of ocean temperatures over this time (Huang et al., 2007; LaRiviere et al., 2012).

Total concentration of C_{37} alkenones (C_{37}total) per dry weight of sediment correlates with the production and preservation of haptophyte algae (Bolton et al., 2011; Herbert, 2003; Incarbona et al., 2010) and covaries with organic content in Plio-Pleistocene sediments of the Mediterranean (Cleaveland and Herbert, 2009). In the Mediterranean, higher than average freshwater discharge in to the basin inhibits water column mixing, leading to increased productivity and preservation of marine organic matter (Daux et al., 2006; De Lange et al., 2008; Fhlaithearta et al., 2010; Incarbona et al., 2011; Meijer and Tuenter, 2007; Rossignol-Strick, 1985; Schenau et al., 1999). As discussed below, the C_{37}total proxy therefore provides a relative measure of the hydrological signal for the Mediterranean.

1.2 Methods

1.2.1 Site and sampling strategy

Continuous, pelagic sedimentation at Monte dei Corvi (Figure 2) occurred through the Serravallian, the Tortonian and the earlier portion of the Messinian stages (Montanari et al., 1997) as confirmed by an orbital chronology in a magnetic polarity stratigraphy (Husing et al., 2009). Sapropels map to Northern Hemisphere precession minima, when high freshwater input from northern African and southern Europe results in an influx of terrigenous matter and higher organic content. Conversely, limestones reflect marine biogenous sedimentation under dryer conditions (Hilgen et al., 2003; Lourens et al., 1996; Rossignol-Strick, 1985). In addition to the intercalation of dark sapropels into the carbonate-marl sequence, two distinctive units occur in the upper Tortonian and middle Messinian. The Rossini interval straddling the latest Tortonian and earliest Messinian is a highly calcareous and condensed sequence lacking well developed marls or sapropels (Figures 3-4). Approximately 6 m above the top of the Rossini interval, brackish Euxinic Shales take the marine sequence to the Messinian evaporites (Figures 3-4) (Husing et al., 2007; Husing et al., 2009; Husing et al., 2010; Kouwenhoven et al., 2003; Krijgsman et al., 1999).

Reconstructions of sedimentation rates and sapropel occurrence guided our sampling strategy in order to address long term (10^6 yr) and orbital-scale (10^4 yr) changes through key intervals. As seen in Figure 5, sedimentation rates rapidly increase in the Euxinic shale interval after ~6.7 Ma (Husing et al., 2009). The established chronology also suggests a severe reduction in sedimentation rate in the latest Tortonian, with a possible hiatus of ~80 kyr at ~7.1 Ma (Husing et al., 2009). We sampled the entire sequence at a minimum of two samples per eccentricity cycle, and, in four high-resolution windows (between 9.25 and 8.95 Ma; 8.45 and 8.15 Ma; 7.4 and 6.7 Ma; and, 6.69 and 6.45 Ma), at three to four samples per precession cycle (Figure 4). These intervals cover four regimes of Late Miocene Mediterranean climate beginning from the early Late Miocene to the increased isolation of the basin and truncation of our record prior to the MSC (Cleaveland et al., 2002; Hilgen et al., 2003; Husing et al., 2007; Husing et al., 2009; Montanari et al., 1997). Our resolution is insufficient to resolve precession-scale variability outside of those windows. Samples obtained in outcrop were tied via the cyclical pattern of light, carbonate-rich layers and dark, organic-rich sapropels to the published orbitally-tuned chronology of Husing et al. (2009) with an inferred accuracy of +/- 10 kyr. As we will demonstrate, precessional wet-dry cycles in the sequence lead to cycles in the concentration of C_{37} alkenones that further tie our time series to the orbital model of (Hilgen et al., 2003; Husing et al., 2009).

Our sampling terminates ~280 kyr before the onset of MSC sediments because of deep weathering and poor outcrop exposure above 144m. We were able to obtain a limited number of samples in the upper Euxinic Shale interval, preventing us from tracking SST continuously to the MSC.

1.2.2 Alkenone analysis

Alkenones were extracted from ~8-14 g of finely ground sediment in a Dionex Accelerated Solvent Extractor (ASE 200) using 9:1 (methylene chloride: methanol). The total lipid extract was evaporated under a nitrogen stream. The complex matrix required saponification of the total lipid extract, using 0.5ml of 0.5M KOH in 95% methanol/water for 2.5h at 65°C and subsequently extracted with hexane. The saponification procedure was adjusted with respect to time and temperature to yield maximum alkenone recovery, minimum bias in $U^{K'}_{37}$ as determined by replicates of the same sample and the cleanest chromatographic baseline for Gas Chromatographic (GC) analysis. Saponification and silica gel separation were necessary to prevent gas chromatographic column deterioration, which would otherwise result in notable upward drift in $U^{K'}_{37}$ over the course of a GC run, and an increase in column retention of C_{37} alkenones. Following silica gel separation, each sample was reconstituted in 200 μl of toluene containing a known amount of C_{36} and C_{37} n-alkane standards. The C_{37} alkenones were quantified by flame ionization detection on an Agilent 6890 GC equipped with an Agilent Technologies DB-1 column (60 m analytical column, 5 m fused guard column). To minimize changes in the GC response, we injected a toluene GC-FID blank every 3 samples and monitored system stability by running replicate extracts and a laboratory alkenone standard every 12 samples. We changed the system's inlet liners and trimmed the column every 12-24 samples or as indicated by drifts in the GC behavior of the standard. In addition to the $U^{K'}_{37}$ index, the C_{37}total was determined by reference to internal standards and is reported per gram dry weight of sediment. The reproducibility of the alkenone unsaturation index in the Monte dei Corvi dataset is +/- 0.003 $U^{K'}_{37}$ units corresponding to +/- 0.09°C, as determined by replicate and duplicate analysis of ~8% of the samples. C_{37}total replicates showed a relative reproducibility of +/- 13.8%. C_{37}total values for the section follow a highly non-gaussian (tail toward high C_{37}total) distribution; we chose to use a log normalization for the C_{37}total data we present (Figure 3).

1.3 Results

Figure 3 presents the first continuous record of Mediterranean SST spanning ~12.9 Ma to 6.2 Ma to provide insight into couplings between temperatures, regional hydrological cycle (reflected in lithology) and evolution in adjacent terrestrial environments. For much of the Late Miocene, Mediterranean temperatures exceeded the modern mean annual SST of 19°C at the site by as much as 10°C (Figure 3); secular cooling began at ~8 Ma - punctuated by two transient episodes of major cooling at 7.2 Ma and 6.9 Ma. C_{37}total trends mirror SST, with periods of lowest SST corresponding to periods of low C_{37}total and low sedimentation rate (Figure 5). The long-term trends can be broken down into 3 subsections based on temperature variance and relationship between temperature and lithology. Within time windows, we use standard deviation of estimated SST as a proxy for the range of SST that would be recovered by sampling on the precessional scale.

1.3.1 Stability and warmth between 12.9 and ~8 Ma

The oldest part of the record exhibits strikingly warm SST. We chose to use the Prahl et al. (1988) calibration because it provides the most conservative estimate of paleo-SST. The alternative linear Muller et al. (1998) calibration results in SST that are on average ~0.4°C warmer, but does not alter the sense or timing of SST variations. Alkenone SST determinations in this interval may underestimate the magnitude of warmth, because the $U^{K'}_{37}$ index approaches a value of 1, where the $C_{37:2}$ alkenone is the only alkenone present in the sample. At the limit of $U^{K'}_{37}$~=1, the 28.3°C temperature (based on the Prahl et al. (1988) calibration) provides a lower bound - temperatures could have exceeded this figure. 2% of the samples had a $U^{K'}_{37}$ analytically indistinguishable from 1.0 and 4% returned a $U^{K'}_{37}$ of 0.99 or over. Average reconstructed SST over this interval is 27.5°C with a standard deviation of 0.5°C; therefore, the Late Miocene SST at the site was as warm as "warm pool" regions of the modern ocean. C_{37}total shows a good correspondence with the presence of well-developed sapropels, with higher total alkenone abundance in sapropel layers (Figures 3 and 4). In this part of the record sections with closely clustered sapropels also have higher baseline C_{37}total values (Figure 3).

1.3.2 Onset of cooling and increase in variability between ~8 and 6.7 Ma

The period spanning ~8 Ma to ~6.7 Ma marks the onset of SSTs that are significantly colder than the mean for 12.9 - 8 Ma. The average sampling resolution in this section is ~12 kyr except in a ~500 kyr-long window of orbital resolution (Figure 4) which is discussed in a following section. The beginning of sustained Mediterranean cooling coincides with a transition to the Brownish interval in lithology (Figure 3). It includes a cold episode at the Tortonian/Messinian boundary and ends with a rebound in temperature preceding the MSC During this period, Mediterranean SST decreased significantly and at times reached values similar to the modern average of 19°C (NOAA, 2005). This strong cooling helps to explain the micropaleontological events that define the Tortonian/Messinian boundary at 7.2 Ma, which have been interpreted as an influx of colder Atlantic waters into the Mediterranean (Hodell et al., 1989; Krijgsman et al., 1997). Variability increases over this interval, from 1-2°C oscillations at ~8 Ma to 6-7°C temperature swings during the coldest episode at the Tortonian/Messinian boundary. A ~0.7 Myr long cold excursion began at ~7.4 Ma, with a sharp drop in SST, followed by a recovery and a second drop in SST around 6.9 Ma. After this second interval of cool

SST, temperatures recovered to ~25°C at ~ 6.7 Ma. The entire cold excursion (~7.4 – 6.7 Ma) falls into two lithologic units – the Rossini (devoid of sapropels) and the Transitional intervals (Figure 3), which begin at 7.6 Ma and 7.2 Ma respectively. Temperatures reached their lowest at the Tortonian/Messinian boundary, dated at ~7.2 Ma based on the available age constraints (Husing et al., 2009; Krijgsman et al., 1997).

C_{37}total trends indicate a combination of organic matter preservation and productivity and follow the trends in SST. Conditions of estuarine circulation such as high productivity and preservation of marine organic matter, as well as high rates of and input of terrigenous material, show as high C_{37}total while the converse lagoonal circulation results in low haptophyte productivity and low preservation of alkenones. C_{37}total starts to decrease in the Brownish interval (Figure 3) and the decreasing trend continues through the Rossini interval, which begins at 7.6 Ma. The lowest C_{37}total values match the Transitional interval between 7.2 – 6.9 Ma. Alkenone concentrations are nearly at the limit of detection in these very light colored sediments, where sedimentation rate is the lowest and where Husing et al. (2009) suggest a potential hiatus of ~80 kyr or a sharp drop in the sedimentation rate at 7.1 Ma (Figure 5). The strong reduction in C_{37}total in the interval of condensed sedimentation is consistent with our interpretation that alkenone accumulation is positively correlated to runoff to the Mediterranean basin, through the estuarine versus lagoonal influence on phytoplankton productivity and organic matter preservation. In this interpretation, the region experienced prolonged aridity from 7.2-6.9 Ma. As the color of the sediments darkens and sedimentation rate increases in the Euxinic shale interval beginning at 6.9 Ma, C_{37}total surges concurrently (Figure 5).

1.3.3 Temperature rebound and stability into the onset of the Messinian Salinity Crisis between 6.7 and 6.3 Ma

Following the two-part cold episode ending at ~6.7 Ma, Mediterranean SSTs rebounded to an average of 25.5°C with a standard deviation of 0.8°C preceding the MSC. Such warmth exceeds modern temperatures at the site but is notably cooler than the tropical-like temperatures (~28°C) reconstructed for the oldest part of the record. This interval corresponds to the Euxinic shales and high organic content preceding the desiccation of the Mediterranean (Husing et al., 2009). C_{37}total maxima increase slightly from the 500 kyr interval preceding ~6.9 Ma though they remain lower than the maxima in sapropels in the older part of the record (Figures 3 and 4). C_{37}total and temperature continue to co-vary as in previous sections (Figure 3).

1.3.4 Orbital scale SST variability in the Late Miocene Mediterranean

Integrating our record of Late Miocene Mediterranean SSTs with the lithological sequence at Monte dei Corvi allows us to compare patterns to the well-studied Plio-Pleistocene Mediterranean sedimentary cycles (Hilgen, 1991). Individual sapropels result when a insolation maximum leads to extreme positive summer heating in the Northern Hemisphere and a drastic increase in rainfall over Northern tropical Africa and the Nile catchment (Rossignol-Strick, 1985). The Mediterranean receives greater freshwater input and the wetter conditions lead to increased terrigenous input, dilution of marine $CaCO_3$, a diminishment in vertical circulation and increased productivity (Schenau et al., 1999). Conversely, limestone layers rich in $CaCO_3$ occur at dryer times (De Lange et al., 1999; Hilgen et al., 2003; Rossignol-Strick, 1985; van der Laan et al., 2012). Our sampling does not capture precession-scale changes throughout; however, four windows with a sampling resolution of ~3-6 kyr capture SST variability on orbital timescales (Figure 4). For all of our Late Miocene data, peaks in the C_{37}total index correspond to sapropel layers, as documented previously for the Plio-Pleistocene (Cleaveland and Herbert, 2009).

In the oldest high-resolution window (9.25 Ma to 8.95 Ma) the average SST is 27.4°C with a standard deviation of 0.5°C with three notable cold excursions of ~3°C positioned between prominent sapropel layers (as shown by C_{37}total) that occur between 9.05 and 8.95 Ma. High amplitude of SST changes mirrors the inferred high amplitude variation in precession in that time window (Hilgen et al., 2003; Husing et al., 2009; Lourens et al., 1996). In the second orbital resolution interval between ~8.45 and 8.15 Ma, SST averages 27.3°C with a standard deviation of 0.5°C. These values are comparable the oldest orbital interval, but the average C_{37}total maxima decreases. The decrease in C_{37}total corresponds to a node of low amplitude in the precession cycle that falls in this window according to the published chronology (Husing et al., 2009). The four prominent maxima in C_{37}total in this interval again correspond to peaks in SST.

In the third interval with orbital resolution (7.4 to 6.7 Ma), a two-step cold episode (Figures 3 and 4) marks the coldest interval at Monte dei Corvi during the Late Miocene. The lowest SST correspond to the Tortonian/Messinian boundary and the first appearance of *Globorotalia conomiozea* in the Mediterranean (Sierro, 1985). During this interval, precessional scale cyclical fluctuations in both SST and C_{37}total are superimposed on the general cooling trend, where C_{37}total and SST maxima map to maximum Northern Hemisphere insolation. Additionally, the majority of the cold episode (7.4 to 6.9 Ma) corresponds to a highly calcareous bench with no sapropels. The precessional scale SST changes during this interval are as much as ~7°C. The association of cooler and more arid climates expressed at the precessional scale therefore appears to carry over to the longer timescale of the Tortonian-Messinian cold excursion. In the last interval (6.69 to 6.45 Ma) that precedes the MSC, the average SST rebounds to 25.5°C, which is lower than the mean SST prior to 8 Ma, but notably higher than the average during the coldest interval straddling the T/M boundary.

1.4 Discussion

1.4.1 Sapropel formation in the Late Miocene Mediterranean

Alkenone data suggest that sapropel formation corresponded to SST maxima during the Late Miocene, similar to the precession-paced Plio-Pleistocene sapropels (Figure 1.4). However, the absolute values of SST during sapropel formation, and the values during the adjacent layers indicative of arid conditions, are much warmer than the more recent expression of sapropel formation (Emeis et al., 2000; Rogerson et al., 2012). It seems clear, therefore, that the intensity of summer rainfall over northern Africa and Southern Europe did not depend on the absolute regional temperature of the Late Miocene climate system, but instead, on anomalies of seasonal heating driven by orbital precession. The $U^{K'}_{37}$ data also indicate that the coldest episodes of climate alternated directly with sapropel conditions in the Miocene- this feature is unlike that in the late Pleistocene, where minimum temperatures in the region coincided with minima in the ~100 kyr eccentricity cycle. The Rossini and Transitional intervals (Figure 3) deviate from the Late Miocene pattern of precessionally paced SST maxima and sapropel/hydrology link. SST fluctuates by as much as 7°C on a precessional timescale yet these two lithological units lack sapropels indicating insufficient flux of freshwater resulting in decoupling of temperature and hydrology.

1.4.2 Mediterranean SSTs link aridification and cooling

Our 6.6 Myr long record of Mediterranean SST provides a quantitative measure of regional temperatures in the context of nearby continental hydrology, floral and faunal evolution during the Late Miocene. As seen in Figure 3, the extreme warmth of the Middle Miocene is followed by a steady cooling trend starting at 8 Ma and culminating with a notable cold episode. In the Mediterranean terrestrial realm the Late Miocene was warmer than present with temperatures cooling and aridity expanding from the Serravalian into the Tortonian-Messinian as inferred by the relative boundaries of biomes (Pound et al., 2012; Pound et al., 2011). The end of the Tortonian marks the most pronounced shift in Mediterranean SST and the most extended period of arid regional hydrology. Similarly to the orbital scale coupling observed between temperature and hydrology, the long-term trend in Mediterranean SST demonstrates that on Myr timescales aridity and cooling covary. As temperatures cooled from ~28°C, nearly 10°C over the modern annual average, the lithology of the Monte dei Corvi section shifts to predominantly limestone deposition, indicative of highly arid regional climate between 7.4 – 6.7 Ma.

The earliest significant vertebrate evolutionary transition occurred with the Vallesian Crisis at ~9.6-9.7 Ma when hominoids, rhinoceroses, artiodactyls and many rodents underwent turnover in Europe and the fauna occupying the region shows adaptations to dryer and more open spaces (Agusti et al., 2013; Agusti et al., 2003). The Monte dei Corvi record during this time (Figure 6) is at or near a $U^{K'}_{37}$=1 providing no evidence of strong temperature shift. It is possible that the limitation of the alkenone proxy at the warm extreme prevents us from detecting a temperature change corresponding to the Vallesian Crisis.

The evidence for a Late Miocene cooling of the Mediterranean does, however, correlate to the major shift in the European and North African landscape to cooler and dryer, with an increasingly open landscape inhabited by fauna and flora adapted to such conditions (Ivanov et al., 2002; Jimenez-Moreno et al., 2010; Pound et al., 2012; Pound et al., 2011). Cooling inferred from the Monte dei Corvi section match the coeval increase in herbs and conifers in the Iberian peninsula and the Alps (Jimenez-Moreno et al., 2008, 2010) along with a contemporaneous decrease in amphibian and reptile species richness ~8 Ma (Bohme et al., 2008; Bohme et al., 2011). These floral and faunal changes are interpreted as both a response to cooling and drying during the Tortonian. As SSTs reach their lowest values for the Late Miocene at the Tortonian/Messinian boundary, the first dunes appeared in the Sahara (Schuster et al., 2006) at ~7 Ma suggesting simultaneous drying of the landscape.

The timing of expansion of C_4 grasslands in the global mid-latitudes (Cerling et al., 1997; Quade and Cerling, 1995) closely corresponds to the period of onset of cooling in the Mediterranean (Figure 6). Similarly, succulent plants first appeared in the geological record along with the glaciation of Antarctica, but rapidly diversified much later at ~8 Ma (Arakaki et al., 2011). The delayed diversification suggests the T/M cooling and substantial swings in temperatures, as seen in Figure 6, were associated with conditions that gave CAM and C_4 photosynthetic pathways a competitive edge to expand rapidly, especially during the period of strongest cooling (Arakaki et al., 2011; Cerling et al., 1993; Edwards et al., 2010; Ehleringer et al., 1997). The recovery from the cold episode at 6.7 Ma and resumption sapropelic conditions at Monte dei Corvi suggests that cooling and aridification were not, however, monotonic or step-function events, explaining why a further transition to C_4 vegetation dominance in subtropical regions was delayed until the onset of cyclical Northern Hemisphere Glaciation at the close of the Pliocene (Feakins et al., 2005; Feakins et al., 2007; Jimenez-Moreno et al., 2010).

We acknowledge the potential role of regional tectonics and events associated with the evolution of the Tethyan basin, restriction of Mediterranean/Atlantic corridors and the uplift of Tibet as factors in cooling, aridification and floral and faunal transitions in Europe and Eurasia. The Mediterranean Sea is a remnant of the Tethys Ocean and during the Late Miocene tectonic reconstructions show the possibility of remnants of isolated basins, which disappeared through the study period (Rogl, 1999). The drying and cooling of Mediterranean and Asian climates during this time can be related and exacerbated in part by decrease in moisture sources and shift in the land/ocean temperature contrast (ter Borgh et al., 2014; Wang et al., 2014).

The few available records of SST during this time from the Pacific Ocean and the Arabian Sea (Huang et al., 2007; LaRiviere et al., 2012) suggest that the Late Miocene cooling documented in the Mediterranean is not a regional aberration (see Chapter 3, this work). As with our record, SSTs exceed modern values by ~10°C in the early Late Middle Miocene in the North Pacific (LaRiviere et al., 2012) before cooling in approximate tandem with our estimates. In the Arabian Sea, a low resolution record (Huang et al., 2007) shows a weak, but definite cooling centered around 7 Ma accompanied with a large enrichment in leaf wax hydrogen isotopes, interpreted as drying. In comparison, however, the cooling is accentuated in the Mediterranean; we hypothesize that the cooling was enhanced over the more continentally-influenced Mediterranean. The tectonic restriction of the Mediterranean/Atlantic connection during this time can amplify the importance of cooling by winter winds and magnify the decrease in SST (Krijgsman et al., 1999).

The concurrence of drying and SST decrease in the Mediterranean and the Arabian Seas and Pacific Ocean suggests the Mediterranean Sea SST deterioration may be symptomatic of a large-scale mid-latitude shift in temperatures and aridity. We correlate the Mediterranean cooling and aridification pattern to a hemispheric strengthening in the equator to pole temperature gradient and a resulting intensification and equatorward contraction of the Hadley cell. The dry descending limb of the Hadley cell is expected to move poleward during warmer climates and contracts equatorward during episodes of cooling (Kamae et al., 2011; Sun et al., 2013). This mechanism links the ocean cooling that we and others have begun to document with previous evidence for aridification on land (Griffin, 2002; Steinke et al., 2010; Tipple and Pagani, 2010). For example, high-latitude cooling and sea-ice cover can weaken the African and Asian monsoons in response to Hemisphere scale climate change (Clark et al., 1999; Kutzbach et al., 1998; Prell and Kutzbach, 1987).

Our sampling clearly resolves a discrete cold episode with high amplitude variance at the time of the Tortonian/Messinian boundary followed by a rebound in temperatures at ~6.7 Ma (Figure 3). The Monte dei Corvi SSTs extend to 6.3 Ma which is a time when the Mediterranean – Atlantic connection was closing (Barhoun and Taoufio, 2008; Husing et al., 2010; Kouwenhoven et al., 2003; Krijgsman et al., 1999;

Seidenkrantz et al., 2000). The SST and lithological data indicate that the cause of the distinct cold event cannot be attributed to unidirectional tectonic forcing during this time. The lithological transition to the Euxinic shale interval towards the end of the SST record shows the strong overprint of local climate related to Mediterranean isolation so caution should be used in interpreting the apparent SST rise leading up to the Messinian desiccation as representative of hemisphere-wide climate.

1.4.3 Implications for Modeling Late Miocene Climates

Mediterranean SSTs have implications for modeling the climate transitions of the Late Miocene by providing regional boundary conditions and validating model simulations. Key differences between Late Miocene and modern conditions in the models are atmospheric CO_2 levels, vegetation-albedo effects, the elevation of the Tibet Plateau and sea-ways (Herold et al., 2009; Knorr et al., 2011; Pound et al., 2011). We compare our data prior to the onset of cooling at ~8 Ma to two models (Knorr et al., 2011; Pound et al., 2011), which, however, integrate the entire Tortonian (11-7 Ma). Knorr et al. (2011) obtain a ~3°C warming globally and a ~3°C increase over the Mediterranean, which our data shows is a large underestimate prior to ~8 Ma. The Mediterranean SSTs agree with the vegetation reconstruction of Pound et al., (2011) where global warming, polar warmth, seasonality, latitudinal temperature gradient and SST are prescribed to match paleobotanical coverage. The authors find that that the best fit between modeled biomes and paleobotanical data is the simulation that prescribes ~4.5°C of warming globally and ~8-9°C warming in the region of the Mediterranean.

Beginning at ~8 Ma Mediterranean SSTs fall below the average for the Late Miocene punctuated by a cold and arid episode in the Mediterranean between 7.2 Ma and

6.7 Ma (Figure 3) which is absent in the available model simulations (Butzin et al., 2011; Knorr et al., 2011). These simulations rely on paleofloral and paleofaunal data that integrates a much larger time slice. The short-lived, drastic cold episode demonstrates the need for robustly dated, continuous paleo-records at a resolution capable of capturing such episodes. The Monte dei Corvi SSTs suggest that even small mismatch between records can lead to large errors in prescribed boundary conditions for models. If the rapid cooling recorded in the Mediterranean is representative of a hemisphere-wide sequence (see Chapter 3, this work), then care will need to be taken to choose narrow stratigraphic windows for compiling Late Miocene paleoclimatic data. Paleoclimatic and paleoecological time series should be examined not only in the context of a significant cooling, but also in the context of large orbital-scale temperature changes in the Late Tortonian-Early Messinian, and then a potential temperature recovery in latest Miocene and early Pliocene time.

Late Miocene cooling of the magnitude we deduce raises the likelihood of regional or hemispheric positive feedbacks to initial forcing. Our SST results indicate that temperatures during the most pronounced cooling at the T/M boundary reached modern values,. This finding provides support of far-reaching cooling to the enigmatic in light of the benthic oxygen isotope record (Zachos et al., 2001) occurrence of IRD off Greenland and in the North Pacific at ~ 7 Ma (St John, 2008; St John and Krissek, 2002) as a potential indicator of Late Miocene Northern Hemisphere Glaciation. Cooling preceding the T/M boundary may have allowed for the development of seasonal or permanent sea ice in the Arctic. Expansion of Northern Hemisphere sea ice would be invisible in the deep-sea isotope record, but contribute to substantial regional cooling via its high albedo (Semmler et al., 2012).

Concurrent cooling and aridification also would contribute to higher terrestrial albedo at mid-latitudes through vegetation feedbacks (Kamae et al., 2011; Knorr et al., 2011; Pound et al., 2012; Pound et al., 2011). Conversely, a more active hydrological cycle, absence of large deserts and greater vegetation cover can translate to the warmer conditions prior to ~10 Ma. Increased albedo associated with the establishment of the Sahara at ~7 Ma and at least ephemeral Arctic ice-cover during the Late Miocene (Schuster et al., 2006; St John, 2008; St John and Krissek, 2002) could shift the planet toward colder temperatures.

1.5 Conclusions

The $U^{K'}_{37}$ SST record from the Monte dei Corvi section shows that extraordinarily warm temperatures characterized this mid-latitude setting for the Late Miocene until ~8 Ma. The orbitally resolved intervals in the record demonstrate that Miocene sapropels formed under conditions notably warmer than the Plio-Pleistocene. Sapropel layers match precession-paced warming, whereas SST minima fall in limestone layers suggestive of colder and more arid excursions. The pronounced cooling we detect spanning the Tortonian/ Messinian boundary coincides with the lowest clay influx to the basin and the absence of sapropels. The long-term increase in aridity was likely linked to cooling and a retraction in the latitudinal extent of the Hadley cell, which also resulted in the appearance of the Sahara desert at ~ 7 Ma (Schuster et al., 2006; Zhang et al., 2014). The cold excursion most likely exemplifies a transient phenomenon within the gradual cooling and aridification that was at least hemispheric.

Mediterranean SSTs provide context for concurrent terrestrial evolutionary change during the Late Miocene. We demonstrate that terrestrial ecosystems in the Northern Hemisphere would have experienced tropical-like temperatures prior to ~8 Ma and then sustained, but not monotonic, cooling after that time. Miocene climate models will need to test hypotheses for simulating higher than anticipated mid-latitude temperature prior to 10 Ma and producing concurrent cooling and aridification similar to what is observed between ~8 and 6 Ma. They will also need to satisfy the concurrent Late Miocene steepening of equator-pole temperature gradients and intensifying aridity revealed by the Monte dei Corvi time series. Lastly, we suggest that the evidence of notable cooling accompanying floral and faunal evolution during the Late Miocene revives the much-debated link between a possible decline in CO_2 and Late Miocene changes in vegetation on land (Arakaki et al., 2011; Cerling et al., 1997; Schuster et al., 2006).

1.6 Acknowledgements

The authors would like to thank Alessandro Montanari at Geological Observatory of Coldigioco for his help with fieldwork and his valuable input, Selja Husing for sharing samples and Caitlin Chazen and Rocio Caballero Gill for useful discussions. The work was made possible by American Chemical Society grant PRF 48032-AC2.

References

Agusti, J., Cabrera, L., Garces, M., 2013. The Vallesian Mammal Turnover: A Late Miocene record of decoupled land-ocean evolution. Geobios 46, 151-157.

Agusti, J., de Siria, A.S., Garces, M., 2003. Explaining the end of the hominoid experiment in Europe. J. Hum. Evol. 45, 145-153.

Arakaki, M., Christin, P.A., Nyffeler, R., Lendel, A., Eggli, U., Ogburn, R.M., Spriggs, E., Moore, M.J., Edwards, E.J., 2011. Contemporaneous and recent radiations of the world's major succulent plant lineages. Proc. Natl. Acad. Sci. U. S. A. 108, 8379-8384.

Barhoun, N., Taoufio, N.B., 2008. Biostratigraphic and environmental events recordedin the Riffian southern corridor (Northern Morocco) in late Miocene before the Messinian salinity crisis. Geodiversitas 30, 21-40.

Behrensmeyer, A.K., Quade, J., Cerling, T.E., Kappelman, J., Khan, I.A., Copeland, P., Roe, L., Hicks, J., Stubblefield, P., Willis, B.J., Latorre, C., 2007. The structure and rate of late Miocene expansion of C-4 plants: Evidence from lateral variation in stable isotopes in paleosols of the Siwalik Group, northern Pakistan. Geol. Soc. Am. Bull. 119, 1486-1505.

Beltran, C., Flores, J.A., Sicre, M.A., Baudin, F., Renard, M., de Rafelis, M., 2011. Long chain alkenones in the Early Pliocene Sicilian sediments (Trubi Formation - Punta di Maiata section): Implications for the alkenone paleothermometry. Paleogeogr. Paleoclimatol. Paleoecol. 308, 253-263.

Bohme, M., Ilg, A., Winklhofer, M., 2008. Late Miocene "washhouse" climate in Europe. Earth Planet. Sci. Lett. 275, 393-401.

Bohme, M., Winklhofer, M., Ilg, A., 2011. Miocene precipitation in Europe: Temporal trends and spatial gradients. Paleogeogr. Paleoclimatol. Paleoecol. 304, 212-218.

Bolton, C.T., Lawrence, K.T., Gibbs, S.J., Wilson, P.A., Herbert, T.D., 2011. Biotic and geochemical evidence for a global latitudinal shift in ocean biogeochemistry and export productivity during the late Pliocene. Earth Planet. Sci. Lett. 308, 200-210.

Brunet, M., 2010a. Short note The track of a new cradle of mankind in Sahelo-Saharan Africa (Chad, Libya, Egypt, Cameroon). J. Afr. Earth Sci. 58, 680-683.

Brunet, M., 2010b. Two new Mio-Pliocene Chadian hominids enlighten Charles Darwin's 1871 prediction. Philos. Trans. R. Soc. B-Biol. Sci. 365, 3315-3321.

Butzin, M., Lohmann, G., Bickert, T., 2011. Miocene ocean circulation inferred from marine carbon cycle modeling combined with benthic isotope records. Paleoceanography 26.

Cerling, T.E., Harris, J.M., MacFadden, B.J., Leakey, M.G., Quade, J., Eisenmann, V., Ehleringer, J.R., 1997. Global vegetation change through the Miocene/Pliocene boundary. Nature 389, 153-158.

Cerling, T.E., Wang, Y., Quade, J., 1993. Expansion of C4 ecosystems as an indicator of global ecological change in the Late Miocene. Nature 361, 344-345.

Clark, P.U., Alley, R.B., Pollard, D., 1999. Climatology - Northern hemisphere ice-sheet influences on global climate change. Science 286, 1104-1111.

Cleaveland, L.C., Herbert, T.D., 2009. Preservation of the alkenone paleotemperature proxy in uplifted marine sequences: A test from the Vrica outcrop, Crotone, Italy. Geology 37, 179-182.

Cleaveland, L.C., Jensen, J., Goese, S., Bice, D.M., Montanari, A., 2002. Cyclostratigraphic analysis of pelagic carbonates at Monte dei Corvi (Ancona, Italy) and astronomical correlation of the Serravallian-Tortonian boundary. Geology 30, 931-934.

Cramer, B.S., Toggweiler, J.R., Wright, J.D., Katz, M.E., Miller, K.G., 2009. Ocean overturning since the Late Cretaceous: Inferences from a new benthic foraminiferal isotope compilation. Paleoceanography 24.

Daux, V., Foucault, A., Melieres, F., Turpin, M., 2006. Sapropel-like Pliocene sediments of Sicily deposited under oxygenated bottom water. Bull. Soc. Geol. Fr. 177, 79-88.

De Lange, G.J., Thomson, J., Reitz, A., Slomp, C.P., Principato, M.S., Erba, E., Corselli, C., 2008. Synchronous basin-wide formation and redox-controlled preservation of a Mediterranean sapropel. Nat. Geosci. 1, 606-610.

De Lange, G.J., Van Santvoort, P.J.M., Langereis, C., Thomson, J., Corselli, C., Michard, A., Rossignol-Strick, M., Paterne, M., Anastasakis, G., 1999. Palaeo-environmental variations in eastern Mediterranean sediments: a multidisciplinary approach in a prehistoric setting. Prog. Oceanogr. 44, 369-386.

Demicco, R.V., Lowenstein, T.K., Hartdie, L.A., 2003. Atmospheric pCO2 since 60 Ma from records of seawater pH, calcium and primary carbonate mineralogy. Geology 31, 793-796.

Di Stefano, A., Verducci, M., Lirer, F., Ferraro, L., Iaccarino, S.M., Husing, S.K., Hilgen, F.J., 2010. Paleoenvironmental conditions preceding the Messinian Salinity Crisis in the Central Mediterranean: Integrated data from the Upper Miocene Trave section (Italy). Paleogeogr. Paleoclimatol. Paleoecol. 297, 37-53.

Edwards, E.J., Osborne, C.P., Stromberg, C.A.E., Smith, S.A., Bond, W.J., Christin, P.A., Cousins, A.B., Duvall, M.R., Fox, D.L., Freckleton, R.P., Ghannoum, O., Hartwell, J., Huang, Y.S., Janis, C.M., Keeley, J.E., Kellogg, E.A., Knapp, A.K., Leakey, A.D.B., Nelson, D.M., Saarela, J.M., Sage, R.F., Sala, O.E., Salamin, N., Still, C.J., Tipple, B., Consortium, C.G., 2010. The Origins of C-4 Grasslands: Integrating Evolutionary and Ecosystem Science. Science 328, 587-591.

Ehleringer, J.R., Cerling, T.E., Helliker, B.R., 1997. C-4 photosynthesis, atmospheric CO2 and climate. Oecologia 112, 285-299.

Emeis, K.C., Schulz, H.-M., Struck, U., Sakamoto, T., Doose, H., Erlenkeuser, H., Howell, M., Kroon, D., Paterne, M., 1998. Stable isotope and alkenone temperature records of sapropels from sites 964 and 968: Constraining the physical environment of sapropel formation in the Eastern Mediterranean Sea, In: Robertson, A.H.F., Emeis, K.C., Richter, C., Camerlenghi, A. (Eds.), Proceedings of the Ocean Drilling Program Scientific Results pp. 309-331.

Emeis, K.C., Struck, U., Schulz, H.M., Rosenberg, R., Bernasconi, S., Erlenkeuser, H., Sakamoto, T., Martinez-Ruiz, F., 2000. Temperature and salinity variations of Mediterranean Sea surface waters over the last 16,000 years from records of planktonic stable oxygen isotopes and alkenone unsaturation ratios. Paleogeogr. Paleoclimatol. Paleoecol. 158, 259-280.

Feakins, S.J., deMenocal, P.B., Eglinton, T.I., 2005. Biomarker records of late Neogene changes in northeast African vegetation. Geology 33, 977-980.

Feakins, S.J., Eglinton, T.I., deMenocal, P.B., 2007. A comparison of biomarker records of northeast African vegetation from lacustrine and marine sediments (ca. 3.40 Ma). Org. Geochem. 38, 1607-1624.

Fhlaithearta, S.N., Reichart, G.J., Jorissen, F.J., Fontanier, C., Rohling, E.J., Thomson, J., De Lange, G.J., 2010. Reconstructing the seafloor environment during sapropel formation using benthic foraminiferal trace metals, stable isotopes, and sediment composition. Paleoceanography 25.

Griffin, D.L., 2002. Aridity and humidity: two aspects of the late Miocene climate of North Africa and the Mediterranean. Paleogeogr. Paleoclimatol. Paleoecol. 182, 65-91.

Hawks, J., 2012. Longer time scale for human evolution. Proc. Natl. Acad. Sci. U. S. A. 109, 15531-15532.

Herbert, T.D., 2003. Alkenone Paleotemperature Determinations, In: Elderfield, H., Turekian, K.K. (Ed.), Treatise in Marine Geochemistry. Elsevier, pp. 391-432.

Herold, N., You, Y., Muller, R.D., Seton, M., 2009. Climate model sensitivity to changes in Miocene paleotopography. Aust. J. Earth Sci. 56, 1049-1059.

Hilgen, F.J., 1991. Astronomical calibration of Gauss to Matuyama sapropels in the Mediterranean and implication for the Geomagnetic Polarity Time Scale. Earth Planet. Sci. Lett. 104, 2226-2244.

Hilgen, F.J., Aziz, H.A., Krijgsman, W., Raffi, I., Turco, E., 2003. Integrated stratigraphy and astronomical tuning of the Serravallian and lower Tortonian at Monte dei Corvi (Middle-Upper Miocene, northern Italy). Paleogeogr. Paleoclimatol. Paleoecol. 199, 229-264.

Hodell, D.A., Benson, R.H., Kennett, J.P., Rakic-El Bied, K., 1989. Stable isotope stratigraphy of latest miocene sequences in northwest Morocco: the Bou Regreg section. Paleoceanography 4, 467-482.

Holbourn, A., Kuhnt, W., Schulz, M., Erlenkeuser, H., 2005. Impacts of orbital forcing and atmospheric carbon dioxide on Miocene ice-sheet expansion. Nature 438, 483-487.

Huang, Y.S., Clemens, S.C., Liu, W.G., Wang, Y., Prell, W.L., 2007. Large-scale hydrological change drove the late Miocene C-4 plant expansion in the Himalayan foreland and Arabian Peninsula. Geology 35, 531-534.

Husing, S.K., Hilgen, F.J., Aziz, H.A., Krijgsman, W., 2007. Completing the Neogene geological time scale between 8.5 and 12.5 Ma. Earth Planet. Sci. Lett. 253, 340-358.

Husing, S.K., Kuiper, K.F., Link, W., Hilgen, F.J., Krijgsman, W., 2009. The upper Tortonian-lower Messinian at Monte dei Corvi (Northern Apennines, Italy): Completing a Mediterranean reference section for the Tortonian Stage. Earth Planet. Sci. Lett. 282, 140-157.

Husing, S.K., Oms, O., Agusti, J., Garces, M., Kouwenhoven, T.J., Krijgsman, W., Zachariasse, W.J., 2010. On the late Miocene closure of the Mediterranean-Atlantic gateway through the Guadix basin (southern Spain). Paleogeogr. Paleoclimatol. Paleoecol. 291, 167-179.

Incarbona, A., Martrat, B., Di Stefano, E., Grimalt, J.O., Pelosi, N., Patti, B., Tranchida, G., 2010. Primary productivity variability on the Atlantic Iberian Margin over the last 70,000 years: Evidence from coccolithophores and fossil organic compounds. Paleoceanography 25.

Incarbona, A., Sprovieri, M., Lirer, F., Sprovieri, R., 2011. Surface and deep water conditions in the Sicily channel (central Mediterranean) at the time of sapropel S5 deposition. Paleogeogr. Paleoclimatol. Paleoecol. 306, 243-248.

Ivanov, D., Ashraf, A.R., Mosbrugger, V., Palamarev, E., 2002. Palynological evidence for Miocene climate change in the Forecarpathian Basin (Central Paratethys, NW Bulgaria. Paleogeogr. Paleoclimatol. Paleoecol. 178, 19-37.

Jansen, E., Sjoholm, J., 1991. Reconstruction of glaciation over the past 6Myr from ice-borne deposits in the Norwegian Sea Nature 349, 600-603.

Jimenez-Moreno, G., Fauquette, S., Suc, J.P., 2008. Vegetation, climate and palaeoaltitude reconstructions of the Eastern Alps during the Miocene based on pollen records from Austria, Central Europe. J. Biogeogr. 35, 1638-1649.

Jimenez-Moreno, G., Fauquette, S., Suc, J.P., 2010. Miocene to Pliocene vegetation reconstruction and climate estimates in the Iberian Peninsula from pollen data. Rev. Palaeobot. Palynology 162, 403-415.

Kamae, Y., Ueda, H., Kitoh, A., 2011. Hadley and Walker Circulations in the Mid-Pliocene Warm Period Simulated by an Atmospheric General Circulation Model. J. Meteorol. Soc. Jpn. 89, 475-493.

Kennett, J.P., 1977. Cenozoic evolution of Antarctic glaciation, circum-Antarctic ocean, and their impact of global paleoceanography. Journal of Geophysical Research-Oceans and Atmospheres 82, 3843-3860.

Knorr, G., Butzin, M., Micheels, A., Lohmann, G., 2011. A warm Miocene climate at low atmospheric CO2 levels. Geophys. Res. Lett. 38.

Kohler, C.M., Heslop, D., Krijgsman, W., Dekkers, M.J., 2010. Late Miocene paleoenvironmental changes in North Africa and the Mediterranean recorded by geochemical proxies (Monte Gibliscemi section, Sicily). Paleogeogr. Paleoclimatol. Paleoecol. 285, 66-73.

Kouwenhoven, T.J., Hilgen, F.J., van der Zwaan, G.J., 2003. Late Tortonian-early Messinian stepwise disruption of the Mediterranean-Atlantic connections: constraints from benthic foraminiferal and geochemical data. Paleogeogr. Paleoclimatol. Paleoecol. 198, 303-319.

Kouwenhoven, T.J., Seidenkrantz, M.S., van der Zwaan, G.J., 1999. Deep-water changes: the near-synchronous disappearance of a group of benthic foraminifera from the Late Miocene Mediterranean. Paleogeogr. Paleoclimatol. Paleoecol. 152, 259-281.

Krijgsman, W., Hilgen, F.J., Negri, A., Wijbrans, J.R., Zachariasse, W.J., 1997. The Monte del Casino section (Northern Apennines, Italy): a potential Tortonian/Messinian boundary stratotype? Paleogeogr. Paleoclimatol. Paleoecol. 133, 27-47.

Krijgsman, W., Hilgen, F.J., Raffi, I., Sierro, F.J., Wilson, D.S., 1999. Chronology, causes and progression of the Messinian salinity crisis. Nature 400, 652-655.

Kutzbach, J., Gallimore, R., Harrison, S., Behling, P., Selin, R., Laarif, F., 1998. Climate and biome simulations for the past 21,000 years. Quat. Sci. Rev. 17, 473-506.

LaRiviere, J., Ravelo, A.C., Crimmins, A., Dekens, P.S., Ford, H.L., Lyle, M., Wara, M.W., 2012. Late Miocene decoupling of oceanic warmth and atmospheric carbon dioxide forcing. Nature 486, 97-100.

Lawrence, K.T., Sosdian, S., White, H.E., Rosenthal, Y., 2010. North Atlantic climate evolution through the Plio-Pleistocene climate transitions. Earth Planet. Sci. Lett. 300, 329-342.

Lewis, A.R., Marchant, D.R., Ashworth, A.C., Hedenas, L., Hemming, S.R., Johnson, J.V., Leng, M.J., Machlus, M.L., Newton, A.E., Raine, J.I., Willenbring, J.K., Williams, M., Wolfe, A.P., 2008. Mid-Miocene cooling and the extinction of tundra in continental Antarctica. Proc. Natl. Acad. Sci. U. S. A. 105, 10676-10680.

Lewis, A.R., Marchant, D.R., Ashworth, A.C., Hemming, S.R., Machlus, M.L., 2007. Major middle Miocene global climate change: Evidence from East Antarctica and the Transantarctic Mountains. Geol. Soc. Am. Bull. 119, 1449-1461.

Lourens, L.J., Antonarakou, A., Hilgen, F.J., VanHoof, A.A.M., VergnaudGrazzini, C., Zachariasse, W.J., 1996. Evaluation of the Plio-Pleistocene astronomical timescale. Paleoceanography 11, 391-413.

Meijer, P.T., Tuenter, E., 2007. The effect of precession-induced changes in the Mediterranean freshwater budget on circulation at shallow and intermediate depth. J. Mar. Syst. 68, 349-365.

Montanari, A., Odin, G.S., Coccioni, R., 1997. Miocene Stratigraphy An Integrated Approach. Elsevier Science, The Netherlands.

Mudelsee, M., Raymo, M.E., 2005. Slow dynamics of the Northern Hemisphere glaciation. Paleoceanography 20.

Muller, P.J., Kirst, G., Ruhland, G., von Storch, I., Rosell-Mele, A., 1998. Calibration of the alkenone paleotemperature index U-37(K ') based on core-tops from the eastern South Atlantic and the global ocean (60 degrees N-60 degrees S). Geochim. Cosmochim. Acta 62, 1757-1772.

NOAA, 2005. World Ocean Atlas.

Pagani, M., Freeman, K.H., Arthur, M.A., 1999. Late Miocene atmospheric CO2 concentrations and the expansion of C-4 grasses. Science 285, 876-879.

Pearson, P.N., Palmer, M.R., 2000. Atmospheric carbon dioxide concentrations over the past 60 million years. Nature 406, 695-699.

Pekar, S.F., 2008. Climate change - When did the icehouse cometh? Nature 455, 602-603.

Perez-Asensio, J.N., Aguirre, J., Schmiedl, G., Civis, J., 2012. Messinian paleoenvironmental evolution in the lower Guadalquivir Basin (SW Spain) based on benthic foraminifera. Paleogeogr. Paleoclimatol. Paleoecol. 326, 135-151.

Pound, M.J., Haywood, A.M., Salzmann, U., Riding, J.B., 2012. Global vegetation dynamics and latitudinal temperature gradients during the Mid to Late Miocene (15.97-5.33 Ma). Earth-Sci. Rev. 112, 1-22.

Pound, M.J., Haywood, A.M., Salzmann, U., Riding, J.B., Lunt, D.J., Hunter, S.J., 2011. A Tortonian (Late Miocene, 11.61-7.25 Ma) global vegetation reconstruction. Paleogeogr. Paleoclimatol. Paleoecol. 300, 29-45.

Prahl, F.G., Rontani, J.F., Zabeti, N., Walinsky, S.E., Sparrow, M.A., 2010. Systematic pattern in U-37(K ') - Temperature residuals for surface sediments from high latitude and other oceanographic settings. Geochim. Cosmochim. Acta 74, 131-143.

Prahl, F.G., Wakeham, S.G., 1988. Calibration of unsaturation patterns in long-chain ketone compositions for paleotemperature assessment Nature 330, 367-369.

Prell, W.L., Kutzbach, J.E., 1987. Monsoon variability over the past 150,000 years Journal of Geophysical Research-Atmospheres 92, 8411-8425.

Quade, J., Cerling, T.E., 1995. Expansion of C-4 grasses in the Late Miocene of Northern Pakistan - evidence from stable isotopes in paleosols Paleogeogr. Paleoclimatol. Paleoecol. 115, 91-116.

Rogerson, M., Rohling, E.J., Bigg, G.R., Ramirez, J., 2012. Paleoceanography of the Atlantic-Mediterranean exchange: overview and first quantitative assessment of climatic forcing. Rev. Geophys. 50.

Rogl, F., 1999. Mediterranean and Paratethys. Facts and hypotheses of an Oligocene to Miocene paleogeography (short overview). Geol. Carpath. 50, 339-349.

Rohling, E.J., Hilgen, F.J., 1991. The Eastern Mediterranean climate at times of sapropel formation - a review. Geol. Mijnb. 70, 253-264.

Rossignol-Strick, M., 1985. Mediterranean quaternary sapropels, and immediate response of the African monsoon to variation of insolation. Paleogeogr. Paleoclimatol. Paleoecol. 49, 237-263.

Roveri, M., Flecker, R., Krijgsman, W., Lofi, J., Lugli, S., Manzi, V., Sierro, F.J., Bertini, A., Carnerlenghi, A., De Lange, G., Govers, R., Hilgen, F.J., Hubscher, C., Meijer, P.T., Stoica, M., 2014. The Messinian Salinity Crisis: Past and future of a great challenge for marine sciences. Mar. Geol. 352, 25-58.

Schenau, S.J., Antonarakou, A., Hilgen, F.J., Lourens, L.J., Nijenhuis, I.A., van der Weijden, C.H., Zachariasse, W.J., 1999. Organic-rich layers in the Metochia section (Gavdos, Greece): evidence for a single mechanism of sapropel formation during the past 10 My. Mar. Geol. 153, 117-135.

Schuster, M., Duringer, P., Ghienne, J.F., Vignaud, P., Mackaye, H.T., Likius, A., Brunet, M., 2006. The age of the Sahara Desert. Science 311, 821-821.

Seidenkrantz, M.S., Kouwenhoven, T.J., Jorissen, F.J., Shackleton, N.J., van der Zwaan, G.J., 2000. Benthic foraminifera as indicators of changing Mediterranean-Atlantic water exchange in the late Miocene. Mar. Geol. 163, 387-407.

Semmler, T., McGrath, R., Wang, S.Y., 2012. The impact of Arctic sea ice on the Arctic energy budget and on the climate of the Northern mid-latitudes. Clim. Dyn. 39, 2675-2694.

Sierro, F.J., 1985. The replacement of the Globorotalia - menardii group by the Globorotalia - miotumida group - an ait to recognizing the Tortonian - Messinian boundary in the Mediterranean adn adjacent Atlantic. Mar. Micropaleontol. 9, 525-535.

St John, K., 2008. Cenozoic ice-rafting history of the central Arctic Ocean: Terrigenous sands on the Lomonosov Ridge. Paleoceanography 23.

St John, K., Krissek, L.A., 2002. The late Miocene to Pleistocene ice-rafting history of southeast Greenland. Boreas 31, 28-35.

Steinke, S., Groeneveld, J., Johnstone, H., Rendle-Buhring, R., 2010. East Asian summer monsoon weakening after 7.5 Ma: Evidence from combined planktonic foraminifera Mg/Ca and delta(18)O (ODP Site 1146; northern South China Sea). Paleogeogr. Paleoclimatol. Paleoecol. 289, 33-43.

Sun, Y., Ramstein, G., Contoux, C., Zhou, T., 2013. A comparative study of large-scale atmospheric circulation in the context of a future scenario (RCP4.5) and past warmth (mid-Pliocene). Clim. Past. 9, 1613-1627.

ter Borgh, M., Stoica, M., Donselaar, M.E., Matenco, L., Krijgsman, W., 2014. Miocene connectivity between the Central and Eastern Paratethys: Constraints from the western Dacian Basin. Paleogeogr. Paleoclimatol. Paleoecol. 412, 45-67.

Tipple, B.J., Pagani, M., 2010. A 35 Myr North American leaf-wax compound-specific carbon and hydrogen isotope record: Implications for C-4 grasslands and hydrologic cycle dynamics. Earth Planet. Sci. Lett. 299, 250-262.

van der Laan, E., Hilgen, F.J., Lourens, L.J., de Kaenel, E., Gaboardi, S., Iaccarino, S., 2012. Astronomical forcing of Northwest African climate and glacial history during the late Messinian (6.5-5.5 Ma). Paleogeogr. Paleoclimatol. Paleoecol. 313, 107-126.

Vanderburgh, J., Visscher, H., Dilcher, D.L., Kurschner, W.M., 1993. Paleoatmospheric signatures in neogene fossil leaves Science 260, 1788-1790.

Wang, X., Sun, D.H., Chen, F.H., Wang, F., Li, B.F., Popov, S.V., Wu, S., Zhang, Y.B., Li, Z.J., 2014. Cenozoic paleo-environmental evolution of the Pamir-Tien Shan convergence zone. J. Asian Earth Sci. 80, 84-100.

Zachos, J., Pagani, M., Sloan, L., Thomas, E., Billups, K., 2001. Trends, rhythms, and aberrations in global climate 65 Ma to present. Science 292, 686-693.

Zhang, Y.G., Pagani, M., Liu, Z.H., Bohaty, S.M., DeConto, R., 2013. A 40-million-year history of atmospheric CO2. Philos. Trans. R. Soc. A-Math. Phys. Eng. Sci. 371.

Zhang, Z.S., Ramstein, G., Schuster, M., Li, C., Contoux, C., Yan, Q., 2014. Aridification of the Sahara desert caused by Tethys Sea shrinkage during the Late Miocene. Nature 513, 401-+.

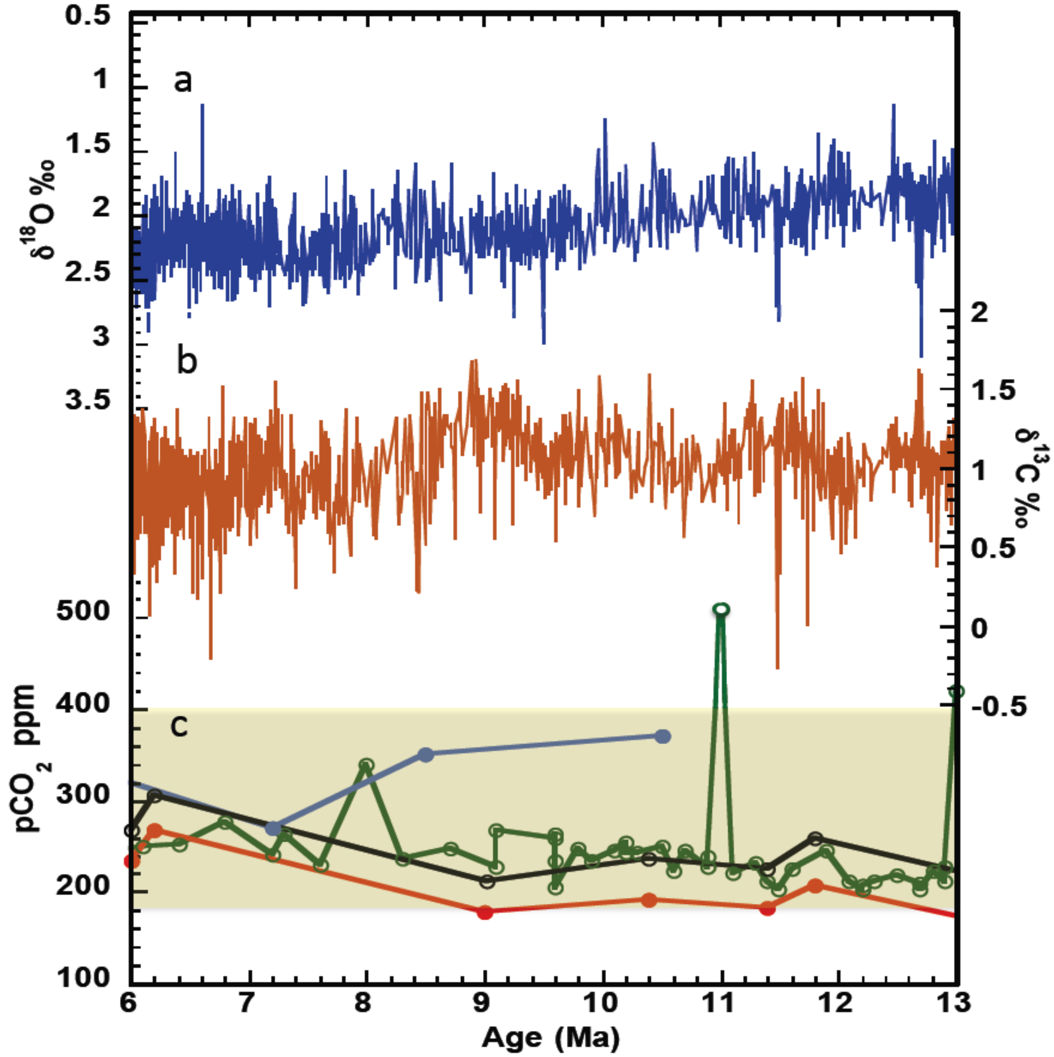

Figure 1.1 Late Miocene records of global significance spanning the time period covered by the Monte dei Corvi section. (a) North Atlantic benthic $\delta^{18}O$ record (Cramer et al., 2009). (b) North Atlantic $\delta^{13}C$ benthic record (Cramer et al., 2009). (c) Late Miocene paleoreconstructions of CO_2 from Pagani et al., (1999) as green open circles, Pearson and Palmer (2000) as black open circles, Vanderburgh et al., (1993) as blue closed circles and Demicco et al., (2003) as red closed circles. The shaded box in the lower graph represents the range in CO_2 between the LGM and today.

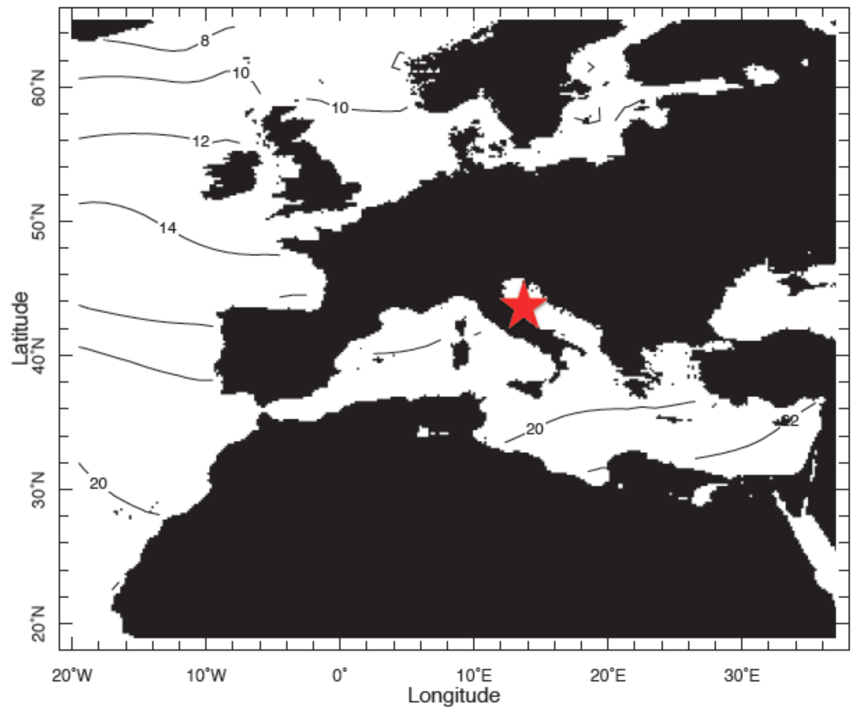

Figure 1.2 Location map of Monte dei Corvi section of uplifted hemipelagic sediments (red star). Modern annual sea surface temperatures are shown after the World Ocean Atlas (NOAA, 2005).

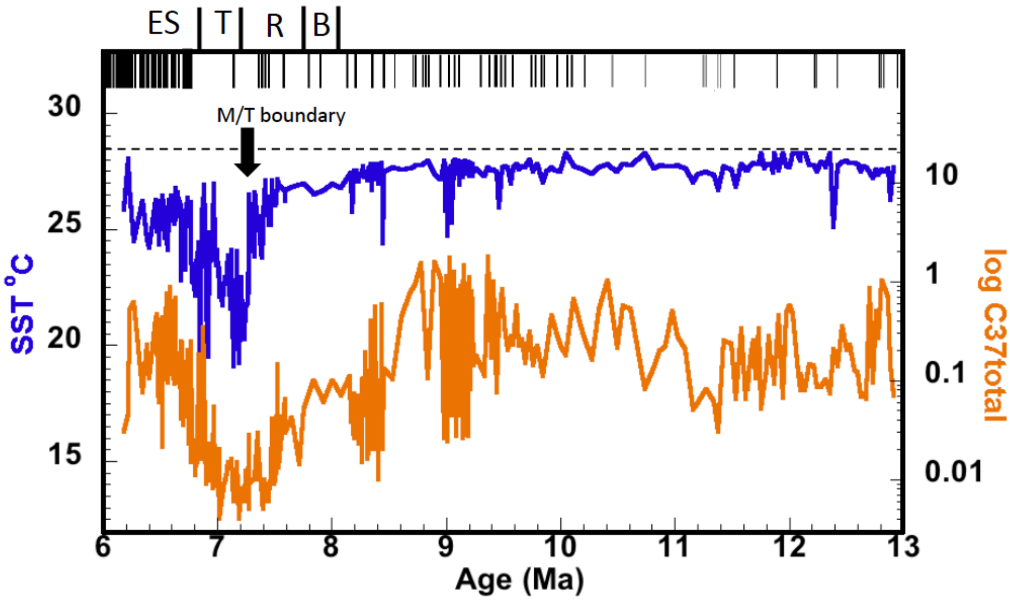

Figure 1.3 Mediterranean SSTs and C_{37}total values (plotted on log scale) derived from alkenone analyses for the Late Miocene. The shaded bars on the top of the panel indicate the positions of sapropels in the Monte dei Corvi section after (Husing et al., 2009). The dashed line shows the upper limit of the Prahl and Wakeham (1988) calibration of the $U^{K'}_{37}$ index for SST. ES indicates Euxinic Shale interval at Monte dei Corvi, T indicates Transitional, R indicates Rossini interval and B indicates Brownish interval.

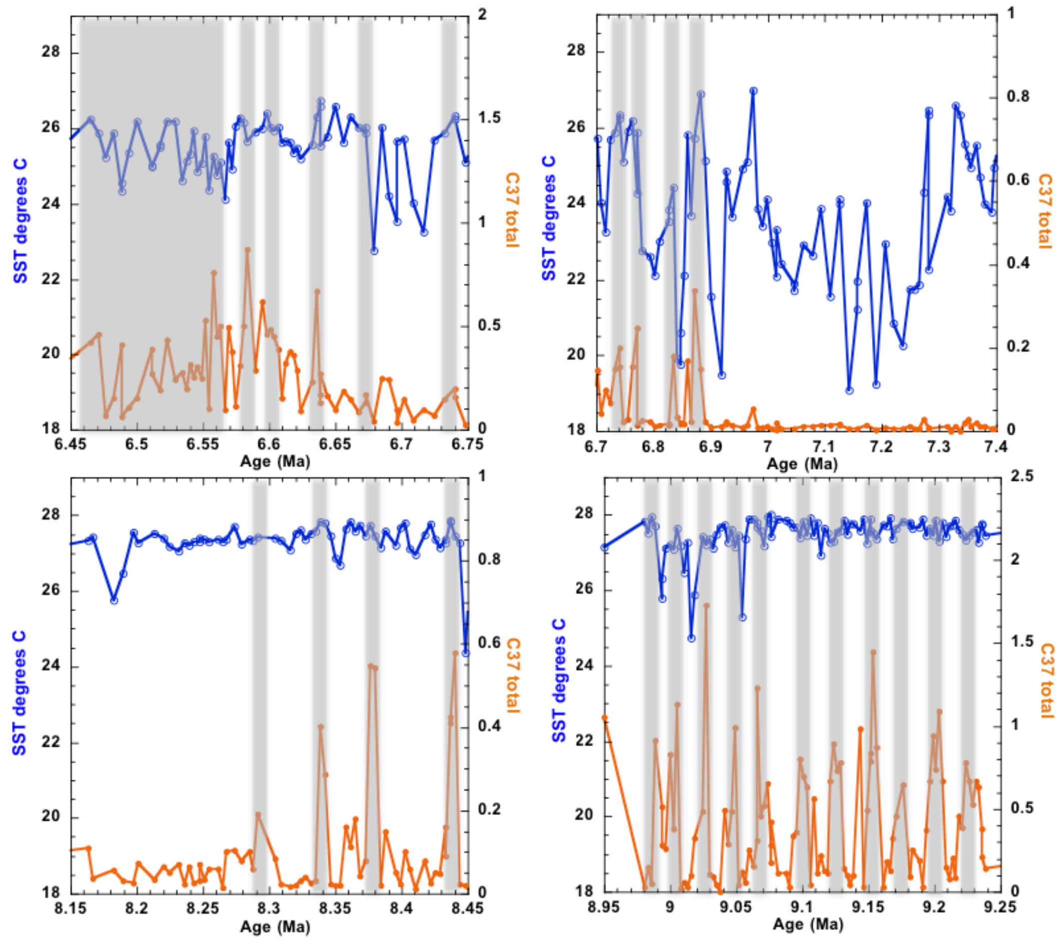

Figure 1.4 Orbitally resolved intervals of Late Miocene Mediterranean SST (open circles) and C_{37}total (closed circles) at Monte dei Corvi. Gray bars show the position of prominent sapropel layers after Husing et al. (2009). Note the change in scale between panels.

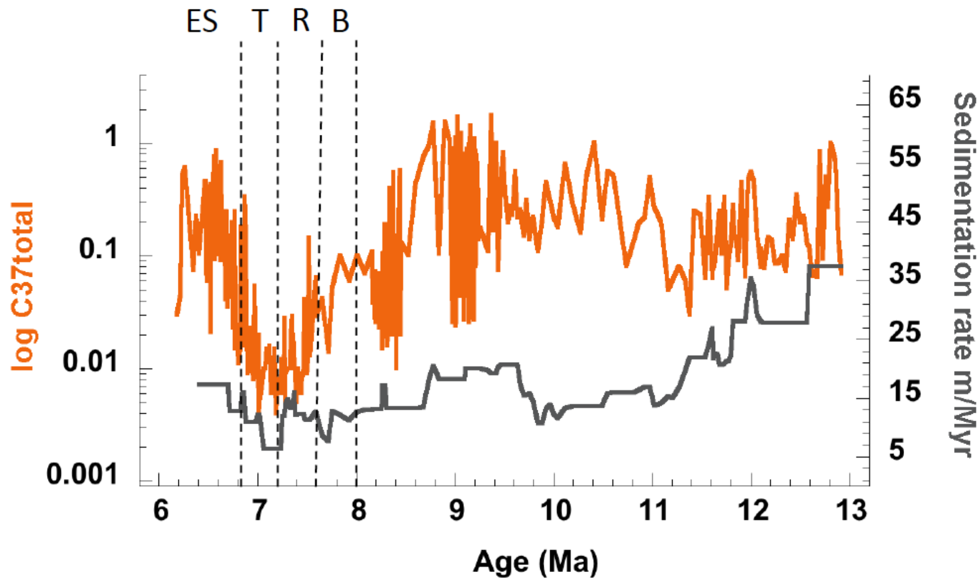

Figure 1.5 Late Miocene Mediterranean C_{37}total (orange) and average sedimentation rate (gray) at Monte dei Corvi after Husing et al. (2009) as determined by orbitally tuned paleomagnetic and biostratigraphic datums (note potential hiatus at ~7.1 Ma). ES indicates Euxinic Shale interval at Monte dei Corvi, T indicates Transitional, R indicates Rossini interval and B indicates Brownish interval.

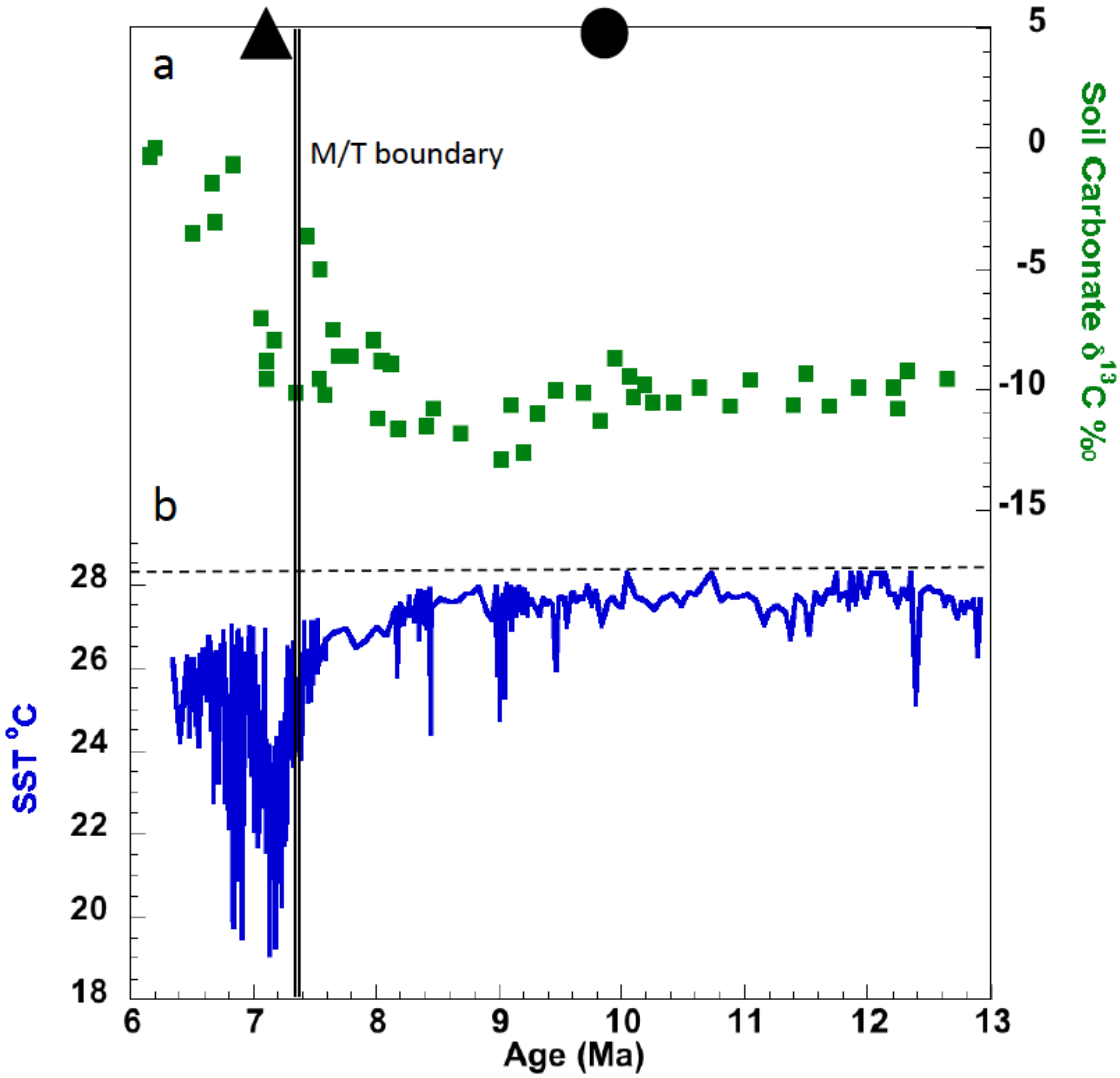

Figure 1.6 Comparison of Mediterranean SSTs and $\delta^{13}C$ of soil carbonates from Pakistan. (a) Pakistani soil carbonate values from Quade and Cerling (1995). (b) Mediterranean SSTs for the Late Miocene, derived from alkenone analyses. The dashed line shows the upper limit of the Prahl and Wakeham (1988) calibration of the $U^{K'}_{37}$ index for SST. The black triangle indicates the first evidence of desert in the Sahara (Schuster et al., 2006; Zhang et al., 2014). The black circle shows the Vallesian crisis in Europe (Bohme et al., 2008). The horizontal double line is the position of the Tortonian/Messinian boundary at 7.246 Ma.

CHAPTER 2

LATE MIOCENE SALINITY RECONSTRUCTIONS FOR THE MEDITERRANEAN SEA BASED ON TEMPERATURE DECONVOLUTION OF PLANKTONIC δ18O TIME SERIES

Alexandrina Tzanova[1]

Timothy D. Herbert[1]

1. *Department of Earth, Environmental and Planetary Sciences, Brown University, Providence, RI 02912*

Abstract

Published $\delta^{18}O$ values of planktonic foraminifera from the Monte del Casino and Gibliscemi sections in central Italy and Sicily are used in conjunction with alkenone-based, sea surface temperature estimates from the Monte dei Corvi section to estimate the salinity component of the isotopic signal ($\delta^{18}O_{Med}$) of the Mediterranean Sea for ~6 Myr (12 – 6 Ma) prior to the isolation and desiccation of the basin at 5.9 Ma. Both isotopic and temperature records contain orbital-scale (dominantly precessionally-driven) and longer variance. Late Miocene $\delta^{18}O_{Med}$ varied by 3‰, similar to the Pleistocene (Emeis et al., 2003), while our inferred mean salinities are similar to modern. Because temperatures in the basin cooled significantly after 7.5 Ma, the revision to the salinity component of planktonic $\delta^{18}O$ becomes significant in the late Tortonian and early Messinian. We therefore revise the timing of the salinity increase preceding Messinian desiccation to begin at ~6.7 Ma and assess the timing of this isolation with terrestrial and marine proxy data previously attributed to early phases of Messinian event. On orbital timescales, $\delta^{18}O_{Med}$ shows precessional scale oscillations that continue through ~6.7 Ma after which we cannot characterize the orbital variance because we lack temporal resolution.

2.1 Introduction

The thick evaporites that lie under the Mediterranean Sea attest to a dramatic event in the history of the basin known as the Messinian Salinity Crisis (MSC) which lasted from 5.9 to 5.3 Ma (Duggen et al., 2003; Hilgen et al., 2007; Hsu et al., 1973; Orszag-Sperber et al., 2009). However, decades after its discovery, several competing hypotheses remain regarding the onset and progression of desiccation (Rogerson et al., 2012; Rogerson et al., 2006)). Tectonic restriction, glacioeustatic changes, and increase in aridity could have led to drastic regional increases in salinity on both tectonic (Myr) and orbital (kyr) timescales, though their individual contributions to the MSC is unresolved (Clauzon et al., 1996; Di Stefano et al., 2010; Gladstone et al., 2007; Perez-Asensio et al., 2013).

The most widely cited hypothesis for Mediterranean isolation is tectonic restriction. In the Late Miocene, the Mediterranean communicated with the Atlantic through the Betic and Rifian Corridors in place of the modern Strait of Gibraltar (Gladstone et al., 2007; Husing et al., 2010). Evidence for intermittent closures and restrictions of these corridors exists, such as the appearance of continental fauna in the Betic Foreland basin dating to 9.6 Ma (Martin-Suarez et al., 2012), which indicates a period when the basin was above sea level. Benthic foraminifera faunal abundance from the Mediterranean shows the dominance of low-oxygen and high-salinity tolerant species indicating instances of sluggish communication between the Mediterranean and the global ocean as early as 8.5 Ma, and again at ~7.2 Ma (Kouwenhoven et al., 2003; Seidenkrantz et al., 2000), which the authors attribute to corridor closure. The timing of final closures of the Betic and Rifian Corridors is debated, with a cited range of 6.5 Ma, 6.2 Ma and even later (Perez-Asensio et al., 2012). Restriction of the corridors and sluggish communication between the open ocean and the Mediterranean Sea undoubtedly predated the MSC, but we have yet to constrain the timing of when salinities exceeded the orbital-scale wet-arid variance that runs through millions of years of climate history in the basin (Di Stefano et al., 2010; Husing et al., 2007; Husing et al., 2009; Kohler et al., 2010a; Roveri et al., 2014).

Another predominant hypothesis for Mediterranean isolation invokes glacioeustatic control in the otherwise warm Late Miocene (Butler et al., 1999; Hilgen et al., 2007; Kastens, 1992; Perez-Asensio et al., 2013). Several authors link pre - post MSC strata on both sides of the Gibraltar strait to global marine $\delta^{18}O$ peaks and troughs to suggest that glacioeustasy contributed to the isolation and to the re-flooding of the Mediterranean basin (Aharon et al., 1993; Kastens, 1992; Perez-Asensio et al., 2013). The Betic and Rifian corridors, which connected the Mediterranean to the Atlantic, were relatively shallow (~100m) (Perez-Asensio et al., 2013). Nevertheless, Perez-Asensio et al. (2013) suggest that modest 24 m tectonic uplift is insufficient to isolate the Mediterranean and cannot be considered the ultimate trigger, but a more significant 60m sea-level drop at 5.97 Ma, inferred from benthic isotopes can do that (Kastens, 1992; Perez-Asensio et al., 2013). However, this interpretation depends on accurately correlating Mediterranean strata to onset of MSC and times of sea level change prior to the MSC (Haq et al., 1987; Miller et al., 2011; Zachos et al., 2001).

Lastly, regional climate change might have affected the onset of the MSC by driving the water budget of the basin into more evaporative conditions. The Late Miocene was a time of increasing aridity in North Africa and the Middle East (Griffin, 2002; Schuster et al., 2006a; Steinke et al., 2010; van der Laan et al., 2012), which could have provided an additional forcing on Mediterranean surface salinity. In the Eurasian region, floral and faunal species show a relative increase towards cold and drought tolerant taxa around 8 Ma; however, the final establishment of modern taxa in the region did not occur until much after the MSC in the Pliocene (Bohme et al., 2008; Bohme et al., 2011; Jimenez-Moreno et al., 2008, 2010). Globally, aridity-adapted grasslands proliferated (Cerling et al., 1997; Cerling et al., 1993; Quade and Cerling, 1995), succulents diversified across the mid-latitudes (Arakaki et al., 2011) and in the region of Northern Africa, the first dunes indicative of modern desert conditions in the Sahara date to 7 Ma (Schuster et al., 2006a).

Superimposed on tectonic and glacioeustatic influences on Mediterranean salinity, the regional hydrological cycle could fluctuate drastically on a precessional scale (Hilgen et al., 2007; Hilgen and Krijgsman, 1999; Kohler et al., 2010b; Rossignol-Strick, 1985). The resulting dark organic-rich layers (wet phases of climate), alternating with $CaCO_3$-rich light layers (arid phases), demonstrate drastic surface salinity changes the Mediterranean experienced on precessional timescale (Rogerson et al., 2012; Schenau et al., 1999; van der Laan et al., 2012). The precession-controlled cycles persisted up to the MSC (Flores et al., 2005; Hilgen and Krijgsman, 1999; Husing et al., 2009; Kohler et al., 2010a; Steenbrink et al., 2006; Suc et al., 1995), and continued after the basin re-flooded (Husing et al., 2009; Langereis and Hilgen, 1991). The magnitude of precessional scale salinity fluctuations must be quantitatively constrained in order to separate the long-term MSC salinity increase from background variability.

We seek to apply a local temperature correction to available planktonic $\delta^{18}O$ records (Kouwenhoven et al., 1999; Sprovieri et al., 2003; Turco et al., 2001) in order to address the timing and pace of increasingly saline surface conditions leading up to the Messinian desiccation and to estimate the superimposed orbital-scale variance. The planktonic oxygen isotope signal combines the influences of local isotopic exchange with the atmosphere and inputs of fresh water, local sea surface temperature, and global oxygen isotopic signature of seawater, driven by continental ice volume. The available Mediterranean planktonic isotope data come from well-dated, orbitally tuned, uplifted marine sections (Hilgen et al., 2003; Husing et al., 2009; Krijgsman et al., 1997) in the Mediterranean (Figure 2.1). The precession-scale cyclicity in the sections allows for cycle to cycle correlation between the locales, which are on discrete orbitally tuned age models (Kouwenhoven et al., 1999; Sprovieri et al., 2003; Turco et al., 2001). Additionally, orbitally-tuned $\delta^{18}O$ can easily be matched to independent SST from Mediterranean locations with similar age control and minimal gradient in the $\delta^{18}O$ of seawater today (Schmidt et al., 1999).

The concurrent Monte dei Corvi SST record (Tzanova et al., 2015) extends the application of the alkenone paleotemperature proxy ($U^{K'}_{37}$) on Mediterranean marine sections (Cleaveland and Herbert 2009; Beltran, Flores et al. 2011) to the Late Miocene and allows us to isolate $\delta^{18}O_{Med}$, which is the isotopic signature of Mediterranean surface water as recorded by planktonic foraminifera. In the Late Miocene, $\delta^{18}O_{Med}$ reflects the effect of global ice volume, regional salinity and regional temperature. We constrain the $\delta^{18}O_{Med}$ component of Mediterranean $\delta^{18}O$ by correlating the temperature time series from Monte dei Corvi to the published planktonic $\delta^{18}O$ data (Figure 2.2). The temperature correction is especially important in the 7.2 – 6.7 Ma interval when SST cooled drastically (Tzanova et al., 2015).

2.2 Background

The Late Miocene oxygen isotope records are based on mixed planktonics from the Monte del Casino section in the period of 7.5 – 6.3 Ma, sampled at a temporal resolution that varies between 10 – 40 kyr (Kouwenhoven et al., 1999), and from *G. quadrilobatus* from the Gibliscemi section between 7.5 – 12.1 Ma at a resolution of 3 – 7 kyr (Sprovieri et al., 2003; Turco et al., 2001) (Figures 2.1 and 2.2). The SST record from the Monte dei Corvi section spans 12.9 – 6.3 Ma (Tzanova et al., 2015) at an average resolution of 20 kyr, with orbitally resolved windows (Figure 2.3). Neither the isotope nor the SST reconstructions extend to the canonical onset of the crisis as defined by evaporite deposits at ~5.9 Ma (Roveri et al., 2014); however, projecting the $\delta^{18}O_{Med}$ component up to 5.9 Ma provides a useful view of the pace of desiccation leading to the MSC.

Mediterranean surface conditions vary greatly on both long (tectonic) and short (orbital) timescales. The range (combining orbital and long-term components) in planktonic foraminifera Mediterranean $\delta^{18}O$ must indicate either regional temperature and/or salinity changes over the Late Miocene, which we can isolate with a temperature deconvolution. This is particularly important because the desiccation of the Mediterranean was not a singular event, but rather a progression over a poorly specified interval of time. Therefore, we propose a re-evaluation of evidence interpreted as Mediterranean isolation in the context of orbital and long-term variance in both salinity and temperature. For example, the first occurrence of *Globorotalia conomiozea* in the Mediterranean at the Tortonian/Messinian boundary (T/M) at 7.25 Ma (Hodell et al., 1989; Krijgsman et al., 1995) and the inferred reduction in deep-water ventilation shortly after at 7.15 Ma (Kouwenhoven et al., 2003; Kouwenhoven et al., 1999; Seidenkrantz et al., 2000) could be driven by salinity, temperature or another change in basin conditions. Similarly, deposition of diatom-rich and opal-rich sediments increased between 7.15 – 6.7 Ma and following this sedimentation shift the Mediterranean experienced an abrupt crash in calcareous plankton diversity at 6.7 Ma (Roveri et al., 2014). The impending desiccation of the basin at the MSC has tended to dominate interpretations of preceding micropaleontological and lithological changes.

In the Mediterranean, $\delta^{18}O$ of planktonic foraminifera in conjunction with $U^{K'}_{37}$ based SST estimates reproduce patterns of $\delta^{18}O_{Med}$ (temperature deconvolved $\delta^{18}O$) depletion during sapropel formation in the late Quaternary (Emeis et al., 2003). The $U^{K'}_{37}$ index uses the relative abundance of alkenones haptophyte algae produced and correlates to mean annual SST (Herbert, 2003; Muller et al., 1998; Prahl and Wakeham, 1988). We assume that any seasonal bias, in either the alkenone or planktonic $\delta^{18}O$ proxy, is dwarfed by precessional and tectonic scale variance in either proxy during the Late Miocene, and that SSTs at Monte dei Corvi are representative of SST at all sites. Today, the distance between our sites (Figure 2.1) represents a 1.5°C range in SST (NOAA, 2005) and ~0.5 ‰ range in surface $\delta^{18}O$ (Pierre, 1999; Schmidt et al., 1999).

2.3 Methods -Temperature deconvolution of the Mediterranean $\delta^{18}O$ signal

We employ the widely used relationship between temperature and $\delta^{18}O$ of planktonic foraminiferal calcite (Erez and Luz, 1983) to isolate $\delta^{18}O_{Med}$ of the Mediterranean (Figure 2.4). The relationship is shown by the equation below:

$$SST = 17.0 - 4.52(\delta^{18}O - \delta^{18}O_{Med}) + 0.03(\delta^{18}O - \delta^{18}O_{Med})^2$$

Our first assumption is that the experimentally derived relationship between $\delta^{18}O$ and temperature (Erez and Luz, 1983) applies to the planktonic species used to generate the isotope records. We assume that this relationship holds for extinct species, for which there is no direct calibration of isotopic values to temperature or $\delta^{18}O_{Med}$. Diagenesis remains an unconstrained variable, especially in the mixed planktonic record of Kouwenhoven et al. (1999), where the authors try to control for it by utilizing a mix of species; however, to what degree it may still affect the final isotope values is unclear. Additionally, we presume that the use of mixed planktonics does not introduce depth or seasonal habitat bias relative to the temperatures recorded by alkenone paleothermometry.

In order to correlate $\delta^{18}O$ to SST values we must interpolate the two proxy records to a common chronology. We assume that multi-investigator, multi-proxy sampling at the Monte dei Corvi, Gibliscemi, and Monte del Casino sections does not lead to an uncertainty greater than half a precessional cycle, and therefore, we can resolve orbital scale variability in a temperature-deconvolved salinity signal to approximately 10 kyr precision. Interpolation produces inherent uncertainty because the temporal resolution of sampling varies between ~3-4 kyr to ~40 kyr between the records. However, our SST record contains orbital resolution windows through the Late Miocene (Figure 2.3), which allows us to constrain the range of orbital SST variance, even if we cannot resolve the orbital temperature component in $\delta^{18}O_{Med}$ continuously in the Late Miocene.

The $\delta^{18}O$ data from Monte del Casino (6.3 – 7.5 Ma) (Kouwenhoven et al., 1999) presented a challenge in that their temporal resolution was notably coarser than the resolution of the other $\delta^{18}O$ data, and furthermore they come from mixed planktonics versus the single species by Turco et al, (2001) and Sprovieri et al, (2003). We selected six samples of similar age from Monte dei Corvi where we previously estimated SST and measured $\delta^{18}O$ to compare to published data from Monte del Casino (Kouwenhoven et al., 1999). Our primary concern was to test if diagenetic processes have altered the primary $\delta^{18}O$ signal in this key interval covering the time considered as harbinger of MSC (Roveri et al., 2014). Additionally, we were concerned that the mixed planktonic signal (Kouwenhoven et al., 1999) might introduce a bias not seen in the single species planktonic $\delta^{18}O$ (Sprovieri et al., 2003; Turco et al., 2001). In order to assess these possibilities, we measured $\delta^{18}O$ on mixed planktonics, mixed benthics and *G. quadrilobatus*. The six analyzed samples represented the examples that had the best-preserved foraminifera; however, that limited our analysis to the 7.1 – 6.7 Ma interval, which falls in an anomalous window of large SST variance, but no sapropels at Monte dei Corvi, because preservation and foraminiferal abundances were too poor in our younger samples. We discuss our findings in more detail in the subsequent sections.

Another assumption we made in our attempt to isolate the salinity component of Mediterranean planktonic $\delta^{18}O$ was to presume that we can discount any notable changes in global $\delta^{18}O$ (Miller et al., 2011) during the study interval overprinted the Mediterranean signal. We correct our isotope balance and salinity inference for global ice build at the high end of Plio-Pleistocene values (+0.5‰) (Zachos et al., 2001), but do not control for short-term isotope excursions as major contributors to our signal. The availability of planktonic $\delta^{18}O$ for this interval is poor; however, the few available, but sparse, records from the North and central Atlantic Ocean (Williams et al., 2005) do not show a notable enrichment concurrent with the trends in Mediterranean $\delta^{18}O$. We cannot constrain the orbital scale variance on the Atlantic side, because no continuous orbital resolution record of planktonic $\delta^{18}O$ from the Atlantic side of Gibraltar exists.

$\delta^{18}O_{Med}$ is essentially modified Atlantic water that enters the Mediterranean, where its isotopic signature changes due to river inflow and evaporation. The Mediterranean, along with the similarly warm, saline and geographically close Red Sea and Persian Gulf, exhibits positively correlated enriched $\delta^{18}O$, high salinities and warm SST, which we consider as the paradigm for the Late Miocene as well. Modern $\delta^{18}O_{Med}$ reflects the competing processes of evaporation (F_{evap}), which enriches the isotopic composition of surface waters; and freshwater input (F_{precip}), which depletes it (Gat, 1996). In a steady state F_{evap}, F_{precip} and the incoming Atlantic water ($F_{Atlantic}$) balance the outflow (F_{out}), which represents both deep-water formation and advection (Gat et al., 1996). The following equation describes the relationship between the mass balance components and their respective isotopic signatures for the Mediterranean:

$$\delta^{18}O_{Med} = F_{Atlantic}\,\delta^{18}O_{Atlantic} + F_{precip}\,\delta^{18}O_{precip} - F_{evap}\,\delta^{18}O_{evap} - F_{out}\,\delta^{18}O_{Med}$$

Table 2.1 lists the individual components and their isotopic signature for the modern Mediterranean. In our efforts to represent the Late Miocene Mediterranean, we utilize the modern values of evaporation and precipitation, but we substitute $\delta^{18}O_{Med}$ with our temperature deconvolved planktonic $\delta^{18}O$ as $\delta^{18}O_{Med}$ and we solve for the change in $F_{Atlantic}$ relative to the Late Miocene. The isotopic composition of $F_{Atlantic}$ in the Late Miocene was undoubtedly different from the modern value; however, for the purposes of an approximation to the change in the Mediterranean hydrologic budget we assume a near modern $\delta^{18}O$ in the Gulf of Cadiz.

In our calculations we cannot quantitatively isolate changes in evaporation or freshwater sources (see Table 2.1), so we treat them as constants in the calculation, which is an unavoidable oversimplification (Griffin, 2002). However, the effects of evaporation and freshwater input remain in the signal and potentially introduces error in our quantification of $F_{Atlantic.}$ We assume a range in the slope relating $\Delta\delta^{18}O_{Med}$ to Δpsu of 0.25 to 0.41 ‰/psu, to represent the uncertainty of the isotopic composition of the freshwater sources and their origins (Emeis et al., 2000; Gat et al., 1996; LeGrande and Schmidt, 2006; Rohling and Bigg, 1998). Thus, our approach to estimate salinity follows previous work that has translated $\delta^{18}O_{Med}$ into psu (Emeis et al., 2003; Emeis et al., 2000; Kallel et al., 1997; Myers et al., 1998; Thunell and Williams, 1989).

2.4 Results

We deconvolve the $\delta^{18}O$ signal with a temperature correction over the period of 12.1 – 6.3 Ma and identify the significant differences between Mediterranean $\delta^{18}O$ and the inferred $\delta^{18}O_{Med}$ component. We cannot continuously constrain the orbital-scale variability in Late Miocene isotopic data, but in the intervals where we do not have orbitally resolved SST, we use the range to estimate the potential contribution of temperature to planktonic $\delta^{18}O$ variance on a precessional scale. We also subdivide our orbital scale analysis of the relationship between SST, $\delta^{18}O$, and $\delta^{18}O_{Med}$ into three different inferred climatic regimes. The first period spans 12.1 Ma up to Tortonian/Messinian boundary (Cleaveland et al., 2002; Hilgen et al., 2003; Schuster et al., 2006a) as this is considered to be the first prominent shift in the Mediterranean marine environment to herald the MSC (Roveri et al., 2014). At Monte dei Corvi, this interval represents a cyclic alternation of limestones, marls and sapropels (Husing et al., 2009). The second division starts with the onset of a major cold episode in the basin that begins at ~7.2 Ma, which coincides with the inception of enrichment in planktonic $\delta^{18}O$ as well and the disappearance of sapropel beds for ~0.4 Myr (Husing et al., 2009). The second interval includes the coldest SST between 7.2 – 6.7 Ma. The third and last division begins at the SST rebound at 6.7 Ma, corresponds to the Euxinic shale interval at Monte dei Corvi (Husing et al., 2009) and continues to the end of the SST record at ~6.3 Ma.

In the first two intervals, which encompass the majority of the Late Miocene, Mediterranean planktonic $\delta^{18}O$ values were ~2‰ more depleted on average than in the Plio-Pleistocene (Kouwenhoven et al., 1999; Lourens, 2004; Sprovieri et al., 2003; Turco et al., 2001; Zachos et al., 2001) (Figure 2.2). However, the Late Miocene Mediterranean SST was significantly warmer than present by 6-10°C (Tzanova et al., 2015), which makes the Late Miocene isotopic depletion expected with the offset due to warmer temperatures and a ~0.5‰ ice volume correction.

The orbital scale correspondence of temperature-deconvolved $\delta^{18}O_{Med}$ follows the documented sapropel-forming conditions of the Plio-Pleistocene (Emeis et al., 2003; Emeis et al., 1998; Emeis et al., 2000). SST and deconvolved $\delta^{18}O_{Med}$ between 12.1 – 7.2 Ma show a weak negative relationship that implies that warmer conditions coincided with depleted $\delta^{18}O_{Med}$ (Figure 2.5), suggestive of Mediterranean freshening at the time of sapropel formation. The relationship between SST and $\delta^{18}O_{Med}$ is likely weakened by interpolation error. We use the high-resolution windows of SST as a template of SST variance for the periods during which the resolution of the SST record is coarser than that of the isotopes. This is another confounding factor; however, the orbitally resolved SST windows suggest a relatively small range in SST, which supports the relationship we infer. We use the orbital scale variance to determine trends outside of the recurring orbital cycles and isolate anomalies, which could herald the MSC.

The mean $\delta^{18}O_{Med}$ for the Late Miocene is 1.08‰ versus the -1.2‰ in $\delta^{18}O$. The variance of the $\delta^{18}O$ signal is 0.68‰ compared to 0.56‰ in $\delta^{18}O_{Med}$. $\delta^{18}O_{Med}$ values (Figure 2.4) oscillate within 2 standard deviations (2σ) of the Late Miocene mean until ~6.9 Ma, after which time they consistently exceed the mean, and at ~6.7 Ma, they become enriched beyond the 2σ envelope (Figure 2.4). Conversely, $\delta^{18}O$ consistently exceeds the Late Miocene mean starting at 7.2 Ma, which is 300 kyr earlier than in the temperature corrected $\delta^{18}O_{Med}$. The beginning of enrichment in the isotope signal changes by 300 – 500 kyr once $\delta^{18}O$ is corrected for SST change.

In the interval from 7.2 – 6.7 Ma, SSTs plummet at the Tortonian/Messinian boundary (Figures 2.2, 2.5-2.6), while planktonic $\delta^{18}O$ show a concurrent enrichment trend (Figures 2.3-2.4). The strong decrease in SST results in a significant temperature correction to the stable isotopic values. Therefore, the $\delta^{18}O$ enrichment does not indicate salinity enhancement, but rather the imprint of cooling that is part of a larger climatic episode in the late Miocene (see Chapter 3).

Surprisingly, for the second and third intervals of interest (represented as the predominantly limestone lithology of the second interval and the Euxinic shales in the third interval), between the Messinian/Tortonian boundary and the end of the record, SST and $\delta^{18}O_{Med}$ are strongly positively correlated (Figure 2.5). This would imply that warmer temperatures coincided with more saline conditions in the Mediterranean, which is the opposite of the well-known sapropel paradigm (Rossignol-Strick, 1985). However, during this period, where our inferred $\delta^{18}O_{Med}$ exhibits a strong enrichment trend, we do not have sufficient temporal resolution to capture precession scale variance, which means that we cannot assess if the sapropel-forming paradigm changed with the approach of the MSC. Additionally, during this time the SST record includes a notable cold event, which may skew the inferred statistical relationship further. In the six samples where we obtained $\delta^{18}O$ the results support the initial statistical relationship inferred from Kouwenhoven et al, (1999) (Figures 2.5 and 2.8), which shows enriched $\delta^{18}O$ corresponding to SST maxima after ~ 7.4 Ma. The findings are valid in both mixed planktonics and *G. quadrilobatus* samples (Figure 2.5) and the measured isotope values are within error of the published record (Kouwenhoven et al., 1999). Age model error and species bias are therefore not the source of the reversal. We enumerate and examine the different explanations in more detail in the discussion section see below. Our mixed benthic data (Figure 2.8) also show good correspondence to the published record (Kouwenhoven et al., 1999) and imply bottom water temperatures 2-4°C cooler than SST. This gradient is significantly reduced compared to the 7°C gradient in the modern Mediterranean, which appears to otherwise persist through much of the Late Miocene (Sprovieri et al., 2003; Turco et al., 2001)

2.5 Discussion

This study seeks to constrain Mediterranean salinity through the Late Miocene in order to evaluate the pace of salinity increase prior to the actual desiccation event at the MSC. We will discuss trends in $\delta^{18}O_{Med}$ as well as calculated salinity.

The deconvolved $\delta^{18}O_{Med}$ spanning 12.1 – 6.3 Ma is a good representation of orbital scale variance in the salinity component in the Mediterranean until the T/M boundary. One exception is a short-lived enrichment at 9.6 Ma, which cannot be attributed to a large temperature decrease at the same time (Figure 2.4) and is outside of the 2σ envelope. It corresponds to the timing of the Vallesian and faunal evidence of at least partial isolation (Perez-Asensio et al., 2012). We infer a regional event, driven by eustatic fall in sea level without a Northern hemisphere temperature component or a temperature component, which we cannot isolate near the limit of the SST proxy (see Chapter 1). Outside of this singular enrichment event the sedimentary cyclicity matches the steady, precession scale variance (Figures 2.4), and we do not see significant trends in the Mediterranean isotope system until the T/M boundary, which marks both a lithological (Hilgen et al., 2003; Husing et al., 2007; Husing et al., 2009) and SST shift (Figures 2.2 and 2.4). SST at that time accounts for only 0.2‰ of the variance in $\delta^{18}O$ values, leaving the vast majority of the signal (~2‰) attributed to cyclical hydrological changes. This range falls within the range reconstructed in the Pleistocene (Emeis et al., 2000), and shows that sapropel and limestone deposition occurred at comparable salinities in the Late Miocene as in the Pliocene.

The major revision to interpreting the planktonic $\delta^{18}O$ record (Figure 2.4) comes at the T/M boundary, which marks the onset of a cold episode in the Mediterranean along with numerous sedimentary shifts (Husing et al., 2009; Roveri et al., 2014). Previous work considers the T/M boundary as the onset of pre-conditioning the Mediterranean for the MSC (Roveri et al., 2014); however, we argue that our SST data show that this event was not accompanied by a change in surface $\delta^{18}O_{Med}$ outside of the 2σ envelope for the

Late Miocene. Indeed, the large SST decrease (Figure 2.4) brings the variance in $\delta^{18}O_{Med}$ well within the range for the Late Miocene up until 6.9- 6.7 Ma, when values systematically exceed the mean. Therefore, temperature and not salinity dominated the basin's surface conditions during this dynamic interval. Furthermore, we now suspect that the cooling is a widespread feature and not a change confined to the basin, as would be needed for a local tectonic hypothesis linking the changes in fauna to early closing.

In order to evaluate competing causes for Mediterranean isolation we focus on estimating how large the reduction in Atlantic water inflow would have to be to lead to the trend and isotope balance that began at ~6.7 Ma. We consider evaporation and rainfall as fixed during this the entire interval, which is an oversimplification, in order to isolate the Atlantic inflow component (see Table 2.1). Evaporation and freshwater input are indisputably linked through humidity and temperature; therefore, an adjustment to one term leads to a shift in the other. The flux and the isotopic signature of precipitation introduce a smaller degree of uncertainty, but they also need to be recognized as ambiguities for the Late Miocene. Unfortunately, in the Late Miocene neither the isotope signatures nor the volumetric flows of the components listed in Table 2.1 have been constrained. Increased evaporation will act in the same direction as decreased Atlantic input, which implies that increasing evaporation as the basin was becoming more isolated can amplify a relatively small reduction in Atlantic inflow. Today evaporation is highly dependent on the origin of air masses over the Mediterranean and can vary between 1.2 - 1.8 times precipitation on a seasonal basis (Gat et al., 1996). Due to its large isotopic signature (Table 2.1), evaporation is a major source of uncertainty in the isotope mass balance (section 2.1). However, we note that the period of significant enrichment (Figure

2.2) post-dates the persistent limestone deposition indicative of dry conditions and instead falls in a predominantly "wet" shale phase (Husing et al., 2009) and low variance in SST (see Chapter 1).

We use a simplified mass balance to derive the approximate decrease in Atlantic input between 6.7 – 6.3 Ma. We prescribe the modern isotope and volumetric fluxes contribution of freshwater to Atlantic water into the Mediterranean, while varying the F_{out} isotope composition. Notable decrease in freshwater sources during this time is indeed possible; however, we treat it as unlikely during this 400 kyr timespan, because the first appearance of the Sahara (Schuster et al., 2006a) and the concurrent thick limestone bed at Monte dei Corvi (Hilgen et al., 2003; Husing et al., 2007; Husing et al., 2009), both signifying an arid period, pre-date the enrichment in $\delta^{18}O_{Med}$ and salinity at 6.7 Ma. These indicators of regional cooling and decreased terrigenous sediment input closely match the timing of cold SSTs. Mediterranean sedimentary cyclicity resumed at Monte dei Corvi once SST rebounded (Husing et al., 2009; Schuster et al., 2006b; Swezey, 2006; Tzanova et al., 2015; Zhang et al., 2014). Prescribing a 1.6‰ signature ($\delta^{18}O_{Med}$ corrected by 0.5‰ for global ice volume) of F_{out} as our initial isotopic composition, we obtain an Atlantic flux analogous to modern (Table 2.1). The 2‰ enrichment above the Late Miocene mean documented in $\delta^{18}O_{Med}$ (Figure 2.4) implies a 60% reduction in Atlantic inflow.

We also convert $\delta^{18}O_{Med}$ to salinity (Figure 2.7) in order to provide a new view into the evolution of Mediterranean surface salinity prior to MSC and evaluate the existing hypotheses for the timing and cause(s) of Mediterranean isolation. Our conversion relates the difference between modern surface $\delta^{18}O_{Med}$ and Late Miocene reconstructed $\delta^{18}O_{Med,}$ and converts it to practical salinity units assuming the $\delta^{18}O$/Salinity constants 0.25 and 0.41. Salinity remained in the 36- 42 psu range on an orbital timescale up to 6.7 Ma (Figure 2.7), which is not far from the range of the modern Mediterranean and conditions in the near-by Red Sea (NOAA, 2005). Salinity values climb to ~47 psu by 6.3 Ma and if the trend is extrapolated to the MSC at 5.9 Ma, then salinities would have reached about 56 psu. These values are not near the 130 psu required for gypsum precipitation nor the 350 psu required for the precipitation of halite (Meijer and Krijgsman, 2005). Thus, rates of desiccation must have increased significantly in the last ~0.4 Ma preceding the MSC.

The newly revised timing of increased salinity and calculated decrease in Atlantic inflow into the Mediterranean can shed light on which Mediterranean events can be considered as part of the pre-conditioning phase of the MSC (Roveri et al., 2014) and which may be unrelated. For example, the first occurrence of *Globorotalia conomiozea* at 7.2 Ma (Hodell et al., 1989; Krijgsman et al., 1995; Roveri et al., 2014), which marks the T/M boundary, is now clearly symptomatic of a large temperature perturbation, but not a concurrent salinity increase (Figure 2.6). Similarly, reduction in deep-water ventilation, as indicated by foraminiferal faunal assemblages (Kouwenhoven et al., 1999; Seidenkrantz et al., 2000), may have resulted from a temperature - aridity driven decrease in nutrient supply not a salinity anomaly. Diatom-rich sediments in the Tripoli formation and opal-rich deposits in southern Spain dated between 7.15 – 6.7 Ma (Roveri et al., 2014) likewise pre-date any change in salinity outside of the precession scale variance. Beginning at 6.7 Ma, documented reorganization in Mediterranean marine fauna and shifts in sediment lithology (Husing et al., 2009; Husing et al., 2010; Roveri et al., 2014) correspond to what we infer to be the onset of a long-term trend in increased salinity. Our reconstruction confirms that the sharp decrease in diversity of calcerous plankton dated to 6.7 Ma corresponds to an increase in the salinity of the surface waters (Roveri et al., 2014 and references within), which also affects stratification, mixing and the nutrient balance of the basin.

We evaluate the existing hypotheses for the onset of MSC, which are currently split between glacioeustatic and tectonic controls. Our deconvolution clearly demonstrates that the progression to MSC must have been a multi step process that began at 6.7 Ma. The salt volume locked beneath the Mediterranean is larger than the salt contained in Mediterranean waters, which presents an obvious conundrum explained by either multiple re-flooding and draw-down events or the presence of a sill so shallow that Mediterranean inflow is completely balanced by the evaporation (Roveri et al., 2014; Topper and Meijer, 2015). Projected salinities at 5.9 Ma do not reach the required levels for gypsum or halite deposition, and therefore rates of salinity increase must have risen after 6.3 Ma. The deconvolved $\delta^{18}O_{Med}$ indicates that evidence previously considered as onset of MSC prior to 6.7 Ma does not link to increased surface salinity and explain why modeling studies face ambiguities when relating their simulation of sill depth restriction to previously inferred Late Miocene conditions (Alhammoud et al., 2010; Topper and Meijer, 2015). Today, the Strait of Gibraltar is relatively shallow at ~300 m (Karami et al., 2009; Stow, 2011), while the depths of the Betic and Rifian Corridors of the Late Miocene are poorly constrained, but likely even shallower at ~100 m (Perez-Asensio et al., 2013), which indicates that tectonic restriction of the corridors can have notable impact, especially if accompanied by sea level fall.

This work demonstrates that neither tectonics nor sea level can independently account for pre-MSC conditions. The strong, persistent increase in $\delta^{18}O_{Med}$ following 6.7 Ma suggests a unidirectional forcing like tectonics, which corresponds to 24m in uplift in the area of the Betic and Rifian Corridors (Perez-Asensio et al., 2013). Uplift can contribute to a reduction of ~60% in incoming Atlantic waters, but falls short of the 50m decrease in sill depth, which modeling shows is in line with our reconstructed water budget and surface salinity (Alhammoud et al., 2010). Reconstructed uplift also does not account for salt precipitation and deposition, which require a greater deficit corresponding to a modeled sill depth of 5-10 m (Topper and Meijer, 2015).

Glacioeustatic control can magnify the effect of tectonic restriction leading to the MSC as first evoked by a 60 m sea level drop at 5.9 Ma based on paleodepth indicated by benthic foraminifera (Perez-Asensio et al., 2013). The earlier history is murky - a pulse of ice rafted debris at 7.3 Ma is the strongest physical evidence of notable ice formation during the Late Miocene, which is concurrent with Mediterranean drop in SSTs (St John, 2008; St John and Krissek, 2002; Tzanova et al., 2015). This major cooling is a singular episode that pre-dates increase in $\delta^{18}O_{Med}$ and therefore does not account for the initial salinity increase at 6.7 Ma. However, the isotope record from ODP Site 982 in the North Atlantic (Hodell et al., 2001) shows an enrichment event at 6.69 Ma, which closely coincides with our revised timing of Mediterranean salinity increase. The isotope record indicates that we cannot discount the role of glaciation driven sea-level drop in the onset of the MSC, especially because a cyclical glacial-interglacial succession overprinted on a tectonically driven isolation trend easily explains the large cycles we observe in $\delta^{18}O_{Med}$ to the very end of the record at 6.3 Ma. We suggest that combined tectonic and sea level fall driven sill depth decrease is the only mechanism supported by our reconstruction.

Lastly, we address the puzzling reversal in the SST and $\delta^{18}O_{Med}$ precessional scale relationship in the 7.2 – 6.3 Ma interval. Prior to the T/M boundary the relationship between SST and $\delta^{18}O_{Med}$ shows a weak correspondence of warmer surface waters to more depleted $\delta^{18}O_{Med}$ values (Figures 2.3 and 2.5). This relationship translates to orbitally paced maxima in SST, freshwater input and organic matter productivity and preservation, most notably in sapropel intervals. In the 7.2 – 6.7 Ma interval the alkenone-derived indices show concurrent relative maxima in SST and C_{37}total indicative of higher haptophyte productivity at warmer temperatures and increased nutrient delivery presumably from increased precipitation and runoff. However, after ~7 Ma, $\delta^{18}O_{Med}$ indicates lower salinities at cold and not warm SST excursions (Figure 2.5), implying the inverse of the sapropel paradigm.

We reproduced the published relationship between planktonic foraminieral $\delta^{18}O$ and SST (Figure 2.5) discounting the possibility of an age model discrepancy between the Monte del Casino and Monte dei Corvi records. Therefore, only a few potential sources of this apparent divergence remain. We cannot discredit a recrystallization overprint on $\delta^{18}O$, as the foraminiferal tests at Monte dei Corvi show signs of poor preservation, and at Monte del Casino Kowenhoven et al., (1999) attempted to mitigate for diagenesis by performing their analysis on mixed species samples. Diagenesis would alter both planktonic and benthic foraminifera and therefore, the gradient between their isotopic signatures can provide some insight into the degree of diagenesis. We compared planktonic $\delta^{18}O$ and benthic $\delta^{18}O$ in the Mediterranean through the Late Miocene to establish the temperature difference that would correspond to the offset between them. Specifically, we wanted to see if there is a notable decrease in the planktonic-benthic gradient that cannot be explained by a surface-deep temperature difference. In the older section of the isotope records (12 – 7.2 Ma) (Sprovieri et al., 2003; Turco et al., 2001) the difference in the isotope indices translates to a 6-7°C gradient between surface and bottom water temperatures. In the Mediterranean, this is analogous to the difference we observe today (NOAA, 2005). However, in the interval between 7.2 – 6.3 Ma the isotope data of Kowenhoven et al. (1999), as well as our data (Figure 2.8), indicate a ~2-4°C difference between bottom water and surface temperatures.

At first glance these findings would suggest diagenesis because of the clear decrease in the offset between surface and bottom water temperatures in this one interval compared to the rest of the Late Miocene. Nevertheless, we must not forget that the pre-MSC Mediterranean could potentially have behaved unlike that for most other periods because water volume decreased, Atlantic inflow decreased, the influence of evaporation and rainfall increased, as did the capacity for mixing. Progressively saltier surface waters would mix more easily with bottom waters and thus decrease the temperature gradient in the water column. In summary, we think there is not sufficient evidence to definitively support or discount diagenesis in the last interval. Therefore, the most likely explanation for the observed puzzling relationship between inferred salinity and temperature is that in this section of the record we do not have precession scale resolution and therefore, the relationship could result from a super-orbital trend. Salinity increased sharply as result of decreased Atlantic inflow pre-MSC, while SST variance remained at ~2°C (Figure 2.4), which led to the observed contradictory relationship for the Mediterranean (Figure 2.5).

2.6 Conclusions

Late Miocene $\delta^{18}O_{Med}$ varied between -0.5‰ to 2.5‰ range between 12.1 and ~6.7 Ma, corresponding to Late Miocene surface salinity between 36-42 psu. The presence of strong Mediterranean cooling at the Tortonian/Messinian boundary significantly changes the interpretation of the available planktonic $\delta^{18}O$ from the region (Kouwenhoven et al., 1999; Sprovieri et al., 2003; Turco et al., 2001). We suggest that previous benthic foraminiferal evidence for changes at 7.2 Ma reflect basin changes related to the cooling, rather than the onset of salinification. We infer unidirectional enrichment in deconvolved $\delta^{18}O_{Med}$ after 6.7 Ma, instead of ~7.2 Ma, to result from the onset of significant tectonic restriction at that time aided by sea level fall. Calculated salinity values climbed to 46 psu by 6.3 Ma, which translates to a 60% decrease in supply of Atlantic waters as inferred by isotopic mass balance. Projected salinities at 5.9 Ma are not sufficient for gypsum or halite deposition, implying that rates of salinification escalated after the end of our deconvolution at 6.3 Ma.

2.7 Acknowledgements

We would like to thank Fabrizio Lirer at the Institute for Coastal Marine Environment IAMC for useful discussions and obtaining the published datasets, April Martin at Brown University for her expertise and help with planktonic foraminifera, Joe Orchardo at Brown University for sample analysis, Rachel Flecker at University of Bristol for her insightful feedback and Alessandro Montanari at the Geological Observatory of Coldigioco for his invaluable help with field work. Additional thanks go to Warren Prell and Steve Clemens for useful insight and feedback. This work was funded by American Chemical Society grant PRF 48032-AC2.

References

Aharon, P., Goldstein, S.L., Wheeler, C.W., Jacobson, G., 1993. Sea-level events in the South-Pacific linked with the Messinian salinity crisis. Geology 21, 771-775.

Alhammoud, B., Meijer, P.T., Dijkstra, H.A., 2010. Sensitivity of Mediterranean thermohaline circulation to gateway depth: A model investigation. Paleoceanography 25.

Arakaki, M., Christin, P.A., Nyffeler, R., Lendel, A., Eggli, U., Ogburn, R.M., Spriggs, E., Moore, M.J., Edwards, E.J., 2011. Contemporaneous and recent radiations of the world's major succulent plant lineages. Proc. Natl. Acad. Sci. U. S. A. 108, 8379-8384.

Bohme, M., Ilg, A., Winklhofer, M., 2008. Late Miocene "washhouse" climate in Europe. Earth Planet. Sci. Lett. 275, 393-401.

Bohme, M., Winklhofer, M., Ilg, A., 2011. Miocene precipitation in Europe: Temporal trends and spatial gradients. Paleogeogr. Paleoclimatol. Paleoecol. 304, 212-218.

Bryden, H.L., Candela, J., Kinder, T.H., 1994. Exchange through the Strait of Gibraltar. Prog. Oceanogr. 33, 201-248.

Butler, R.W.H., McClelland, E., Jones, R.E., 1999. Calibrating the duration and timing of the Messinian salinity crisis in the Mediterranean: linked tectonoclimatic signals in thrust-top basins of Sicily. J. Geol. Soc. 156, 827-835.

Cerling, T.E., Harris, J.M., MacFadden, B.J., Leakey, M.G., Quade, J., Eisenmann, V., Ehleringer, J.R., 1997. Global vegetation change through the Miocene/Pliocene boundary. Nature 389, 153-158.

Cerling, T.E., Wang, Y., Quade, J., 1993. Expansion of C4 ecosystems as an indicator of global ecological change in the Late Miocene. Nature 361, 344-345.

Clauzon, G., Suc, J.P., Gautier, F., Berger, A., Loutre, M.F., 1996. Alternate interpretation of the Messinian salinity crisis: Controversy resolved? Geology 24, 363-366.

Cleaveland, L.C., Jensen, J., Goese, S., Bice, D.M., Montanari, A., 2002. Cyclostratigraphic analysis of pelagic carbonates at Monte dei Corvi (Ancona, Italy) and astronomical correlation of the Serravallian-Tortonian boundary. Geology 30, 931-934.

Di Stefano, A., Verducci, M., Lirer, F., Ferraro, L., Iaccarino, S.M., Husing, S.K., Hilgen, F.J., 2010. Paleoenvironmental conditions preceding the Messinian Salinity Crisis in the Central Mediterranean: Integrated data from the Upper Miocene Trave section (Italy). Paleogeogr. Paleoclimatol. Paleoecol. 297, 37-53.

Duggen, S., Hoernle, K., van den Bogaard, P., Rupke, L., Morgan, J.P., 2003. Deep roots of the Messinian salinity crisis. Nature 422, 602-606.

Emeis, K.C., Schulz, H., Struck, U., Rossignol-Strick, M., Erlenkeuser, H., Howell, M.W., Kroon, D., Mackensen, A., Ishizuka, S., Oba, T., Sakamoto, T., Koizumi, I., 2003. Eastern Mediterranean surface water temperatures and delta O-18 composition during deposition of sapropels in the late Quaternary. Paleoceanography 18.

Emeis, K.C., Schulz, H.-M., Struck, U., Sakamoto, T., Doose, H., Erlenkeuser, H., Howell, M., Kroon, D., Paterne, M., 1998. Stable isotope and alkenone temperature records of sapropels from sites 964 and 968: Constraining the physical environment of sapropel formation in the Eastern Mediterranean Sea, In: Robertson, A.H.F., Emeis, K.C., Richter, C., Camerlenghi, A. (Eds.), Proceedings of the Ocean Drilling Program Scientific Results pp. 309-331.

Emeis, K.C., Struck, U., Schulz, H.M., Rosenberg, R., Bernasconi, S., Erlenkeuser, H., Sakamoto, T., Martinez-Ruiz, F., 2000. Temperature and salinity variations of Mediterranean Sea surface waters over the last 16,000 years from records of planktonic stable oxygen isotopes and alkenone unsaturation ratios. Paleogeogr. Paleoclimatol. Paleoecol. 158, 259-280.

Erez, J., Luz, B., 1983. Experimental paleotemperature equation for planktonic-foraminifera. Geochim. Cosmochim. Acta 47, 1025-1031.

Flores, J.A., Sierro, F.J., Filippelli, G.M., Barcena, M.A., Perez-Folgado, M., Vazquez, A., Utrilla, R., 2005. Surface water dynamics and phytoplankton communities during deposition of cyclic late Messinian sapropel sequences in the western Mediterranean. Mar. Micropaleontol. 56, 50-79.

Gat, J.R., 1996. Oxygen and hydrogen isotopes in the hydrologic cycle. Annu. Rev. Earth Planet. Sci. 24, 225-262.

Gat, J.R., Shemesh, A., Tziperman, E., Hecht, A., Georgopoulos, D., Basturk, O., 1996. The stable isotope composition of waters of the eastern Mediterranean Sea. J. Geophys. Res.-Oceans 101, 6441-6451.

Gladstone, R., Flecker, R., Valdes, P., Lunt, D., Markwick, P., 2007. The Mediterranean hydrologic budget from a Late Miocene global climate simulation. Paleogeogr. Paleoclimatol. Paleoecol. 251, 254-267.

Griffin, D.L., 2002. Aridity and humidity: two aspects of the late Miocene climate of North Africa and the Mediterranean. Paleogeogr. Paleoclimatol. Paleoecol. 182, 65-91.

Haq, B.U., Hardenbol, J., Vail, P.R., 1987. Chronology of fluctuating sea levels since the Triassic. Science 235, 1156-1167.

Herbert, T.D., 2003. Alkenone Paleotemperature Determinations, In: Elderfield, H., Turekian, K.K. (Ed.), Treatise in Marine Geochemistry. Elsevier, pp. 391-432.

Hilgen, F., Kuiper, K., Krijgsman, W., Snel, E., van der Laan, E., 2007. Astronomical tuning as the basis for high resolution chronostratigraphy: the intricate history of the Messinian Salinity Crisis. Stratigraphy 4, 231-238.

Hilgen, F.J., Aziz, H.A., Krijgsman, W., Raffi, I., Turco, E., 2003. Integrated stratigraphy and astronomical tuning of the Serravallian and lower Tortonian at Monte dei Corvi (Middle-Upper Miocene, northern Italy). Paleogeogr. Paleoclimatol. Paleoecol. 199, 229-264.

Hilgen, F.J., Krijgsman, W., 1999. Cyclostratigraphy and astrochronology of the Tripoli diatomite formation (pre-evaporite Messinian, Sicily, Italy). Terr. Nova 11, 16-22.

Hodell, D.A., Benson, R.H., Kennett, J.P., Rakic-El Bied, K., 1989. Stable isotope stratigraphy of latest miocene sequences in northwest Morocco: the Bou Regreg section. Paleoceanography 4, 467-482.

Hodell, D.A., Curtis, J.H., Sierro, F.J., Raymo, M.E., 2001. Correlation of late Miocene to early Pliocene sequences between the Mediterranean and North Atlantic. Paleoceanography 16, 164-178.

Hsu, K.J., Ryan, W.B.F., Cita, M.B., 1973. Late Miocene desiccation of the Mediterranean Nature 242, 240-244.

Husing, S.K., Hilgen, F.J., Aziz, H.A., Krijgsman, W., 2007. Completing the Neogene geological time scale between 8.5 and 12.5 Ma. Earth Planet. Sci. Lett. 253, 340-358.

Husing, S.K., Kuiper, K.F., Link, W., Hilgen, F.J., Krijgsman, W., 2009. The upper Tortonian-lower Messinian at Monte dei Corvi (Northern Apennines, Italy): Completing a Mediterranean reference section for the Tortonian Stage. Earth Planet. Sci. Lett. 282, 140-157.

Husing, S.K., Oms, O., Agusti, J., Garces, M., Kouwenhoven, T.J., Krijgsman, W., Zachariasse, W.J., 2010. On the late Miocene closure of the Mediterranean-Atlantic gateway through the Guadix basin (southern Spain). Paleogeogr. Paleoclimatol. Paleoecol. 291, 167-179.

Jimenez-Moreno, G., Fauquette, S., Suc, J.P., 2008. Vegetation, climate and palaeoaltitude reconstructions of the Eastern Alps during the Miocene based on pollen records from Austria, Central Europe. J. Biogeogr. 35, 1638-1649.

Jimenez-Moreno, G., Fauquette, S., Suc, J.P., 2010. Miocene to Pliocene vegetation reconstruction and climate estimates in the Iberian Peninsula from pollen data. Rev. Palaeobot. Palynology 162, 403-415.

Kallel, N., Paterne, M., Duplessy, J.C., VergnaudGrazzini, C., Pujol, C., Labeyrie, L., Arnold, M., Fontugne, M., Pierre, C., 1997. Enhanced rainfall in the Mediterranean region during the last sapropel event. Oceanol. Acta 20, 697-712.

Karami, M.P., Meijer, P.T., Dijkstra, H.A., Wortel, M.J.R., 2009. An oceanic box model of the Miocene Mediterranean Sea with emphasis on the effects of closure of the eastern gateway. Paleoceanography 24.

Kastens, K.A., 1992. Did glacio-eustatic sea level drop trigger the Messinian salinity crisis? New evidence from Ocean Drilling Program Site 654 in the Tyrrhenian Sea Paleoceanography 7, 333-356.

Kohler, C.M., Heslop, D., Krijgsman, W., Dekkers, M.J., 2010a. Late Miocene paleoenvironmental changes in North Africa and the Mediterranean recorded by geochemical proxies (Monte Gibliscemi section, Sicily). Paleogeogr. Paleoclimatol. Paleoecol. 285, 66-73.

Kohler, C.M., Krijgsman, W., van Hinsbergen, D.J.J., Heslop, D., Dupont-Nivet, G., 2010b. Concurrent tectonic and climatic changes recorded in upper Tortonian sediments from the Eastern Mediterranean. Terr. Nova 22, 52-63.

Kouwenhoven, T.J., Hilgen, F.J., van der Zwaan, G.J., 2003. Late Tortonian-early Messinian stepwise disruption of the Mediterranean-Atlantic connections: constraints from benthic foraminiferal and geochemical data. Paleogeogr. Paleoclimatol. Paleoecol. 198, 303-319.

Kouwenhoven, T.J., Seidenkrantz, M.S., van der Zwaan, G.J., 1999. Deep-water changes: the near-synchronous disappearance of a group of benthic foraminifera from the Late Miocene Mediterranean. Paleogeogr. Paleoclimatol. Paleoecol. 152, 259-281.

Krijgsman, W., Hilgen, F.J., Negri, A., Wijbrans, J.R., Zachariasse, W.J., 1997. The Monte del Casino section (Northern Apennines, Italy): a potential Tortonian/Messinian boundary stratotype? Paleogeogr. Paleoclimatol. Paleoecol. 133, 27-47.

Krijgsman, W., Hilgren, F.J., Langereis, C.G., Santarelli, A., Zachariasse, W.J., 1995. Late Miocene magnetostratigraphy, biostratigraphy and cyclostratigraphy in the Mediterranean. Earth Planet. Sci. Lett. 136, 475-494.

Langereis, C.G., Hilgen, F.J., 1991. The Rossello composite - a Mediterranean and global reference section for the Early to early Late Pliocene. Earth Planet. Sci. Lett. 104, 211-225.

LeGrande, A.N., Schmidt, G.A., 2006. Global gridded data set of the oxygen isotopic composition in seawater. Geophys. Res. Lett. 33.

Lourens, L.J., 2004. Revised tuning of Ocean Drilling Program Site 964 and KC01B (Mediterranean) and implications for the delta O-18, tephra, calcareous nannofossil, and geomagnetic reversal chronologies of the past 1.1 Myr. Paleoceanography 19.

Martin-Suarez, E., Garcia-Alix, A., Minwer-Barakat, R., Agusti, J., Freudenthal, M., 2012. Filling the gap: First evidence of Early Tortonian continental deposits in southern Iberia. J. Vertebr. Paleontol. 32, 1421-1428.

Meijer, P.T., Krijgsman, W., 2005. A quantitative analysis of the desiccation and re-filling of the Mediterranean during the Messinian Salinity Crisis. Earth Planet. Sci. Lett. 240, 510-520.

Miller, K.G., Mountain, G.S., Wright, J.D., Browning, J.V., 2011. A 180-Million-Year Record of Sea Level and Ice Volume Variations from Continental Margin and Deep-Sea Isotopic Records. Oceanography 24, 40-53.

Muller, P.J., Kirst, G., Ruhland, G., von Storch, I., Rosell-Mele, A., 1998. Calibration of the alkenone paleotemperature index U-37(K ') based on core-tops from the eastern South Atlantic and the global ocean (60 degrees N-60 degrees S). Geochim. Cosmochim. Acta 62, 1757-1772.

Myers, P.G., Haines, K., Rohling, E.J., 1998. Modeling the paleocirculation of the Mediterranean: The last glacial maximum and the Holocene with emphasis on the formation of sapropel S-1. Paleoceanography 13, 586-606.

NOAA, 2005. World Ocean Atlas.

Orszag-Sperber, F., Caruso, A., Blanc-Valleron, M.M., Merle, D., Rouchy, J.M., 2009. The onset of the Messinian salinity crisis: Insights from Cyprus sections. Sediment. Geol. 217, 52-64.

Perez-Asensio, J.N., Aguirre, J., Jimenez-Moreno, G., Schmiedl, G., Civis, J., 2013. Glacioeustatic control on the origin and cessation of the Messinian salinity crisis. Glob. Planet. Change 111, 1-8.

Perez-Asensio, J.N., Aguirre, J., Schmiedl, G., Civis, J., 2012. Messinian paleoenvironmental evolution in the lower Guadalquivir Basin (SW Spain) based on benthic foraminifera. Paleogeogr. Paleoclimatol. Paleoecol. 326, 135-151.

Pierre, C., 1999. The oxygen and carbon isotope distribution in the Mediterranean water masses. Mar. Geol. 153, 41-55.

Prahl, F.G., Wakeham, S.G., 1988. Calibration of unsaturation patterns in long-chain ketone compositions for paleotemperature assessment Nature 330, 367-369.

Quade, J., Cerling, T.E., 1995. Expansion of C-4 grasses in the Late Miocene of Northern Pakistan - evidence from stable isotopes in paleosols Paleogeogr. Paleoclimatol. Paleoecol. 115, 91-116.

Rogerson, M., Rohling, E.J., Bigg, G.R., Ramirez, J., 2012. Paleoceanography of the Atlantic-Mediterranean exchange: overview and first quantitative assessment of climatic forcing. Rev. Geophys. 50.

Rogerson, M., Rohling, E.J., Weaver, P.P.E., 2006. Promotion of meridional overturning by Mediterranean-derived salt during the last deglaciation. Paleoceanography 21.

Rohling, E.J., Bigg, G.R., 1998. Paleosalinity and delta O-18: A critical assessment. J. Geophys. Res.-Oceans 103, 1307-1318.

Rossignol-Strick, M., 1985. Mediterranean quaternary sapropels, and immediate response of the African monsoon to variation of insolation. Paleogeogr. Paleoclimatol. Paleoecol. 49, 237-263.

Roveri, M., Flecker, R., Krijgsman, W., Lofi, J., Lugli, S., Manzi, V., Sierro, F.J., Bertini, A., Carnerlenghi, A., De Lange, G., Govers, R., Hilgen, F.J., Hubscher, C., Meijer, P.T., Stoica, M., 2014. The Messinian Salinity Crisis: Past and future of a great challenge for marine sciences. Mar. Geol. 352, 25-58.

Sanchez-Gomez, E., Somot, S., Josey, S.A., Dubois, C., Elguindi, N., Deque, M., 2011. Evaluation of Mediterranean Sea water and heat budgets simulated by an ensemble of high resolution regional climate models. Clim. Dyn. 37, 2067-2086.

Schenau, S.J., Antonarakou, A., Hilgen, F.J., Lourens, L.J., Nijenhuis, I.A., van der Weijden, C.H., Zachariasse, W.J., 1999. Organic-rich layers in the Metochia section (Gavdos, Greece): evidence for a single mechanism of sapropel formation during the past 10 My. Mar. Geol. 153, 117-135.

Schmidt, G.A., Bigg, G.R., Rohling, E.J., 1999. Global Seawater Oxygen-18 Database - v1.21.

Schuster, M., Duringer, P., Ghienne, J.F., Vignaud, P., Mackaye, H.T., Likius, A., Brunet, M., 2006a. The age of the Sahara Desert. Science 311, 821-821.

Schuster, M., Duringer, P., Ghienne, J.F., Vignaud, P., Mackaye, H.T., Likius, A., Brunet, M., 2006b. Revisiting the age of the Sahara desert - Response. Science 312, 1139-1139.

Seidenkrantz, M.S., Kouwenhoven, T.J., Jorissen, F.J., Shackleton, N.J., van der Zwaan, G.J., 2000. Benthic foraminifera as indicators of changing Mediterranean-Atlantic water exchange in the late Miocene. Mar. Geol. 163, 387-407.

Sprovieri, M., Sacchi, M., Rohling, E.J., 2003. Climatically influenced interactions between the Mediterranean and the Paratethys during the Tortonian. Paleoceanography 18.

St John, K., 2008. Cenozoic ice-rafting history of the central Arctic Ocean: Terrigenous sands on the Lomonosov Ridge. Paleoceanography 23.

St John, K., Krissek, L.A., 2002. The late Miocene to Pleistocene ice-rafting history of southeast Greenland. Boreas 31, 28-35.

Steenbrink, J., Hilgen, F.J., Krijgsman, W., Wijbrans, J.R., Meulenkamp, J.E., 2006. Late Miocene to Early Pliocene depositional history of the intramontane Florina-Ptolemais-Servia Basin, NW Greece: Interplay between orbital forcing and tectonics. Paleogeogr. Paleoclimatol. Paleoecol. 238, 151-178.

Steinke, S., Groeneveld, J., Johnstone, H., Rendle-Buhring, R., 2010. East Asian summer monsoon weakening after 7.5 Ma: Evidence from combined planktonic foraminifera Mg/Ca and delta(18)O (ODP Site 1146; northern South China Sea). Paleogeogr. Paleoclimatol. Paleoecol. 289, 33-43.

Stow, D., Hernandez-Molina, F.J., Hodell, D., and Alvarez Zarikian, C.A., 2011. Mediterranean outflow: environmental significance of the Mediterranean Outflow Water and its global implications. IODP Sci. Prosp 339.

Suc, J.P., Violanti, D., Londeix, L., Poumot, C., Robert, C., Clauzon, G., Gautier, F., Turon, J.L., Ferrier, J., Chikhi, H., Cambon, G., 1995. Evolution of the Messinian Mediterranean environments - the Tripoli formation at Capodarso (Sicily, Italy) Rev. Palaeobot. Palynology 87, 51-79.

Swezey, C.S., 2006. Revisiting the age of the Sahara desert. Science 312, 1138-1139.

Thunell, R.C., Williams, D.F., 1989. Glacial-Holocene salinity changes in the Mediterraenan Sea - hydrographic and depositional effects Nature 338, 493-496.

Topper, R.P.M., Meijer, P.T., 2015. Changes in Mediterranean circulation and water characteristics due to restruction of the Atlantic Connection: a high-resolution model. Clim. Past. 11, 233-251.

Turco, E., Hilgen, F.J., Lourens, L.J., Shackleton, N.J., Zachariasse, W.J., 2001. Punctuated evolution of global climate cooling during the late Middle to early Late Miocene: High-resolution planktonic foraminiferal and oxygen isotope records from the Mediterranean. Paleoceanography 16, 405-423.

Tzanova, A., Herbert, T., Peterson, L.C., 2015. Cooling Mediterranean sea surface temperatures during the Late Miocene provide a climate context for evolutionary transitions in Africa and Eurasia. Earth Planet. Sci. Lett. 419, 71-80.

van der Laan, E., Hilgen, F.J., Lourens, L.J., de Kaenel, E., Gaboardi, S., Iaccarino, S., 2012. Astronomical forcing of Northwest African climate and glacial history during the late Messinian (6.5-5.5 Ma). Paleogeogr. Paleoclimatol. Paleoecol. 313, 107-126.

Williams, M., Haywood, A.M., Taylor, S.P., Valdes, P.J., Sellwood, B.W., Hillenbrand, C.D., 2005. Evaluating the efficacy of planktonic foraminifer calcite delta O-18 data for sea surface temperature reconstruction for the Late Miocene. Geobios 38, 843-863.

Zachos, J., Pagani, M., Sloan, L., Thomas, E., Billups, K., 2001. Trends, rhythms, and aberrations in global climate 65 Ma to present. Science 292, 686-693.

Zhang, Z.S., Ramstein, G., Schuster, M., Li, C., Contoux, C., Yan, Q., 2014. Aridification of the Sahara desert caused by Tethys Sea shrinkage during the Late Miocene. Nature 513, 401-+.

Table 2.1 Modern Mediterranean mass balance

Component	**Flux** x10^{12} m^3/y	$\delta^{18}O$ ‰	**Source**
$F_{Atlantic}$	22.70	0.6-0.7	(Bryden et al., 1994; Gat et al., 1996; Schmidt et al., 1999)
F_{precip}	1.15	~-7	(Gat et al., 1996)
F_{evap}	2.42	~ -12	(Gat et al., 1996; Sanchez-Gomez et al., 2011)
F_{out}	$F_{Atlantic}$ - F_{evap} + F_{precip}		(Bryden et al., 1994; Gat et al., 1996; Sanchez-Gomez et al., 2011; Stow, 2011)

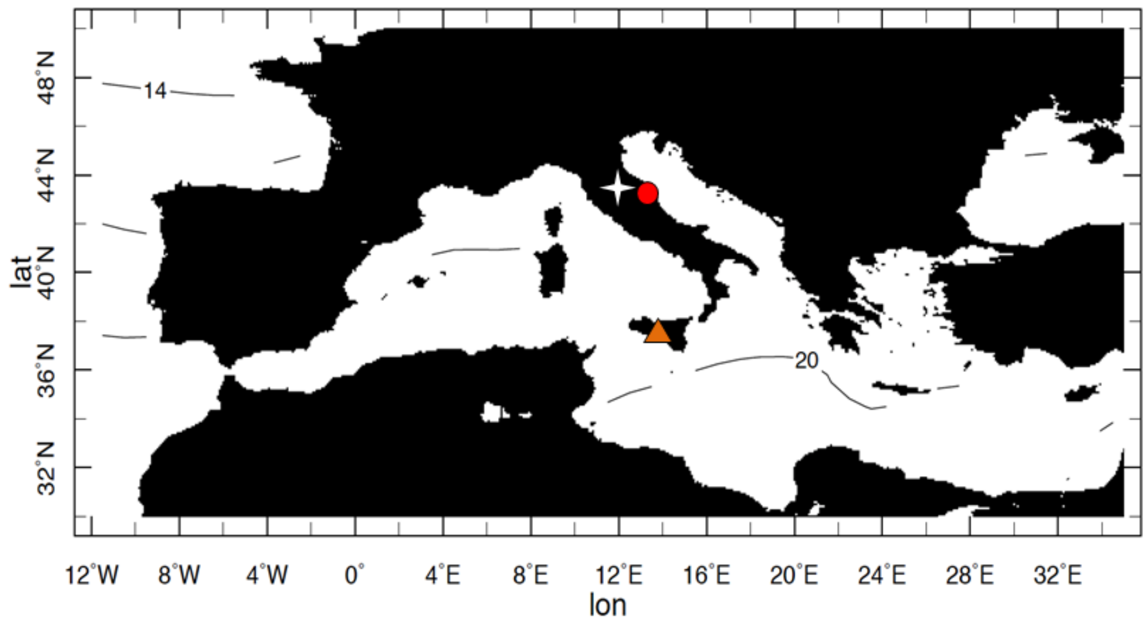

Figure 2.1 Location map of Monte dei Corvi section (circle), Monte dei Casino (star) and Monte Gibliscemi (triangle). Modern sea surface temperatures are shown after the World Ocean Atlas (NOAA, 2005).

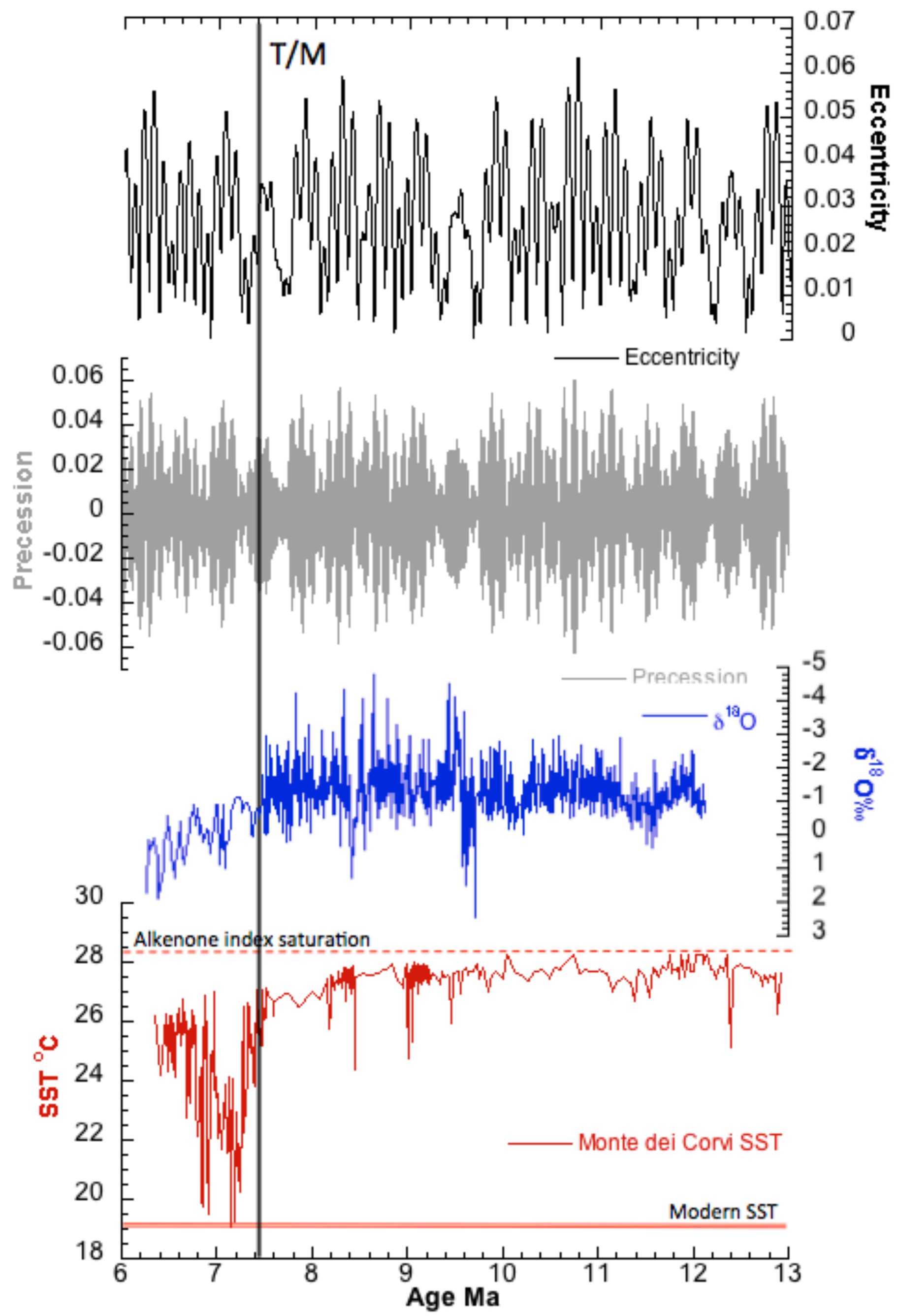

Figure 2.2 Late Miocene orbital configuration of eccentricity (black), precession and (gray) spanning the time period covered by the records. Published $\delta^{18}O$ after Kouwenhoven et al. (1999), Turco et al. (2001) and Sprovieri et al. (2003) in blue (Monte del Casino 7.5 – 6.3 Ma and Gibliscemi 12-1 – 7.5 Ma). Monte dei Corvi sea surface temperatures after Tzanova et al, (Accepted) in red. Black vertical line denotes the T/M boundary.

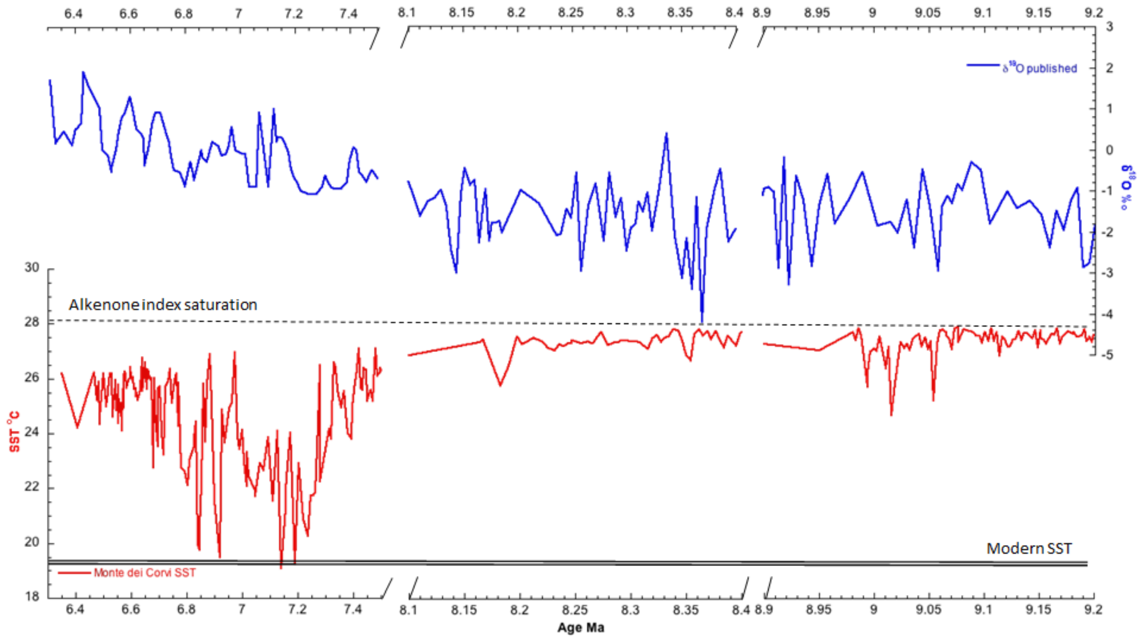

Figure 2.3 High-resolution windows of SST (red) and the corresponding $\delta^{18}O$ after Kouwenhoven et al. (1999), Turco et al. (2001) and Sprovieri et al. (2003) in blue.

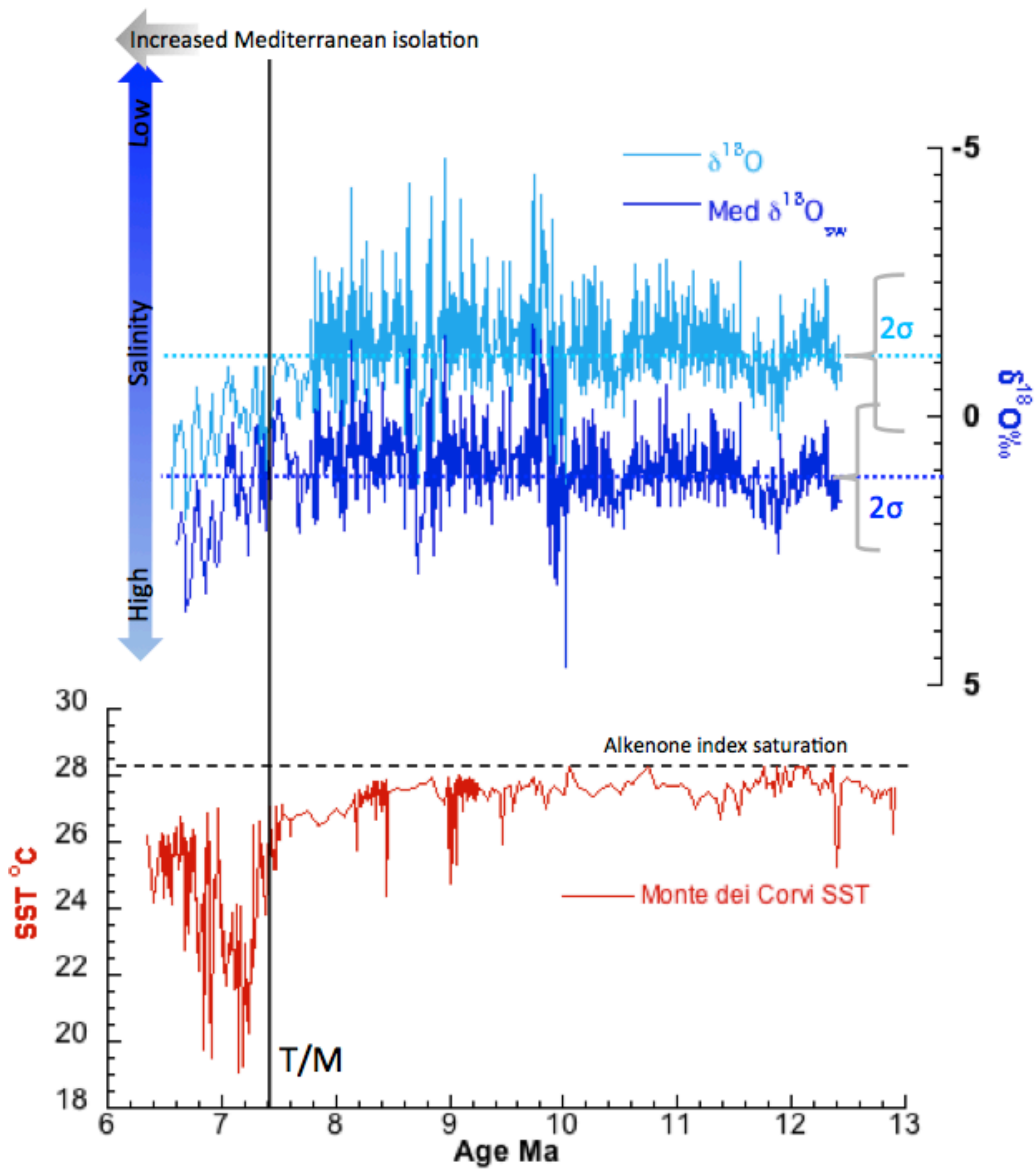

Figure 2.4 Published $\delta^{18}O$ after Kouwenhoven et al., 1999, Turco et al., 2001 and Sprovieri et al., 2003 in light blue and deconvolved $\delta^{18}O_{Med}$ in dark blue. Dashed line is the Late Miocene mean with 2 sigma range shown by brackets. Monte dei Corvi SST in red. Black vertical line denotes the T/M boundary.

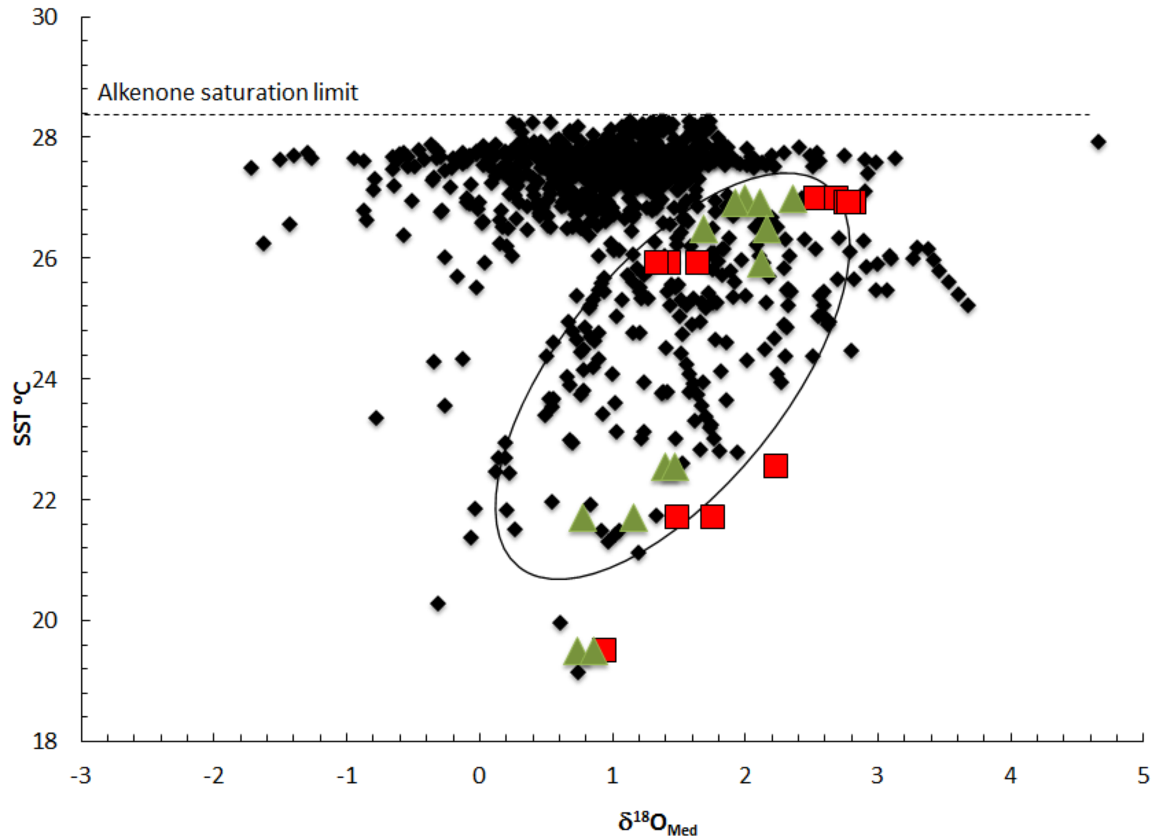

Figure 2.5 Scatter plot of $\delta^{18}O_{Med}$ and SST depicting the relationship between the variables between 6.3 – 12.1 Ma. The circled data shows the period of ~6.4 – 7.3 Ma where warmer SST correspond to higher productivity and higher surface salinity as inferred by $\delta^{18}O_{Med}$. The replicated on Monte dei Corvi samples $\delta^{18}O_{Med}$ from G. quadrilobatus (red squares) and mixed planktonics (green triangles) covers the period of 7.2 – 6.7 Ma.

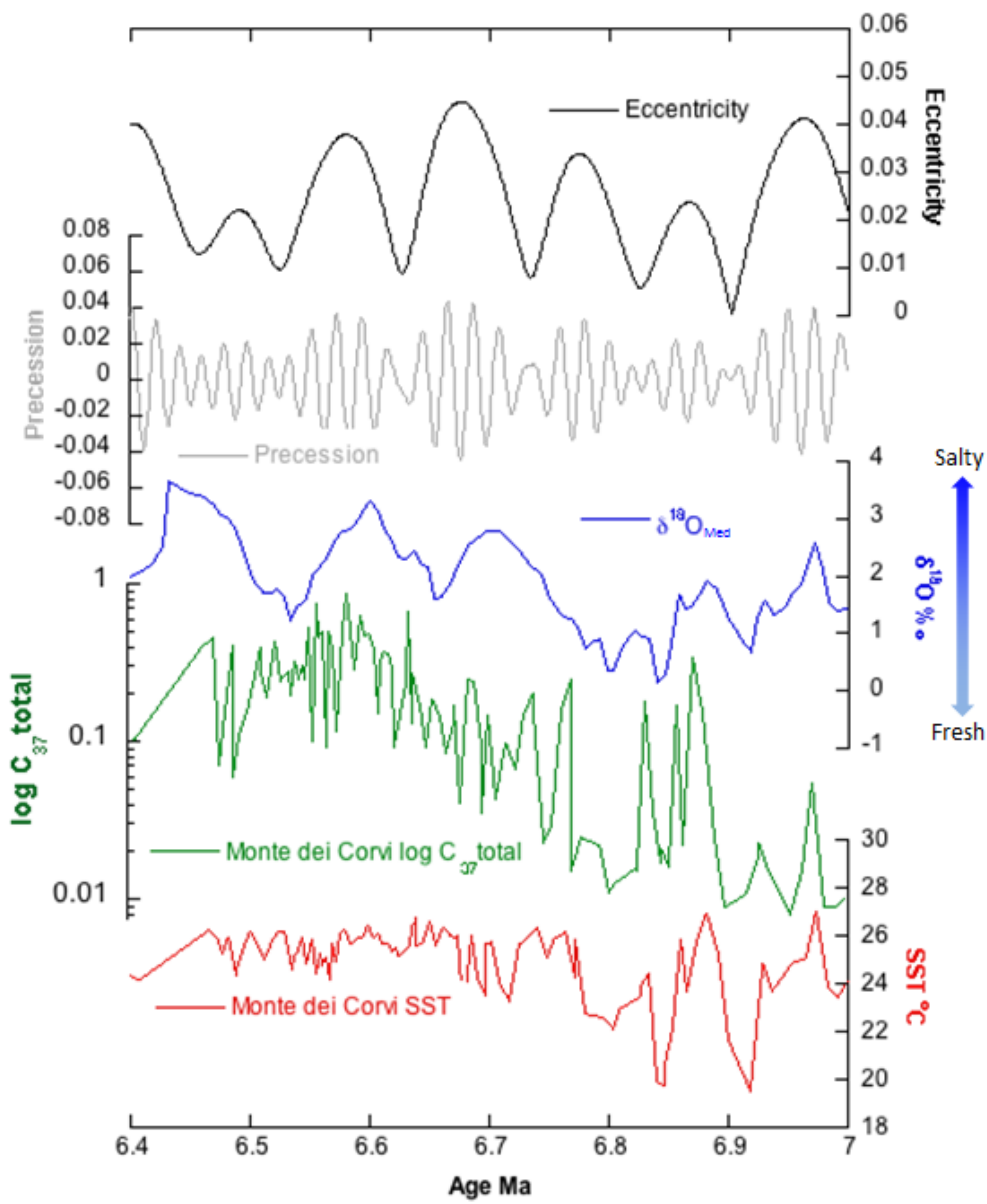

Figure 2.6 Orbital configuration of eccentricity (black), precession (gray) between 6.4 – 7 Ma. Deconvolved $\delta^{18}O_{Med}$ in blue. C_{37}total (green) and SST (red) at Monte dei Corvi spanning the concurrent time period.

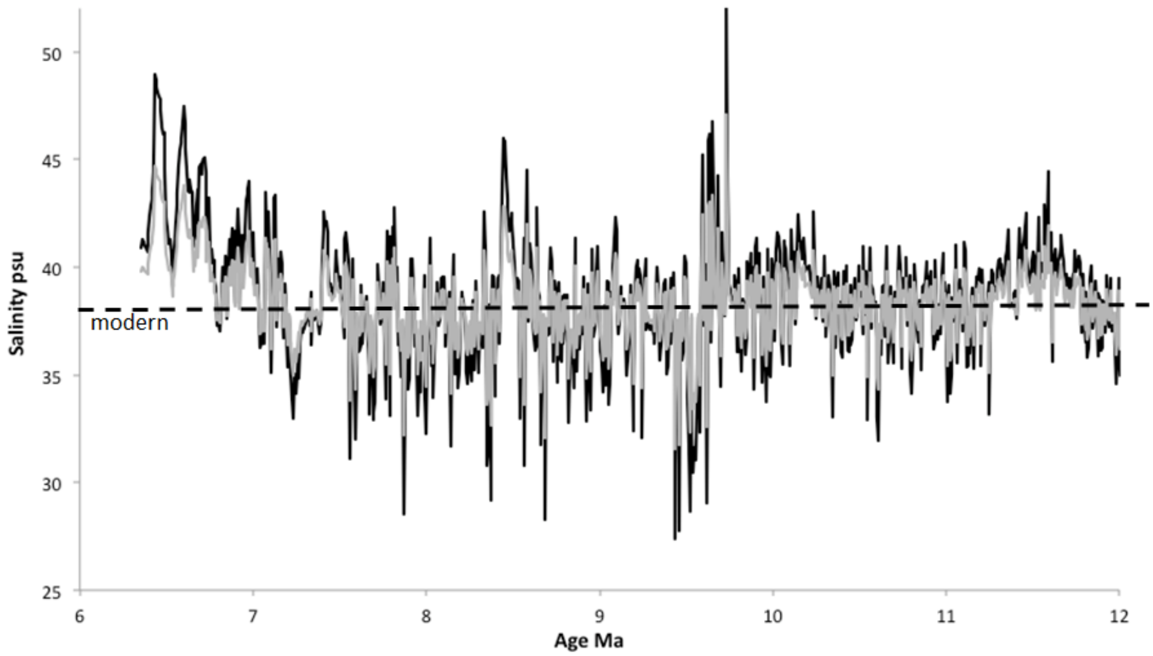

Figure 2.7 Salinity calculation based on deconvolved $\delta^{18}O$ based on two constants, 0.41 (black) and 0.25 (gray), relating salinity and $\delta^{18}O_{Med}$.

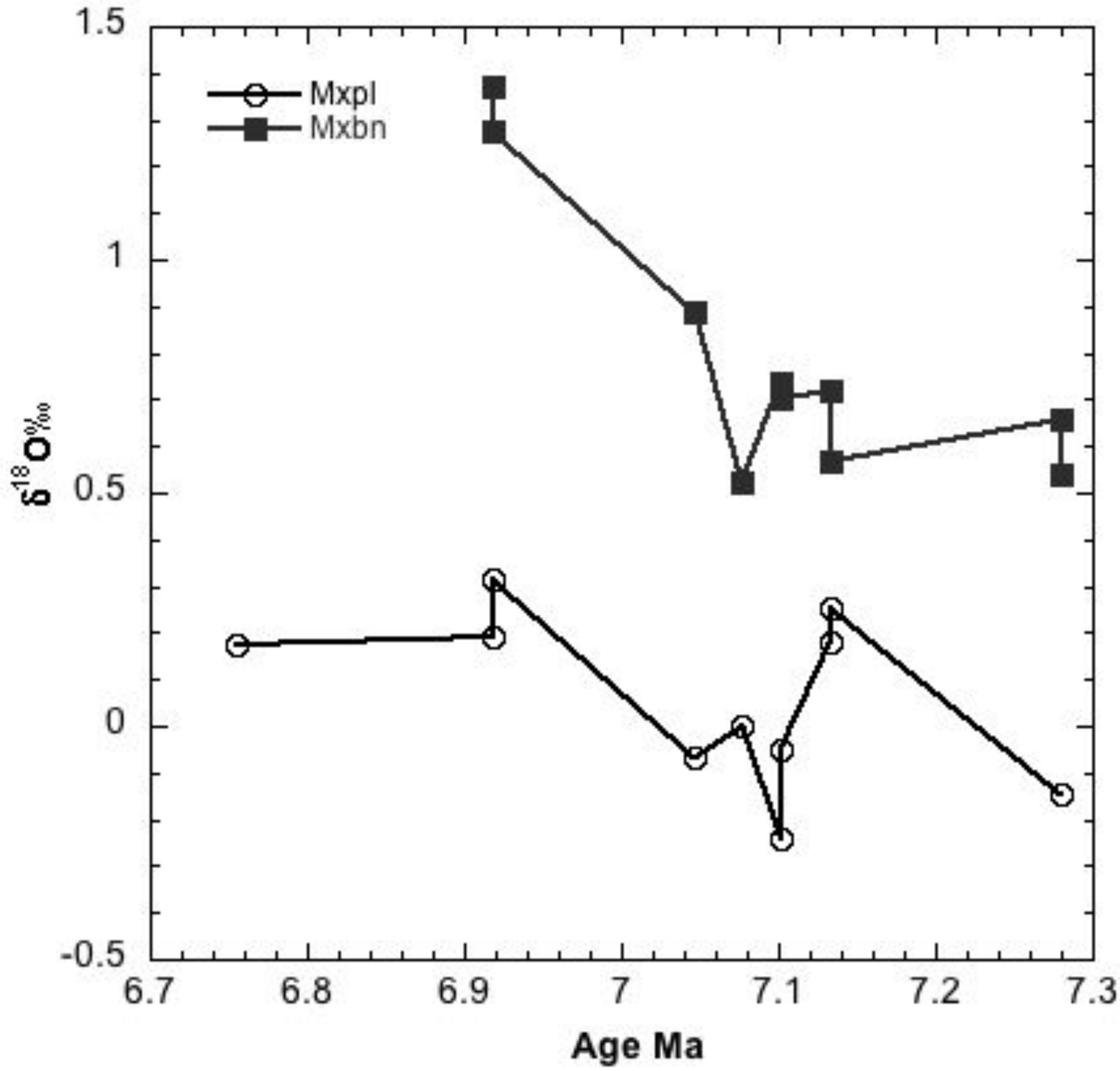

Figure 2.8 Planktonic and benthic $\delta^{18}O$ from Monte dei Corvi.

CHAPTER 3

GLOBAL COOLING IN THE LATE MIOCENE ACCOMPANIES TERRESTRIAL BIOME SHIFTS

Alexandrina Tzanova[1]

Timothy D. Herbert[1]

Kira T. Lawrence[2]

Chris Kelly[1]

1. *Department of Earth, Environmental and Planetary Sciences, Brown University, Providence, RI 02912*
2. *Department of Geology and Environmental Geosciences, Lafayette College, Easton, PA 18042*

Abstract

The first appearance of dunes in the Sahara, global expansion of grasslands, diversification of succulent flora and important steps on the road to bipedalism and hominoid evolution all date to a narrow window between 6 – 8 Ma. Paradoxically, deep sea stable isotope records and reconstructions of atmospheric CO_2 for the same time period lack evidence of rapid cooling, while ice rafted debris from the Northern hemisphere suggests terrestrial transitions have a correspondence to evidence for an episode of high latitude Northern Hemisphere glaciation. New alkenone-based sea surface temperatures (SST) from six globally distributed sites: ODP Sites 907 and 982 in the North Atlantic, ODP Site 1088 in the South Atlantic and ODP Sites 883, 884 and 887 in the North Pacific, and the Monte dei Corvi marine section in the Mediterranean unequivocally establish a dramatic, Late Miocene cold episode of approximately 2.5 Myr duration. All sites were 5 – 15°C warmer than their modern annual average at ~9 Ma and exhibit sustained cooling beginning at ~8 Ma. The cooling reverses in the earliest Pliocene (~5.6 Ma). The newly reconstructed SSTs highlight the role of cooling and an increase in equator to pole temperature gradients in terrestrial evolution at this time. SSTs suggesting that Late Miocene cooling poised the Northern Hemisphere near the threshold for onset of large continental glaciation. The spatial extent of the cold episode implicates a global causal mechanism such as CO_2, which calls into question the validity of currently available reconstructions of CO_2.

3.1 Introduction

Modern terrestrial biomes can trace their origins to a narrow window in the Late Miocene beginning at around ~8 Ma, the climate history of which is still poorly constrained. The best-known shift is the well-documented global expansion of C_4 grasslands between 6 – 8 Ma (Behrensmeyer et al., 2007; Cerling et al., 1997; Cerling et al., 1993; Ehleringer et al., 1997; Quade and Cerling, 1995). Concurrently, cacti and other succulent plants expanded their range and increased their diversity across most continents (Arakaki et al., 2011). Notable regional transitions such as the first desert dunes in the Sahara date to ~7 Ma (Schuster et al., 2006). Likewise in Africa the roots of bi-pedalism began at 6 Ma and 7 Ma (Agusti et al., 2013; Agusti et al., 2003; Brunet, 2010).

The proxy records of global climate during such well-constrained in time biome transitions present a paradoxical view of stable warmth during dynamic evolution accompanied by some evidence of sporadic and enigmatic glaciations (Krissek, 1995; Rea et al., 1993; St John and Krissek, 2002a; St John and Krissek, 2002b)(Figure 3.1). The reconstructions of atmospheric CO_2 (Figure 3.1), which are low-resolution, indicate that values remained in the last glacial maximum to pre-industrial range (Demicco et al., 2003; Pagani et al., 1999; Pagani et al., 2010; Tipple et al., 2010; Zhang et al., 2013) at a time when the Northern hemisphere lacked large continental ice sheets. The global benthic $\delta^{18}O$ stack (Cramer et al., 2009; Zachos et al., 2001), which records ice volume and ocean bottom water temperatures, shows no large cold or ice-forming excursions and overall warm conditions at ~7-8 Ma. Many authors have combined the atmospheric and marine records to hypothesize that the Late Miocene was a monotonously warm period during which the Earth had a different sensitivity to CO_2 (LaRiviere et al., 2012; Pagani et al., 2010). Under such interpretations the predominant mechanism for biome transformation such as the expansion of grasslands is aridification and not cooling (Edwards et al., 2010; Huang et al., 2007; Pagani et al., 1999; Scheiter et al., 2012). However, evidence of ice rafted debris (IRD) symptomatic of sporadic glaciation in the Northern hemisphere around ~7 Ma (Krissek, 1995; Lagoe et al., 1993; St John, 2008; St John and Krissek, 2002a) presents an obvious inconsistency, and suggests that the role of temperature in terrestrial evolution at this time may need to be reconsidered.

Temperature data for the Late Miocene is sparse; nevertheless, the few marine reconstructions, which have become available recently (LaRiviere et al., 2012), imply that temperatures decreased near the interval of evolutionary changes on land. In the Mediterranean, well-dated SST reconstructions based on the $U^{K'}_{37}$ index show sustained cooling beginning at ~8 Ma (Tzanova et al., 2015) with temperature deterioration of as much as 10°C consistent with major biota shifts on land. Similarly, records from the Arabian Sea (Huang et al., 2007) and the North Pacific (LaRiviere et al., 2012) exhibit a similar temperature shift, though the magnitude of cooling is notably smaller.

In order to address the role of temperature decrease on Late Miocene biotic shifts, we sought to improve geographic coverage of marine paleotemperatures over the interval of greatest biotic reorganization around 8-7 Ma. We sought sites in the mid-latitudes to connect to floral and faunal evolutionary records and sites in the high-latitudes to correlate with evidence of sporadic IRD (Figure 3.2). ODP Sites 907 (69°N) and 982 (57°N) in the North Atlantic provide the material for the two highest latitude temperature records. ODP Sites 887 (54°N) and 883/884 (51°N) provide coverage in the North Pacific. In the mid-latitudes we selected ODP Site 1088 (40°S) in the South Atlantic and the Monte dei Corvi (MDC) uplifted marine section in the Mediterranean (43°N). The Monte Dei Corvi section is a global reference section for the Late Miocene chronology (Hilgen et al., 2003; Husing et al., 2007; Husing et al., 2009) and has the most robust age control, which makes it the template SST record with orbital resolution. Biostratigraphy and magnetostratigraphy determine the age models at the remaining ODP sites (Beerling et al., 2012; Channell et al., 1999; Hodell et al., 2001; Jansen, 1996; Marino and Flores, 2002; Rea et al., 1993; Schreck et al., 2012).

We seek to establish if Late Miocene biome shifts correspond to strong, unidirectional temperature cooling globally, as initially observed in the Mediterranean (Tzanova et al., 2015). We used alkenone paleothermometry, also referred to as the $U^{K'}_{37}$ index, in order to maximize internal proxy consistency and to directly relate new data to pre-existing temperature records from the Mediterranean (Tzanova et al., 2015), the Arabian Sea (ODP Site 722) (Huang et al., 2007) and the Pacific Ocean (ODP Sites 1010, 1021, 1028) (LaRiviere et al., 2012). The index relies on the organic biomarker trace left by haptophyte algae, which are ubiquitous across a wide range of surface temperatures and salinities (Herbert, 2003). Therefore, the alkenone paleothermometry is the most appropriate choice for our study. However, the warm Miocene temperatures (Huang et al., 2007; LaRiviere et al., 2012; Tzanova et al., 2015) preclude us from capturing SST in the warmest areas of ocean with the alkenone paleothermometer.

3.2 Methods

Alkenones were extracted from ~6-14 g of finely ground sediment in a Dionex Accelerated Solvent Extractor (ASE 200) using 9:1 (methylene chloride: methanol). The total lipid extract was evaporated under a nitrogen stream. In the case of samples from MDC the complex matrix required saponification of the total lipid extract, using 0.5ml of 0.5M KOH in 95% methanol/water for 2.5h at 65°C and was subsequently extracted with hexane. The saponification procedure was adjusted with respect to time and temperature to yield maximum alkenone recovery (95+%), minimum bias in $U^{K'}_{37}$ (< 0.2°C) as determined by replicates of the same sample and the cleanest chromatographic baseline for Gas Chromatographic (GC) analysis. Saponification for MDC samples and silica gel separation for MDC and ODP Site 907 samples were necessary to prevent gas chromatographic column deterioration, which would otherwise result in notable upward drift in $U^{K'}_{37}$ over the course of a GC run, and an increase in column retention of C_{37} alkenones. Prior to GC analysis, each sample was reconstituted in 200 μl of toluene containing a known amount of C_{36} and C_{37} n-alkane standards. The C_{37} alkenones were quantified by flame ionization detection on an Agilent 6890 GC equipped with an Agilent Technologies DB-1 column (60 m analytical column, 5 m fused guard column). To minimize changes in the GC response, we injected a toluene GC-FID blank every 3 samples and monitored system stability by running replicate extracts and a laboratory alkenone standard every 12 samples. We changed the system's inlet liners and trimmed the column every 12-24 samples or as indicated by drifts in the GC behavior of the standard. In addition to the $U^{K'}_{37}$ index, the C_{37}total was determined by reference to internal standards and is reported per gram dry weight of sediment. C_{37}total values for the MDC section follow a highly non-gaussian (tail toward high C_{37}total) distribution; we chose to use a log normalization for the C_{37}total data we present from that site.

We chose to translate the $U^{K'}_{37}$ index into SST using the linear calibration of Muller at al., (1998). The original calibration of Prahl and Wakeham (1988) provides the most conservative estimate of SST, while using the calibration of Muller et al, (1998) results in an overall shift towards warmer SSTs by 0.2 – 0.5°C, which is not a statistically significant difference. This shift is well within the error of the alkenone proxy (~0.2°C laboratory analytical error and 2.1°C inter-laboratory error) (Herbert, 2003) and does not influence our results in a significant way.

The precision and accuracy of stratigraphic control vary between our sites (Tzanova et al., 2015). Pelagic sedimentation at Monte dei Corvi and ODP Sites 907, 982, 887, 883/884, 1088 continued through the 8-5 Ma interval (Jansen, 1996; Marino and Flores, 2002; Montanari et al., 1997; Rea et al., 1993). At Monte dei Corvi we visually correlated our sampling to the published orbitally resolved stratigraphy (Hilgen et al., 2003; Husing et al., 2007; Husing et al., 2009). Subsequently, we used the precessionally paced variance in haptophyte productivity (C_{37}total) to tune our data to the precession parameter (Laskar et al., 2004). At Site ODP 907 our age model is constrained by the existing biostratigraphic and magnetostratigraphic data (Myhre, 1995; Schreck et al., 2012). At Site ODP 982 we utilized the dating information provided by the expedition scientific party (Jansen, 1996) in conjunction with existing isotope correlations to Mediterranean orbitally tuned marine sections (Hodell et al., 2001). In the South Atlantic, at ODP Site 1088 the age model data are biostratigraphic control points (Marino and Flores, 2002). At ODP Sites 883/884 we base our age model biostratigraphic and magnetostratigraphic data (Rea et al., 1993; Shimada et al., 2009; Swann, 2010); ODP Site 883 has incomplete recovery in the 8 – 6 Ma interval; however, we supplemented our data with samples from ODP Site 884, which is just one degree of longitude east of ODP Site 883. Site 883 has only biostratigraphic control, but because of its close proximity to Site 884, we correlate it to the magnetostratigraphic data of that site Finally, at ODP Site 887, we relied on the magnetostratigraphy and biostratigraphy framework provided by the scientific party at the time of the expedition (Rea et al., 1993).

3.3 Results

3.3.1 North Atlantic & Mediterranean

In reporting our results, we group the North Atlantic sites with the Mediterranean Sea site because the Mediterranean receives a large portion of its water from the Atlantic Ocean and is far more influenced by the Atlantic than the Pacific Ocean. The two highest latitude sites, ODP Site 907 and ODP Site 982 are in the North Atlantic while the Mediterranean falls in the mid-latitudes. In the beginning of the study period, around 9 Ma, SSTs at all three sites show significantly warmer temperatures compared to modern (Figure 3.3). In the North Atlantic they exceed the modern SST average by as much as 15°C, while in the MDC section they are ~5° over present (Figures 3.3 and 3.4). We reconstruct sustained cooling at all sites beginning between ~8 – 7.5 Ma.

In this study, we present additional high resolution data (3-4 kyr) from the Mediterranean, spanning 7.5 – 6.7 Ma, which is the interval of coldest SST at this site (Figures 3.3 and 3.4). We stress that Late Miocene temperatures reflect the combined influence of orbital pacing and long-term trends, which makes the orbitally resolved SSTs from Monte dei Corvi particularly telling. During this coldest excursion, SSTs cool to the modern annual average of 19.5°C (Figure 3.3). SSTs in the Mediterranean warm at 6.7 Ma by 5-6°C over the modern value. The significance of this rebound needs to be treated with caution as it may reflect the regional influence of the isolation of the basin from the Atlantic Ocean (Husing et al., 2010).

ODP Site 907 and ODP Site 982 begin to cool at 7.2 Ma and 7 Ma, respectively (Figures 3.3-4). We define the onset of cooling as the time when interglacial SST consistently falls below the glacial SST in the beginning of our reconstruction (~9 Ma). We acknowledge uncertainty in these data by as much as 200 – 300 kyr because of the inescapable ambiguity in their stratigraphic control in comparison to the Monte dei Corvi section. The sustained cooling at ODP Site 907 culminates in SST only ~1°C warmer than modern values followed by a plateau where SST remain ~5°C warmer than modern until 5 Ma. The temperature pattern at the other North Atlantic site, ODP Site 982, is similar to the SST pattern at MDC because of a discrete two part cold episode between 6.6 – 6 Ma when SSTs are analogous to modern. SSTs plateau at an average of ~8° warmer than present between 6 Ma and the end of the ODP Site 982 record at 5 Ma.

C_{37}total reconstructs the haptophyte productivity at ODP Sites 907, 982 and Monte dei Corvi and shows remarkable coherence between the sites. C_{37}total values are low (~0.5) until a marked spike at 7 Ma at the two North Atlantic sites. In the Mediterranean the significant increase in C_{37}total is later, at 6.7 Ma, which may reflect regional influences (e.g. "Euxinic Shale" deposition reported in Husing et al. 2009).

3.3.2 North Pacific

The two North Pacific sites, ODP Sites 883/884 and 887, are at a slightly lower latitude than the North Atlantic Sites (Figure 3.2). At 9 Ma, both North Pacific locations were 6-7°C warmer than the modern annual average, but such warmth is less than the warming over the North Atlantic. Sustained cooling began at ~7.6 – 7.5 Ma in the North Pacific. The coldest SSTs at the eastern Pacific site, ODP 887, are at 6.8 Ma at which time they are 2-3°C colder than modern (Figure 3.3). ODP Site 887 shows a rebound reminiscent of MDC and ODP Site 982 as SSTs warm between 5.7 and the younger end of the record.

At the western Pacific site, ODP 883/884, the coldest reconstructed SST occurred at 6.2 Ma when SSTs are close to the modern annual average. After 6.2 Ma until the end of the record at 5 Ma, SSTs remain ~4-5°C warmer than present (Figures 3.3 and 3.4). We reconstruct a sharp increase in haptophyte productivity in the North Pacific at ~7 Ma, in a similar timing to that seen in the North Atlantic (Figure 3.5)

3.3.3 South Atlantic

ODP Site 1088 is located in the South Atlantic at a mid-latitude similar to the Monte dei Corvi site (Figure 3.2). In the beginning of our record at 9 Ma, SSTs at ODP Site 1088 are 5°C warmer than modern. Sustained cooling began at ~7 Ma (Figures 3.3 and 3.4), defined as the onset on interglacial SST which fell below glacial SST in the beginning of the record. This datum falls well within the range of onset of cooling at all other sites. The coldest SST was recorded at ~5.5 Ma, when reconstructed surface temperatures are as much as 6°C colder than the modern annual average (Figure 3.3). Temperatures rebound slightly in the period between 5.5 Ma and the end of the record at 5 Ma and remain an average of 2.5°C warmer than today. ODP Site 1088 shows sustained cooling followed by a plateau that mirrors SSTs at ODP Sites 883/884 in the eastern North Pacific and ODP Site 907 in the North Atlantic. Haptophyte productivity at

ODP Site 1088 mirrors the trend of low productivity followed by a notable increase; however, the increase at ODP Site 1088 occurs at 7.5 Ma, which is 500 kyr earlier than at most other sites.

3.4 Discussion

The initial reconstruction of SST at Monte dei Corvi (Tzanova et al., 2015) first suggested the strong cooling associated with major evolutionary transitions across the global mid-latitudes, such as the appearance of the Sahara (Schuster et al., 2006), C_4 grassland expansion (Cerling et al., 1997; Cerling et al., 1993; Quade and Cerling, 1995), diversification of succulents (Arakaki et al., 2011) and initiation of bi-pedalism and related adaptations in the homininae line (Brunet, 2010). The cooling is clearly synchronous across basins and latitudes (Figure 3.3). In this paper we show that the onset of temperature decrease supports the hypothesis that temperature and not just aridity contributed to biome reorganization at this time and that aridification was accompanied by a pole to equator temperature gradient change (Figure 3.3).

The SSTs from the North Pacific, North Atlantic, South Atlantic and Mediterranean Sea show that during the Late Miocene, temperatures deteriorated globally, which is consistent with the timing of dynamic biome changes on land (Figures 3.1 and 3.3). The onset of cooling is comparable at ~8 – 7 Ma across all sites, with temperatures decreasing to close to, or even below, the modern annual average at the sites. SSTs do not return to pre-cooling values even at the sites where they rebound at the onset of the Pliocene. Such widespread cooling significantly modifies the climate view suggested by the available benthic oxygen isotope records (stable warmth) and CO_2 reconstructions (pre-industrial to Last Glacial Maximum values) (Figure 3.1). Instead, it corroborates Northern hemisphere IRD as evidence of beginning of glaciation (Figure 3.1) reconstructed at ODP sites in the North Atlantic and North Pacific. At ODP 887 a sharp peak in terrigenous input at 6.4 Ma and an increase in sedimentation rates at ~6 Ma (Rea and Snoeckx, 1995) matches the lowest reconstructed SST (Figure 3.4) and suggests a link to increased glaciation. We cannot stratigraphically match other evidence of glaciation to our SST because the IRD data come from different ODP sites (ODP 918/919); however, the timing of IRD occurrences (Figure 3.1) corresponds to SST decrease.

The presence of IRD in the North Pacific and North Atlantic during the Late Miocene (Krissek, 1995; Lagoe et al., 1993; St John, 2008; St John and Krissek, 2002a) is consistent with SST evidence of notable cooling, but is at odds with the absence of significant isotopic enrichment in the global benthic $\delta^{18}O$ stack in the latest Miocene (Zachos et al., 2001). However, the Greenland ice cap today would only account for a ~0.074‰ shift, which suggests that an equivalent amount of ice would be easy to overlook in the Late Miocene. Additionally, at the time the majority of ice is locked in Antarctica, where even if SSTs were to be ~10°C warmer they would still be well below freezing and the temperatures we reconstruct will not sway Antarctic ice volume and the benthic oxygen isotope records (Cramer et al., 2009; DeConto et al., 2008; Miller et al., 2005; Zachos et al., 2001). The coldest SSTs at all of our Northern hemisphere sites match documented pulses of IRD near ~7 Ma in the Pacific and Atlantic Oceans (Krissek, 1995; Lagoe et al., 1993; St John, 2008; St John and Krissek, 2002a). Notably, the coldest SST at Monte dei Corvi corresponds to first Late Miocene evidence of IRD in the North Atlantic, while the coldest SST at ODP Site 887 matches the first record of IRD in the North Pacific (Figure 3.1).

Late Miocene cooling hints at glacial events predating large Northern hemisphere glaciation at 2.7 Ma, but the SST rebounds suggest the descent into this regime was not monotonic. The SSTs at all sites rebound nearly concurrently at all sites, which shows that the threshold for large scale ice build-up was not crossed until much later. Global benthic isotopes records (Figure 1) (Zachos et al., 2001) similarly place NHG much later than the Late Miocene; however, the SST show a much more detailed view of the progression into the bi-polar glaciation of Plio-Pleistocene. The orbital scale coherence of SST cooling and rebound trends is hard to evaluate between the sites, which prevents us from evaluating the full spectrum of climate change and climate system links during this time.

The quality of stratigraphic control is site specific and is the most robust at the Mediterranean locale. At Monte dei Corvi, the SST pattern shows a cold episode mirrored at ODP Site 982 (Figure 3.4). However, the increasing isolation of the Mediterranean into the Messinian and the termination of the Mediterranean record at 6.3 Ma precludes us from quantitatively evaluating similarities and differences between these two records. Additionally, we cannot constrain orbital pacing or make orbital scale correlations between the sites due to stratigraphic limitations at some sites such as ODP Sites 907 and 982 and low alkenone abundance and difficult sample matrix at ODP Site 887. However, if orbital stratigraphies can be established, we will have the prospect of testing whether SST oscillations within the overall cold episode are synchronous.

Remarkably, all of the open ocean study sites show a synchronous increase in the C_{37}total index in the late Miocene, which suggests a global scale shift in nutrient availability and carries implications for the global carbon cycle at this time. Regardless of basin or latitude, we observe orders of magnitude increase in haptophyte productivity (Figure 3.5), which coincides with the drop in SST at ~7 Ma. The surge in alkenone producers echoes increases in opal and total organic carbon, first documented in the initial expedition findings for ODP Sites 907, 982 and 887 (Jansen, 1996; Rea et al., 1993; Rea and Snoeckx, 1995) and further supported by a global shift in opal sedimentation in the subtropical and high-latitudes between 7 – 5 Ma (Cortese et al., 2004). This implies that marine productivity increased significantly at this time, likely as a result of greater nutrient availability. The simplest explanation is that colder surface temperatures led to decreased water column stratification and facilitated mixing. Additionally, the proportionally greater decrease in polar versus mid-latitude SST (Figure 3.3) steepened the temperature gradient and led to stronger winds, which further aids mixing. The shift in temperatures could also impact the position of the global nutricline through changes in gyre structure. Yet another explanation for the widespread increase in marine productivity is the proliferation of C_4 plants on land, which can mobilize dissolved silica from the continental to the ocean reservoir (Cortese et al., 2004).

The Monte dei Corvi section shows the same structure of increased haptophyte productivity (Figure 3.2) as in open ocean sites, but the increase those for post-dates the other locations. In the Mediterranean, the majority of nutrient delivery is through river runoff (De Lange et al., 2008; Rossignol-Strick, 1985; Schenau et al., 1999) and therefore local marine productivity is highly sensitive to hydrological conditions in the Eurasian and Northern African region. At Monte dei Corvi, the sharp increase in the C_{37}total index (Figure 3.5) directly follows the termination of an arid excursion (Tzanova et al., 2015) and thus reflects a regional event.

The new SSTs from ODP Sites 907, 982, 887, 883/884, 1088 and the Monte dei Corvi Mediterranean section present a unified depiction of global temperature deterioration coinciding with transient Northern hemisphere glaciation and global biome shifts (Pound et al., 2012; Pound et al., 2011); however, they challenge the available CO_2 reconstructions (Demicco et al., 2003; Ekart et al., 1999; Pagani et al., 1999; Pearson and Palmer, 2000; Vanderburgh et al., 1993)(Figure 3.1). Generally, authors who support the reliability of current CO_2 reconstructions imply a different sensitivity of climate to CO_2 from modern (LaRiviere et al., 2012), and suggest biome shifts such as grassland proliferation resulted from increased aridity and changed seasonality (Behrensmeyer et al., 2007; Huang et al., 2007; Pagani et al., 1999; Scheiter et al., 2012). We acknowledge the contribution of aridity to biome shift (Tzanova et al., 2015), but question reconstructions of CO_2 stasis at the time of notable biotic and temperature change (Figures 3.1, 3.3 and 3.4). Modelers have tried to reconcile low and stable CO_2 with Late Miocene warmth; nevertheless, models cannot account for the notable warmth shown by SST reconstructions (Huang et al., 2007; LaRiviere et al., 2012; Tzanova et al., 2015) at less than pre-industrial CO_2 values (Butzin et al., 2011; Knorr et al., 2011).

In addition, the global increase in C_{37}total (Figure 3.5) and global marine biogenic bloom (Cortese et al., 2004; Jansen, 1996; Rea et al., 1993; Rea and Snoeckx, 1995) suggest a perturbation of the global carbon cycle, which likely affected atmospheric CO_2. Increased marine productivity would draw down atmospheric CO_2, though we acknowledge that we cannot determine if this process initiated or was a feedback to already decreasing CO_2 and cooling temperatures. The $\delta^{13}C$ signals from the Pacific and Atlantic Oceans diverge at 7 Ma, further indicating a carbon cycle change (Cramer et al., 2009; Diester-Haass et al., 2006; Wright et al., 1992). Lastly, a shift in coccolith size suggests a drop in CO_2 at ~7 Ma (Bolton and Stoll, 2013), which is mirrored in the cooling shown by our SST data.

We suggest that the global SST trends in the 9-5 Ma interval support a relatively small-scale glaciation prior to NHG, which drove terrestrial biome shifts. This event primed the system for the large glacial-interglacial cycles of the Plio-Pleistocene (Zachos et al., 2001). Global biome transition (Pound et al., 2011), the emergence of the Sahara (Schuster et al., 2006) and sea ice in the Northern hemisphere can set off an albedo feedback to contribute to cooling climate.

3.5 Conclusions

New SST time series spanning 9 – 5 Ma from ODP Sites 982 and 907 in the North Atlantic, ODP Sites 887 and 883/884 in the North Pacific, ODP Site 1088 in the South Atlantic and the Monte dei Corvi marine section in the Mediterranean unequivocally show deteriorating temperatures beginning at ~8 Ma. The coexistence of decreasing temperatures at a time of significant biome shift on land, such as the appearance of the Sahara, expansion of grasslands and diversification of succulent plants, suggests that cooling temperatures and enhanced equator-pole temperature gradients played a role in Late Miocene evolution. Prior to these new data, the main hypothesis for the dynamic changes in the terrestrial landscape invoked increased aridity. Instead, we suggest an interpretation that attributes aridification to decreasing temperatures.

We argue that decreasing temperatures accompanied transient Northern hemisphere glaciations, which are indicated by evidence of IRD in the North Atlantic and North Pacific at the same time. A glaciation with magnitude lesser than NHG would not significantly affect the benthic isotope record and therefore can be reconciled with the existing global benthic stack.

Global cooling of SSTs corresponds to a parallel increase in the C_{37}total index, which signifies a jump in haptophyte productivity. Other indices of overall marine biological productivity such as silica deposition and organic carbon peak concurrently, which indicates a biogenic bloom of global proportions centered around ~7 Ma. We believe such a widespread and significant increase resulted from increased nutrient availability and must have perturbed the global carbon cycle.

The concurrent global increase in productivity, decreasing temperatures, Northern hemisphere IRD and major biome shifts imply a global forcing such as CO_2 decrease. However, the available CO_2 records, which lack resolution in this interval, indicate stable values between the last glacial maximum and pre-industrial levels. We believe that in light of newly available evidence of global temperature decrease and widespread marine biogenic bloom, the CO_2 records should be re-evaluated and potentially revised.

3.6 Acknowledgements

This work was sponsored by American Chemical Society grand PRF 48032-AC2 and support from the Evolving Earth Foundation. We also thank IODP for providing core material.

References

Agusti, J., Cabrera, L., Garces, M., 2013. The Vallesian Mammal Turnover: A Late Miocene record of decoupled land-ocean evolution. Geobios 46, 151-157.

Agusti, J., de Siria, A.S., Garces, M., 2003. Explaining the end of the hominoid experiment in Europe. J. Hum. Evol. 45, 145-153.

Arakaki, M., Christin, P.A., Nyffeler, R., Lendel, A., Eggli, U., Ogburn, R.M., Spriggs, E., Moore, M.J., Edwards, E.J., 2011. Contemporaneous and recent radiations of the world's major succulent plant lineages. Proc. Natl. Acad. Sci. U. S. A. 108, 8379-8384.

Beerling, D.J., Taylor, L.L., Bradshaw, C.D.C., Lunt, D.J., Valdes, P.J., Banwart, S.A., Pagani, M., Leake, J.R., 2012. Ecosystem CO2 starvation and terrestrial silicate weathering: mechanisms and global-scale quantification during the late Miocene. J. Ecol. 100, 31-41.

Behrensmeyer, A.K., Quade, J., Cerling, T.E., Kappelman, J., Khan, I.A., Copeland, P., Roe, L., Hicks, J., Stubblefield, P., Willis, B.J., Latorre, C., 2007. The structure and rate of late Miocene expansion of C-4 plants: Evidence from lateral variation in stable isotopes in paleosols of the Siwalik Group, northern Pakistan. Geol. Soc. Am. Bull. 119, 1486-1505.

Bolton, C.T., Stoll, H.M., 2013. Late Miocene threshold response of marine algae to carbon dioxide limitation. Nature 500, 558-562.

Brunet, M., 2010. Two new Mio-Pliocene Chadian hominids enlighten Charles Darwin's 1871 prediction. Philos. Trans. R. Soc. B-Biol. Sci. 365, 3315-3321.

Butzin, M., Lohmann, G., Bickert, T., 2011. Miocene ocean circulation inferred from marine carbon cycle modeling combined with benthic isotope records. Paleoceanography 26.

Cerling, T.E., Harris, J.M., MacFadden, B.J., Leakey, M.G., Quade, J., Eisenmann, V., Ehleringer, J.R., 1997. Global vegetation change through the Miocene/Pliocene boundary. Nature 389, 153-158.

Cerling, T.E., Wang, Y., Quade, J., 1993. Expansion of C4 ecosystems as an indicator of global ecological change in the Late Miocene. Nature 361, 344-345.

Channell, J.E.T., Amigo, A.E., Fronval, T., Rack, F., Lehman, B., 1999. Magnetic Stratigraphy at Sites 907 and 985 in the Norwegian-Greenland Sea and a revision of the Site 907 composite section. Proc. ODP, SCi. Results 162, 131-148.

Cortese, G., Gersonde, R., Hillenbrand, C.D., Kuhn, G., 2004. Opal sedimentation shifts in the World Ocean over the last 15 Myr. Earth Planet. Sci. Lett. 224, 509-527.

Cramer, B.S., Toggweiler, J.R., Wright, J.D., Katz, M.E., Miller, K.G., 2009. Ocean overturning since the Late Cretaceous: Inferences from a new benthic foraminiferal isotope compilation. Paleoceanography 24.

De Lange, G.J., Thomson, J., Reitz, A., Slomp, C.P., Principato, M.S., Erba, E., Corselli, C., 2008. Synchronous basin-wide formation and redox-controlled preservation of a Mediterranean sapropel. Nat. Geosci. 1, 606-610.

DeConto, R.M., Pollard, D., Wilson, P.A., Palike, H., Lear, C.H., Pagani, M., 2008. Thresholds for Cenozoic bipolar glaciation. Nature 455, 652-U652.

Demicco, R.V., Lowenstein, T.K., Hartdie, L.A., 2003. Atmospheric pCO2 since 60 Ma from records of seawater pH, calcium and primary carbonate mineralogy. Geology 31, 793-796.

Diester-Haass, L., Billups, K., Emeis, K.C., 2006. Late Miocene carbon isotope records and marine biological productivity: Was there a (dusty) link? Paleoceanography 21.

Edwards, E.J., Osborne, C.P., Stromberg, C.A.E., Smith, S.A., Bond, W.J., Christin, P.A., Cousins, A.B., Duvall, M.R., Fox, D.L., Freckleton, R.P., Ghannoum, O., Hartwell, J., Huang, Y.S., Janis, C.M., Keeley, J.E., Kellogg, E.A., Knapp, A.K., Leakey, A.D.B., Nelson, D.M., Saarela, J.M., Sage, R.F., Sala, O.E., Salamin, N., Still, C.J., Tipple, B., Consortium, C.G., 2010. The Origins of C-4 Grasslands: Integrating Evolutionary and Ecosystem Science. Science 328, 587-591.

Ehleringer, J.R., Cerling, T.E., Helliker, B.R., 1997. C-4 photosynthesis, atmospheric CO2 and climate. Oecologia 112, 285-299.

Ekart, D.D., Cerling, T.E., Montanez, I.P., Tabor, N.J., 1999. A 400 million year carbon isotope record of pedogenic carbonate: Implications for paleoatmospheric carbon dioxide. Am. J. Sci. 299, 805-827.

Fronval, T., Jansen, E., 1996. Late Neogene paleoclimates and paleoceanography in the Iceland-Norwegian Sea: Evidence from the Iceland or Vøring plateaus, In: Thiede, J., Firth, J.V., Johnson, G.L., Ruddiman, W.F. (Eds.), Proc. ODP, Sci. Results, pp. 455-468.

Herbert, T.D., 2003. Alkenone Paleotemperature Determinations, In: Elderfield, H., Turekian, K.K. (Ed.), Treatise in Marine Geochemistry. Elsevier, pp. 391-432.

Hilgen, F.J., Aziz, H.A., Krijgsman, W., Raffi, I., Turco, E., 2003. Integrated stratigraphy and astronomical tuning of the Serravallian and lower Tortonian at Monte dei Corvi (Middle-Upper Miocene, northern Italy). Paleogeogr. Paleoclimatol. Paleoecol. 199, 229-264.

Hodell, D.A., Curtis, J.H., Sierro, F.J., Raymo, M.E., 2001. Correlation of late Miocene to early Pliocene sequences between the Mediterranean and North Atlantic. Paleoceanography 16, 164-178.

Huang, Y.S., Clemens, S.C., Liu, W.G., Wang, Y., Prell, W.L., 2007. Large-scale hydrological change drove the late Miocene C-4 plant expansion in the Himalayan foreland and Arabian Peninsula. Geology 35, 531-534.

Husing, S.K., Hilgen, F.J., Aziz, H.A., Krijgsman, W., 2007. Completing the Neogene geological time scale between 8.5 and 12.5 Ma. Earth Planet. Sci. Lett. 253, 340-358.

Husing, S.K., Kuiper, K.F., Link, W., Hilgen, F.J., Krijgsman, W., 2009. The upper Tortonian-lower Messinian at Monte dei Corvi (Northern Apennines, Italy): Completing a Mediterranean reference section for the Tortonian Stage. Earth Planet. Sci. Lett. 282, 140-157.

Husing, S.K., Oms, O., Agusti, J., Garces, M., Kouwenhoven, T.J., Krijgsman, W., Zachariasse, W.J., 2010. On the late Miocene closure of the Mediterranean-Atlantic gateway through the Guadix basin (southern Spain). Paleogeogr. Paleoclimatol. Paleoecol. 291, 167-179.

Jansen, E., Raymo, M.E., Blum, P., et al, 1996. Proc. ODP. Init. Repts, Ocean Drilling Program, College Station, TX.

Knorr, G., Butzin, M., Micheels, A., Lohmann, G., 2011. A warm Miocene climate at low atmospheric CO2 levels. Geophys. Res. Lett. 38.

Krissek, L.A., 1995. Late Cenozoic ice-rafting records from Leg 145 Sites in the North Pacific: Late Miocene onset, Late Pliocene intensification, and Plio-Pleistocene Events, In: Rea, D.K., Basov, I.A., Scholl, D.W., Allan, J.F. (Eds.), Proc. ODP, Sci. Results. Ocean Drilling Program, pp. 179-194.

Lagoe, M.B., Eyles, C.H., Eyles, N., Hale, C., 1993. Timing of Late Cenozoic tidewater glaciation in the far North Pacific Geol. Soc. Am. Bull. 105, 1542-1560.

LaRiviere, J., Ravelo, A.C., Crimmins, A., Dekens, P.S., Ford, H.L., Lyle, M., Wara, M.W., 2012. Late Miocene decoupling of oceanic warmth and atmospheric carbon dioxide forcing. Nature 486, 97-100.

Laskar, J., Robutel, P., Joutel, F., Gastineau, M., Correia, A.C.M., Levrard, B., 2004. A long-term numerical solution for the insolation quantities of the Earth. Astron. Astrophys. 428, 261-285.

Marino, M., Flores, J.A., 2002. Calcareous nannofossil stratigraphy at Sites 1088 and 1090 (ODP Leg 177, Southern Ocean), In: Gersonde, R., Hodell, D., Blum, P. (Eds.), Proc. ODP, Sci. Results, pp. 1-14.

Miller, K.G., Kominz, M.A., Browning, J.V., Wright, J.D., Mountain, G.S., Katz, M.E., Sugarman, P.J., Cramer, B.S., Christie-Blick, N., Pekar, S.F., 2005. The phanerozoic record of global sea-level change. Science 310, 1293-1298.

Montanari, A., Odin, G.S., Coccioni, R., 1997. Miocene Stratigraphy An Integrated Approach. Elsevier Science, The Netherlands.

Muller, P.J., Kirst, G., Ruhland, G., von Storch, I., Rosell-Mele, A., 1998. Calibration of the alkenone paleotemperature index U-37(K ') based on core-tops from the eastern South Atlantic and the global ocean (60 degrees N-60 degrees S). Geochim. Cosmochim. Acta 62, 1757-1772.

Myhre, A.M., Thiede, J., Firth, J.V. et al.,, 1995. Proc. ODP. Init. Repts, Ocean Drilling Program, College Station, TX.

NOAA, 2005. World Ocean Atlas.

Pagani, M., Freeman, K.H., Arthur, M.A., 1999. Late Miocene atmospheric CO2 concentrations and the expansion of C-4 grasses. Science 285, 876-879.

Pagani, M., Liu, Z.H., LaRiviere, J., Ravelo, A.C., 2010. High Earth-system climate sensitivity determined from Pliocene carbon dioxide concentrations. Nat. Geosci. 3, 27-30.

Pearson, P.N., Palmer, M.R., 2000. Atmospheric carbon dioxide concentrations over the past 60 million years. Nature 406, 695-699.

Pound, M.J., Haywood, A.M., Salzmann, U., Riding, J.B., 2012. Global vegetation dynamics and latitudinal temperature gradients during the Mid to Late Miocene (15.97-5.33 Ma). Earth-Sci. Rev. 112, 1-22.

Pound, M.J., Haywood, A.M., Salzmann, U., Riding, J.B., Lunt, D.J., Hunter, S.J., 2011. A Tortonian (Late Miocene, 11.61-7.25 Ma) global vegetation reconstruction. Paleogeogr. Paleoclimatol. Paleoecol. 300, 29-45.

Quade, J., Cerling, T.E., 1995. Expansion of C-4 grasses in the Late Miocene of Northern Pakistan - evidence from stable isotopes in paleosols Paleogeogr. Paleoclimatol. Paleoecol. 115, 91-116.

Rea, D.K., Basov, I.A., Janecek, T.R., Palmer-Julson, A., al, e., 1993. Proc. ODP. Init. Repts, Ocean Drilling Program, College Station, TX.

Rea, D.K., Snoeckx, H., 1995. Sediment fluxes in the Gulf of Alaska: Paleoceanographic record from Site 887 on the Patton-Murray seamount platform, In: Rea, D.K., Basov, I.A., Scholl, D.W., Allan, J.F. (Eds.), Proceedings of the Ocean Drilling Program Scientific Results. College Station, TX (Ocean Drilling Program), pp. 247-256.

Rossignol-Strick, M., 1985. Mediterranean quaternary sapropels, and immediate response of the African monsoon to variation of insolation. Paleogeogr. Paleoclimatol. Paleoecol. 49, 237-263.

Scheiter, S., Higgins, S.I., Osborne, C.P., Bradshaw, C., Lunt, D., Ripley, B.S., Taylor, L.L., Beerling, D.J., 2012. Fire and fire-adapted vegetation promoted C4 expansion in the late Miocene. New Phytol. 195, 653-666.

Schenau, S.J., Antonarakou, A., Hilgen, F.J., Lourens, L.J., Nijenhuis, I.A., van der Weijden, C.H., Zachariasse, W.J., 1999. Organic-rich layers in the Metochia section (Gavdos, Greece): evidence for a single mechanism of sapropel formation during the past 10 My. Mar. Geol. 153, 117-135.

Schreck, M., Matthiessen, J., Head, M.J., 2012. A magnetostratigraphic calibration of Middle Miocene through Pliocene dinoflagellate cyst and acritarch events in the Iceland Sea (Ocean Drilling Program Hole 907A). Rev. Palaeobot. Palynology 187, 66-94.

Schuster, M., Duringer, P., Ghienne, J.F., Vignaud, P., Mackaye, H.T., Likius, A., Brunet, M., 2006. The age of the Sahara Desert. Science 311, 821-821.

Shimada, C., Sato, T., Yamasaki, M., Hasegawa, S., Tanaka, Y., 2009. Drastic change in the late Pliocene subarctic Pacific diatom community associated with the onset of the Northern Hemisphere Glaciation. Paleogeogr. Paleoclimatol. Paleoecol. 279, 207-215.

St John, K., 2008. Cenozoic ice-rafting history of the central Arctic Ocean: Terrigenous sands on the Lomonosov Ridge. Paleoceanography 23.

St John, K., Krissek, L.A., 2002a. The late Miocene to Pleistocene ice-rafting history of southeast Greenland. Boreas 31, 28-35.

St John, K.E.K., Krissek, L.A., 2002b. The late Miocene to Pleistocene ice-rafting history of southeast Greenland. Boreas 31, 28-35.

Swann, G.E.A., 2010. Salinity changes in the North West Pacific Ocean during the late Pliocene/early Quaternary from 2.73 Ma to 2.52 Ma. Earth Planet. Sci. Lett. 297, 332-338.

Tipple, B.J., Meyers, S.R., Pagani, M., 2010. Carbon isotope ratio of Cenozoic CO2: A comparative evaluation of available geochemical proxies. Paleoceanography 25.

Tzanova, A., Herbert, T., Peterson, L.C., 2015. Cooling Mediterranean sea surface temperatures during the Late Miocene provide a climate context for evolutionary transitions in Africa and Eurasia. Earth Planet. Sci. Lett. 419, 71-80.

Vanderburgh, J., Visscher, H., Dilcher, D.L., Kurschner, W.M., 1993. Paleoatmospheric signatures in neogene fossil leaves Science 260, 1788-1790.

Wright, J.D., Miller, K.G., Fairbanks, R.G., 1992. Early and middle Miocene stable isotopes; implications for deepwater circulation and climate. Paleoceanography 7, 357-389.

Zachos, J., Pagani, M., Sloan, L., Thomas, E., Billups, K., 2001. Trends, rhythms, and aberrations in global climate 65 Ma to present. Science 292, 686-693.

Zhang, Y.G., Pagani, M., Liu, Z.H., Bohaty, S.M., DeConto, R., 2013. A 40-million-year history of atmospheric CO2. Philos. Trans. R. Soc. A-Math. Phys. Eng. Sci. 371.

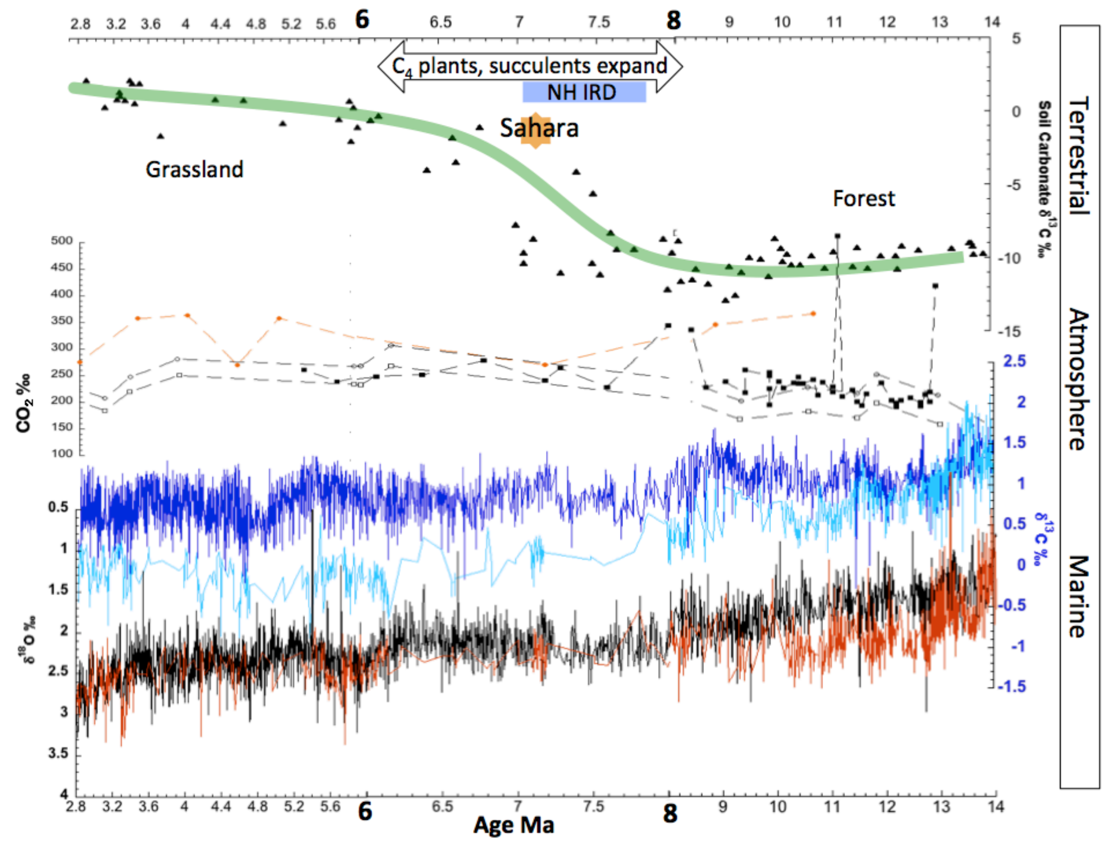

Figure 3.1 Late Miocene trends in global benthic $\delta^{18}O$ in blue (North Atlantic in dark blue and Pacific in light blue) and $\delta^{13}C$ in black and red (North Atlantic in black and Pacific in red) (Cramer et al., 2009). Atmospheric CO_2 reconstructions for the same time interval shown by open and closed circles (Demicco et al., 2003; Pagani et al., 1999; Pearson and Palmer, 2000; Vanderburgh et al., 1993). Soil carbonate $\delta^{13}C$ shown as triangles (Cerling et al., 1993; Quade and Cerling, 1995) with overlain markers indicating first appearance of the Sahara (Schuster et al., 2006) and ice rafted debris presence in the Northern hemisphere (St John, 2008; St John and Krissek, 2002a). Note the change in time scale providing additional detail in the 6 – 8 Ma window.

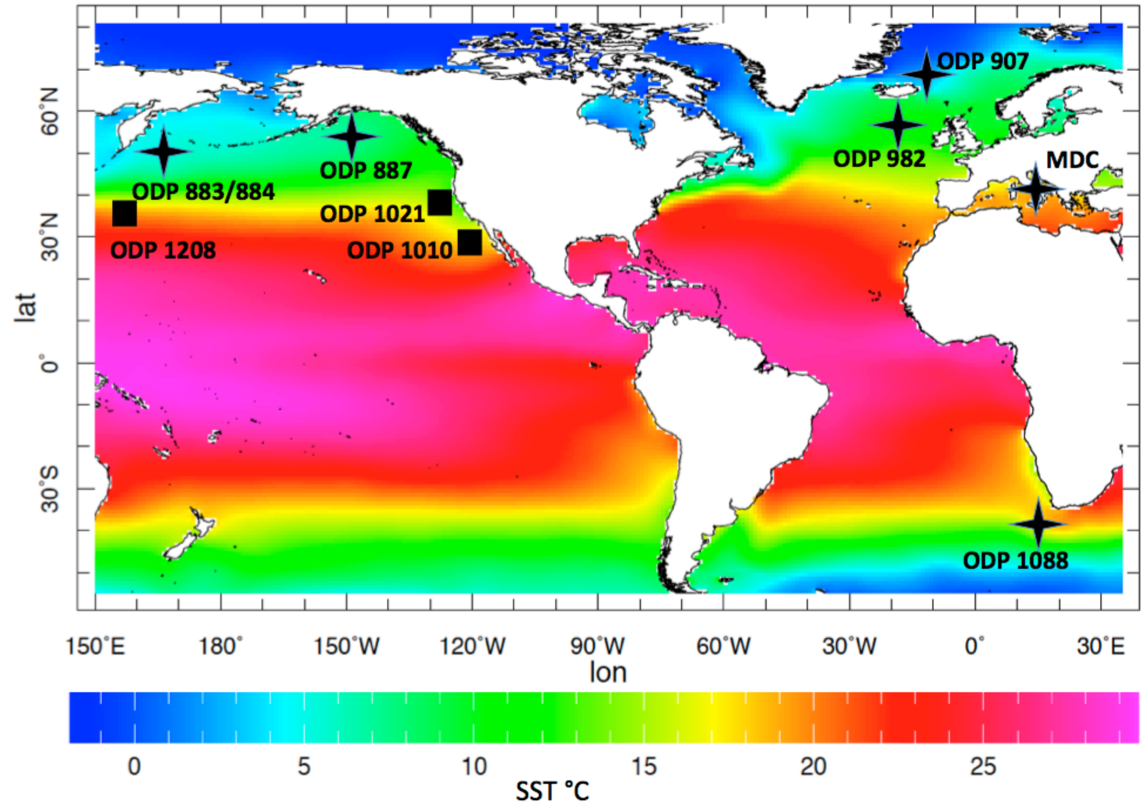

Figure 3.2 Modern sea surface temperatures at the study sites (NOAA, 2005) with locations shown as stars (this study) and squares for previously published SST (LaRiviere et al., 2012).

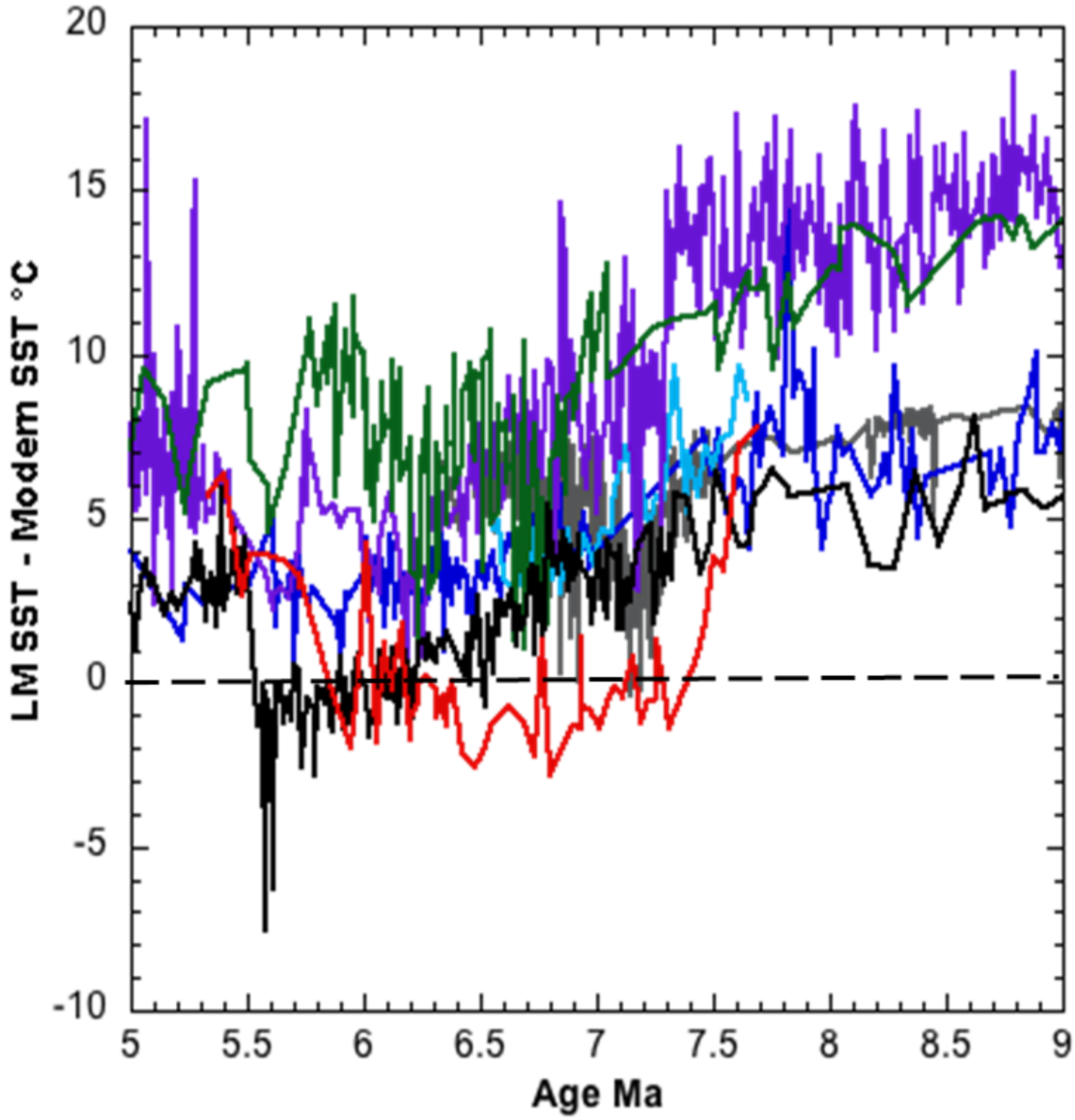

Figure 3.3 Differences between reconstructed Late Miocene sea surface temperatures and modern annual temperatures at ODP 907 in purple, OPD 982 in green, ODP 883/884 in blue, ODP 887 in red, Monte dei Corvi in gray and ODP 1088 in black

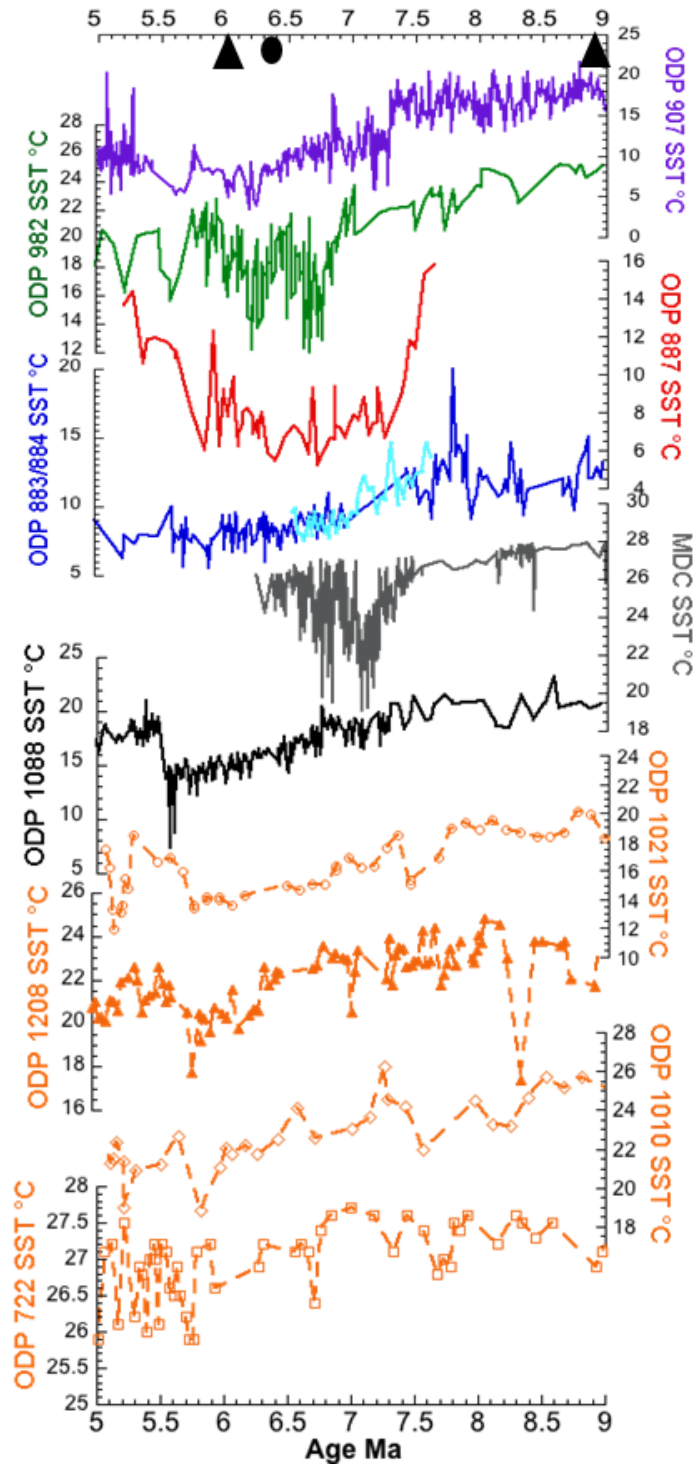

Figure 3.4 Reconstructed Late Miocene sea surface temperatures for ODP 907 in purple, OPD 982 in green, ODP 883/884 in blue, ODP 887 in red, Monte dei Corvi in gray and ODP 1088 in black. In orange we show published records from the North Pacific (LaRiviere et al., 2012) and Arabian Sea (Huang et al., 2007). Black triangles indicate increases in sedimentation rates at Site 887 and black circle shows a local peak in terrigenous input at Site 887 (Fronval and Jansen, 1996)

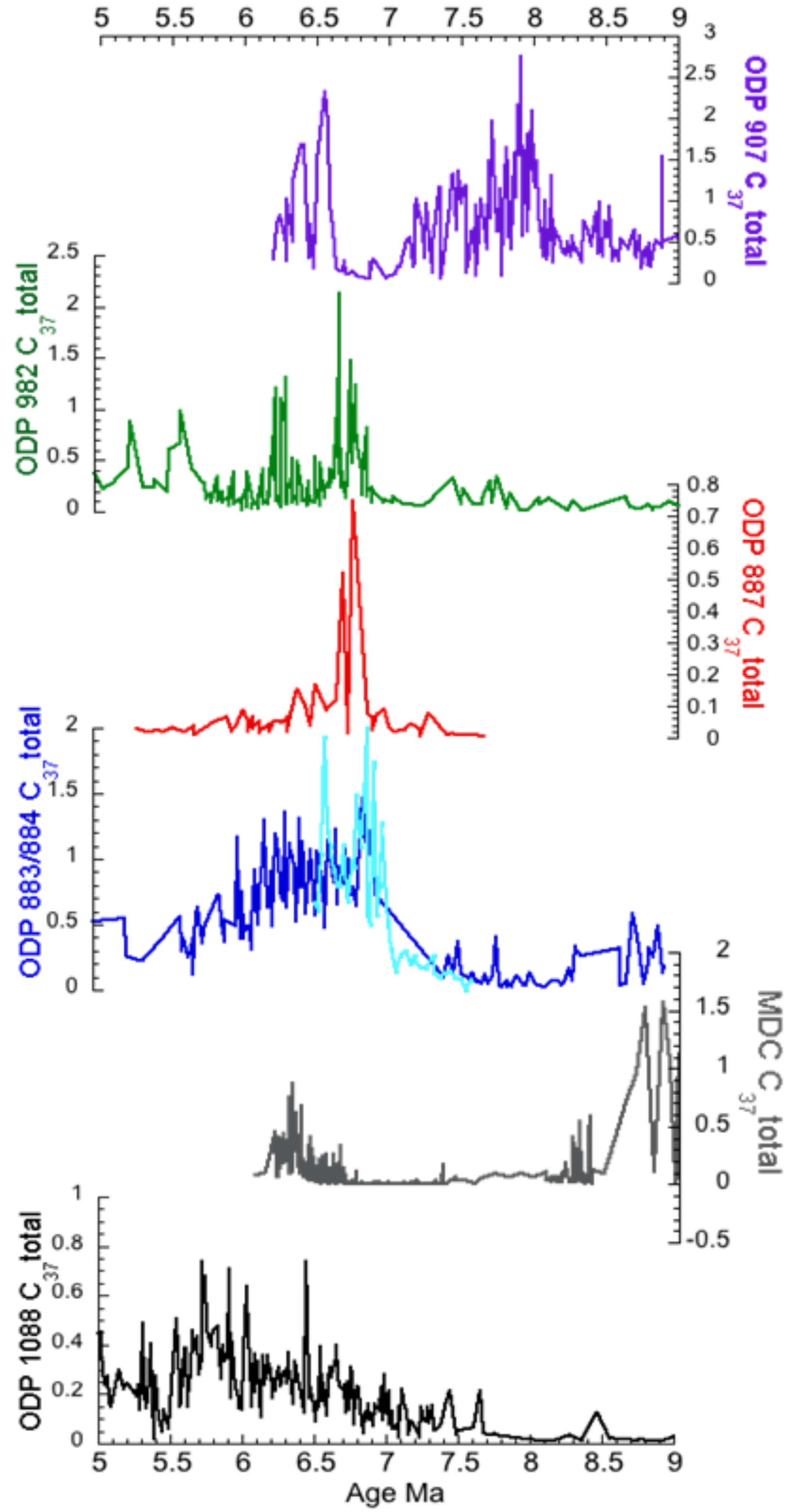

Figure 3.5 Reconstructed Late Miocene C_{37}total for ODP 907 in purple, OPD 982 in green, ODP 883/884 in blue, ODP 887 in red, Monte dei Corvi in gray and ODP 1088 in black. Dashed line indicates sea surface temperatures analogous to modern.

CHAPTER 4

REGIONAL AND GLOBAL SIGNIFICANCE OF PLIOCENE SEA SURFACE TEMPERATURES FROM THE GULF OF CADIZ (SITE U1387) AND THE MEDITERRANEAN

Alexandrina Tzanova[1]

Timothy D. Herbert[1]

1. Department of Geological Sciences, Brown University, 324 Brook Street, Providence RI, 02906

Submitted Global and Planetary Change Special Issue: Mediterranean Outflow

Abstract

The Atlantic – Mediterranean water exchange is a component of global ocean circulation capable of influencing deep water formation in the North Atlantic, yet it is poorly constrained for the time period preceding the intensification of Northern Hemisphere Glaciation (NHG). The sea surface temperature (SST) gradient between the Atlantic and Mediterranean sides of the Strait of Gibraltar can shed light on the communication between the two basins. IODP Site U1387 in the Gulf of Cadiz provides the first alkenone based reconstruction of SST for the Atlantic waters that flowed into the Mediterranean Sea during the Pliocene. This site reflects open ocean North Atlantic subtropical temperature trends while the published SST records from the Rossello composite section in the Mediterranean reflect the addition of regional, continentally-influenced signals from Europe and Northern Africa. The Mediterranean, in particular, may be influenced by high latitude Northern hemisphere climatic evolution. In the modern regime the sites discussed in this work have comparable SST and uninhibited surface connection; however, change in local heat loss/gain over the Mediterranean due to variability in latent heat loss and obstructed connection can result in a gradient between the sites in the Pliocene. The Pliocene surface waters of the Gulf of Cadiz and the Mediterranean Sea were as much as 7°C warmer than the modern average of ~19-20°C. The reconstructed temperatures show a ~1°C cooling for the Atlantic side of the Strait of Gibraltar from ~6 Ma to ~2.7 Ma and increasingly cooler glacials. The long-term SST record from Site U1387 provides a basis for future studies into the hydrological balance of the Mediterranean and the temperature component of Mediterranean Outflow Water (MOW) density. We compared SST on either side of Gibraltar between ~3.4 – 2.7

Ma and found that between ~2.7 and ~3.1 Ma the Mediterranean and Atlantic surface waters show comparable average temperatures and comparable variance.

4.1 Introduction

The intensification of bi-polar glaciation in the Northern Hemisphere delivered a cold end to the warm Pliocene (Lawrence et al., 2010; Lisiecki and Raymo, 2005; Zachos et al., 2001). The transition was most striking in the high Northern latitudes, which were enveloped in ice, but the Mediterranean region though located in the mid-latitudes could potentially respond and contribute to the freeze as well through the global thermohaline contribution of Mediterranean Outflow Water (MOW) (Khelifi et al., 2009; Rogerson et al., 2006; Voelker et al., 2006). Today, the MOW is an important component for North Atlantic Deep Water (NADW) formation (Iorga and Lozier, 1999a, b; McCartney and Mauritzen, 2001) by supplying a water mass with a uniquely high salt content to the North Atlantic. MOW has a signature that reflects the high evaporation in the Mediterranean region, which produces a distinctly dense water mass of salty yet warm water. MOW is essentially modified Atlantic Ocean water that enters the Mediterranean as surface flow through the Strait of Gibraltar and leaves the basin flowing under the incoming Atlantic waters (Rogerson et al., 2012). The temperature and salinity driven density gradient across the Strait of Gibraltar is a powerful control on the strength of MOW, yet there are no data from the region providing continuous reconstruction of sea surface temperature (SST) (Fauquette et al., 2006; Stow, 2011) during the warm Pliocene. Temperature is a component of density within the Mediterranean, which is fundamental to regional and potentially global water circulation. Additionally, the heat budget over the basin relates to the balance of precipitation and evaporation, which further controls the density of outflowing Mediterranean waters. The SSTs on the Atlantic side of Gibraltar provide the initial parameters of the water, and the SSTs on the Mediterranean side attest to the processes that have changed its temperature and salinity.

Ultimately, the modification of Atlantic water in the Mediterranean reflects the temperature and evaporation over the Mediterranean basin, which connect back to the Atlantic through MOW. The Mediterranean Sea, due to its small size and landlocked nature, has the potential to amplify temperature signals and respond to the heat of Africa in the summer and the cool of the northern winds in winter (Figure 1) (Bakun and Agostini, 2001; Garrett et al., 1993; Matsoukas et al., 2005). On orbital timescales the precessionally-paced shift in the reach of the African monsoon can greatly affect the temperature and salinity of the surface Mediterranean (Rossignol-Strick, 1985; Tuenter et al., 2003). The most obvious expression of the oscillation is the alternating cycle of sapropels and carbonate-rich layers in the Mediterranean (Krijgsman et al., 1995) and even in the Gulf of Cadiz (Hodell et al., 1989). Sapropels are the expression of a northern shift in the monsoon, fresher Mediterranean waters and warmer temperatures (Emeis et al., 2003; Emeis et al., 1998; Emeis et al., 2000). The heat budget across Gibraltar reflects a balance between sub-tropical forcing represented in the Atlantic (Figure 1) and a mixture of local, continental and high-latitude forcing exemplified in the Mediterranean (Rogerson et al., 2012).

The transition from a warm world to a world with large glacial-interglacial cycles coupled with the onset of MOW during the Pliocene (Hernandez-Molina et al., 2014a; Hernandez-Molina et al., 2014b; Stow, 2011) highlight the need for further investigation of Mediterranean region SST and MOW properties preceding large scale glaciation. Previous work has linked increase in MOW intensity to Pliocene glaciation (Voelker et al., 2006) and even hypothesized future glaciations based on saltier MOW due to decreased Nile freshwater contribution to the Mediterranean (Johnson, 1997).

In this work we address MOW density through the lens of Pliocene temperatures. Terrestrial biota reconstructions show the Pliocene Mediterranean region as 1 – 4 °C warmer than present (Fauquette et al., 2006; Fauquette et al., 1999; Jimenez-Moreno et al., 2010; Utescher et al., 2011) consistent with warm climate conditions reconstructed across the globe (Dowsett et al., 2011; Dowsett et al., 2012; Fauquette et al., 1999; Haywood et al., 2011; Lawrence et al., 2010; Meyers and Hinnov, 2010; Zachos et al., 2001), however not as warm as a recent Mediterranean SST reconstruction spanning a portion of the interval (Herbert et al., 2015). MOW, which was turned off during the Messinian Salinity Crisis, began to flow into the North Atlantic after 4.5 Ma even though the Mediterranean-Atlantic connection was reestablished at 5.33 Ma (Hernandez-Molina et al., 2014b). A comprehensive view into regional temperatures at the time of MOW initiation can highlight potential climate factors that resulted in the apparent lag between the opening of Gibraltar and MOW.

We build on the foundations set by IODP Expedition 339 to the Gulf of Cadiz and provide an alkenone-based reconstruction of SST that spans ~6 – 2.7 Ma. The SSTs can be combined with SST reconstructions from inside of the Mediterranean Sea (Herbert et al., 2015) to identify the temperature component of the temperature and salinity equation on either side of Gibraltar, which determines the signature of MOW. Our work builds on the original objective for Site U1387, which was to evaluate the correlation and influence of cold and warm periods with MOW variability and cold-period intensification of MOW during the Pliocene (Hernandez-Molina et al. 2014b, Expedition 339 Scientists 2012).

4.2 Background

The modern heat balance between the Gulf of Cadiz and the Mediterranean Sea results in similar SSTs on both sides of Gibraltar at our study sites (Figure 1), which may not have been the case in the Pliocene. Local evaporative processes and winds lead to a West to East temperature gradient, which attests to the influence of regional processes on Mediterranean SST. Warm summer winds that originate over Africa (Bakun and Agostini, 2001; Zecchetto and De Biasio, 2007) enhance warmth in the Eastern basin during the summer season (NOAA, 2005) aided by surface circulation (Figure 1) that piles warm water towards the East. In winter time frigid northern winds make the Mediterranean basin colder than the Gulf of Cadiz by cooling the surface and aiding in MOW formation (Stow, 2011). On an annual basis the warming and cooling cancel out, which leads to the comparable SSTs at our Mediterranean and Gulf of Cadiz study sites.

IODP Expedition 339, which marked the first time the Gulf of Cadiz was drilled for scientific study on million year (Myr) timescales (Stow, 2011), made possible the comparison between the SST in the Mediterranean to SST of the incoming Atlantic waters during the Pliocene. IODP Site U1387 (Figure 1) provides the most continuous (Expedition 339 Scientists 2012), biostratigraphically dated (Figure 2) sediment record from the expedition, spanning the re-flooding of the Mediterranean at 5.3 Ma to the onset and intensification of bipolar glaciation at ~2.7 Ma. Site U1387 is located on the eastern end of Faro Drift (36°48′N, 7°43 ′W) at 560 m water depth. Core recovery is 85%, however, it is notably better in the Pleistocene than in the Pliocene. Additionally, the initial operations show numerous erosional surfaces, which resulted from periods of strong MOW currents obliterating parts of the geological record in the Pliocene. Marine sedimentation dominates the site; however, initial reports document a slight relative increase in the terrestrial component during the Pliocene (Expedition_339_Scientists, 2012), possibly driven by local rivers.

Biostratigraphic control (Figure 3) shows our reconstruction spans ~6.2 – 2.6 Ma with an orbitally resolved (3-4 kyr) resolution between 2.6 – 3.3 Ma and 10-20 kyr resolution between ~3.5 Ma and the end of our record. In the older portion of our record, the resolution is not uniform because we were limited by sections of poor core recovery (for a detailed list consult the initial expedition logs) and erosional surfaces, interpreted as MOW intensification (Hernandez-Molina et al., 2014b). The most notable stratigraphic discontinuity comes between 3.2 – 3 Ma (Hernandez-Molina et al., 2014b) and is attributed to MOW strengthening potentially linked to the M2 glaciation at 3.3 Ma (Lisiecki and Raymo, 2005). Our age model for Site U1387 follows the available biostratigraphic datums (Expedition 339 Scientists 2012) as an initial framework and was subsequently orbitally tuned (in sections of orbitally resolved data) using insolation at 65°N (Laskar et al., 2004) and the Mediterranean record of Herbert et al, (2015) as target curves. Long-term, Pliocene structure in the global benthic isotope record (Lisiecki and Raymo, 2005) anchors our data further; however, as our orbitally resolved portion of the record does not extend past ~3.3 Ma, we acknowledge an enduring degree of age uncertainty particularly in the older portion of the record.

In the Mediterranean, SST reconstructions rely on composite of sites combining uplifted marine sections (locations listed in Herbert et al, 2015). Land sections (Punta Piccola, San Nicola, Vrica) (Herbert et al, 2015) have continuous, pelagic sedimentation over the Pliocene as confirmed by an orbital chronology embedded in a magnetic polarity stratigraphy (Langereis and Hilgen, 1991; Lourens et al., 1996). Sapropels map to Northern hemisphere precession maxima, when high freshwater input from Northern Africa and southern Europe results in an influx of terrigenous matter and higher organic content. Conversely, carbonate-rich beds reflect marine biogenous sedimentation under drier conditions (Hilgen et al., 2003; Lourens et al., 1996; Rossignol-Strick, 1985). The sapropel-limestone pattern provides a visual guide for time-targeted sampling. In this manuscript we present the record originally published in Herbert et al, (2015), extended by additional sampling to ~3.66 Ma. The chronology of the samples is tightly constrained by the astronomically-dated lithological cycles (Langereis and Hilgen, 1991; Lourens et al., 1996). The Mediterranean record does not extend to the onset of MOW at ~4.5 Ma (Hernandez-Molina et al., 2014b), which prevents us from constraining the Mediterranean-Atlantic heat balance during this pivotal time.

The proxy we choose for obtaining paleo – SST from Site U1387 and the Mediterranean is alkenone paleothermometer, the $U^{K'}_{37}$ index. The proxy relies on the ratios of organic molecules produced by haptophyte algae inhabiting the surface of the water and preserved in sediment (Herbert, 2003). The proxy can resolve SST over a wide range of timescales and salinity conditions in the Mediterranean effectively capturing orbital scale fluctuations (Emeis et al., 2003; Emeis et al., 1998; Emeis et al., 2000). Recent work shows that the utility of the $U^{K'}_{37}$ index can extend to uplifted marine sections (Beltran et al., 2011; Cleaveland and Herbert, 2009) of the Pliocene/Pleistocene.

4.3 Methods

Alkenones were extracted from finely ground sediment in a Dionex Accelerated Solvent Extractor (ASE 200) using 100% methylene chloride. Sample weights were ~2 g from Site U1387 and ~5 g for Mediterranean samples. The total lipid extract was evaporated under a nitrogen stream. Each sample was reconstituted in 200 ml of toluene containing a known amount of C_{36} and C_{37} n-alkane standards. The C_{37} alkenones were quantified by flame ionization detection on an Agilent 6890 GC equipped with an Agilent Technologies DB-1 column (60 m analytical column, 5 m fused guard column). To minimize changes in the GC response, we injected a toluene GC-FID blank after every 12 samples and monitored system stability by running replicate extracts and a laboratory alkenone standard. We changed the system's inlet liners and trimmed the column every 12-24 samples or as indicated by drifts in the GC behavior of the standard. In addition to the $U^{K'}_{37}$ index, the C_{37}total was determined by reference to internal standards and is reported per gram dry weight of sediment. SSTs were computed using the Muller et al., (1998) calibration.

4.4 Results

In this manuscript we report the results from Site U1387 in the Gulf of Cadiz during the Pliocene and compare them to the concurrent alkenone indices inside the Mediterranean. Between 6 – 2.6 Ma the average SST at Site U1387 was ~27°C, which is ~7-8°C warmer than modern annual average of ~20°C (Figures 1, 3-5). SSTs fall in the range of 24.6°C to 28.6°C, which makes the Gulf of Cadiz significantly warmer than today during the entire study interval. The decrease in the minima/glacial SST is ~2°C between 6 – 2.7 Ma versus a 1.2°C decrease in interglacial SST, which suggests increased amplitude in the temperature signal; however, we acknowledge that some structure is masked by relatively coarser resolution in the older section of our record. We note that Pliocene glacial SST were 11°C warmer than the temperatures reconstructed from the Last Glacial Maximum (LGM) in the region (Penaud et al., 2011), which further illustrates the degree of warming over the Mediterranean region in the Pliocene.

We note that the dating of the two-step decreases in interglacial SST at ~4 Ma (0.7°C) and ~3.4 Ma (0.5°C) has a degree of uncertainty as it is associated with poor temporal resolution and a discontinuity at ~3.3 Ma. The younger decrease closely precedes the erosional hiatus reported ~3.2 – 3 Ma (Hernandez-Molina et al., 2014b).

The Mediterranean (3.5 - 2.5 Ma) was on average ~6°C warmer than modern with mean SST of 26°C (Herbert et al., 2014). The range in SST is 23.6°C to 27.9°C (Herbert et al., 2014), which is nearly identical to the SST in the Gulf of Cadiz for the time period (between 2.7 Ma and 3.5 Ma) when the two records overlap.

C_{37}total values in the Gulf of Cadiz reconstruct haptophyte productivity and co-vary with SST similarly documented in the Mediterranean (Herbert et al., 2015). C_{37}total values show great variability of as much as a factor of 10 on a precessional scale (Figures 3 and 4). We used the orbital pacing of the C_{37}total index to provide additional age control for our data by correlating bundles of high amplitude C_{37}total cycles to high amplitude nodes in insolation (Laskar et al., 2004). We further correlated individual peaks and throughs in haptophyte productivity to peaks and throughs in insolation.

4.5 Discussion

4.5.1 Site U1387 in the Pliocene framework

At Site U1387, as well as the Mediterranean Sea (Herbert et al., 2014), we reconstruct warming that is as much as ~6-7°C over the modern mean annual SST (Figure 3), which is about 1-2°C warmer than the relative warming reconstructed at Site U1313/DSDP 607 (Fedorov et al., 2013; Naafs et al., 2010), and in pollen reconstructions in the Mediterranean (Fauquette et al., 1999) for the same time period. The North Atlantic Current (NAC) that passes over Site U1313 ultimately reaches Site U1387 and therefore the similarities in SST corroborate our findings. SSTs at U1313/DSDP 607, ODP 662 and ODP 958 show a lesser degree of warming at lower latitudes compared to the Mediterranean, which fits well with our understanding of Pliocene equator to pole temperature gradients (Fedorov et al., 2013). However, as in the Mediterranean (Herbert et al., 2015), the Gulf of Cadiz is notably warmer than PRISM data (Dowsett et al., 2012; Haywood et al., 2011), which suggests that at least in this region the PRISM reconstruction should be adjusted toward warmer temperatures by as much as 5-6°C.

The varied resolution of the Site U1387 SSTs record does not allow for continuous orbital scale comparison with the global record of glacial/interglacial cyclicity (Lisiecki and Raymo, 2005), but it does shed light on long-term Pliocene temperature evolution of the subtropical North Atlantic. We evaluate the orbital scale features of high-resolution data in the next section. The relative larger decrease in glacial SST versus the decrease in interglacial SST (Figure 3), clearly observed at Site U1387, mirrors the trends shown by the global benthic isotope record (Lisiecki and Raymo, 2005; Zachos et al., 2001) and the Mediterranean (Herbert et al., 2015). Long-term trends in the Gulf of Cadiz and the

Mediterranean suggest prolonged cooling prior to the intensification of NHG (Figures 3 and 4). Therefore, we interpret the Gulf of Cadiz SST as the results of a gradually cooling climate accompanied with progressively colder glacials.

4.5.2 Site U1387 and the Mediterranean Sea

On orbital scales, Site U1387 and Mediterranean SST anchor future Pliocene work in the area and illustrate the temperature component of the Mediterranean – Atlantic connection. In the Mediterranean, the SST record (Herbert et al, 2015) comes from uplifted marine sections (Figure 1), which though superbly dated (Hilgen et al., 2007; Langereis and Hilgen, 1991; Lourens et al., 1996) present the hurdle of potential degradation of the organic alkenone biomarker. However, results from pelagic Site U1387 clearly demonstrate that the trends and absolute values first reported in the Mediterranean (Herbert et al, 2015) are reliable. In the interval of overlap (Figure 4), alkenone productivity on either side of Gibraltar shows clear correspondence with the precession parameter, while calculated absolute SST are nearly identical. The Mediterranean region's potential for providing climate records, which speak to the continental conditions of the past is unparalleled; thus, Site U1387 bridges the enclosed Mediterranean and the open Atlantic and opens the doors for future investigations.

We compare orbital scale patterns in SST in the interval spanning 3.3 - 2.6 Ma to evaluate notable similarities and differences between the incoming Atlantic waters and the surface waters of the basin. The comparison separates hemisphere-wide patterns from regional events recorded or amplified in the Mediterranean. Both the Mediterranean and Site U1387 show a strong precessional signal in SST, as well as C_{37}total, which supports the interpretation of Pliocene sapropel formation driven by periodic pacing of rainfall and terrigenous input of nutrients (Herbert et al., 2015). The pacing is independent of background SST as Pliocene SST exceed Pleistocene conditions by as much as ~7°C.

The main differences between the enclosed Mediterranean and the Gulf of Cadiz concern the precessional scale variance in SST and C_{37}total, which reflect regional influences. The Mediterranean has a lagoonal circulation and poor productivity overall, except for precession paced cycles of high terrigenous input of nutrients (Rossignol-Strick, 1985). Haptophyte productivity at Site U1387 eclipses that of the Mediterranean Sea (Figure 4) (Herbert et al., 2015), which is not surprising given the open ocean setting of Site U1387. In the Gulf of Cadiz, background haptophyte productivity was higher, with variance greater than in the Mediterranean. Contrariwise, SSTs in the Mediterranean have greater precessional variance than SST at Site U1387 because the landlocked Mediterranean reflects the continental influence of the land-ocean temperature contrast. While Mediterranean and Site U1387 interglacial SST show nearly identical correspondence through the comparison interval, glacial SST in the Mediterranean were at least 0.5°C cooler between 3.3 – 2.6 Ma.

We interpret precessional scale differences between SST on either side of Gibraltar as the influence of either winter winds or continental cooling over the Mediterranean Sea. We stress that these local processes result in ~1°C difference between the sites today (Figure 1) (NOAA, 2005). This interpretation implies that this period (3.3 – 2.6 Ma) was analogous to the modern dynamics between the sites as Mediterranean glacials are marginally colder. The period between 3.1 – 2.6 Ma corresponds to maximal warmth in equatorial Africa and the Mediterranean, which might not correspond to maximum ocean warming (Bertini, 2010), highlighting regional influences over the Mediterranean.

4.5.3 Site U1387 SST, MOW and future applications

The Mediterranean region's sensitivity to high-latitude climate implies that the region not only responds to the high-latitude signal, but also mediates it through changes in MOW (Calmanti et al., 2006; Expedition_339_Scientists, 2012; Hodell et al., 2001; Khelifi et al., 2009; Rahmstorf, 1998; Rogerson et al., 2012; Voelker et al., 2006). High-latitude climate propagates to the Mediterranean with the cold winter winds that contribute to MOW formation, while the resulting response in MOW feeds back into NADW formation and global ocean circulation. The changes in MOW can be the amount or the density of the MOW plume, both of which bear the signature of evaporation, freshwater input and temperature over the Mediterranean Sea. SSTs at Site U1387 help to unlock the temperature component of this equation because they show the initial Atlantic waters that the Mediterranean modifies into MOW and link them to MOW intensity. Intensifications in MOW link to amplifications in North Atlantic Deep Water formation and modified thermohaline circulation globally (Hernandez-Molina et al., 2014b; Khelifi et al., 2009; Stow, 2011). This process invokes the density contribution of MOW to high latitudes, strengthening NADW formation, which in turn results in higher moisture supply to the polar region and increased ice and snow accumulation in the area. We can infer that cold excursions in the Gulf of Cadiz would be amplified in the Mediterranean Sea similarly to the marginally colder Mediterranean glacials we observe between 3.3 – 2.6 Ma. The cooler Mediterranean exemplifies the evaporative heat loss and cooling over the enclosed basin, which would lead to denser MOW.

Site U1387 demonstrates when the SST and aridity amplified the strength of MOW and when aridity was the dominant factor. We match the documented increases in MOW intensity at 4.5 – 4.2 Ma (Hernandez-Molina et al., 2014b), 3.8 Ma (Hernandez-Molina et al., 2014a) and 3.5 Ma (Khelifi et al., 2009) to surface temperatures in the Gulf of Cadiz and show instances where cooling accompanied MOW increase. The first step-decrease in SST in the Gulf of Cadiz is at ~4 Ma, which is surprising in view of the Mediterranean presence of *Globorotalia puncticula* signifying cooling earlier, at 4.5 Ma, and coinciding with MOW's onset; however, this implied cooling is also not reflected in pollen records (Fauquette et al., 1999). We lack SSTs from the Mediterranean during this time, but if we consider the presence of *Globorotalia puncticula* as expression of Mediterranean cooling we can infer denser MOW resulting from greater heat loss over the enclosed basin. In the late Pliocene section of the SST reconstruction, the Mediterranean and the Gulf of Cadiz show remarkable orbital synchronization in SST during the interval between ~2.6 3.3 Ma suggesting stable MOW properties. We cannot evaluate the covariance of Mediterranean and Atlantic SST near the documented 3.8 - 3.5 amplifications of MOW because of age uncertainties and poor recovery in that section.

Our interpretation suggests that the erosional hiatus between 3.2 – 3 Ma in the Gulf of Cadiz (Hernandez-Molina et al., 2014b) instead occurred closer to 3.3 – 3.45 Ma and is expressed as a modest step decrease in our SST from Site U1387. Mediterranean and Site U1387 SST track each other closely in absolute values and trends and do not allow for a hiatus up to 3.3 Ma. Furthermore, the haptophyte productivity inside and outside Mediterranean (Figure 4) shows remarkable correspondence to the precession cycle and at Site U1387, as in the Mediterranean, the low amplitude in insolation seamlessly parallels the low amplitude alkenone abundance. The revised timing shows better correspondence to the intensification of MOW at ~3.5 Ma (Khelifi et al., 2009), which the authors linked to Mediterranean aridification. Additionally, while the Mediterranean clearly shows the M2 glaciation at 3.3 Ma (Lisiecki and Raymo, 2005), SSTs from Site U1387 are missing this revealing feature. Increase in MOW would result in obliteration of part of the sediment record similar to the features that imply MOW onset at 4.5 Ma (Hernandez-Molina et al., 2014b), and should correspond to cooling excursions.

Our SST provide a stepping stone for future work to unlock the evolution of the hydrological budget of the Mediterranean Sea and unravel the properties of MOW during the Pliocene intensification of NHG. Detailed records of stable isotopes from the Gulf of Cadiz (this volume) can be combined with SST from Site U1387 (Figure 3) to generate a comprehensive view of the temperature and salinity of the source waters for the Mediterranean. Similarly, SST from the Mediterranean Sea (Herbert et al, 2015) and readily available isotope records (Lourens, 2004) can reconstruct how the Atlantic waters were modified once they were in the enclosed Mediterranean. Such reconstructions benefit paleoceanography studies of MOW strength and signature prior to NHG, as well as contribute to better understanding of regional aridity and climate in the Pliocene.

4.6 Conclusions

We present the first record of SST from the Gulf of Cadiz (Site U1387) spanning the re-establishment of the Mediterranean-Atlantic connection and the intensification of Northern Hemisphere Glaciation almost 2.5 Myr later, which contributes to our understanding of Pliocene warmth as well as regional ocean dynamics. Between 6 – 2.7 Ma SSTs at Site U1387 were as much as ~6°C warmer than present. The record shows a gradual cooling trend that mirrors the global benthic stack (Lisiecki and Raymo, 2005;

Zachos et al., 2001). At ~4 Ma and ~3.4 Ma SST maxima show a stepwise decrease, which is very close to documented increases in MOW intensity at 4.5 – 4.2 Ma (Hernandez-Molina et al., 2014b), 3.8 Ma (Hernandez-Molina et al., 2014a) and 3.5 Ma (Khelifi et al., 2009). We infer that the increase in MOW can be in part attributed to cooling conditions.

The SST record of Site U1387 is the first of its kind and length from the region and provides a firm basis for future work. SSTs from the Gulf of Cadiz closely match those reconstructed in the Mediterranean between 3.6 – 2.7 Ma (Herbert et al, 2015), which further validates the use of uplifted marine sections for alkenone paleothermometry. Future work on either side of Gibraltar needs to focus on continuous reconstruction of SST and stable isotopes to reconstruct the hydrological budget of the Mediterranean on both orbital and long-term timescales during the Pliocene. Better understanding of Mediterranean and MOW dynamics preceding NHG can help us to elucidate the role of MOW during this pivotal time in Earth's climate history.

4.7 Acknowledgements

This work reflects the generous support of the International Ocean Discovery Program through a Post Expedition Award to A. Tzanova and also support from the Petroleum Research Fund of the American Chemical Society to T.D. Herbert. We thank Daniel McGill, Oliver McLellan, Aaron Rachels and Klara Zimmerman for their assistance with sample analysis.

References

Bakun, A., Agostini, V.N., 2001. Seasonal patterns of wind-induced upwelling/downwelling in the Mediterranean Sea. Sci. Mar. 65, 243-257.

Beltran, C., Flores, J.A., Sicre, M.A., Baudin, F., Renard, M., de Rafelis, M., 2011. Long chain alkenones in the Early Pliocene Sicilian sediments (Trubi Formation - Punta di Maiata section): Implications for the alkenone paleothermometry. Paleogeogr. Paleoclimatol. Paleoecol. 308, 253-263.

Bertini, A., 2010. Pliocene to Pleistocene palynoflora and vegetation in Italy: State of the art. Quat. Int. 225, 5-24.

Calmanti, S., Artale, V., Sutera, A., 2006. North Atlantic MOC variability and the Mediterranean outflow: a box-model study. Tellus Ser. A-Dyn. Meteorol. Oceanol. 58, 416-423.

Cleaveland, L.C., Herbert, T.D., 2009. Preservation of the alkenone paleotemperature proxy in uplifted marine sequences: A test from the Vrica outcrop, Crotone, Italy. Geology 37, 179-182.

Dowsett, H.J., Haywood, A.M., Valdes, P.J., Robinson, M.M., Lunt, D.J., Hill, D., Stoll, D.K., Foley, K.M., 2011. Sea surface temperatures of the mid-Piacenzian Warm Period: A comparison of PRISM3 and HadCM3. Paleogeogr. Paleoclimatol. Paleoecol. 309, 83-91.

Dowsett, H.J., Robinson, M.M., Haywood, A.M., Hill, D.J., Dolan, A.M., Stoll, D.K., Chan, W.L., Abe-Ouchi, A., Chandler, M.A., Rosenbloom, N.A., Otto-Bliesner, B.L., Bragg, F.J., Lunt, D.J., Foley, K.M., Riesselman, C.R., 2012. Assessing confidence in Pliocene sea surface temperatures to evaluate predictive models. Nat. Clim. Chang. 2, 365-371.

Emeis, K.C., Schulz, H., Struck, U., Rossignol-Strick, M., Erlenkeuser, H., Howell, M.W., Kroon, D., Mackensen, A., Ishizuka, S., Oba, T., Sakamoto, T., Koizumi, I., 2003. Eastern Mediterranean surface water temperatures and delta O-18 composition during deposition of sapropels in the late Quaternary. Paleoceanography 18.

Emeis, K.C., Schulz, H.-M., Struck, U., Sakamoto, T., Doose, H., Erlenkeuser, H., Howell, M., Kroon, D., Paterne, M., 1998. Stable isotope and alkenone temperature records of sapropels from sites 964 and 968: Constraining the physical environment of sapropel formation in the Eastern Mediterranean Sea, In: Robertson, A.H.F., Emeis, K.C., Richter, C., Camerlenghi, A. (Eds.), Proceedings of the Ocean Drilling Program Scientific Results pp. 309-331.

Emeis, K.C., Struck, U., Schulz, H.M., Rosenberg, R., Bernasconi, S., Erlenkeuser, H., Sakamoto, T., Martinez-Ruiz, F., 2000. Temperature and salinity variations of Mediterranean Sea surface waters over the last 16,000 years from records of planktonic stable oxygen isotopes and alkenone unsaturation ratios. Paleogeogr. Paleoclimatol. Paleoecol. 158, 259-280.

Expedition_339_Scientists, 2012. Mediterranean outflow: environmental significance of the Mediterranean Outflow Water and its global implications, IODP Prel. Rept. TAMU.

Fauquette, S., Suc, J.P., Bertini, A., Popescu, S.M., Warny, S., Taoufiq, N.B., Villa, M.J.P., Chikhi, H., Feddi, N., Subally, D., Clauzon, G., Ferrier, J., 2006. How much did climate force the Messinian salinity crisis? Quantified climatic conditions from pollen records in the Mediterranean region. Paleogeogr. Paleoclimatol. Paleoecol. 238, 281-301.

Fauquette, S., Suc, J.P., Guiot, J., Diniz, F., Feddi, N., Zheng, Z., Bessais, E., Drivaliari, A., 1999. Climate and biomes in the West Mediterranean area during the Pliocene. Paleogeogr. Paleoclimatol. Paleoecol. 152, 15-36.

Fedorov, A.V., Brierley, C.M., Lawrence, K.T., Liu, Z., Dekens, P.S., Ravelo, A.C., 2013. Patterns and mechanisms of early Pliocene warmth. Nature 496, 43-+.

Garrett, C., Outerbridge, R., Thompson, K., 1993. Iinterannual variability in Mediterranean heat and buoyancy fluxes J. Clim. 6, 900-910.

Haywood, A.M., Ridgwell, A., Lunt, D.J., Hill, D.J., Pound, M.J., Dowsett, H.J., Dolan, A.M., Francis, J.E., Williams, M., 2011. Are there pre-Quaternary geological analogues for a future greenhouse warming? Philos. Trans. R. Soc. A-Math. Phys. Eng. Sci. 369, 933-956.

Herbert, T., Ng, G., Peterson, L.C., 2015. Evolution of Mediterranean sea surface temperatures 3.5–1.5 Ma: Regional and hemispheric influences. Earth Planet. Sci. Lett. 409, 307-318.

Herbert, T.D., 2003. Alkenone Paleotemperature Determinations, In: Elderfield, H., Turekian, K.K. (Ed.), Treatise in Marine Geochemistry. Elsevier, pp. 391-432.

Hernandez-Molina, F.J., Llave, E., Preu, B., Ercilla, G., Fontan, A., Bruno, M., Serra, N., Gomiz, J.J., Brackenridge, R.E., Sierro, F.J., Stow, D.A.V., Garcia, M., Juan, C., Sandoval, N., Arnaiz, A., 2014a. Contourite processes associated with the Mediterranean Outflow Water after its exit from the Strait of Gibraltar: Global and conceptual implications. Geology 42, 227-230.

Hernandez-Molina, F.J., Stow, D.A.V., Alvarez-Zarikian, C.A., Acton, G., Bahr, A., Balestra, B., Ducassou, E., Flood, R., Flores, J.A., Furota, S., Grunert, P., Hodell, D., Jimenez-Espejo, F., Kim, J.K., Krissek, L., Kuroda, J., Li, B.H., Llave, E., Lofi, J., Lourens, L., Miller, M., Nanayama, F., Nishida, N., Richter, C., Roque, C., Pereira, H., Goni, M.F.S., Sierro, F.J., Singh, A.D., Sloss, C., Takashimizu, Y., Tzanova, A., Voelker, A., Williams, T., Xuan, C., 2014b. PALEOCEANOGRAPHY Onset of Mediterranean outflow into the North Atlantic. Science 344, 1244-1250.

Hilgen, F., Kuiper, K., Krijgsman, W., Snel, E., van der Laan, E., 2007. Astronomical tuning as the basis for high resolution chronostratigraphy: the intricate history of the Messinian Salinity Crisis. Stratigraphy 4, 231-238.

Hilgen, F.J., Aziz, H.A., Krijgsman, W., Raffi, I., Turco, E., 2003. Integrated stratigraphy and astronomical tuning of the Serravallian and lower Tortonian at Monte dei Corvi (Middle-Upper Miocene, northern Italy). Paleogeogr. Paleoclimatol. Paleoecol. 199, 229-264.

Hodell, D.A., Benson, R.H., Kennett, J.P., Rakic-El Bied, K., 1989. Stable isotope stratigraphy of latest miocene sequences in northwest Morocco: the Bou Regreg section. Paleoceanography 4, 467-482.

Hodell, D.A., Curtis, J.H., Sierro, F.J., Raymo, M.E., 2001. Correlation of late Miocene to early Pliocene sequences between the Mediterranean and North Atlantic. Paleoceanography 16, 164-178.

Iorga, M.C., Lozier, M.S., 1999a. Signatures of the Mediterranean outflow from a North Atlantic climatology 1. Salinity and density fields. J. Geophys. Res.-Oceans 104, 25985-26009.

Iorga, M.C., Lozier, M.S., 1999b. Signatures of the Mediterranean outflow from a North Atlantic climatology 2. Diagnostic velocity fields. J. Geophys. Res.-Oceans 104, 26011-26029.

Jimenez-Moreno, G., Fauquette, S., Suc, J.P., 2010. Miocene to Pliocene vegetation reconstruction and climate estimates in the Iberian Peninsula from pollen data. Rev. Palaeobot. Palynology 162, 403-415.

Johnson, R.G., 1997. Climate control requires a dam at the Strait of Gibraltar. Eos Trans. AGU 78, 277-281.

Khelifi, N., Sarnthein, M., Andersen, N., Blanz, T., Frank, M., Garbe-Schonberg, D., Haley, B.A., Stumpf, R., Weinelt, M., 2009. A major and long-term Pliocene intensification of the Mediterranean outflow, 3.5-3.3 Ma ago. Geology 37, 811-814.

Krijgsman, W., Hilgren, F.J., Langereis, C.G., Santarelli, A., Zachariasse, W.J., 1995. Late Miocene magnetostratigraphy, biostratigraphy and cyclostratigraphy in the Mediterranean. Earth Planet. Sci. Lett. 136, 475-494.

Langereis, C.G., Hilgen, F.J., 1991. The Rossello composite - a Mediterranean and global reference section for the Early to early Late Pliocene. Earth Planet. Sci. Lett. 104, 211-225.

Laskar, J., Robutel, P., Joutel, F., Gastineau, M., Correia, A.C.M., Levrard, B., 2004. A long-term numerical solution for the insolation quantities of the Earth. Astron. Astrophys. 428, 261-285.

Lawrence, K.T., Sosdian, S., White, H.E., Rosenthal, Y., 2010. North Atlantic climate evolution through the Plio-Pleistocene climate transitions. Earth Planet. Sci. Lett. 300, 329-342.

Lisiecki, L.E., Raymo, M.E., 2005. A Pliocene-Pleistocene stack of 57 globally distributed benthic delta O-18 records. Paleoceanography 20.

Lourens, L.J., 2004. Revised tuning of Ocean Drilling Program Site 964 and KC01B (Mediterranean) and implications for the delta O-18, tephra, calcareous nannofossil, and geomagnetic reversal chronologies of the past 1.1 Myr. Paleoceanography 19.

Lourens, L.J., Antonarakou, A., Hilgen, F.J., VanHoof, A.A.M., VergnaudGrazzini, C., Zachariasse, W.J., 1996. Evaluation of the Plio-Pleistocene astronomical timescale. Paleoceanography 11, 391-413.

Matsoukas, C., Banks, A.C., Hatzianastassiou, N., Pavlakis, K.G., Hatzidimitrou, D., Drakadis, E., Stackhouse, P.W., Vardavas, I., 2005. Seasonal heat budget of the Mediterranean Sea. Journal of Geophysical Research- Oceans 110.

McCartney, M.S., Mauritzen, C., 2001. On the origin of the warm inflow to the Nordic Seas. Prog. Oceanogr. 51, 125-214.

Meyers, S.R., Hinnov, L.A., 2010. Northern Hemisphere glaciation and the evolution of Plio-Pleistocene climate noise. Paleoceanography 25.

Muller, P.J., Kirst, G., Ruhland, G., von Storch, I., Rosell-Mele, A., 1998. Calibration of the alkenone paleotemperature index U-37(K ') based on core-tops from the eastern South

Atlantic and the global ocean (60 degrees N-60 degrees S). Geochim. Cosmochim. Acta 62, 1757-1772.

Naafs, B.D.A., Stein, R., Hefter, J., Khelifi, N., De Schepper, S., Haug, G.H., 2010. Late Pliocene changes in the North Atlantic Current. Earth Planet. Sci. Lett. 298, 434-442.

NOAA, 2005. World Ocean Atlas.

Penaud, A., Eynaud, F., Voelker, A., Kageyama, M., Marret, F., Turon, J.L., Blamart, D., Mulder, T., Rossignol, L., 2011. Assessment of sea surface temperature changes in the Gulf of Cadiz during the last 30 ka: implications for glacial changes in the regional hydrography. Biogeosciences 8, 2295-2316.

Rahmstorf, S., 1998. Influence of Mediterranean outflow on climate. Eos Trans. AGU 79, 281-282.

Rogerson, M., Rohling, E.J., Bigg, G.R., Ramirez, J., 2012. Paleoceanography of the Atlantic-Mediterranean exchange: overview and first quantitative assessment of climatic forcing. Rev. Geophys. 50.

Rogerson, M., Rohling, E.J., Weaver, P.P.E., 2006. Promotion of meridional overturning by Mediterranean-derived salt during the last deglaciation. Paleoceanography 21.

Rossignol-Strick, M., 1985. Mediterranean quaternary sapropels, and immediate response of the African monsoon to variation of insolation. Paleogeogr. Paleoclimatol. Paleoecol. 49, 237-263.

Stow, D., Hernandez-Molina, F.J., Hodell, D., and Alvarez Zarikian, C.A., 2011. Mediterranean outflow: environmental significance of the Mediterranean Outflow Water and its global implications. IODP Sci. Prosp 339.

Tuenter, E., Weber, S.L., Hilgen, F.J., Lourens, L.J., 2003. The response of the African summer monsoon to remote and local forcing due to precession and obliquity. Glob. Planet. Change 36, 219-235.

Utescher, T., Bruch, A.A., Micheels, A., Mosbrugger, V., Popova, S., 2011. Cenozoic climate gradients in Eurasia - a palaeo-perspective on future climate change? Paleogeogr. Paleoclimatol. Paleoecol. 304, 351-358.

Voelker, A.H.L., Lebreiro, S.M., Schonfeld, J., Cacho, I., Erlenkeuser, H., Abrantes, F., 2006. Mediterranean outflow strengthening during northern hemisphere coolings: A salt source for the glacial Atlantic? Earth Planet. Sci. Lett. 245, 39-55.

Zachos, J., Pagani, M., Sloan, L., Thomas, E., Billups, K., 2001. Trends, rhythms, and aberrations in global climate 65 Ma to present. Science 292, 686-693.

Zecchetto, S., De Biasio, F., 2007. Sea surface winds over the Mediterranean basin from satellite data (2000-04): Meso- and local-scale features on annual and seasonal time scales. J. Appl. Meteorol. Climatol. 46, 814-827.

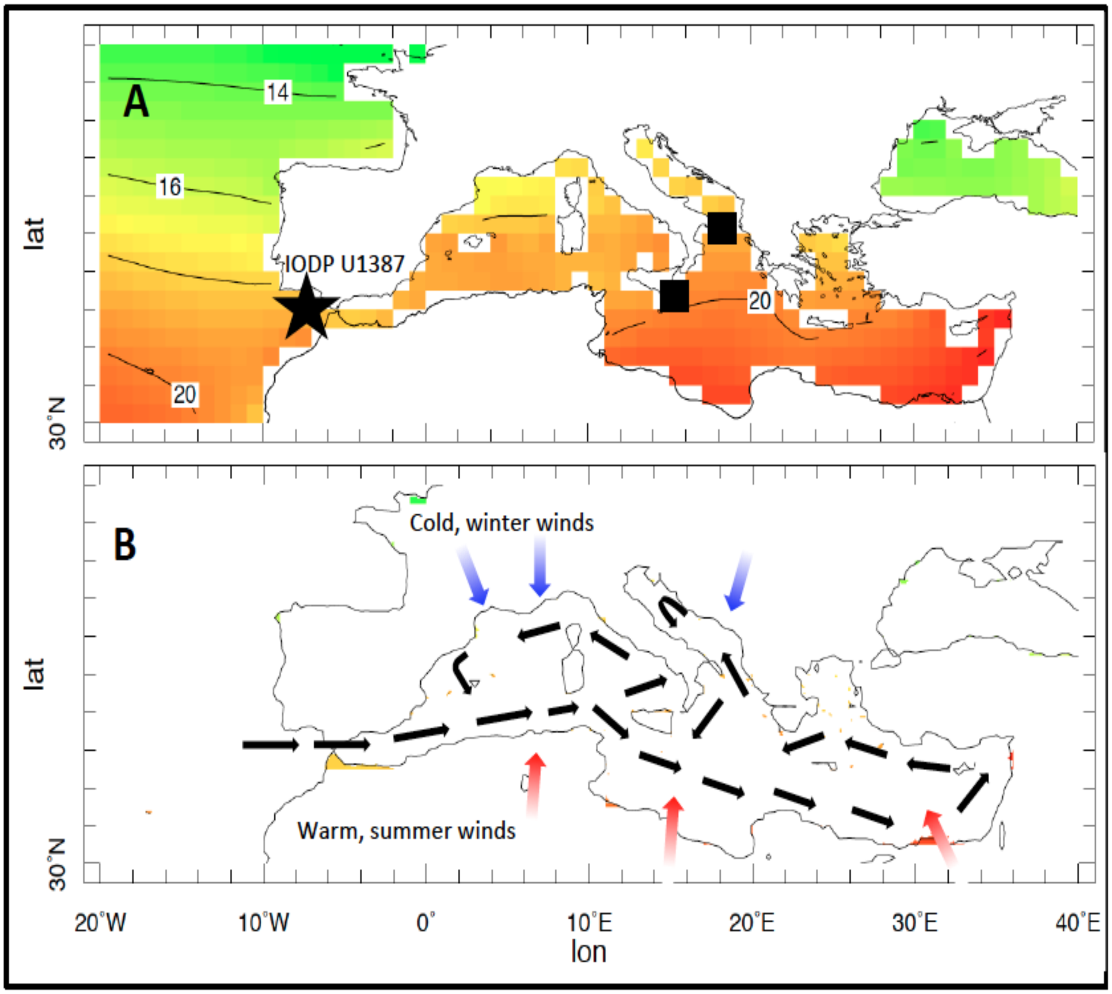

Figure 4.1 A) Location map of IODP Site U1387 (star) and Mediterranean land sections from Herbert et al., (2015). Modern sea surface temperatures are shown after the World Ocean Atlas (NOAA, 2005). B) Predominant winds over the Mediterranean region and idealized surface circulation.

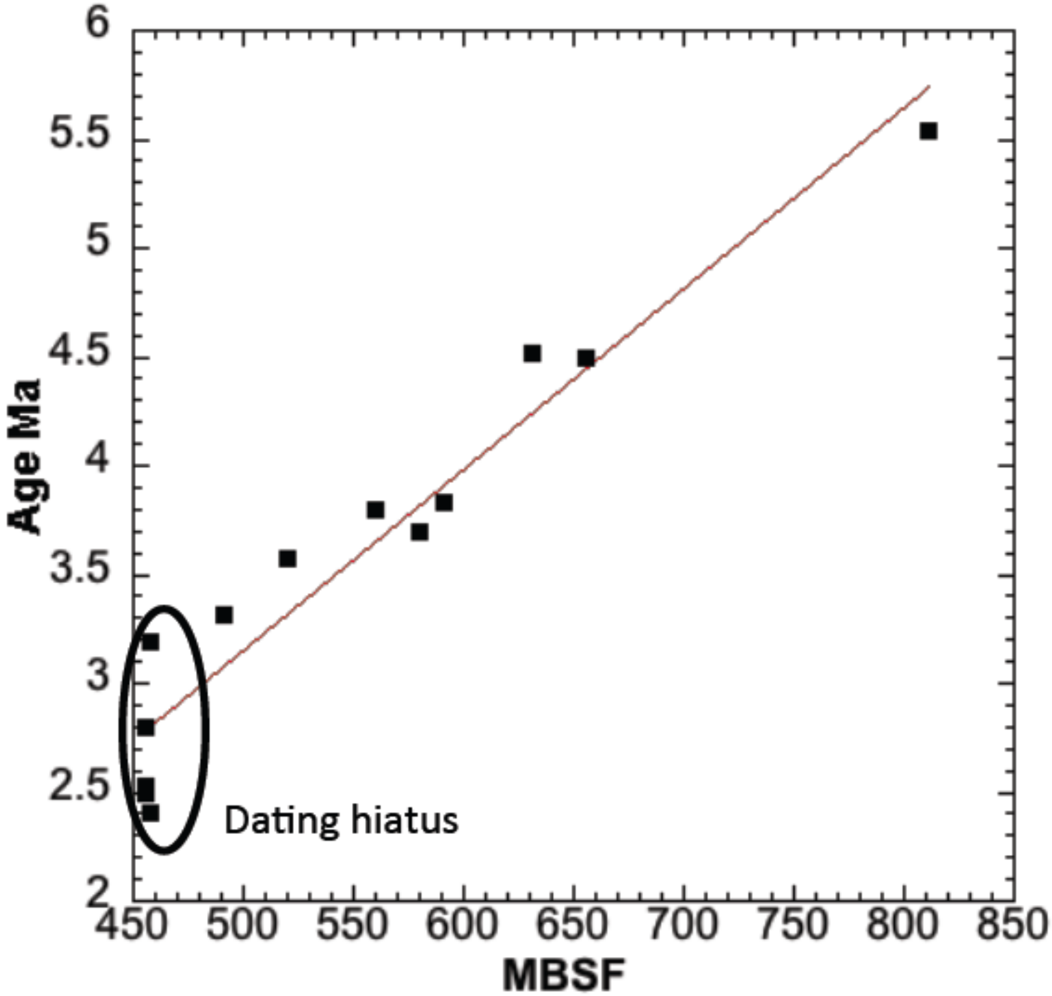

Figure 4.2 Plot of biostratigraphic datums of Site U1387 with a line illustrating the deviation from a linear age model.

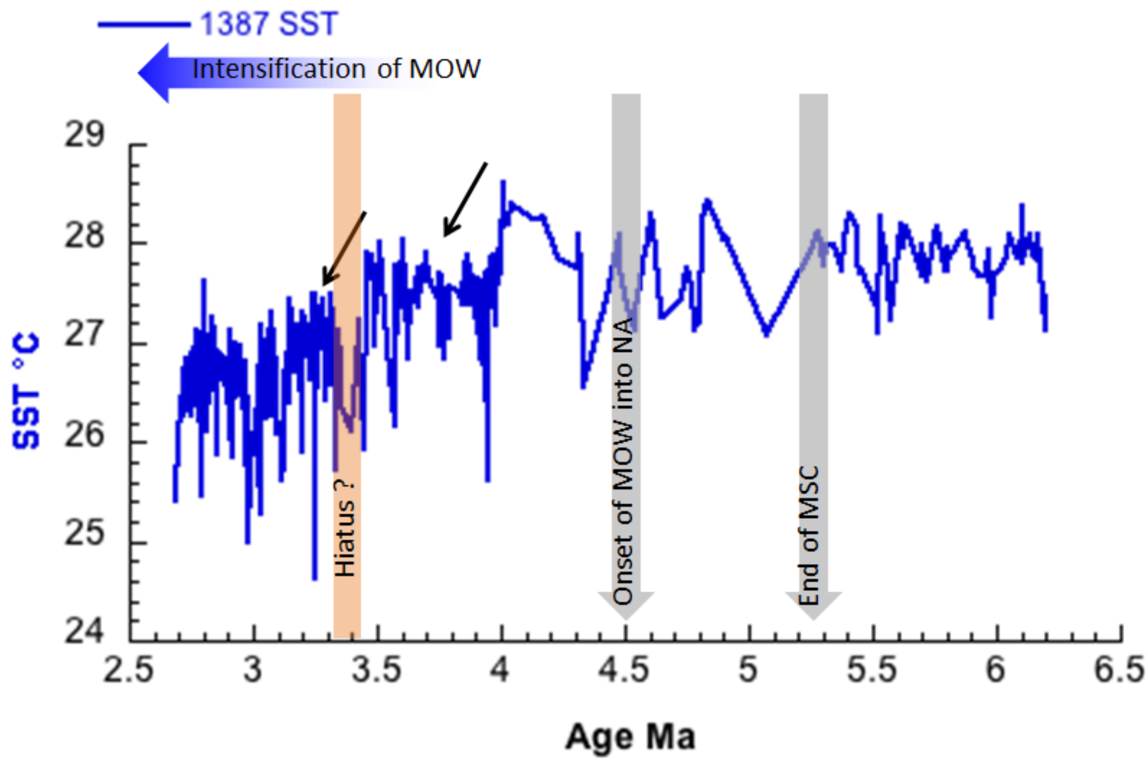

Figure 4.3 $U^{K'}_{37}$ SST reconstruction for Site U1387 with black arrows showing notable step decreases in SST. The two gray arrows indicate the onset of MOW into the North Atlantic and the end of the Messinian Salinity Crisis (re-flooding of the Mediterranean)

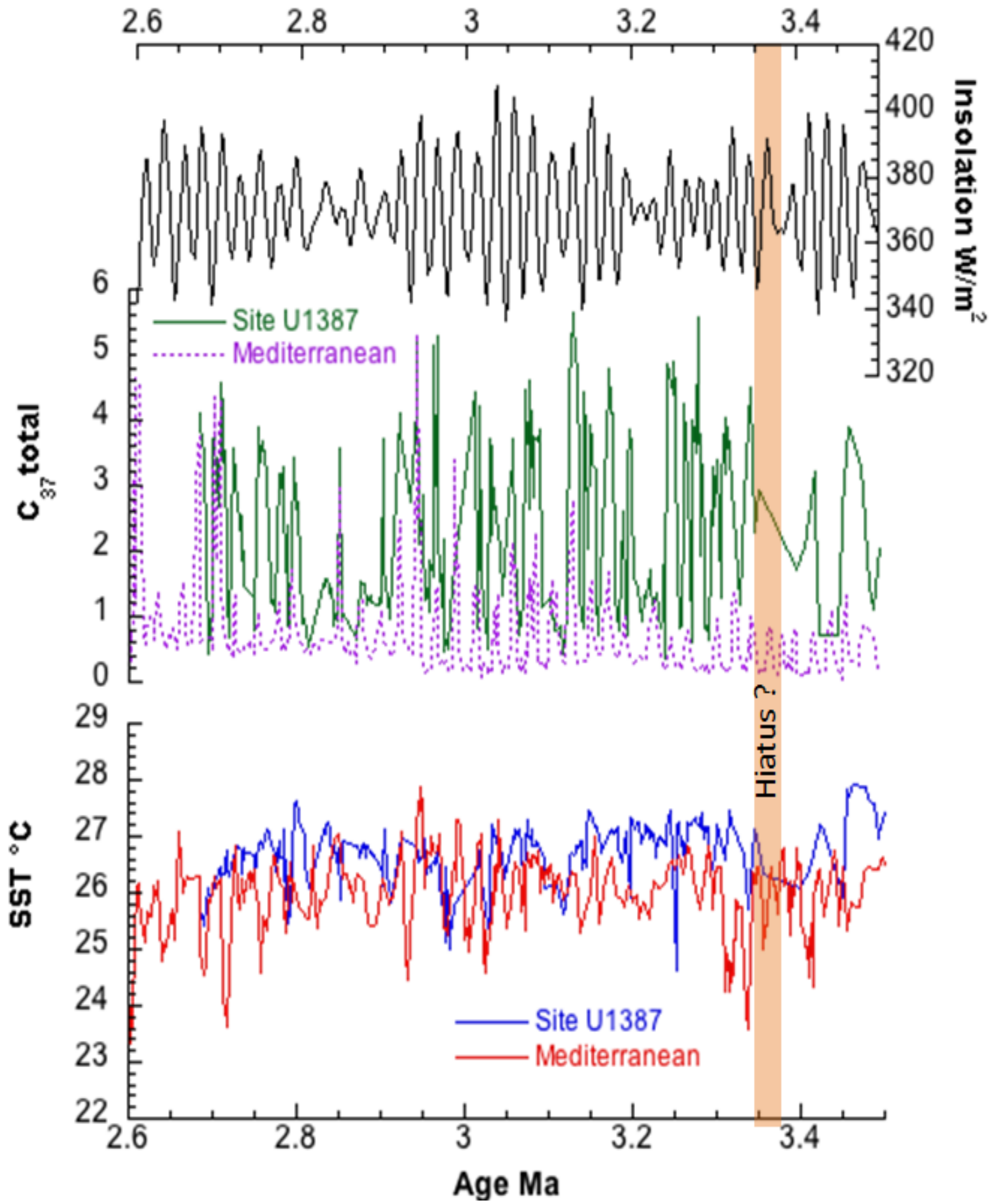

Figure 4.4 $U^{K'}_{37}$ SST reconstruction for Site U1387 (blue) and Mediterranean SST of Herbert et al., (2015) (red) shown with Site U1387 C_{37}total (green) and Mediterranean C_{37}total (purple) along with insolation at 65°N (black).

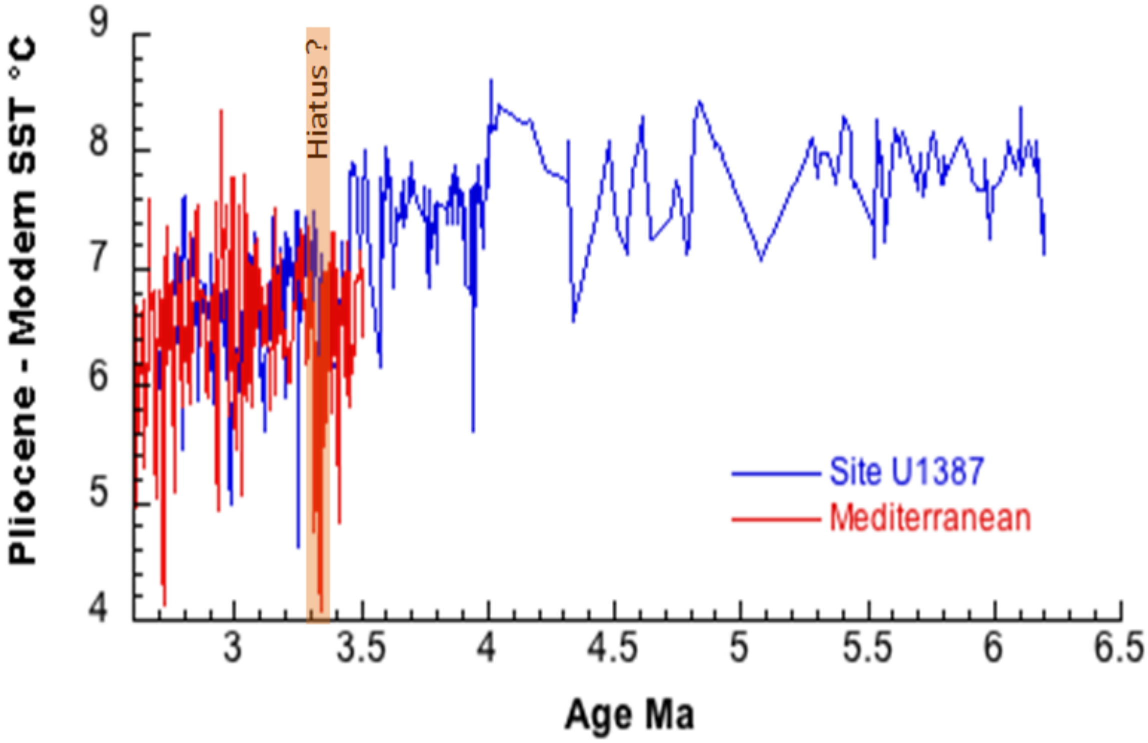

Figure 4.5 Difference in Pliocene to modern SST in the Gulf of Cadiz (blue) and the Mediterranean Sea (red).

APPENDIX A

MONTE DEI CORVI ALKENONE INDICES

Appendix A Monte dei Corvi Alkenone Indices Monte dei Corvi Alkenone Indices

Site	Depth (m)	Age(Ma)	Analysis	UK'37	SST (°C) PW	SST (°C) M	[C37] total (nmol/g)
MDC	144	6.3496	A3	0.930	26.20	26.84	0.08
MDC	143	6.3990	A3	0.862	24.20	24.78	0.10
MDC	142	6.4652	A2	0.931	26.24	26.88	0.42
MDC	141.9	6.4860	A1	0.919	25.89	26.53	0.46
MDC	141.8	6.4767	A1	0.897	25.22	25.84	0.07
MDC	141.7	6.4860	A1	0.919	25.89	26.53	0.15
MDC	141.6	6.4883	A2	0.874	24.56	25.15	0.06
MDC	141.6	6.4956	A1	0.866	24.34	24.92	0.41
MDC	141.5	6.4941	A2	0.901	25.34	25.96	0.11
MDC	141.4	6.4999	A1	0.930	26.20	26.85	0.15
MDC	141.2	6.5114	A1	0.890	25.03	25.63	0.39
MDC	141.1	6.5172	A1	0.906	25.50	26.12	0.19
MDC	141	6.5230	A3	0.930	26.20	26.84	0.43
MDC	140.9	6.5288	A1	0.930	26.20	26.84	0.24
MDC	140.8	6.5345	A2	0.876	24.61	25.21	0.28
MDC	140.75	6.5374	A2	0.894	25.15	25.76	0.20
MDC	140.7	6.5403	A2	0.900	25.33	25.95	0.32
MDC	140.65	6.5432	A1	0.921	25.94	26.58	0.25
MDC	140.6	6.5461	A2	0.884	24.86	25.47	0.30
MDC	140.55	6.5490	A2	0.892	25.09	25.70	0.24
MDC	140.5	6.5575	A1	0.916	25.80	26.43	0.53
MDC	140.45	6.5578	A2	0.868	24.38	24.97	0.10
MDC	140.4	6.5580	A2	0.898	25.26	25.88	0.76
MDC	140.35	6.5605	A1	0.882	24.78	25.38	0.45
MDC	140.3	6.5634	A2	0.893	25.11	25.72	0.50
MDC	140.25	6.5663	A1	0.859	24.11	24.69	0.09
MDC	140.2	6.5692	A2	0.910	25.63	26.25	0.49
MDC	140.15	6.5721	A1	0.887	24.93	25.53	0.38
MDC	140.1	6.5750	A1	0.925	26.06	26.70	0.12
MDC	140.05	6.5820	A2	0.932	26.27	26.91	0.31
MDC	140	6.5821	A3	0.928	26.15	26.79	0.50
MDC	139.95	6.5837	A1	0.911	25.66	26.29	0.87
MDC	139.85	6.5894	A1	0.920	25.91	26.55	0.29
MDC	139.75	6.5952	A2	0.923	26.01	26.65	0.62
MDC	139.7	6.5981	A2	0.937	26.42	27.07	0.46
MDC	139.65	6.6010	A2	0.924	26.03	26.66	0.49
MDC	139.6	6.6039	A1	0.921	25.95	26.58	0.45
MDC	139.55	6.6068	A1	0.925	26.05	26.69	0.39
MDC	139.5	6.6097	A1	0.911	25.63	26.26	0.15
MDC	139.45	6.6125	A1	0.911	25.65	26.28	0.32
MDC	139.4	6.6154	A1	0.911	25.64	26.27	0.38
MDC	139.35	6.6183	A1	0.901	25.35	25.97	0.36
MDC	139.3	6.6212	A1	0.905	25.47	26.09	0.29
MDC	139.25	6.6241	A1	0.896	25.20	25.81	0.09
MDC	139.1	6.6328	A2	0.908	25.57	26.20	0.23
MDC	139.05	6.6357	A1	0.933	26.30	26.95	0.67
MDC	139	6.6385	A1	0.908	25.55	26.17	0.27
MDC	139	6.6385	A2	0.943	26.60	27.26	0.13
MDC	138.95	6.6414	A1	0.926	26.09	26.73	0.15
MDC	138.9	6.6443	A1	0.915	25.78	26.41	0.16

Appendix A Monte dei Corvi Alkenone Indices

Site	Depth (m)	Age(Ma)	Analysis	UK'37	SST (°C) PW	SST (°C) M	[C37] total (nmol/g)
MDC	138.85	6.6472	A1	0.929	26.18	26.82	0.07
MDC	138.8	6.6501	A1	0.943	26.59	27.24	0.09
MDC	138.75	6.6530	A1	0.927	26.13	26.77	0.09
MDC	138.7	6.6559	A1	0.910	25.62	26.24	0.19
MDC	138.65	6.6588	A1	0.919	25.89	26.53	0.17
MDC	138.6	6.6617	A1	0.934	26.32	26.96	0.14
MDC	138.55	6.6646	A1	0.873	24.52	25.11	0.05
MDC	138.5	6.6674	A1	0.924	26.02	26.66	0.08
MDC	138.45	6.6703	A1	0.916	25.81	26.44	0.14
MDC	138.45	6.6703	A2	0.919	25.88	26.51	0.15
MDC	138.4	6.6732	A1	0.924	26.02	26.66	0.17
MDC	138.4	6.6732	A2	0.919	25.89	26.52	0.13
MDC 11	138.35	6.6761	A1	0.932	26.28	26.92	0.33
MDC 11	138.3	6.6840	A1	0.813	22.77	23.31	0.04
MDC 11	138.25	6.6918	A1	0.921	25.95	26.58	0.27
MDC 11	138.2	6.6938	A1	0.924	26.03	26.67	0.25
MDC 11	138.15	6.6954	A1	0.920	25.90	26.53	0.41
MDC 11	138.1	6.6964	A1	0.862	24.21	24.79	0.24
MDC 11	138.05	6.6971	A1	0.856	24.02	24.60	0.08
MDC 11	138	6.7050	A1	0.839	23.52	24.09	0.09
MDC	138	6.7050	A1	0.912	25.67	26.30	0.04
MDC 11	137.95	6.7200	A2	0.933	26.28	26.93	0.22
MDC 11	137.95	6.7200	A1	0.936	26.38	27.03	0.30
MDC 11	137.9	6.7219	A1	0.914	25.72	26.35	0.14
MDC 11	137.85	6.7220	A1	0.846	23.74	24.30	0.05
MDC 11	137.8	6.7240	A1	0.856	24.02	24.59	0.04
MDC 11	137.75	6.7260	A1	0.928	26.14	26.78	0.23
MDC 11	137.7	6.7300	A1	0.829	23.24	23.79	0.10
MDC 11	137.65	6.7360	A1	0.871	24.47	25.06	0.02
MDC 11	137.6	6.7380	A1	0.912	25.68	26.31	0.07
MDC 11	137.55	6.7382	A1	0.927	26.12	26.76	0.10
MDC 11	137.5	6.7384	A1	0.919	25.88	26.51	0.15
MDC 11	137.45	6.7394	A2	0.910	25.62	26.25	0.10
MDC 11	137.45	6.7402	A1	0.925	26.05	26.69	0.14
MDC 11	137.4	6.7430	A2	0.932	26.26	26.91	0.16
MDC 11	137.4	6.7430	A1	0.935	26.35	26.99	0.20
MDC 11	137.35	6.7442	A1	0.941	26.54	27.19	0.22
MDC 11	137.3	6.7510	A1	0.893	25.11	25.72	0.02
MDC 11	137.25	6.7550	A1	0.902	25.37	25.99	0.01
MDC 11	137.2	6.7589	A1	0.920	25.92	26.56	0.03
MDC 11	137.15	6.7620	A1	0.952	26.85	27.51	0.15
MDC 11	137.1	6.7670	A1	0.929	26.18	26.82	0.16
MDC 11	137.05	6.7755	A2	0.935	26.35	27.00	0.13
MDC 11	137.05	6.7755	A1	0.943	26.58	27.24	0.14
MDC-11	137	6.7810	A1	0.864	24.28	24.86	0.25
MDC	137	6.7810	A1	0.919	25.87	26.50	0.02
MDC 11	136.95	6.7890	A1	0.912	25.67	26.29	0.08
MDC-11	136.9	6.7935	A1	0.812	22.75	23.29	0.03
MDC-11	136.75	6.7985	A1	0.885	24.89	25.49	0.25
MDC-11	136.7	6.8010	A1	0.807	22.59	23.13	0.02

Appendix A Monte dei Corvi Alkenone Indices

Site	Depth (m)	Age(Ma)	Analysis	UK'37	SST (°C) PW	SST (°C) M	[C37] total (nmol/g)
MDC 11	136.65	6.8040	A1	0.860	24.14	24.72	0.01
MDC-11	136.6	6.8090	A1	0.791	22.12	22.64	0.01
MDC 11	136.55	6.8125	A1	0.887	24.95	25.56	0.01
MDC-11	136.5	6.8175	A1	0.821	23.00	23.55	0.01
MDC 11	136.45	6.8215	A1	0.900	25.31	25.93	0.01
MDC-11	136.3	6.8300	A1	0.850	23.84	24.41	0.02
MDC-11	136.3	6.8300	A2	0.839	23.54	24.10	0.02
MDC 11	136.25	6.8399	A1	0.957	26.99	27.66	0.26
MDC-11	136.2	6.8450	A1	0.870	24.43	25.02	0.18
MDC 11	136.15	6.8460	A1	0.908	25.56	26.19	0.08
MDC-11	136.1	6.8490	A1	0.716	19.91	20.36	0.04
MDC 11	136.05	6.8510	A1	0.803	22.48	23.01	0.02
MDC-11	136	6.8550	A1	0.711	19.76	20.21	0.02
MDC	136	6.8550	A1	0.740	20.61	21.08	0.02
MDC 11	135.95	6.8580	A1	0.847	23.77	24.34	0.00
MDC-11	135.9	6.8592	A1	0.791	22.11	22.63	0.02
MDC 11	135.85	6.8610	A1	0.911	25.66	26.29	0.01
MDC-11	135.8	6.8640	A1	0.916	25.81	26.44	0.17
MDC 11	135.75	6.8666	A1	0.900	25.33	25.95	0.02
MDC-11	135.7	6.8696	A1	0.845	23.70	24.27	0.02
MDC 11	135.65	6.8710	A1	0.940	26.50	27.15	0.05
MDC-11	135.6	6.8750	A1	0.914	25.74	26.36	0.34
MDC 11	135.55	6.8810	A2	0.949	26.76	27.42	0.27
MDC 11	135.55	6.8810	A1	0.949	26.77	27.43	0.28
MDC-11	135.5	6.8845	A1	0.953	26.89	27.56	0.15
MDC 11	135.45	6.8930	A1	0.749	20.89	21.37	0.02
MDC-11	135.4	6.9010	A1	0.894	25.13	25.74	0.02
MDC 11	135.35	6.9050	A1	0.886	24.90	25.51	0.01
MDC-11	135.3	6.9085	A1	0.772	21.55	22.05	0.01
MDC 11	135.25	6.9125	A1	0.946	26.68	27.34	0.13
MDC 11	135.15	6.9190	A1	0.864	24.28	24.86	0.03
MDC-11	135.1	6.9270	A1	0.702	19.49	19.93	0.01
MDC 11	135.05	6.9280	A1	0.886	24.90	25.50	0.01
MDC-11	135	6.9287	A1	0.875	24.57	25.17	0.02
MDC	135	6.9287	A1	0.885	24.87	25.47	0.02
MDC 11	134.95	6.9380	A1	0.932	26.27	26.91	0.01
MDC-11	134.9	6.9484	A1	0.843	23.65	24.21	0.02
MDC 11	134.85	6.9501	A1	0.934	26.33	26.98	0.01
MDC 11	134.75	6.9526	A1	0.913	25.72	26.35	0.01
MDC-11	134.7	6.9551	A1	0.886	24.91	25.51	0.01
MDC 11	134.65	6.9600	A1	0.944	26.61	27.26	0.04
MDC 11	134.65	6.9600	A2	0.947	26.71	27.37	0.04
MDC-11	134.6	6.9710	A1	0.893	25.11	25.72	0.02
MDC 11	134.55	6.9750	A1	0.944	26.62	27.27	0.01
MDC-11	134.5	6.9780	A1	0.956	26.98	27.65	0.05
MDC 11	134.45	6.9795	A1	0.943	26.58	27.24	0.12
MDC-11	134.4	6.9836	A1	0.850	23.87	24.44	0.01
MDC 11	134.35	6.9872	A1	0.915	25.77	26.40	0.01
MDC-11	134.3	6.9915	A1	0.835	23.42	23.98	0.01
MDC 11	134.25	6.9956	A1	0.902	25.37	25.99	0.00

Appendix A Monte dei Corvi Alkenone Indices

Site	Depth (m)	Age(Ma)	Analysis	UK'37	SST (°C) PW	SST (°C) M	[C37] total (nmol/g)
MDC-11	134.2	6.9997	A1	0.859	24.12	24.70	0.01
MDC 11	134.15	7.0038	A1	0.955	26.94	27.61	0.01
MDC-11	134.1	7.0079	A1	0.820	22.98	23.52	0.01
MDC 11	134.05	7.0120	A1	0.839	23.52	24.08	0.01
MDC	134	7.0161	A1	0.832	23.32	23.87	0.02
MDC-11	134	7.0161	A1	0.790	22.08	22.60	0.00
MDC 11	133.95	7.0290	A1	0.932	26.26	26.90	0.01
MDC-11	133.9	7.0410	A1	0.801	22.42	22.94	0.01
MDC 11	133.85	7.0480	A1	0.898	25.26	25.88	0.01
MDC 11	133.75	7.0510	A1	0.907	25.53	26.15	0.00
MDC-11	133.7	7.0610	A1	0.777	21.70	22.21	0.01
MDC-11	133.7	7.0610	A2	0.784	21.91	22.42	0.01
MDC-11	133.6	7.0688	A1	0.818	22.92	23.46	0.01
MDC 11	133.55	7.0750	A2	0.886	24.92	25.52	0.00
MDC 11	133.55	7.0750	A1	0.868	24.38	24.97	0.00
MDC-11	133.5	7.0820	A1	0.809	22.65	23.18	0.01
MDC 11	133.45	7.0858	A1	0.934	26.34	26.98	0.01
MDC-11	133.4	7.0898	A1	0.850	23.86	24.43	0.02
MDC 11	133.35	7.0948	A1	0.954	26.91	27.58	0.02
MDC-11	133.3	7.1028	A1	0.772	21.55	22.05	0.01
MDC 11	133.25	7.1090	A1	0.821	23.00	23.55	0.01
MDC-11	133.2	7.1190	A2	0.859	24.11	24.69	0.02
MDC-11	133.2	7.1278	A1	0.855	24.01	24.59	0.02
MDC 11	133.15	7.1318	A1	0.805	22.54	23.07	0.01
MDC-11	133.1	7.1338	A1	0.687	19.07	19.49	0.01
MDC 11	133.05	7.1450	A1	0.812	22.75	23.29	0.00
MDC-11	133	7.1530	A1	0.761	21.23	21.72	0.01
MDC	133	7.1530	A1	0.785	21.95	22.46	0.01
MDC 11	132.95	7.1580	A1	0.830	23.27	23.82	0.01
MDC 11	132.95	7.1580	A2	0.832	23.31	23.87	0.01
MDC-11	132.9	7.1600	A1	0.856	24.04	24.62	0.02
MDC 11	132.85	7.1638	A2	0.823	23.06	23.61	0.00
MDC 11	132.85	7.1638	A1	0.822	23.03	23.58	0.00
MDC-11	132.8	7.1788	A1	0.693	19.24	19.67	0.00
MDC 11	132.75	7.1810	A1	0.865	24.29	24.87	0.00
MDC-11	132.7	7.1848	A1	0.819	22.93	23.47	0.01
MDC 11	132.65	7.1918	A1	0.854	23.97	24.54	0.00
MDC-11	132.6	7.1988	A1	0.748	20.85	21.33	0.01
MDC 11	132.55	7.2058	A1	0.877	24.65	25.24	0.01
MDC-11	132.5	7.2300	A1	0.728	20.27	20.73	0.01
MDC 11	132.45	7.2350	A1	0.826	23.15	23.70	0.01
MDC-11	132.4	7.2380	A1	0.779	21.75	22.26	0.01
MDC 11	132.35	7.2410	A1	0.806	22.56	23.09	0.00
MDC-11	132.3	7.2490	A1	0.778	21.73	22.24	0.01
MDC 11	132.25	7.2620	A1	0.884	24.85	25.45	0.00
MDC-11	132.2	7.2675	A1	0.782	21.86	22.37	0.01
MDC 11	132.15	7.2690	A1	0.821	22.99	23.54	0.00
MDC-11	132.1	7.2710	A2	0.866	24.32	24.90	0.03
MDC-11	132.1	7.2710	A1	0.865	24.29	24.88	0.03
MDC 11	132.05	7.2758	A1	0.912	25.68	26.31	0.01

Appendix A Monte dei Corvi Alkenone Indices

Site	Depth (m)	Age(Ma)	Analysis	UK'37	SST (°C) PW	SST (°C) M	[C37] total (nmol/g)
MDC 11	132	7.2806	B1	0.939	26.48	27.14	0.01
MDC 11	132	7.2806	B2	0.935	26.34	26.99	0.01
MDC	132	7.2806	A1	0.796	22.26	22.79	0.01
MDC	131.5	7.3141	A1	0.861	24.18	24.76	0.01
MDC	131.45	7.3175	A1	0.896	25.21	25.82	0.01
MDC	131.4	7.3253	A2	0.848	23.81	24.38	0.00
MDC	131.35	7.3280	A1	0.931	26.23	26.87	0.02
MDC	131.3	7.3350	A1	0.943	26.60	27.26	0.01
MDC	131.25	7.3380	A1	0.843	23.66	24.22	0.01
MDC	131.2	7.3400	A2	0.935	26.35	26.99	0.00
MDC	131.15	7.3420	A1	0.856	24.02	24.60	0.01
MDC	131.1	7.3440	A1	0.909	25.57	26.20	0.02
MDC	131.05	7.3460	A1	0.874	24.55	25.15	0.01
MDC	131	7.3490	A3	0.898	25.26	25.88	0.03
MDC	130.95	7.3520	A1	0.887	24.95	25.56	0.01
MDC	130.85	7.3560	A1	0.899	25.30	25.92	0.01
MDC	130.8	7.3657	A1	0.908	25.55	26.18	0.02
MDC	130.75	7.3689	A1	0.913	25.70	26.33	0.02
MDC	130.7	7.3720	A1	0.879	24.72	25.32	0.01
MDC	130.65	7.3761	A1	0.888	24.98	25.59	0.01
MDC	130.65	7.3761	A2	0.887	24.94	25.55	0.01
MDC	130.6	7.3802	A1	0.855	23.99	24.56	0.01
MDC	130.45	7.3925	A1	0.848	23.79	24.36	0.01
MDC	130.4	7.3936	A1	0.887	24.94	25.55	0.01
MDC	130.35	7.3956	A1	0.879	24.72	25.32	0.01
MDC	130.3	7.3986	A2	0.915	25.77	26.40	0.01
MDC	130.3	7.4000	A1	0.908	25.57	26.19	0.01
MDC	130.25	7.4010	A1	0.923	26.01	26.65	0.01
MDC	130.2	7.4040	A1	0.934	26.32	26.97	0.01
MDC	130.15	7.4050	A1	0.932	26.27	26.91	0.00
MDC	130.1	7.4065	A2	0.950	26.80	27.46	0.01
MDC	130.1	7.4080	A1	0.960	27.09	27.75	0.00
MDC	130.05	7.4130	A1	0.911	25.64	26.26	0.01
MDC	129.95	7.4180	A1	0.909	25.58	26.20	0.01
MDC	129.9	7.4265	A1	0.937	26.40	27.05	0.01
MDC	129.85	7.4290	A1	0.922	25.99	26.62	0.01
MDC	129.8	7.4327	A1	0.934	26.32	26.97	0.01
MDC	129.75	7.4368	A1	0.895	25.17	25.78	0.01
MDC	129.7	7.4398	A1	0.900	25.32	25.93	0.01
MDC	129.65	7.4479	A1	0.920	25.91	26.54	0.01
MDC	129.6	7.4520	A1	0.909	25.59	26.21	0.01
MDC	129.55	7.4661	A1	0.919	25.87	26.50	0.01
MDC	129.5	7.4690	A1	0.896	25.19	25.80	0.01
MDC	129.4	7.4749	A1	0.960	27.09	27.75	0.04
MDC	129.35	7.4833	A1	0.941	26.52	27.17	0.02
MDC	129.3	7.4876	A1	0.926	26.08	26.72	0.01
MDC	129.25	7.4920	A1	0.909	25.58	26.21	0.01
MDC	129.2	7.4984	A1	0.937	26.41	27.06	0.01
MDC	129.2	7.4984	A2	0.931	26.24	26.88	0.01
MDC	129.1	7.5053	A1	0.924	26.04	26.68	0.01

Appendix A Monte dei Corvi Alkenone Indices

Site	Depth (m)	Age(Ma)	Analysis	UK'37	SST (°C) PW	SST (°C) M	[C37] total (nmol/g)
MDC	129	7.5141	B1	0.928	26.15	26.79	0.01
MDC	128.95	7.5185	A1	0.957	27.00	27.66	0.17
MDC	128.9	7.5230	A1	0.962	27.15	27.82	0.14
MDC	128.85	7.5274	A1	0.918	25.87	26.50	0.01
MDC	128.8	7.5318	A1	0.953	26.90	27.56	0.01
MDC	128.75	7.5363	A1	0.926	26.08	26.72	0.00
MDC	128.6	7.5446	A1	0.920	25.91	26.54	0.00
MDC	128.55	7.5490	A1	0.881	24.77	25.37	0.00
MDC	128.45	7.5520	A1	0.748	20.87	21.35	0.00
MDC	128.4	7.5676	A1	0.939	26.48	27.14	0.00
MDC	128.4	7.5676	A2	0.887	24.93	25.53	0.00
MDC	128.35	7.5732	A1	0.871	24.46	25.05	0.01
MDC	128.3	7.5767	A1	0.937	26.40	27.05	0.02
MDC	128.25	7.5813	A1	0.928	26.14	26.78	0.01
MDC	128.2	7.5855	A1	0.930	26.22	26.86	0.02
MDC	128.15	7.5891	A1	0.936	26.39	27.03	0.03
MDC	128.1	7.5928	A1	0.942	26.57	27.22	0.01
MDC	128.1	7.5928	A2	0.926	26.08	26.72	0.01
MDC	128.05	7.5931	A1	0.947	26.72	27.38	0.01
MDC	128	7.5942	A1	0.946	26.68	27.34	0.06
MDC	127.95	7.5953	A1	0.914	25.73	26.36	0.01
MDC	127.9	7.5964	A1	0.929	26.19	26.83	0.03
MDC	127.85	7.5976	A1	0.932	26.27	26.91	0.01
MDC	127.8	7.5987	A1	0.974	27.50	28.18	0.01
MDC	127.75	7.5998	A1	0.954	26.91	27.57	0.02
MDC	127.7	7.6000	A1	0.954	26.91	27.57	0.02
MDC	127.7	7.6000	A2	0.942	26.57	27.23	0.02
MDC	127.65	7.6100	A1	0.946	26.67	27.32	0.03
MDC	127.6	7.6200	A1	0.959	27.05	27.72	0.02
MDC	127.55	7.6300	A1	0.969	27.36	28.04	0.02
MDC	127.5	7.6400	A1	0.946	26.67	27.32	0.03
MDC	127.45	7.6500	A1	0.955	26.94	27.60	0.01
MDC	127.4	7.6600	A1	0.969	27.35	28.02	0.03
MDC	127.35	7.6650	A1	0.956	26.96	27.63	0.01
MDC	127.35	7.6750	A2	0.920	25.90	26.53	0.01
MDC	127.3	7.6850	A1	0.952	26.86	27.52	0.01
MDC	127.25	7.6950	A1	0.827	23.17	23.72	0.01
MDC	127.2	7.7048	A1	0.870	24.43	25.02	0.01
MDC	127.15	7.7050	A1	0.925	26.05	26.69	0.01
MDC	127.1	7.7090	A1	0.882	24.79	25.39	0.01
MDC	127.05	7.7100	A1	0.941	26.54	27.20	0.01
MDC	127.05	7.7180	A2	0.927	26.12	26.76	0.01
MDC	127	7.7220	A1	0.951	26.82	27.48	0.04
MDC	126.95	7.7260	A1	0.921	25.95	26.58	0.01
MDC	126.9	7.7260	A1	0.861	24.17	24.75	0.02
MDC	126.85	7.7265	A1	0.945	26.65	27.30	0.02
MDC	126.8	7.7270	A1	0.928	26.16	26.80	0.01
MDC	126.7	7.7275	A1	0.944	26.61	27.27	0.01
MDC	126.7	7.7280	A2	0.978	27.63	28.31	0.01
MDC	126.65	7.7285	A1	0.941	26.54	27.19	0.01

Appendix A Monte dei Corvi Alkenone Indices

Site	Depth (m)	Age(Ma)	Analysis	UK'37	SST (°C) PW	SST (°C) M	[C37] total (nmol/g)
MDC	126.6	7.7290	A1	0.936	26.38	27.03	0.01
MDC	126.55	7.7295	A1	0.944	26.60	27.26	0.01
MDC	126.5	7.7300	A3	0.954	26.91	27.57	0.01
MDC	126.4	7.7305	A1	0.942	26.57	27.22	0.01
MDC	126.35	7.7310	A1	0.950	26.80	27.46	0.01
MDC	126.3	7.7353	A1	0.979	27.64	28.33	0.01
MDC	126.3	7.7353	A2	0.947	26.70	27.36	0.01
MDC	126.25	7.7392	A1	0.984	27.79	28.48	0.01
MDC	126.2	7.7431	A1	0.979	27.64	28.32	0.01
MDC	126.15	7.7470	A1	0.967	27.29	27.97	0.01
MDC	126.1	7.7509	A1	0.967	27.30	27.98	0.02
MDC	126.05	7.7548	A1	0.920	25.92	26.55	0.02
MDC	126.05	7.7548	A2	0.976	27.56	28.24	0.02
MDC	126	7.7587	A1	0.955	26.95	27.61	0.05
MDC	125	7.8408	A1	0.940	26.49	27.14	0.10
MDC	124	7.9305	A1	0.946	26.68	27.34	0.06
MDC	123	8.0093	A1	0.956	26.98	27.64	0.10
MDC	122	8.0865	A1	0.949	26.76	27.42	0.07
MDC	121	8.1632	A1	0.969	27.34	28.02	0.11
MDC	120.95	8.1670	A1	0.972	27.44	28.12	0.04
MDC	120.75	8.1823	B1	0.915	25.76	26.39	0.06
MDC	120.65	8.1899	B1	0.939	26.47	27.12	0.03
MDC	120.55	8.1975	B1	0.975	27.54	28.22	0.03
MDC	120.5	8.2013	A1	0.966	27.26	27.94	0.07
MDC	120.35	8.2128	B1	0.974	27.51	28.19	0.04
MDC	120.25	8.2204	B1	0.970	27.38	28.06	0.06
MDC	120.2	8.2242	A1	0.963	27.18	27.85	0.05
MDC	120.1	8.2318	A2	0.959	27.05	27.72	0.07
MDC	120.05	8.2356	B1	0.966	27.27	27.94	0.02
MDC	120	8.2394	A1	0.964	27.22	27.89	0.07
MDC	119.95	8.2432	B1	0.967	27.29	27.97	0.03
MDC	119.9	8.2470	A1	0.970	27.40	28.07	0.07
MDC	119.9	8.2470	B1	0.967	27.29	27.97	0.03
MDC	119.85	8.2509	B1	0.969	27.36	28.04	0.03
MDC	119.8	8.2547	A1	0.967	27.29	27.97	0.06
MDC	119.7	8.2618	A1	0.969	27.36	28.04	0.06
MDC	119.65	8.2647	B1	0.968	27.31	27.99	0.02
MDC	119.6	8.2676	A2	0.969	27.36	28.04	0.10
MDC	119.5	8.2734	A1	0.981	27.70	28.39	0.10
MDC	119.4	8.2793	A1	0.966	27.25	27.93	0.08
MDC	119.3	8.2851	A1	0.969	27.35	28.03	0.10
MDC	119.25	8.2880	A1	0.969	27.34	28.02	0.06
MDC	119.2	8.2909	A1	0.971	27.42	28.10	0.19
MDC	119	8.3048	A1	0.970	27.38	28.06	0.08
MDC	118.95	8.3086	B1	0.969	27.34	28.02	0.02
MDC	118.85	8.3161	B1	0.961	27.10	27.77	0.02
MDC	118.8	8.3199	A1	0.974	27.51	28.19	0.02
MDC	118.75	8.3237	B1	0.977	27.60	28.28	0.03
MDC	118.7	8.3274	A2	0.969	27.35	28.03	0.04
MDC	118.65	8.3312	B1	0.975	27.52	28.21	0.03

Appendix A Monte dei Corvi Alkenone Indices

Site	Depth (m)	Age(Ma)	Analysis	UK'37	SST (°C) PW	SST (°C) M	[C37] total (nmol/g)
MDC	118.6	8.3350	A2	0.977	27.59	28.27	0.03
MDC	118.55	8.3387	B1	0.985	27.82	28.52	0.40
MDC	118.5	8.3425	A1	0.984	27.79	28.48	0.29
MDC	118.45	8.3463	B1	0.973	27.47	28.15	0.02
MDC	118.4	8.3500	A2	0.953	26.88	27.54	0.02
MDC	118.35	8.3538	B1	0.946	26.67	27.33	0.02
MDC	118.3	8.3576	A1	0.979	27.65	28.34	0.16
MDC	118.25	8.3614	B1	0.985	27.82	28.51	0.11
MDC	118.2	8.3651	A1	0.977	27.58	28.26	0.18
MDC	118.15	8.3689	B1	0.982	27.73	28.42	0.04
MDC	118.1	8.3727	A1	0.972	27.45	28.13	0.08
MDC	118.05	8.3764	B1	0.982	27.73	28.42	0.55
MDC	118	8.3802	A2	0.972	27.45	28.13	0.54
MDC	117.95	8.3840	A1	0.962	27.14	27.81	0.02
MDC	117.9	8.3877	A1	0.977	27.58	28.27	0.15
MDC	117.8	8.3953	A2	0.959	27.07	27.74	0.03
MDC	117.8	8.3953	B1	0.964	27.20	27.87	0.05
MDC	117.75	8.3991	B1	0.979	27.66	28.35	0.02
MDC	117.7	8.4028	A2	0.985	27.81	28.51	0.10
MDC	117.65	8.4066	A1	0.961	27.11	27.78	0.06
MDC	117.6	8.4104	A1	0.955	26.95	27.62	0.01
MDC	117.5	8.4179	A1	0.974	27.49	28.17	0.08
MDC	117.45	8.4217	B1	0.983	27.77	28.46	0.03
MDC	117.4	8.4255	A1	0.970	27.37	28.05	0.05
MDC	117.35	8.4292	B1	0.962	27.14	27.81	0.05
MDC	117.3	8.4330	A2	0.966	27.26	27.93	0.09
MDC	117.3	8.4330	A1	0.969	27.36	28.04	0.16
MDC	117.25	8.4368	B2	0.987	27.87	28.57	0.41
MDC	117.25	8.4368	B1	0.986	27.84	28.53	0.42
MDC	117.2	8.4405	A1	0.973	27.47	28.15	0.58
MDC	117.15	8.4443	B1	0.966	27.26	27.94	0.02
MDC	117.1	8.4481	A3	0.868	24.38	24.97	0.02
MDC	117.05	8.4518	B1	0.942	26.54	27.20	0.00
MDC	117	8.4556	A1	0.974	27.49	28.17	0.13
MDC	116	8.5310	A1	0.979	27.65	28.34	0.10
MDC	115	8.6064	A1	0.976	27.56	28.24	0.43
MDC	114	8.6815	A1	0.978	27.61	28.29	0.75
MDC	113	8.7368	A2	0.983	27.77	28.46	0.95
MDC	112	8.7858	A3	0.983	27.76	28.45	1.53
MDC-A	111	8.8407	A1	0.989	27.95	28.65	0.10
MDC -A	110	8.8955	A1	0.970	27.40	28.07	1.56
MDC	109	8.9503	A1	0.962	27.14	27.81	1.05
MDC	108.45	8.9805	A1	0.985	27.82	28.51	0.03
MDC	108.4	8.9832	A1	0.975	27.52	28.20	0.15
MDC	108.35	8.9860	A1	0.989	27.94	28.63	0.05
MDC	108.3	8.9887	A1	0.981	27.69	28.38	0.91
MDC	108.2	8.9942	A1	0.934	26.31	26.96	0.28
MDC	108.2	8.9942	A2	0.916	25.80	26.43	0.51
MDC	108.15	8.9970	A1	0.961	27.11	27.78	0.26
MDC	108.1	8.9997	A1	0.964	27.21	27.88	0.83

Appendix A Monte dei Corvi Alkenone Indices

Site	Depth (m)	Age(Ma)	Analysis	UK'37	SST (°C) PW	SST (°C) M	[C37] total (nmol/g)
MDC	108.05	9.0024	A1	0.960	27.09	27.76	0.38
MDC-A	108	9.0052	A1	0.978	27.63	28.31	1.13
MDC	107.95	9.0079	A1	0.963	27.18	27.85	0.02
MDC	107.9	9.0107	A2	0.939	26.47	27.12	0.06
MDC	107.85	9.0134	A1	0.967	27.28	27.96	0.03
MDC	107.8	9.0162	A1	0.880	24.73	25.33	0.10
MDC	107.75	9.0189	A1	0.919	25.89	26.53	0.32
MDC	107.65	9.0244	A1	0.972	27.44	28.12	0.49
MDC	107.6	9.0271	A1	0.964	27.21	27.89	1.73
MDC	107.55	9.0299	A1	0.969	27.36	28.04	0.10
MDC	107.5	9.0326	A1	0.962	27.13	27.80	0.09
MDC	107.45	9.0353	A1	0.974	27.50	28.19	0.04
MDC	107.4	9.0381	A2	0.980	27.67	28.35	0.00
MDC	107.35	9.0408	A1	0.982	27.73	28.42	0.49
MDC	107.3	9.0436	A3	0.966	27.26	27.94	0.29
MDC	107.25	9.0463	A1	0.978	27.61	28.30	0.48
MDC	107.2	9.0491	A2	0.963	27.16	27.84	0.99
MDC	107.15	9.0518	A1	0.972	27.46	28.14	0.04
MDC	107.1	9.0545	A1	0.899	25.29	25.91	0.12
MDC	107.05	9.0573	A1	0.969	27.35	28.02	0.06
MDC- A	107	9.0600	A1	0.987	27.88	28.57	0.25
MDC	106.95	9.0628	B1	0.987	27.90	28.59	0.15
MDC	106.9	9.0655	B1	0.984	27.80	28.49	0.31
MDC	106.9	9.0655	A2	0.979	27.66	28.34	1.23
MDC	106.85	9.0683	B1	0.977	27.57	28.26	0.45
MDC	106.8	9.0710	A2	0.963	27.17	27.84	0.52
MDC	106.75	9.0737	B1	0.990	27.96	28.65	0.65
MDC	106.7	9.0765	B2	0.983	27.77	28.46	0.18
MDC	106.7	9.0765	B1	0.991	28.01	28.71	0.28
MDC	106.7	9.0765	A2	0.972	27.44	28.12	0.42
MDC	106.6	9.0820	A1	0.988	27.90	28.60	0.11
MDC	106.5	9.0875	A2	0.986	27.85	28.54	0.11
MDC	106.45	9.0902	B2	0.984	27.80	28.49	0.03
MDC	106.4	9.0929	A2	0.980	27.68	28.37	0.34
MDC	106.35	9.0957	B1	0.980	27.68	28.37	0.36
MDC	106.3	9.0984	A2	0.971	27.40	28.08	0.80
MDC	106.25	9.1012	B1	0.985	27.82	28.51	0.70
MDC	106.2	9.1039	A1	0.973	27.47	28.15	0.63
MDC	106.15	9.1065	B1	0.989	27.93	28.62	0.04
MDC	106.1	9.1090	A2	0.973	27.47	28.15	0.56
MDC	106.05	9.1115	B1	0.984	27.80	28.49	0.11
MDC	106	9.1140	A1	0.954	26.92	27.59	0.22
MDC	105.95	9.1165	B1	0.978	27.63	28.32	0.12
MDC	105.9	9.1190	A1	0.974	27.51	28.19	0.11
MDC	105.85	9.1215	B1	0.966	27.28	27.95	0.67
MDC	105.8	9.1240	A1	0.967	27.29	27.97	0.89
MDC	105.75	9.1264	B1	0.976	27.55	28.23	0.73
MDC	105.7	9.1289	A1	0.977	27.58	28.27	0.78
MDC	105.65	9.1314	B1	0.986	27.86	28.55	0.14
MDC	105.6	9.1339	A1	0.974	27.50	28.19	0.10

Appendix A Monte dei Corvi Alkenone Indices

Site	Depth (m)	Age(Ma)	Analysis	UK'37	SST (°C) PW	SST (°C) M	[C37] total (nmol/g)
MDC	105.55	9.1364	B1	0.983	27.77	28.46	0.04
MDC	105.5	9.1389	A1	0.983	27.78	28.47	0.10
MDC	105.4	9.1439	A1	0.977	27.59	28.27	0.98
MDC	105.35	9.1464	B1	0.987	27.89	28.58	0.03
MDC	105.3	9.1489	A1	0.965	27.24	27.92	0.49
MDC	105.25	9.1514	B2	0.976	27.57	28.25	0.79
MDC	105.25	9.1514	B1	0.987	27.89	28.58	0.84
MDC	105.2	9.1539	A1	0.975	27.53	28.21	1.45
MDC	105.15	9.1564	B1	0.969	27.36	28.04	0.87
MDC	105.05	9.1614	B1	0.982	27.73	28.42	0.03
MDC	105	9.1639	A1	0.981	27.71	28.39	0.18
MDC	104.95	9.1664	B1	0.989	27.93	28.62	0.12
MDC	104.9	9.1688	A1	0.970	27.37	28.05	0.32
MDC	104.85	9.1713	B1	0.978	27.63	28.32	0.46
MDC	104.75	9.1763	B1	0.985	27.83	28.52	0.64
MDC	104.65	9.1813	B2	0.985	27.81	28.51	0.09
MDC	104.65	9.1813	B1	0.982	27.74	28.43	0.09
MDC	104.6	9.1838	A1	0.979	27.64	28.33	0.25
MDC	104.5	9.1888	A3	0.980	27.67	28.35	0.19
MDC	104.45	9.1913	B1	0.988	27.90	28.60	0.03
MDC	104.4	9.1938	A2	0.973	27.46	28.14	0.37
MDC	104.35	9.1963	B1	0.979	27.65	28.33	0.67
MDC	104.35	9.1963	B2	0.976	27.57	28.25	0.00
MDC	104.3	9.1988	A2	0.972	27.45	28.13	0.94
MDC	104.25	9.2013	B1	0.986	27.86	28.55	0.74
MDC	104.2	9.2038	A1	0.967	27.30	27.97	1.09
MDC	104.15	9.2063	B1	0.984	27.79	28.48	0.67
MDC	104.1	9.2087	A1	0.972	27.44	28.12	0.15
MDC	104.05	9.2112	B1	0.981	27.70	28.39	0.08
MDC	104	9.2137	A2	0.982	27.74	28.43	0.21
MDC	103.95	9.2162	B1	0.986	27.85	28.54	0.08
MDC	103.9	9.2187	A2	0.978	27.62	28.31	0.46
MDC	103.85	9.2212	B1	0.974	27.49	28.17	0.39
MDC	103.8	9.2237	B1	0.968	27.33	28.01	0.78
MDC	103.75	9.2262	B1	0.973	27.47	28.15	0.67
MDC	103.7	9.2287	B1	0.975	27.54	28.22	0.53
MDC	103.65	9.2312	B1	0.978	27.61	28.30	0.67
MDC	103.6	9.2337	A2	0.966	27.27	27.95	0.63
MDC	103.55	9.2362	B2	0.982	27.73	28.42	0.21
MDC	103.55	9.2362	B1	0.983	27.78	28.47	0.38
MDC	103.5	9.2387	A1	0.972	27.45	28.13	0.14
MDC	103	9.2636	A1	0.978	27.62	28.30	0.18
MDC	101.5	9.3396	A1	0.966	27.27	27.95	0.11
MDC	101	9.3656	A2	0.980	27.66	28.35	1.78
MDC	100.5	9.3917	A1	0.975	27.52	28.20	0.17
MDC	100	9.4177	A1	0.977	27.59	28.27	1.00
MDC	99.5	9.4424	A1	0.973	27.47	28.15	0.08
MDC	99	9.4666	A1	0.921	25.94	26.57	0.42
MDC	98.5	9.4908	A3	0.979	27.64	28.33	0.83
MDC	98	9.5150	A1	0.981	27.71	28.40	0.35

Appendix A Monte dei Corvi Alkenone Indices

Site	Depth (m)	Age(Ma)	Analysis	UK'37	SST (°C) PW	SST (°C) M	[C37] total (nmol/g)
MDC	97.5	9.5392	A1	0.980	27.67	28.36	0.20
MDC	97	9.5633	A1	0.956	26.96	27.63	0.28
MDC	96.5	9.5875	A1	0.979	27.66	28.35	0.23
MDC	96	9.6117	A1	0.984	27.79	28.49	0.57
MDC	95.5	9.6359	A2	0.976	27.57	28.26	0.22
MDC	95.5	9.6359	A1	0.976	27.57	28.25	0.22
MDC	95	9.6645	A1	0.981	27.70	28.39	0.26
MDC	94.5	9.6970	A1	0.980	27.67	28.36	0.15
MDC	94	9.7292	A1	0.990	27.97	28.67	0.31
MDC	93.5	9.7608	A1	0.973	27.47	28.16	0.14
MDC	93	9.7953	A1	0.985	27.82	28.52	0.22
MDC	92.5	9.8417	A1	0.957	27.00	27.67	0.11
MDC	92	9.8882	A1	0.975	27.54	28.23	0.21
MDC	91.5	9.9265	A1	0.980	27.68	28.36	0.45
MDC	91	9.9624	A1	0.975	27.54	28.22	0.31
MDC	90.5	10.0030	A1	0.972	27.45	28.13	0.22
MDC	90	10.0460	A1	1.000	28.26	28.97	0.18
MDC	89.06	10.1170	A1	0.981	27.72	28.41	0.66
MDC	87.93	10.2000	A1	0.977	27.59	28.27	0.28
MDC	86.93	10.2740	A1	0.970	27.37	28.05	0.16
MDC	86.11	10.3340	A1	0.979	27.66	28.34	0.50
MDC	85.01	10.4150	A1	0.984	27.78	28.47	1.02
MDC	83.91	10.4950	A2	0.973	27.47	28.15	0.21
MDC	83.06	10.5490	A1	0.984	27.81	28.50	0.57
MDC	82.06	10.6120	A1	0.982	27.74	28.43	0.52
MDC	80.05	10.7370	A1	1.000	28.26	28.97	0.08
MDC	78.86	10.8120	A1	0.978	27.61	28.30	0.13
MDC	77.91	10.8690	A1	0.983	27.77	28.46	0.20
MDC	76.99	10.9240	A1	0.980	27.69	28.37	0.22
MDC	76.03	10.9810	A1	0.981	27.72	28.40	0.50
MDC	75.44	11.0240	A1	0.983	27.77	28.46	0.27
MDC	74.44	11.0950	A1	0.978	27.63	28.32	0.20
MDC	73.42	11.1620	A1	0.958	27.02	27.69	0.05
MDC	72.76	11.2060	A1	0.970	27.38	28.06	0.06
MDC	71.66	11.2710	A1.5	0.973	27.48	28.16	0.08
MDC	70.33	11.3390	A1	0.968	27.33	28.00	0.06
MDC	69.44	11.3800	A1	0.946	26.67	27.33	0.03
MDC	68.43	11.4260	A1	0.982	27.73	28.42	0.25
MDC	67	11.4920	A1	0.976	27.57	28.25	0.23
MDC	66	11.5370	A1	0.951	26.81	27.47	0.06
MDC	65	11.5790	A1	0.984	27.79	28.48	0.33
MDC	64	11.6160	A1	0.975	27.54	28.22	0.06
MDC	63.95	11.6180	A1	0.979	27.66	28.34	0.09
MDC	63.5	11.6380	A1	0.974	27.50	28.18	0.08
MDC	63	11.6600	A1	0.980	27.69	28.37	0.16
MDC	62.5	11.6840	A1	0.986	27.85	28.55	0.25
MDC	62	11.7090	A1	0.984	27.78	28.47	0.10
MDC	61.5	11.7320	A1	0.985	27.81	28.51	0.33
MDC	61	11.7560	A1	1.000	28.26	28.97	0.05
MDC	60.5	11.7800	A1	0.978	27.62	28.31	0.09

Appendix A Monte dei Corvi Alkenone Indices

Site	Depth (m)	Age(Ma)	Analysis	UK'37	SST (°C) PW	SST (°C) M	[C37] total (nmol/g)
MDC	60	11.8020	A1	0.984	27.78	28.47	0.13
MDC	59.5	11.8200	A1	0.983	27.77	28.46	0.28
MDC	59	11.8380	A1	0.984	27.80	28.49	0.15
MDC	58.5	11.8550	A1	0.971	27.41	28.09	0.13
MDC	58	11.8730	A1	1.000	28.26	28.97	0.09
MDC	57	11.9090	A1	0.975	27.52	28.20	0.45
MDC	56	11.9450	A1	1.000	28.26	28.97	0.07
MDC	55	11.9750	A1	0.981	27.71	28.40	0.47
MDC	54	12.0040	A1	0.980	27.68	28.37	0.56
MDC	53	12.0330	A1	1.000	28.26	28.97	0.46
MDC	52	12.0680	A1	1.000	28.26	28.97	0.15
MDC	51	12.1030	A2	0.988	27.93	28.62	0.08
MDC	51	12.1030	A1	1.000	28.26	28.97	0.12
MDC	50	12.1390	A1	1.000	28.26	28.97	0.08
MDC	49	12.1750	A1	0.982	27.74	28.43	0.15
MDC	48	12.2110	A1	0.983	27.77	28.46	0.14
MDC	47	12.2470	A1	0.973	27.46	28.14	0.09
MDC	46	12.2830	A1	0.987	27.88	28.57	0.09
MDC	45	12.3190	A1	0.979	27.66	28.34	0.10
MDC	44	12.3550	A1	1.000	28.26	28.97	0.07
MDC	43	12.3900	A1	0.892	25.10	25.71	0.21
MDC	42	12.4260	A1	0.983	27.75	28.44	0.14
MDC	41	12.4620	A1	0.988	27.90	28.60	0.35
MDC	40	12.4980	A1	0.989	27.94	28.63	0.20
MDC	39	12.5340	A1	0.985	27.84	28.53	0.23
MDC	38	12.5700	A1	0.985	27.83	28.52	0.13
MDC	37	12.5970	A1	0.984	27.81	28.50	0.12
MDC	36	12.6230	B1	0.974	27.49	28.17	0.07
MDC	35	12.6500	B1	0.981	27.70	28.38	0.07
MDC	34	12.6770	B1	0.979	27.65	28.34	0.06
MDC	33	12.7030	A1	0.971	27.42	28.10	0.84
MDC	32	12.7300	A1	0.963	27.17	27.85	0.09
MDC	31	12.7570	A1	0.977	27.58	28.26	0.50
MDC	30	12.7830	A1	0.968	27.31	27.99	0.27
MDC	29	12.8100	A1	0.977	27.58	28.27	1.01
MDC	28	12.8370	A1	0.973	27.46	28.14	0.82
MDC	27	12.8630	B2	0.978	27.62	28.31	0.68
MDC	26	12.8900	B1	0.932	26.27	26.91	0.14
MDC	25	12.9170	B1	0.979	27.64	28.33	0.07

APPENDIX B

ALKENONE INDICES FROM ODP SITES 883, 884, 887, 907, 982, 1088

Appendix B Alkenone Indices from ODP Sites 883, 884, 887, 907, 982, 1088

Core	Section	Interval (cm)	mbsf (m)	Age(Ma)	UK'37	SST (°C) M	[C37] total (nmol/g)
883B	34 - 1	12 - 13	312.32	5.2206	0.252	6.30	0.55
883B	34 - 1	112 - 114	313.33	5.2334	0.275	7.00	6.93
883B	34 - 2	38 - 40	314.09	5.2429	0.296	7.64	7.57
883B	34 - 2	62 - 63	314.27	5.2452	0.309	8.03	7.94
883B	34 - 2	138 - 140	315.09	5.2555	0.288	7.39	7.34
883B	34 - 3	12 - 14	315.33	5.2586	0.310	8.06	7.97
883B	34 - 3	112 - 113	316.27	5.2704	0.306	7.94	7.84
883B	34 - 4	62 - 64	317.33	5.2838	0.379	10.15	9.99
883B	34 - 5	12 - 13	318.27	5.2956	0.267	6.76	6.72
883B	34 - 5	112 - 114	319.33	5.3090	0.313	8.15	8.07
883B	35 - 1	117 - 119	323.08	5.3562	0.298	7.70	7.63
883B	35 - 2	52 - 53	323.92	5.3668	0.307	7.97	7.88
883B	35 - 3	10 - 12	325.01	5.3805	0.333	8.76	8.65
883B	35 - 3	102 - 103	325.92	5.3920	0.276	7.03	6.97
883B	35 - 4	52 - 54	326.93	5.4047	0.291	7.48	7.42
883B	35 - 5	7 - 8	327.97	5.4178	0.352	9.33	9.21
883B	35 - 5	117 - 119	329.08	5.4318	0.299	7.73	7.65
883B	36 - 1	7 - 8	331.57	5.4632	0.291	7.48	7.41
883B	36 - 1	117 - 119	332.68	5.4772	0.308	8.00	7.91
883B	37 - 1	7 - 8	341.27	5.5854	0.271	6.88	6.83
883B	37 - 1	117 - 119	342.38	5.5994	0.282	7.21	7.15
883B	37 - 2	62 - 63	343.32	5.6112	0.227	5.55	5.54
883B	37 - 2	62 - 64	343.33	5.6114	0.227	5.55	5.54
883B	37 - 3	117 - 118	345.37	5.6371	0.301	7.79	7.72
883B	37 - 3	117 - 118	345.38	5.6371	0.291	7.48	7.42
883B	38 - 1	7 - 8	350.97	5.7076	0.317	8.27	8.18
883B	38 - 1	117 - 119	352.08	5.7216	0.326	8.55	8.45
883B	38 - 2	52 - 58	352.90	5.7319	0.358	9.52	9.39
883B	38 - 3	7 - 9	353.98	5.7455	0.286	7.33	7.28
883B	38 - 3	112 - 113	354.90	5.7571	0.330	8.67	8.56
883B	38 - 4	62 - 64	356.03	5.7714	0.330	8.67	8.55
883B	38 - 5	17 - 18	356.95	5.7830	0.318	8.30	8.19
883B	38 - 5	117 - 119	358.08	5.7972	0.359	9.55	9.42
883B	38 - 6	72 - 73	359.00	5.8088	0.266	6.73	6.67
883B	39 - 1	7 - 8	360.57	5.8286	0.344	9.09	8.98
883B	39 - 1	117 - 119	361.68	5.8426	0.345	9.12	9.00
883B	39 - 2	57 - 58	362.51	5.8530	0.278	7.09	7.04
883B	39 - 2	57 - 58	362.58	5.8538	0.276	7.03	6.97
883B	39 - 3	7 - 9	363.58	5.8665	0.306	7.94	7.85
883B	39 - 3	112 - 113	364.49	5.8780	0.311	8.09	7.99
883B	39 - 4	67 - 69	365.68	5.8930	0.323	8.45	8.36
883B	39 - 5	17 - 18	366.54	5.9038	0.268	6.79	6.72
883B	39 - 5	117 - 119	367.68	5.9182	0.333	8.76	8.65
883B	39 - 6	72 - 73	368.59	5.9296	0.342	9.03	8.91
883B	39 - 7	7 - 9	369.58	5.9421	0.322	8.42	8.32
883B	40 - 1	7 - 8	370.27	5.9508	0.290	7.45	7.26
883B	40 - 1	117 - 117	371.37	5.9647	0.290	7.45	7.39
883B	40 - 2	57 - 58	372.27	0.0000	0.279	7.12	7.06
883B	40 - 3	7 - 9	373.28	5.9887	0.297	7.67	7.58
883B	40 - 3	112 - 113	374.32	6.0018	0.348	9.21	9.08

Appendix B Alkenone Indices from ODP Sites 883, 884, 887, 907, 982, 1088

Core	Section	Interval (cm)	mbsf (m)	Age(Ma)	UK'37	SST (°C) M	[C37] total (nmol/g)
883B	40 - 4	67 - 69	375.38	6.0152	0.321	8.39	8.30
883B	40 - 5	17 - 18	376.37	6.0277	0.364	9.70	9.55
883B	40 - 5	117 - 119	377.38	6.0404	0.243	6.03	6.01
883B	40 - 6	72 - 73	378.42	6.0535	0.354	9.39	9.25
883B	40 - 7	67 - 69	379.88	6.0719	0.290	7.45	7.37
883B	41 - 1	7 - 8	380.07	6.0743	0.302	7.82	7.73
883B	41 - 1	117 - 119	381.18	6.0883	0.336	8.85	8.73
883B	41 - 2	57 - 58	382.00	6.0986	0.307	7.97	7.89
883B	41 - 3	7 - 9	383.08	6.1122	0.327	8.58	8.47
883B	41 - 3	112 - 113	384.05	6.1244	0.283	7.24	7.17
883B	41 - 4	67 - 69	385.18	6.1387	0.306	7.94	7.85
883B	41 - 5	17 - 18	386.10	6.1503	0.273	6.94	6.88
883B	41 - 5	127 - 129	387.28	6.1651	0.303	7.85	7.77
883B	41 - 6	72 - 73	388.15	6.1761	0.333	8.76	8.66
883B	42 - 1	17 - 18	389.87	6.1978	0.318	8.30	8.21
883B	42 - 1	127 - 129	390.98	6.2117	0.307	7.97	7.89
883B	42 - 2	57 - 58	391.77	6.2217	0.322	8.42	8.34
883B	42 - 3	7 - 9	392.78	6.2344	0.345	9.12	9.01
883B	42 - 3	112 - 113	393.82	0.0000	0.312	8.12	8.02
883B	42 - 3	117 - 119	393.88	6.2483	0.314	8.18	8.09
883B	42 - 4	67 - 59	394.83	6.2603	0.310	8.06	7.96
883B	42 - 5	17 - 18	395.87	6.2734	0.292	7.52	7.44
883B	42 - 5	127 - 129	396.98	6.2873	0.339	8.94	8.82
883B	42 - 6	72 - 73	397.92	6.2992	0.348	9.21	9.08
883B	42 - 7	17 - 18	398.88	6.3112	0.363	9.67	9.54
883B	43 - 1	117 - 119	400.68	6.3340	0.345	9.12	8.99
883B	43 - 2	57 - 58	401.57	6.3452	0.334	8.79	8.67
883B	43 - 3	7 - 8	402.58	6.3578	0.341	9.00	8.88
883B	43 - 3	112 - 113	403.62	6.3710	0.364	9.70	9.55
883B	43 - 4	67 - 69	404.68	6.3844	0.355	9.42	9.31
883B	43 - 5	7 - 8	405.57	6.3956	0.350	9.27	9.15
883B	43 - 5	117 - 119	406.68	6.4096	0.345	9.12	8.99
883B	43 - 6	72 - 73	407.72	6.4227	0.381	10.21	10.05
883B	43 - 7	55 - 57	409.06	6.4396	0.299	7.73	7.66
883B	44 - 1	7 - 8	409.37	6.4435	0.348	9.21	9.07
883B	44 - 1	117 - 119	410.48	6.4574	0.362	9.64	9.51
883B	44 - 2	57 - 58	411.37	6.4687	0.333	8.76	8.65
883B	44 - 3	7 - 9	412.38	6.4814	0.322	8.42	8.32
883B	44 - 3	112 - 113	413.42	6.4945	0.328	8.61	8.20
883B	44 - 4	67 - 69	414.48	6.5078	0.338	8.91	8.80
883B	44 - 5	17 - 18	415.47	6.5203	0.365	9.73	9.58
883B	44 - 5	117 - 119	416.48	6.5330	0.414	11.21	11.02
883B	44 - 6	72 - 73	417.52	6.5462	0.326	8.55	8.43
883B	45 - 1	7 - 8	419.27	6.5682	0.347	9.18	9.07
883B	45 - 1	117 - 119	420.38	6.5822	0.330	8.67	8.55
883B	45 - 2	57 - 58	421.27	6.5934	0.332	8.73	8.62
883B	45 - 3	7 - 9	422.28	6.6061	0.344	9.09	8.98
883B	45 - 3	112 - 113	423.32	6.6192	0.345	9.12	8.99
883B	45 - 4	67 - 69	424.38	6.6326	0.364	9.70	9.57
883B	45 - 5	17 - 18	425.37	6.6451	0.386	10.36	10.20

Appendix B Alkenone Indices from ODP Sites 883, 884, 887, 907, 982, 1088

Core	Section	Interval (cm)	mbsf (m)	Age(Ma)	UK'37	SST (°C) M	[C37] total (nmol/g)
883B	45 - 5	117 - 119	426.38	6.6578	0.356	9.45	9.33
883B	45 - 6	7 - 9	426.78	6.6628	0.361	9.61	9.46
883B	45 - 6	72 - 73	427.42	6.6709	0.327	8.58	8.46
883B	45 - 6	117 - 119	427.88	6.6767	0.359	9.55	9.42
883B	45 - 7	55 - 57	428.76	6.6878	0.339	8.94	8.82
883B	48 - 1	17 - 18	448.87	6.9412	0.462	12.67	12.45
883B	48 - 1	117 - 119	449.88	6.9539	0.425	11.55	11.37
883B	48 - 2	57 - 58	450.77	6.9651	0.469	12.88	12.66
883B	48 - 3	7 - 9	451.78	6.9778	0.386	10.36	10.21
883B	48 - 3	112 - 113	452.82	6.9909	0.399	10.76	10.59
883B	48 - 4	67 - 69	453.88	7.0043	0.419	11.36	11.17
883B	48 - 5	17 - 18	454.87	7.0168	0.408	11.03	10.85
883B	48 - 5	117 - 119	455.88	7.0295	0.349	9.24	9.11
883B	48 - 6	72 - 73	456.92	7.0426	0.476	13.09	12.86
883B	48 - 7	17 - 19	457.88	7.0547	0.507	14.03	13.76
883B	49 - 1	17 - 18	458.37	7.0609	0.440	12.00	11.61
883B	49 - 1	117 - 118	459.38	7.0735	0.472	12.97	12.74
883B	49 - 2	57 - 58	460.27	7.0848	0.493	13.61	13.35
883B	49 - 3	7 - 9	461.28	7.0975	0.475	13.06	12.81
883B	49 - 3	112 - 113	462.32	7.1106	0.444	12.12	11.91
883B	49 - 4	67 - 69	463.38	7.1240	0.720	20.48	20.02
883B	49 - 5	17 - 18	464.37	7.1365	0.537	14.94	14.65
883B	49 - 5	117 - 118	465.38	7.1491	0.532	14.79	14.51
883B	49 - 6	72 - 73	466.42	7.1623	0.507	14.03	13.78
883B	49 - 6	72 - 73	466.43	7.1624	0.440	12.00	11.80
883B	49 - 7	22 - 24	467.43	7.1750	0.478	13.15	12.92
883B	49 - 7	62 - 63	467.82	7.1799	0.546	15.21	14.91
883B	50 - 1	7 - 8	468.17	7.1843	0.438	11.94	11.75
883B	50 - 1	117 - 119	477.33	7.2998	0.409	11.06	10.87
883B	50 - 2	57 - 58	470.17	7.2095	0.389	10.45	10.29
883B	50 - 3	17 - 19	469.28	7.1983	0.352	9.33	9.22
883B	50 - 3	112 - 113	472.22	7.2354	0.474	13.03	12.80
883B	50 - 4	57 - 59	471.28	7.2235	0.409	11.06	10.89
883B	50 - 5	17 - 18	474.27	7.2612	0.454	12.42	12.21
883B	50 - 5	117 - 119	473.18	7.2475	0.445	12.15	11.95
883B	50 - 7	25 - 27	475.28	7.2739	0.437	11.91	11.71
883B	51 - 1	7 - 8	477.97	7.3078	0.403	10.88	10.71
883B	51 - 1	117 - 119	479.08	7.3218	0.414	11.21	11.04
883B	51 - 2	57 - 58	479.92	7.3324	0.440	12.00	11.80
883B	51 - 3	7 - 9	480.98	7.3457	0.416	11.27	11.10
883B	51 - 3	112 - 113	481.94	7.3578	0.538	14.97	14.68
883B	51 - 4	57 - 59	482.98	7.3709	0.475	13.06	12.83
883B	51 - 5	17 - 18	483.99	7.3837	0.392	10.55	10.39
883B	51 - 5	117 - 119	485.08	7.3974	0.471	12.94	12.70
883B	51 - 6	72 - 73	486.04	7.4095	0.358	9.52	9.39
883B	51 - 7	22 - 24	487.13	7.4232	0.423	11.48	11.30
883B	53 - 1	52 - 53	498.23	7.6673	0.449	12.27	12.06
883B	53 - 1	54 - 55	498.25	7.6688	0.405	10.94	10.76
883B	53 - 2	57 - 58	499.77	7.7872	0.436	11.88	11.67
883B	53 - 3	112 - 113	501.82	7.9462	0.370	9.88	9.73

Appendix B Alkenone Indices from ODP Sites 883, 884, 887, 907, 982, 1088

Core	Section	Interval (cm)	mbsf (m)	Age(Ma)	UK'37	SST (°C) M	[C37] total (nmol/g)
883B	53 - 4	57 - 59	502.78	8.0207	0.475	13.06	12.83
883B	53 - 5	17 - 18	503.87	8.1053	0.509	14.09	13.79
883B	53 - 5	117 - 119	504.88	8.1837	0.552	15.39	15.10
883B	53 - 6	72 - 73	505.92	8.2644	0.449	12.27	12.07
883B	53 - 7	22 - 24	506.93	8.3428	0.476	13.09	12.86
883B	54 - 1	7 - 8	507.67	8.4002	0.448	12.24	12.04
883B	54 - 1	117 - 119	508.78	8.4863	0.568	15.88	15.57
883B	54 - 2	57 - 58	509.67	8.5554	0.472	12.97	12.75
883B	54 - 3	17 - 19	510.78	8.6415	0.469	12.88	12.64
883B	54 - 3	112 - 113	511.72	8.7145	0.474	13.03	12.80
883B	54 - 4	57 - 59	512.68	8.7890	0.409	11.06	11.02
883B	54 - 5	17 - 18	513.77	8.8736	0.467	12.82	12.60
883B	54 - 5	117 - 119	514.78	8.9519	0.447	12.21	11.99
883B	54 - 6	72 - 73	515.82	9.0326	0.480	13.21	12.98
883B	54 - 6	72 - 73	515.83	9.0330	0.491	13.55	13.29
883B	54 - 7	22 - 24	516.83	9.1110	0.385	10.33	10.17
883B	55 - 1	7 - 8	517.47	9.1607	0.349	9.24	9.12
883B	55 - 1	117 - 119	518.58	9.2468	0.387	10.39	10.24
883B	55 - 2	57 - 58	519.47	9.3159	0.379	10.15	10.00
883B	55 - 3	7 - 9	520.48	9.3942	0.491	13.55	13.30
883B	55 - 3	112 - 113	521.52	9.4750	0.409	11.06	10.87
883B	55 - 4	57 - 58	522.48	9.5491	0.447	12.21	12.01
883B	55 - 5	17 - 18	523.57	9.6340	0.337	8.88	8.78
883B	55 - 5	117 - 119	524.58	9.7124	0.404	10.91	10.74
883B	55 - 6	72 - 73	525.62	9.7931	0.474	13.03	12.80
883B	55 - 6	72 - 73	525.63	9.7935	0.517	14.33	14.07
883B	55 - 7	22 - 24	526.63	9.8715	0.385	10.33	10.19
883B	57 - 5	17 - 18	543.27	11.1628	0.474	13.03	12.79
883B	57 - 6	72 - 73	545.32	11.3218	0.512	14.18	13.91
883B	59 - 3	112 - 113	561.12	12.5479	0.595	16.70	16.36

Appendix B Alkenone Indices from ODP Sites 883, 884, 887, 907, 982, 1088

Core	Section	Interval (cm)	mbsf (m)	Age(Ma)	UK'37	SST (°C) M	[C37] total (nmol/g)
884B	38 - 4	110 - 112	339.91	6.2794	0.368	9.82	0.67
884B	38 - 5	50 - 52	340.81	6.3037	0.373	9.97	0.61
884B	38 - 6	5 - 7	341.86	6.3320	0.316	8.24	1.03
884B	38 - 6	145 - 147	343.26	6.3698	0.311	8.09	1.93
884B	39 - 1	5 - 7	343.96	6.3887	0.298	7.70	1.22
884B	39 - 1	105 - 107	344.96	6.4157	0.315	8.21	1.10
884B	39 - 2	55 - 57	345.96	6.4427	0.355	9.42	0.91
884B	39 - 3	5 - 7	346.96	6.4697	0.309	8.03	0.80
884B	39 - 3	105 - 107	347.96	6.4967	0.367	9.79	0.79
884B	39 - 4	55 - 57	348.96	6.5237	0.323	8.45	1.10
884B	39 - 5	5 - 7	349.96	6.5507	0.344	9.09	0.75
884B	39 - 5	55 - 57	350.46	6.5642	0.358	9.52	0.68
884B	39 - 6	5 - 7	351.46	6.5912	0.316	8.24	0.93
884B	39 - 6	105 - 107	352.46	6.6182	0.330	8.67	0.94
884B	39 - 7	5 - 7	352.96	6.6317	0.310	8.06	1.49
884B	40 - 1	105 - 107	354.66	6.6776	0.369	9.85	1.10
884B	40 - 2	55 - 57	355.66	6.7046	0.315	8.21	1.43
884B	40 - 3	5 - 7	356.66	6.7316	0.326	8.55	0.57
884B	40 - 3	105 - 107	357.66	6.7586	0.361	9.61	0.50
884B	40 - 4	55 - 57	358.66	6.7856	0.344	9.09	1.72
884B	40 - 5	5 - 7	359.66	6.8126	0.330	8.67	0.57
884B	40 - 5	105 - 107	360.66	6.8396	0.356	9.45	0.80
884B	40 - 6	5 - 7	361.16	6.8531	0.364	9.70	1.26
884B	40 - 7	50 - 52	363.11	6.9058	0.365	9.73	0.49
884B	41 - 1	5 - 7	363.16	6.9071	0.387	10.39	0.50
884B	41 - 1	105 - 107	364.16	6.9341	0.421	11.42	0.31
884B	41 - 2	55 - 57	365.16	6.9611	0.455	12.45	0.14
884B	41 - 3	5 - 7	366.16	6.9881	0.420	11.39	0.27
884B	41 - 3	105 - 107	367.16	7.0151	0.427	11.61	0.30
884B	41 - 4	55 - 57	368.16	7.0421	0.365	9.73	0.20
884B	41 - 5	5 - 7	369.16	7.0691	0.403	10.88	0.22
884B	41 - 5	105 - 107	370.16	7.0961	0.399	10.76	0.18
884B	41 - 6	55 - 57	371.16	7.1231	0.537	14.94	0.17
884B	41 - 7	45 - 47	372.56	7.1609	0.385	10.33	0.27
884B	42 - 1	5 - 7	372.76	7.1663	0.449	12.27	0.14
884B	42 - 1	105 - 107	373.76	7.1933	0.401	10.82	0.09
884B	42 - 2	55 - 57	374.76	7.2203	0.455	12.45	0.13
884B	42 - 3	5 - 7	375.76	7.2473	0.432	11.76	0.15
884B	42 - 3	105 - 107	376.76	7.2743	0.461	12.64	0.09
884B	42 - 4	55 - 57	377.76	7.3013	0.467	12.82	0.08
884B	42 - 5	5 - 7	378.76	7.3283	0.536	14.91	0.08
884B	42 - 5	105 - 107	379.76	7.3553	0.503	13.91	0.07

Appendix B Alkenone Indices from ODP Sites 883, 884, 887, 907, 982, 1088

Core	Section	Interval (cm)	mbsf (m)	Age(Ma)	UK'37	SST (°C) M	[C37] total (nmol/g)
887C	17 - 5	40 - 42	147.20	5.3323	0.504	13.94	0.03
887C	17 - 6	40 - 42	148.70	5.4049	0.527	14.64	14.35
887C	17 - 7	40 - 42	150.20	5.4775	0.400	10.79	10.61
887C	18 - 1	50 - 52	150.80	5.5065	0.443	12.09	11.89
887C	18 - 2	50 - 52	152.30	5.5791	0.445	12.15	11.95
887C	18 - 3	50 - 52	153.80	5.6517	0.438	11.94	11.74
887C	18 - 4	50 - 52	155.30	5.7243	0.418	11.33	11.15
887C	18 - 6	60 - 62	157.90	5.8502	0.314	8.18	8.09
887C	19 - 1	5 - 7	159.85	5.9445	0.243	6.03	6.01
887C	19 - 1	75 - 77	160.55	5.9784	0.314	8.18	8.09
887C	19 - 2	5 - 7	161.35	6.0171	0.456	12.48	12.27
887C	19 - 2	75 - 77	162.05	6.0510	0.250	6.24	6.21
887C	19 - 3	5 - 7	162.85	6.0897	0.352	9.33	8.91
887C	19 - 3	75 - 77	163.55	6.1236	0.304	7.88	8.10
887C	19 - 4	5 - 7	164.35	6.1623	0.373	9.97	8.85
887C	19 - 4	75 - 77	165.05	6.1962	0.251	6.27	6.24
887C	19 - 5	5 - 7	165.85	6.2349	0.289	7.42	7.36
887C	19 - 5	75 - 77	166.55	6.2688	0.318	8.30	8.21
887C	19 - 6	5 - 7	167.35	6.3075	0.301	7.79	6.89
887C	19 - 6	75 - 77	168.05	6.3414	0.296	7.64	7.57
887C	19 - 7	5 - 7	168.35	6.3559	0.266	6.73	6.67
887C	19 - 7	60 - 62	168.90	6.3826	0.311	8.09	8.01
887C	20 - 1	75 - 77	169.65	6.4189	0.239	5.91	5.87
887C	20 - 2	5 - 7	170.85	6.4769	0.224	5.45	5.44
887C	20 - 2	75 - 77	171.55	6.5108	0.237	5.85	5.84
887C	20 - 3	5 - 7	172.35	6.5495	0.263	6.64	6.58
887C	20 - 4	5 - 7	173.85	6.6221	0.286	7.33	7.26
887C	20 - 5	5 - 7	175.35	6.6947	0.268	6.79	6.74
887C	20 - 5	75 - 77	176.05	6.7286	0.236	5.82	5.80
887C	20 - 6	5 - 7	176.85	6.7673	0.354	9.39	9.26
887C	20 - 6	75 - 77	177.55	6.8012	0.216	5.21	5.20
887C	21 - 1	75 - 77	179.55	6.8980	0.265	6.70	6.65
887C	21 - 2	5 - 7	180.35	6.9367	0.263	6.64	7.33
887C	21 - 2	75 - 77	181.05	6.9706	0.284	7.27	7.21
887C	21 - 3	5 - 7	181.85	7.0093	0.264	6.67	6.61
887C	21 - 3	75 - 77	182.55	7.0432	0.289	7.42	7.34
887C	21 - 4	5 - 7	183.35	7.0819	0.305	7.91	7.84
887C	21 - 4	75 - 77	184.05	7.1158	0.296	7.64	7.56
887C	21 - 5	5 - 7	184.85	7.1545	0.339	8.94	8.82
887C	21 - 5	75 - 77	185.55	7.1884	0.269	6.82	6.75
887C	21 - 6	5 - 7	186.35	7.2271	0.291	7.48	7.42
887C	21 - 6	75 - 77	187.05	7.2610	0.294	7.58	7.49
887C	21 - 7	20 - 22	188.00	7.3070	0.265	6.70	6.64
887C	22 - 2	75 - 77	190.55	7.4304	0.339	8.94	8.82
887C	22 - 3	5 - 7	191.35	7.4691	0.372	9.94	9.78
887C	22 - 3	75 - 77	192.05	7.5030	0.441	12.03	11.82
887C	22 - 4	5 - 7	192.85	7.5417	0.426	11.58	11.38
887C	22 - 5	5 - 7	194.35	7.6143	0.558	15.58	15.26
887C	22 - 6	5 - 7	195.85	7.6869	0.576	16.12	15.79

Appendix B Alkenone Indices from ODP Sites 883, 884, 887, 907, 982, 1088

Core	Section	Interval (cm)	mbsf (m)	Age(Ma)	UK'37	SST (°C) M	[C37] total (nmol/g)
907A	NA	NA	76.10	5.0024	0.369	9.83	
907A	NA	NA	76.15	5.0068	0.378	10.11	
907A	NA	NA	76.18	5.0095	0.381	10.20	
907A	NA	NA	76.25	5.0156	0.400	10.78	
907A	NA	NA	76.30	5.0200	0.320	8.35	
907A	NA	NA	76.35	5.0244	0.397	10.70	
907A	NA	NA	76.40	5.0289	0.413	11.17	
907A	NA	NA	76.45	5.0333	0.326	8.54	
907A	NA	NA	76.50	5.0377	0.376	10.05	
907A	NA	NA	76.55	5.0421	0.402	10.84	
907A	NA	NA	76.60	5.0465	0.364	9.70	
907A	NA	NA	76.65	5.0509	0.414	11.20	
907A	NA	NA	76.70	5.0553	0.405	10.93	
907A	NA	NA	76.75	5.0597	0.420	11.39	
907A	NA	NA	76.80	5.0641	0.376	10.05	
907A	NA	NA	76.85	5.0685	0.725	20.64	
907A	NA	NA	76.90	5.0729	0.427	11.60	
907A	NA	NA	76.95	5.0773	0.436	11.89	
907A	NA	NA	77.00	5.0817	0.444	12.12	
907A	NA	NA	77.05	5.0861	0.454	12.44	
907A	NA	NA	77.10	5.0906	0.382	10.24	
907A	NA	NA	77.14	5.0941	0.390	10.48	
907A	NA	NA	77.15	5.0950	0.343	9.05	
907A	NA	NA	77.16	5.0958	0.391	10.51	
907A	NA	NA	77.19	5.0985	0.480	13.22	
907A	NA	NA	77.25	5.1038	0.222	5.39	
907A	NA	NA	77.30	5.1082	0.397	10.70	
907A	NA	NA	77.35	5.1126	0.413	11.17	
907A	NA	NA	77.36	5.1135	0.423	11.49	
907A	NA	NA	77.40	5.1170	0.357	9.48	
907A	NA	NA	77.45	5.1214	0.336	8.84	
907A	NA	NA	77.50	5.1258	0.326	8.53	
907A	NA	NA	77.55	5.1302	0.352	9.34	
907A	NA	NA	77.60	5.1346	0.392	10.54	
907A	NA	NA	77.65	5.1390	0.363	9.67	
907A	NA	NA	77.70	5.1434	0.401	10.81	
907A	NA	NA	77.73	5.1461	0.436	11.87	
907A	NA	NA	77.75	5.1479	0.362	9.64	
907A	NA	NA	77.80	5.1523	0.326	8.55	
907A	NA	NA	77.85	5.1567	0.314	8.19	
907A	NA	NA	77.90	5.1611	0.309	8.04	
907A	NA	NA	77.95	5.1655	0.378	10.12	
907A	NA	NA	78.00	5.1699	0.313	8.15	
907A	NA	NA	78.05	5.1743	0.331	8.68	
907A	NA	NA	78.10	5.1787	0.439	11.97	
907A	NA	NA	78.15	5.1831	0.290	7.47	
907A	NA	NA	78.18	5.1858	0.382	10.23	
907A	NA	NA	78.25	5.1919	0.361	9.60	
907A	NA	NA	78.30	5.1963	0.371	9.90	
907A	NA	NA	78.35	5.2007	0.456	12.49	

Appendix B Alkenone Indices from ODP Sites 883, 884, 887, 907, 982, 1088

Core	Section	Interval (cm)	mbsf (m)	Age(Ma)	UK'37	SST (°C) M	[C37] total (nmol/g)
907A	NA	NA	78.40	5.2051	0.501	13.85	
907A	NA	NA	78.45	5.2096	0.459	12.58	
907A	NA	NA	78.50	5.2140	0.437	11.90	
907A	NA	NA	78.55	5.2184	0.345	9.11	
907A	NA	NA	78.60	5.2228	0.358	9.52	
907A	NA	NA	78.65	5.2272	0.356	9.47	
907A	NA	NA	78.70	5.2316	0.353	9.37	
907A	NA	NA	78.75	5.2360	0.367	9.80	
907A	NA	NA	78.80	5.2392	0.421	11.44	
907A	NA	NA	78.85	5.2424	0.388	10.43	
907A	NA	NA	78.91	5.2462	0.404	10.90	
907A	NA	NA	78.95	5.2488	0.371	9.92	
907A	NA	NA	79.00	5.2519	0.402	10.84	
907A	NA	NA	79.15	5.2615	0.315	8.23	
907A	NA	NA	79.42	5.2787	0.296	7.62	
907A	NA	NA	79.90	5.3094	0.364	9.69	
907A	NA	NA	79.95	5.3126	0.385	10.33	
907A	NA	NA	79.98	5.3145	0.367	9.79	
907A	NA	NA	80.00	5.3157	0.367	9.79	
907A	NA	NA	80.58	5.3527	0.317	8.26	
907B	NA	NA	80.61	5.2707	0.601	16.89	
907B	NA	NA	80.70	5.2783	0.660	18.67	
907B	NA	NA	81.18	5.3188	0.308	7.99	
907B	NA	NA	81.18	5.3189	0.319	8.32	
907A	NA	NA	81.60	5.4178	0.325	8.52	
907A	NA	NA	81.65	5.4210	0.359	9.56	
907A	NA	NA	81.70	5.4242	0.318	8.31	
907B	NA	NA	81.74	5.3662	0.378	10.12	
907B	NA	NA	82.31	5.4144	0.329	8.63	
907A	NA	NA	84.06	5.5748	0.253	6.34	
907A	NA	NA	84.61	5.6098	0.233	5.74	
907A	NA	NA	84.63	5.6111	0.233	5.74	
907A	NA	NA	85.20	5.6475	0.240	5.93	
907A	NA	NA	85.75	5.6826	0.228	5.58	
907A	NA	NA	86.31	5.7183	0.281	7.18	
907A	NA	NA	86.33	5.7196	0.281	7.18	
907A	NA	NA	86.88	5.7547	0.424	11.51	
907A	NA	NA	86.90	5.7559	0.398	10.73	
907A	NA	NA	86.92	5.7572	0.398	10.73	
907A	NA	NA	87.43	5.7898	0.360	9.58	
907A	NA	NA	88.00	5.8261	0.316	8.23	
907A	NA	NA	88.02	5.8274	0.316	8.23	
907A	NA	NA	88.58	5.8631	0.326	8.55	
907A	NA	NA	88.60	5.8644	0.326	8.55	
907A	NA	NA	89.16	5.9001	0.302	7.82	
907B	NA	NA	89.59	6.0253	0.276	7.03	
907A	NA	NA	89.71	5.9375	0.321	8.38	
907A	NA	NA	89.73	5.9390	0.321	8.38	
907B	NA	NA	90.09	6.0657	0.233	5.72	
907B	NA	NA	90.14	6.0697	0.286	7.32	

Appendix B Alkenone Indices from ODP Sites 883, 884, 887, 907, 982, 1088

Core	Section	Interval (cm)	mbsf (m)	Age(Ma)	UK'37	SST (°C) M	[C37] total (nmol/g)
907A	NA	NA	90.27	5.9812	0.319	8.33	
907A	NA	NA	90.29	5.9827	0.319	8.33	
907B	NA	NA	90.68	6.1134	0.337	8.88	
907A	NA	NA	90.81	6.0233	0.215	5.18	
907A	NA	NA	90.83	6.0249	0.215	5.18	
907B	NA	NA	91.18	6.1538	0.269	6.83	
907B	NA	NA	91.71	6.1967	0.353	9.36	
907C	11H1	42 - 44	92.02	6.1939	0.153	3.32	0.28
907C	11H1	72 - 74	92.32	6.2179	0.196	4.62	0.69
907C	11H1	102 - 104	92.62	6.2418	0.168	3.77	0.82
907C	11H1	132 - 134	92.92	6.2658	0.235	5.80	0.64
907C	11H2	12 - 14	93.22	6.2897	0.324	8.49	0.46
907C	11H2	42 - 44	93.52	6.3136	0.340	8.98	0.39
907C	11H2	72 - 74	93.82	6.3376	0.337	8.87	0.27
907C	11H2	102 - 104	94.12	6.3615	0.314	8.18	1.02
907A	NA	NA	94.23	6.2902	0.302	7.80	
907A	NA	NA	94.25	6.2917	0.302	7.80	
907C	11H2	132 - 134	94.42	6.3855	0.321	8.39	0.50
907C	11H3	12 - 14	94.72	6.4094	0.320	8.38	1.22
907A	NA	NA	94.74	6.3300	0.303	7.84	
907A	NA	NA	94.76	6.3315	0.303	7.84	
907C	11H3	42 - 44	95.02	6.4334	0.270	6.84	1.68
907A	NA	NA	95.26	6.3705	0.302	7.81	
907A	NA	NA	95.28	6.3721	0.302	7.81	
907C	11H3	72 - 74	95.32	6.4573	0.381	10.21	0.72
907C	11H3	102 - 104	95.62	6.4812	0.387	10.39	0.30
907A	NA	NA	95.78	6.4111	0.358	9.51	
907C	11H3	132 - 134	95.92	6.5052	0.390	10.48	0.71
907C	11H4	12 - 14	96.22	6.5291	0.356	9.47	0.18
907A	NA	NA	96.28	6.4501	0.350	9.29	
907A	NA	NA	96.30	6.4517	0.350	9.29	
907C	11H4	42 - 44	96.52	6.5531	0.407	11.01	0.48
907A	NA	NA	96.58	6.4735	0.400	10.78	
907A	NA	NA	96.60	6.4751	0.400	10.78	
907A	NA	NA	96.65	6.4790	0.375	10.02	
907A	NA	NA	96.67	6.4805	0.375	10.02	
907A	NA	NA	96.81	6.4915	0.305	7.91	
907C	11H4	72 - 74	96.82	6.5770	0.411	11.12	1.47
907A	NA	NA	96.83	6.4930	0.305	7.91	
907A	NA	NA	96.91	6.4993	0.407	11.01	
907A	NA	NA	96.93	6.5008	0.407	11.01	
907C	11H4	102 - 104	97.12	6.6009	0.335	8.81	2.32
907A	NA	NA	97.14	6.5172	0.376	10.07	
907A	NA	NA	97.16	6.5188	0.376	10.07	
907A	NA	NA	97.39	6.5367	0.356	9.46	
907A	NA	NA	97.41	6.5383	0.356	9.46	
907C	11H4	132 - 134	97.42	6.6249	0.457	12.52	1.93
907A	NA	NA	97.64	6.5562	0.399	10.76	
907A	NA	NA	97.66	6.5578	0.399	10.76	
907C	11H5	12 - 14	97.72	6.6488	0.390	10.49	0.94

Appendix B Alkenone Indices from ODP Sites 883, 884, 887, 907, 982, 1088

Core	Section	Interval (cm)	mbsf (m)	Age(Ma)	UK'37	SST (°C) M	[C37] total (nmol/g)
907A	NA	NA	97.88	6.5750	0.338	8.91	
907A	NA	NA	97.90	6.5765	0.338	8.91	
907C	11H5	42 - 44	98.02	6.6728	0.455	12.45	0.66
907A	NA	NA	98.13	6.5945	0.322	8.44	
907C	11H5	72 - 74	98.32	6.6967	0.431	11.73	0.18
907A	NA	NA	98.37	6.6132	0.390	10.48	
907A	NA	NA	98.39	6.6147	0.390	10.48	
907C	11H5	102 - 104	98.62	6.7207	0.380	10.18	0.15
907A	NA	NA	98.63	6.6335	0.412	11.14	
907A	NA	NA	98.87	6.6522	0.395	10.63	
907C	11H5	132 - 134	98.92	6.7446	0.402	10.84	0.27
907A	NA	NA	99.12	6.6717	0.380	10.20	
907A	NA	NA	99.14	6.6733	0.380	10.20	
907C	11H6	12 - 14	99.22	6.7685	0.381	10.21	0.11
907A	NA	NA	99.37	6.6912	0.365	9.74	
907A	NA	NA	99.39	6.6928	0.365	9.74	
907C	11H6	42 - 44	99.52	6.7925	0.475	13.05	0.14
907A	NA	NA	99.61	6.7099	0.315	8.21	
907C	11H6	72 - 74	99.82	6.8164	0.463	12.70	0.10
907A	NA	NA	99.86	6.7294	0.464	12.72	
907A	NA	NA	99.88	6.7310	0.464	12.72	
907A	NA	NA	100.10	6.7482	0.382	10.24	
907A	NA	NA	100.12	6.7497	0.382	10.24	0.06
907C	11H6	102 - 104	100.12	6.8404	0.490	13.51	0.06
907A	NA	NA	100.36	6.7685	0.354	9.40	
907B	NA	NA	100.67	6.9212	0.445	12.16	
907C	11H7	12 - 14	100.72	6.8882	0.491	13.53	0.06
907C	11H7	42 - 44	101.02	6.9122	0.444	12.12	0.25
907A	NA	NA	101.10	6.8262	0.267	6.75	
907C	12H1	12 - 14	101.22	6.9281	0.420	11.39	0.11
907A	NA	NA	101.34	6.8449	0.638	18.01	
907C	12H1	42 - 44	101.52	6.9521	0.342	9.04	0.29
907A	NA	NA	101.58	6.8636	0.571	15.97	
907A	NA	NA	101.60	6.8652	0.571	15.97	
907B	NA	NA	101.65	7.0004	0.317	8.28	
907A	NA	NA	101.67	6.8707	0.396	10.67	
907C	12H1	72 - 74	101.82	6.9760	0.457	12.51	0.06
907A	NA	NA	101.83	6.8832	0.401	10.82	
907C	12H1	102 - 104	102.12	7.0000	0.379	10.17	0.09
907B	NA	NA	102.40	7.0611	0.426	11.56	
907C	12H1	132 - 134	102.42	7.0239	0.389	10.46	0.10
907B	NA	NA	102.63	7.0797	0.361	9.61	
907C	12H2	12 - 14	102.72	7.0479	0.416	11.28	0.20
907B	NA	NA	102.89	7.1007	0.373	9.98	
907B	NA	NA	103.13	7.1201	0.526	14.61	
907C	12H2	72 - 74	103.32	7.0957	0.500	13.81	0.52
907B	NA	NA	103.38	7.1403	0.466	12.80	
907C	12H2	102 - 104	103.62	7.1197	0.579	16.22	0.55
907B	NA	NA	103.62	7.1552	0.545	15.19	0.55
907B	NA	NA	103.62	7.1552	0.515	14.26	

Appendix B Alkenone Indices from ODP Sites 883, 884, 887, 907, 982, 1088

Core	Section	Interval (cm)	mbsf (m)	Age(Ma)	UK'37	SST (°C) M	[C37] total (nmol/g)
907B	NA	NA	103.88	7.1665	0.304	7.87	
907B	NA	NA	103.88	7.1665	0.299	7.74	
907B	NA	NA	103.88	7.1666	0.241	5.96	
907C	12H2	132 - 134	103.92	7.1436	0.382	10.23	0.19
907C	12H3	12 - 14	104.22	7.1605	0.335	8.82	0.38
907C	12H3	42 - 44	104.52	7.1749	0.462	12.66	0.23
907C	12H3	72 - 74	104.82	7.1893	0.442	12.08	0.96
907C	12H3	102 - 104	105.12	7.2037	0.491	13.54	0.52
907C	12H3	132 - 134	105.42	7.2180	0.405	10.94	1.02
907A	NA	NA	105.62	7.1680	0.323	8.46	
907C	12H4	12 - 14	105.72	7.2324	0.438	11.93	0.99
907A	NA	NA	105.86	7.1797	0.236	5.82	
907A	NA	NA	105.91	7.1821	0.407	11.01	
907C	12H4	42 - 44	106.02	7.2468	0.408	11.04	0.66
907A	NA	NA	106.11	7.1918	0.282	7.22	
907C	12H4	72 - 74	106.32	7.2612	0.481	13.24	0.30
907C	12H4	102 - 104	106.62	7.2755	0.367	9.79	0.96
907A	NA	NA	106.87	7.2288	0.484	13.35	
907C	12H4	132 - 134	106.92	7.2899	0.479	13.19	0.52
907C	12H5	12 - 14	107.22	7.3043	0.649	18.34	0.26
907C	12H5	42 - 44	107.52	7.3186	0.508	14.05	0.52
907C	12H5	72 - 74	107.82	7.3330	0.610	17.15	0.13
907A	NA	NA	107.88	7.2779	0.256	6.42	
907C	12H5	102 - 104	108.12	7.3474	0.590	16.53	0.44
907A	NA	NA	108.34	7.3003	0.502	13.87	
907A	NA	NA	108.36	7.3013	0.545	15.17	
907C	12H5	132 - 134	108.42	7.3618	0.586	16.43	1.12
907C	12H6	12 - 14	108.72	7.3761	0.644	18.18	1.17
907C	12H6	42 - 44	109.02	7.3905	0.604	16.98	0.05
907C	12H6	72 - 74	109.32	7.4049	0.575	16.09	0.12
907A	NA	NA	109.33	7.3484	0.652	18.42	
907A	NA	NA	109.35	7.3494	0.652	18.42	
907A	NA	NA	109.57	7.3601	0.661	18.70	
907B	NA	NA	109.88	7.4268	0.581	16.28	
907C	12H6	132 - 134	109.92	7.4336	0.531	14.76	0.97
907C	12H7	12 - 14	110.22	7.4480	0.530	14.73	1.31
907B	NA	NA	110.38	7.4484	0.651	18.40	
907C	12H7	42 - 44	110.52	7.4624	0.607	17.07	1.32
907B	NA	NA	110.62	7.4589	0.655	18.53	
907C	13H1	12 - 14	110.72	7.4717	0.622	17.51	0.63
907A	NA	NA	110.91	7.4253	0.623	17.56	
907C	13H1	42 - 44	111.02	7.4828	0.648	18.30	1.36
907C	13H1	72 - 74	111.32	7.4938	0.684	19.40	1.11
907C	13H1	102 - 104	111.62	7.5049	0.609	17.12	0.96
907C	13H1	132 - 134	111.92	7.5159	0.498	13.75	1.13
907C	13H2	42 - 44	112.52	7.5380	0.522	14.48	1.18
907C	13H2	72 - 74	112.82	7.5491	0.665	18.82	0.13
907A	NA	NA	112.97	7.5199	0.539	14.99	
907C	13H2	102 - 104	113.12	7.5601	0.554	15.47	0.32
907C	13H2	132 - 134	113.42	7.5712	0.551	15.35	0.63

Appendix B Alkenone Indices from ODP Sites 883, 884, 887, 907, 982, 1088

Core	Section	Interval (cm)	mbsf (m)	Age(Ma)	UK'37	SST (°C) M	[C37] total (nmol/g)
907C	13H3	12 - 14	113.72	7.5822	0.564	15.75	0.60
907C	13H3	42 - 44	114.02	7.5933	0.542	15.09	0.37
907C	13H3	72 - 74	114.32	7.6043	0.731	20.81	0.95
907C	13H3	102 - 104	114.62	7.6154	0.653	18.45	0.09
907A	NA	NA	114.77	7.5985	0.556	15.51	
907C	13H3	132 - 134	114.92	7.6264	0.489	13.49	0.59
907C	13H4	12 - 14	115.22	7.6374	0.523	14.51	1.02
907C	13H4	132 - 134	116.42	7.6816	0.651	18.40	0.41
907C	13H5	12 - 14	116.72	7.6927	0.543	15.12	1.48
907C	13H5	42 - 44	117.02	7.7037	0.628	17.68	0.78
907C	13H5	72 - 74	117.32	7.7148	0.644	18.19	1.96
907C	13H5	132 - 134	117.92	7.7369	0.697	19.80	
907C	13H6	12 - 14	118.22	7.7479	0.671	18.99	0.63
907A	NA	NA	118.44	7.7455	0.582	16.29	
907A	NA	NA	118.46	7.7462	0.582	16.29	
907C	13H6	42 - 44	118.52	7.7590	0.620	17.47	0.67
907C	13H6	72 - 74	118.82	7.7700	0.726	20.66	1.14
907A	NA	NA	119.11	7.7684	0.579	16.20	
907C	13H6	102 - 104	119.12	7.7811	0.478	13.17	0.09
907C	13H6	132 - 134	119.42	7.7921	0.567	15.85	0.82
907C	13H7	42 - 44	120.02	7.8142	0.633	17.86	1.64
907C	13H7	62 - 64	120.20	7.8208	0.682	19.34	1.34
907C	14H1	12 - 14	120.22	7.8216	0.634	17.86	0.56
907C	14H1	42 - 44	120.52	7.8326	0.711	20.21	0.98
907C	14H1	72 - 74	120.82	7.8437	0.573	16.02	0.41
907C	14H1	102 - 104	121.12	7.8547	0.603	16.94	1.00
907C	14H1	132 - 134	121.42	7.8658	0.652	18.41	1.56
907C	14H2	12 - 14	121.72	7.8768	0.583	16.34	1.03
907C	14H2	42 - 44	122.02	7.8879	0.569	15.92	2.16
907C	14H2	72 - 74	122.32	7.8989	0.600	16.85	1.55
907C	14H2	102 - 104	122.62	7.9099	0.654	18.48	2.75
907C	14H2	132 - 134	122.92	7.9210	0.621	17.48	0.56
907C	14H3	12 - 14	123.22	7.9320	0.608	17.10	1.35
907C	14H3	42 - 44	123.52	7.9431	0.612	17.21	1.44
907C	14H3	72 - 74	123.82	7.9541	0.687	19.49	1.81
907C	14H3	102 - 104	124.12	7.9652	0.621	17.49	0.69
907C	14H3	132 - 134	124.42	7.9762	0.589	16.51	0.63
907A	NA	NA	124.50	7.9526	0.538	14.98	
907C	14H4	12 - 14	124.72	7.9873	0.511	14.16	2.09
907C	14H4	42 - 44	125.02	7.9983	0.615	17.32	1.28
907C	14H4	72 - 74	125.32	8.0094	0.505	13.98	1.17
907C	14H4	102 - 104	125.62	8.0204	0.591	16.58	1.49
907C	14H4	132 - 134	125.92	8.0315	0.480	13.22	0.82
907C	14H5	12 - 14	126.22	8.0425	0.634	17.88	0.69
907C	14H5	72 - 74	126.82	8.0646	0.513	14.20	0.32
907C	14H5	102 - 104	127.12	8.0757	0.659	18.64	1.00
907C	14H5	132 - 134	127.42	8.0867	0.504	13.95	0.29
907C	14H6	12 - 14	127.72	8.0978	0.720	20.49	0.35
907C	14H6	42 - 44	128.02	8.1088	0.737	21.01	0.66
907C	14H6	72 - 74	128.32	8.1198	0.687	19.48	1.14

Appendix B Alkenone Indices from ODP Sites 883, 884, 887, 907, 982, 1088

Core	Section	Interval (cm)	mbsf (m)	Age(Ma)	UK'37	SST (°C) M	[C37] total (nmol/g)
907C	14H6	102 - 104	128.62	8.1309	0.611	17.18	1.30
907C	14H6	132 - 134	128.92	8.1464	0.677	19.19	0.25
907C	14H7	12 - 14	129.22	8.1624	0.577	16.16	0.66
907A	NA	NA	129.52	8.1241	0.713	20.27	0.56
907C	14H7	42 - 44	129.52	8.1784	0.614	17.26	0.56
907C	15H1	12 - 14	129.72	8.1891	0.567	15.84	0.45
907C	15H1	42 - 44	130.02	8.2051	0.485	13.36	0.37
907C	15H1	72 - 74	130.32	8.2212	0.640	18.07	0.33
907C	15H1	102 - 104	130.62	8.2372	0.713	20.27	0.49
907C	15H1	132 - 134	130.92	8.2532	0.590	16.55	0.31
907C	15H2	12 - 14	131.22	8.2692	0.552	15.38	0.57
907C	15H2	42 - 44	131.52	8.2852	0.593	16.64	0.40
907C	15H2	102 - 104	132.12	8.3173	0.603	16.95	0.43
907C	15H2	132 - 134	132.42	8.3333	0.525	14.58	0.30
907C	15H3	12 - 14	132.72	8.3493	0.706	20.06	0.25
907C	15H3	42 - 44	133.02	8.3653	0.610	17.16	0.76
907A	NA	NA	133.22	8.2824	0.506	13.99	
907C	15H3	72 - 74	133.32	8.3813	0.731	20.83	0.63
907C	15H3	102 - 104	133.62	8.3973	0.534	14.86	0.46
907C	15H3	132 - 134	133.92	8.4134	0.572	16.00	0.63
907C	15H4	12 - 14	134.22	8.4294	0.559	15.61	0.85
907C	15H4	42 - 44	134.52	8.4454	0.600	16.86	0.36
907C	15H4	72 - 74	134.82	8.4614	0.653	18.45	0.98
907C	15H4	102 - 104	135.12	8.4774	0.632	17.80	0.47
907C	15H4	132 - 134	135.42	8.4934	0.651	18.41	0.32
907C	15H5	12 - 14	135.72	8.5095	0.645	18.22	0.76
907C	15H5	42 - 44	136.02	8.5255	0.607	17.07	0.71
907A	NA	NA	136.25	8.4536	0.694	19.70	
907C	15H5	72 - 74	136.32	8.5415	0.685	19.44	0.55
907C	15H5	102 - 104	136.62	8.5575	0.536	14.90	0.93
907C	15H5	132 - 134	136.92	8.5735	0.709	20.16	0.26
907A	NA	NA	136.93	8.4920	0.699	19.83	
907A	NA	NA	136.95	8.4932	0.699	19.83	
907C	15H6	12 - 14	137.22	8.5895	0.607	17.06	0.39
907C	15H6	42 - 44	137.52	8.6056	0.603	16.92	0.36
907C	15H6	72 - 74	137.82	8.6216	0.628	17.69	0.28
907C	15H6	102 - 104	138.12	8.6376	0.628	17.70	0.54
907A	NA	NA	138.22	8.5649	0.597	16.75	
907A	NA	NA	138.31	8.5700	0.553	15.43	
907C	15H6	132 - 134	138.42	8.6536	0.679	19.24	0.41
907C	15H7	12 - 14	138.72	8.6696	0.571	15.96	0.49
907B	NA	NA	138.79	8.6950	0.607	17.06	
907B	NA	NA	138.98	8.7033	0.685	19.43	
907C	15H7	42 - 44	139.02	8.6856	0.616	17.32	0.64
907C	15H7	55 - 57	139.15	8.6926	0.640	18.05	0.57
907C	16H1	12 - 14	139.22	8.6963	0.604	16.98	0.34
907C	16H1	42 - 44	139.52	8.7123	0.684	19.39	0.30
907C	16H1	72 - 74	139.82	8.7284	0.600	16.86	0.58
907C	16H1	102 - 104	140.12	8.7444	0.723	20.58	0.17
907B	NA	NA	140.20	8.7568	0.678	19.20	

Appendix B Alkenone Indices from ODP Sites 883, 884, 887, 907, 982, 1088

Core	Section	Interval (cm)	mbsf (m)	Age(Ma)	UK'37	SST (°C) M	[C37] total (nmol/g)
907C	16H1	132 - 134	140.42	8.7604	0.624	17.56	0.27
907C	16H2	12 - 14	140.72	8.7768	0.620	17.46	0.42
907C	16H2	42 - 44	141.02	8.7936	0.773	22.09	0.22
907C	16H2	72 - 74	141.32	8.8105	0.696	19.76	0.38
907C	16H2	102 - 104	141.62	8.8274	0.671	19.01	0.49
907C	16H2	132 - 134	141.92	8.8443	0.684	19.38	0.20
907C	16H3	12 - 14	142.22	8.8612	0.652	18.43	0.34
907A	NA	NA	142.45	8.8027	0.613	17.26	
907A	NA	NA	142.47	8.8038	0.613	17.26	
907C	16H3	42 - 44	142.52	8.8781	0.726	20.66	0.51
907A	NA	NA	142.74	8.8185	0.692	19.63	
907A	NA	NA	142.76	8.8196	0.692	19.63	
907C	16H3	102 - 104	143.12	8.9119	0.638	18.00	0.42
907C	16H3	132 - 134	143.42	8.9288	0.704	20.01	0.51
907C	16H4	12 - 14	143.72	8.9457	0.617	17.36	1.53
907C	16H4	42 - 44	144.02	8.9626	0.653	18.46	0.50
907A	NA	NA	144.10	8.8926	0.652	18.41	
907A	NA	NA	144.12	8.8937	0.652	18.41	
907C	16H5	12 - 14	145.22	9.0301	0.642	18.12	0.57
907C	16H5	42 - 44	145.52	9.0470	0.629	17.72	0.39
907A	NA	NA	145.82	8.9863	0.572	16.00	0.26
907C	16H5	72 - 74	145.82	9.0639	0.682	19.32	0.26
907C	16H5	102 - 104	146.12	9.0808	0.656	18.55	0.59
907C	16H5	132 - 134	146.42	9.0977	0.673	19.07	0.52
907C	16H6	12 - 14	146.72	9.1131	0.715	20.35	0.15
907C	16H6	42 - 44	147.02	9.1274	0.668	18.90	0.39
907C	16H6	72 - 74	147.32	9.1417	0.630	17.76	0.43
907C	16H6	102 - 104	147.62	9.1560	0.635	17.91	0.55
907A	NA	NA	147.73	9.0903	0.671	19.00	
907C	16H6	132 - 134	147.92	9.1702	0.700	19.88	0.36
907C	16H7	12 - 14	148.22	9.1845	0.717	20.40	0.15
907C	17H1	12 - 14	149.54	9.2474	0.719	20.46	0.34
907C	17H1	42 - 44	149.84	9.2617	0.719	20.45	0.49
907C	17H1	72 - 74	150.14	9.2760	0.733	20.88	0.15
907A	NA	NA	152.06	9.3423	0.711	20.22	
907A	NA	NA	152.69	9.3792	0.572	16.00	
907A	NA	NA	157.06	9.6346	0.846	24.30	
907A	NA	NA	165.34	9.9316	0.821	23.56	
907A	NA	NA	165.93	9.9451	0.752	21.47	

Appendix B Alkenone Indices from ODP Sites 883, 884, 887, 907, 982, 1088

Core	Section	Interval (cm)	MCD (m)	Age(Ma)	UK'37	SST (°C) M	[C37] total (nmol/g)
982B	14 - 1	10 - 12	132.21	4.9739	0.759	21.66	0.44
982B	14 - 3	10 - 12	135.21	5.0616	0.737	21.01	0.23
982B	14 - 5	10 - 12	138.21	5.1482	0.704	20.01	0.30
982B	14 - 7	10 - 12	141.21	5.2338	0.590	16.55	0.43
982B	15 - 1	10 - 12	143.17	5.2478	0.619	17.44	0.88
982B	15 - 3	10 - 12	146.17	5.3321	0.724	20.62	0.24
982B	15 - 5	10 - 12	149.17	5.4153	0.733	20.88	0.24
982B	15 - 7	10 - 12	152.16	5.4973	0.737	20.99	0.22
982B	16 - 1	10 - 12	153.35	5.5111	0.648	18.31	0.58
982B	16 - 3	10 - 12	156.35	5.5922	0.614	17.28	0.67
982B	16 - 5	10 - 12	159.35	5.6723	0.637	17.98	0.42
982B	16 - 7	10 - 12	162.35	5.7514	0.757	21.61	0.25
982B	17 - 1	10 - 12	163.69	5.7643	0.789	22.56	0.11
982B	17 - 2	50 - 52	165.14	5.8023	0.701	19.90	0.14
982B	17 - 2	88 - 90	165.18	5.8033	0.721	20.52	0.16
982B	17 - 2	131 - 133	165.22	5.8044	0.707	20.11	0.09
982B	17 - 3	10 - 12	166.69	5.8424	0.773	22.10	0.34
982B	17 - 3	20 - 22	166.61	5.8405	0.781	22.35	0.11
982B	17 - 3	60 - 62	166.65	5.8415	0.774	22.12	0.14
982B	17 - 3	139 - 141	166.73	5.8435	0.724	20.59	0.23
982B	17 - 4	30 - 32	168.12	5.8794	0.805	23.06	0.08
982B	17 - 4	70 - 72	168.16	5.8805	0.766	21.88	0.19
982B	17 - 4	110 - 112	168.20	5.8815	0.607	17.05	0.12
982B	17 - 5	5 - 7	169.60	5.9173	0.779	22.27	0.14
982B	17 - 5	10 - 12	169.69	5.9196	0.776	22.18	0.24
982B	17 - 5	45 - 47	169.64	5.9183	0.774	22.14	0.08
982B	17 - 5	85 - 87	169.68	5.9193	0.762	21.76	0.19
982B	17 - 5	125 - 127	169.72	5.9204	0.761	21.73	0.06
982B	17 - 6	10 - 12	171.20	5.9581	0.688	19.51	0.38
982B	17 - 6	15 - 17	171.11	5.9558	0.707	20.10	0.23
982B	17 - 6	55 - 57	171.15	5.9569	0.770	22.00	0.13
982B	17 - 6	95 - 97	171.19	5.9579	0.813	23.31	0.10
982B	17 - 6	135 - 137	171.23	5.9589	0.775	22.14	0.07
982B	17 - 7	8 - 10	172.60	5.9937	0.756	21.59	0.12
982B	17 - 7	10 - 12	172.70	5.9962	0.755	21.54	0.09
982B	18 - 1	10 - 12	177.12	6.0091	0.635	17.92	0.14
982B	18 - 1	18 - 20	174.10	6.0066	0.615	17.29	0.07
982B	18 - 1	50 - 52	174.13	6.0074	0.622	17.52	0.02
982B	18 - 1	82 - 84	174.16	6.0083	0.714	20.31	0.06
982B	18 - 1	110 - 112	174.19	6.0090	0.726	20.65	0.05
982B	18 - 1	138 - 140	174.22	6.0097	0.666	18.84	0.11
982B	18 - 2	20 - 22	175.60	6.0445	0.581	16.28	0.24
982B	18 - 2	50 - 52	175.63	6.0452	0.655	18.51	0.09
982B	18 - 2	80 - 82	175.66	6.0460	0.678	19.20	0.04
982B	18 - 2	110 - 112	175.69	6.0467	0.663	18.76	0.08
982B	18 - 2	140 - 142	175.72	6.0475	0.612	17.20	0.39
982B	18 - 3	10 - 12	177.19	6.0843	0.690	19.57	0.09
982B	18 - 3	20 - 22	177.10	6.0821	0.680	19.27	0.03
982B	18 - 3	50 - 52	177.13	6.0828	0.724	20.60	0.05
982B	18 - 3	78 - 80	177.16	6.0835	0.670	18.96	0.04

Appendix B Alkenone Indices from ODP Sites 883, 884, 887, 907, 982, 1088

Core	Section	Interval (cm)	MCD (m)	Age(Ma)	UK'37	SST (°C) M	[C37] total (nmol/g)
982B	18 - 3	110 - 112	177.19	6.0843	0.670	18.98	0.11
982B	18 - 3	140 - 142	177.22	6.0851	0.671	19.00	0.08
982B	18 - 4	20 - 22	178.60	6.1194	0.686	19.45	0.10
982B	18 - 4	52 - 54	178.63	6.1202	0.592	16.61	0.17
982B	18 - 4	80 - 82	178.66	6.1209	0.651	18.39	0.03
982B	18 - 4	110 - 112	178.69	6.1217	0.747	21.30	0.09
982B	18 - 5	10 - 12	180.19	6.1587	0.624	17.56	0.42
982B	18 - 5	22 - 24	180.10	6.1567	0.631	17.79	0.22
982B	18 - 5	50 - 52	180.13	6.1574	0.677	19.20	0.09
982B	18 - 5	80 - 82	180.16	6.1581	0.739	21.06	0.15
982B	18 - 5	110 - 112	180.19	6.1589	0.700	19.89	0.07
982B	18 - 5	138 - 140	180.22	6.1595	0.623	17.53	0.11
982B	18 - 6	20 - 22	181.60	6.1936	0.645	18.20	0.09
982B	18 - 6	50 - 52	181.63	6.1944	0.642	18.12	0.19
982B	18 - 6	80 - 82	181.66	6.1951	0.666	18.84	0.16
982B	18 - 6	108 - 110	181.69	6.1958	0.541	15.07	0.42
982B	18 - 6	140 - 142	181.72	6.1966	0.530	14.72	0.25
982B	18 - 7	10 - 12	183.19	6.2325	0.507	14.04	1.10
982B	18 - 7	20 - 22	183.10	6.2304	0.454	12.41	0.54
982B	18 - 7	45 - 47	183.13	6.2310	0.474	13.02	0.49
982B	19 - 1	5 - 7	184.80	6.2423	0.645	18.20	0.12
982B	19 - 1	10 - 12	184.90	6.2448	0.635	17.89	0.20
982B	19 - 1	35 - 37	184.83	6.2430	0.640	18.06	0.11
982B	19 - 1	65 - 67	184.86	6.2437	0.576	16.13	0.36
982B	19 - 1	95 - 97	184.89	6.2445	0.523	14.50	1.21
982B	19 - 1	125 - 127	184.92	6.2452	0.612	17.20	0.17
982B	19 - 2	5 - 7	186.30	6.2788	0.715	20.35	0.05
982B	19 - 2	35 - 37	186.33	6.2795	0.579	16.22	0.70
982B	19 - 2	65 - 67	186.36	6.2803	0.657	18.59	0.16
982B	19 - 2	95 - 97	186.39	6.2810	0.581	16.28	0.32
982B	19 - 2	125 - 127	186.42	6.2817	0.506	13.99	1.10
982B	19 - 3	5 - 7	187.80	6.3151	0.527	14.63	0.83
982B	19 - 3	10 - 12	187.88	6.3171	0.570	15.94	1.26
982B	19 - 3	35 - 37	187.83	6.3159	0.618	17.38	0.08
982B	19 - 3	65 - 67	187.86	6.3166	0.661	18.69	0.09
982B	19 - 3	96 - 98	187.89	6.3173	0.641	18.08	0.13
982B	19 - 3	125 - 127	187.92	6.3180	0.637	17.97	0.21
982B	19 - 4	5 - 7	189.30	6.3513	0.625	17.60	0.33
982B	19 - 4	35 - 37	189.33	6.3520	0.697	19.79	0.18
982B	19 - 4	65 - 37	189.34	6.3524	0.583	16.33	0.42
982B	19 - 4	95 - 97	189.39	6.3535	0.578	16.19	0.53
982B	19 - 4	125 - 127	189.42	6.3542	0.660	18.66	0.09
982B	19 - 5	5 - 7	190.80	6.3873	0.664	18.80	0.16
982B	19 - 5	10 - 12	190.80	6.3874	0.680	19.26	0.43
982B	19 - 5	35 - 37	190.83	6.3880	0.751	21.43	0.08
982B	19 - 5	65 - 67	190.86	6.3887	0.745	21.24	0.08
982B	19 - 5	95 - 97	190.89	6.3894	0.701	19.90	0.18
982B	19 - 5	125 - 127	190.92	6.3902	0.613	17.25	0.50
982B	19 - 6	5 - 7	192.30	6.4231	0.640	18.05	0.21
982B	19 - 6	35 - 37	192.33	6.4238	0.685	19.43	0.10

Appendix B Alkenone Indices from ODP Sites 883, 884, 887, 907, 982, 1088

Core	Section	Interval (cm)	MCD (m)	Age(Ma)	UK'37	SST (°C) M	[C37] total (nmol/g)
982B	19 - 6	65 - 67	192.36	6.4245	0.704	19.99	0.22
982B	19 - 6	95 - 97	192.39	6.4252	0.693	19.66	0.25
982B	19 - 6	125 - 127	192.42	6.4260	0.711	20.21	0.13
982B	19 - 7	5 - 7	193.80	6.4587	0.733	20.89	0.10
982B	19 - 7	10 - 12	193.80	6.4588	0.744	21.22	0.06
982B	19 - 7	35 - 37	193.83	6.4594	0.698	19.80	0.16
982B	20 - 1	10 - 12	195.17	6.4707	0.670	18.96	0.30
982B	20 - 1	15 - 17	195.18	6.4708	0.655	18.53	0.12
982B	20 - 1	45 - 47	195.21	6.4715	0.686	19.47	0.08
982B	20 - 1	75 - 77	195.24	6.4722	0.663	18.77	0.12
982B	20 - 1	105 - 107	195.27	6.4729	0.644	18.17	0.12
982B	20 - 1	135 - 137	195.30	6.4736	0.735	20.95	0.10
982B	20 - 2	15 - 17	196.68	6.5062	0.727	20.69	0.10
982B	20 - 2	45 - 47	196.71	6.5069	0.718	20.43	0.17
982B	20 - 2	75 - 77	196.74	6.5076	0.528	14.67	0.13
982B	20 - 2	105 - 107	196.77	6.5083	0.619	17.41	0.53
982B	20 - 2	135 - 137	196.80	6.5090	0.743	21.18	0.11
982B	20 - 3	10 - 12	198.17	6.5413	0.758	21.63	0.24
982B	20 - 3	15 - 17	198.18	6.5414	0.754	21.52	0.13
982B	20 - 3	45 - 47	198.21	6.5421	0.778	22.25	0.09
982B	20 - 3	75 - 77	198.24	6.5428	0.746	21.28	0.06
982B	20 - 3	105 - 107	198.27	6.5435	0.623	17.56	0.31
982B	20 - 3	135 - 137	198.30	6.5442	0.576	16.14	0.48
982B	20 - 4	15 - 17	199.68	6.5765	0.589	16.51	0.14
982B	20 - 4	45 - 47	199.71	6.5772	0.646	18.24	0.24
982B	20 - 4	75 - 77	199.74	6.5779	0.671	19.00	0.24
982B	20 - 4	105 - 107	199.77	6.5786	0.701	19.92	0.14
982B	20 - 4	135 - 137	199.80	6.5793	0.671	18.99	0.21
982B	20 - 5	15 - 17	201.18	6.6114	0.682	19.35	0.30
982B	20 - 5	45 - 47	201.21	6.6121	0.620	17.45	0.41
982B	20 - 5	75 - 77	201.24	6.6128	0.655	18.52	0.33
982B	20 - 5	105 - 107	201.27	6.6135	0.669	18.95	0.24
982B	20 - 5	136 - 138	201.30	6.6142	0.637	17.96	0.26
982B	20 - 6	15 - 17	202.68	6.6461	0.631	17.80	0.39
982B	20 - 6	45 - 47	202.71	6.6468	0.627	17.67	0.65
982B	20 - 6	75 - 77	202.74	6.6475	0.674	19.09	0.40
982B	20 - 6	105 - 107	202.77	6.6482	0.710	20.17	0.45
982B	20 - 6	135 - 137	202.80	6.6489	0.456	12.49	0.32
982B	20 - 7	10 - 12	204.17	6.6806	0.589	16.53	2.12
982B	20 - 7	15 - 17	204.18	6.6807	0.575	16.09	0.90
982B	20 - 7	45 - 47	204.21	6.6814	0.599	16.81	0.49
982B	21 - 1	10 - 12	205.61	6.6921	0.644	18.18	0.28
982B	21 - 1	75 - 77	205.68	6.6936	0.476	13.10	0.61
982B	21 - 1	105 - 107	205.71	6.6943	0.448	12.23	0.43
982B	21 - 2	15 - 17	207.12	6.7266	0.648	18.30	0.14
982B	21 - 2	75 - 77	207.18	6.7280	0.644	18.17	0.22
982B	21 - 2	105 - 107	207.21	6.7286	0.679	19.24	0.27
982B	21 - 3	10 - 12	208.61	6.7607	0.486	13.41	1.47
982B	21 - 3	15 - 17	208.62	6.7608	0.527	14.65	0.61
982B	21 - 3	45 - 47	208.65	6.7615	0.498	13.75	0.73

Appendix B Alkenone Indices from ODP Sites 883, 884, 887, 907, 982, 1088

Core	Section	Interval (cm)	MCD (m)	Age(Ma)	UK'37	SST (°C) M	[C37] total (nmol/g)
982B	21 - 3	105 - 107	208.71	6.7629	0.603	16.95	0.47
982B	21 - 4	15 - 17	210.12	6.7949	0.526	14.61	1.24
982B	21 - 4	135 - 137	210.24	6.7976	0.637	17.97	0.64
982B	21 - 5	10 - 12	211.61	6.8287	0.666	18.86	0.37
982B	21 - 5	15 - 17	211.62	6.8288	0.649	18.32	0.47
982B	21 - 5	105 - 107	211.71	6.8309	0.703	19.98	0.16
982B	21 - 5	134 - 136	211.74	6.8315	0.708	20.14	0.31
982B	21 - 6	15 - 17	213.12	6.8626	0.610	17.16	0.82
982B	21 - 6	105 - 107	213.21	6.8647	0.683	19.35	0.23
982B	21 - 6	135 - 137	213.24	6.8653	0.696	19.75	0.14
982B	21 - 7	10 - 12	214.61	6.8962	0.714	20.31	0.24
982B	21 - 7	15 - 17	214.62	6.8963	0.711	20.20	0.08
982B	21 - 7	45 - 47	214.65	6.8970	0.686	19.46	0.22
982B	22 - 1	10 - 12	214.62	6.9095	0.705	20.02	0.19
982B	22 - 3	10 - 12	217.62	6.9763	0.814	23.33	0.09
982B	22 - 5	10 - 12	220.62	7.0426	0.846	24.30	0.10
982B	23 - 1	10 - 12	225.53	7.1194	0.744	21.20	0.08
982B	23 - 5	10 - 12	231.53	7.2494	0.782	22.35	0.06
982B	24 - 1	10 - 12	234.06	7.3246	0.791	22.63	0.14
982B	24 - 5	10 - 12	240.06	7.4521	0.794	22.73	0.32
982B	24 - 7	10 - 12	243.06	7.5154	0.807	23.12	0.07
982B	25 - 1	10 - 12	244.70	7.5259	0.739	21.05	0.22
982B	25 - 3	10 - 12	247.70	7.5888	0.802	22.97	0.07
982B	25 - 5	10 - 12	250.70	7.6514	0.838	24.08	0.08
982B	25 - 7	10 - 12	253.70	7.7138	0.825	23.66	0.30
982B	26 - 1	15 - 17	254.25	7.7253	0.842	24.18	0.10
982B	26 - 2	15 - 17	255.75	7.7564	0.737	21.00	0.35
982B	26 - 4	15 - 17	258.75	7.8184	0.836	24.01	0.03
982B	26 - 5	15 - 17	260.25	7.8493	0.780	22.30	0.18
982B	26 - 7	15 - 17	263.25	7.9109	0.808	23.16	0.02
982B	27 - 2	15 - 17	265.25	7.9520	0.823	23.60	0.01
982B	27 - 4	15 - 17	268.25	8.0134	0.844	24.25	0.07
982B	27 - 5	15 - 17	269.75	8.0441	0.842	24.19	0.13
982B	28 - 1	15 - 17	270.05	8.0502	0.884	25.44	0.08
982B	28 - 3	15 - 17	273.05	8.1114	0.886	25.50	0.13
982B	29 - 1	15 - 17	279.65	8.2459	0.867	24.93	0.02
982B	29 - 2	15 - 17	281.15	8.2764	0.857	24.64	0.10
982B	29 - 4	15 - 17	284.15	8.3375	0.816	23.39	0.02
982B	31 - 1	15 - 17	298.95	8.6391	0.890	25.63	0.14
982B	31 - 2	15 - 17	300.45	8.6698	0.894	25.76	0.04
982B	31 - 4	15 - 17	303.45	8.7312	0.895	25.78	0.03
982B	31 - 6	15 - 17	306.45	8.7929	0.873	25.13	0.07
982B	31 - 7	15 - 17	307.95	8.8237	0.895	25.78	0.01
982B	32 - 1	15 - 17	308.55	8.8361	0.893	25.72	0.05
982B	32 - 2	15 - 17	310.05	8.8671	0.864	24.86	0.05
982B	32 - 4	15 - 17	313.05	8.9291	0.878	25.27	0.10
982B	33 - 1	15 - 17	318.15	9.0351	0.903	26.02	0.03
982B	33 - 2	15 - 17	319.65	9.0665	0.903	26.03	0.03
982B	33 - 3	15 - 17	321.15	9.0979	0.877	25.25	0.02
982B	33 - 5	15 - 17	324.15	9.1609	0.885	25.47	0.03

Appendix B Alkenone Indices from ODP Sites 883, 884, 887, 907, 982, 1088

Core	Section	Interval (cm)	MCD (m)	Age(Ma)	UK'37	SST (°C) M	[C37] total (nmol/g)
982B	34 - 1	15 - 17	327.85	9.2391	0.850	24.42	0.01
982B	34 - 2	15 - 17	329.35	9.2709	0.834	23.95	0.01
982B	34 - 4	15 - 17	332.35	9.3349	0.833	23.92	0.01
982B	34 - 5	15 - 17	333.85	9.3670	0.882	25.39	0.03
982B	35 - 1	15 - 17	337.45	9.4445	0.868	24.98	0.02
982B	35 - 2	15 - 17	338.95	9.4770	0.886	25.53	0.02
982B	35 - 3	15 - 17	340.45	9.5096	0.925	26.70	0.02
982B	35 - 4	15 - 17	341.95	9.5423	0.905	26.09	0.03
982B	36 - 1	15 - 17	347.05	9.6543	0.891	25.66	0.02
982B	36 - 2	15 - 17	348.55	9.6875	0.858	24.67	0.02
982B	36 - 3	15 - 17	350.05	9.7209	0.910	26.26	0.03
982B	36 - 4	15 - 17	351.55	9.7544	0.807	23.11	0.01
982B	36 - 5	15 - 17	353.05	9.7880	0.765	21.86	0.01
982B	37 - 1	15 - 17	356.75	9.8715	0.907	26.15	0.02
982B	37 - 2	15 - 17	358.25	9.9056	0.883	25.42	0.08
982B	37 - 3	15 - 17	359.75	9.9398	0.905	26.10	0.02
982B	37 - 4	15 - 17	361.25	9.9742	0.873	25.11	0.02
982B	37 - 5	15 - 17	362.75	10.0088	0.788	22.55	0.01
982B	38 - 2	15 - 17	367.85	10.1275	0.941	27.20	0.02
982B	38 - 3	15 - 17	369.35	10.1627	0.885	25.50	0.03
982B	38 - 4	15 - 17	370.85	10.1982	0.905	26.09	0.02
982B	38 - 5	15 - 17	372.35	10.2338	0.884	25.45	0.05
982B	39 - 1	15 - 17	375.95	10.3200	0.909	26.20	0.02
982B	39 - 2	15 - 17	377.45	10.3562	0.909	26.20	0.04
982B	39 - 3	15 - 17	378.95	10.3926	0.890	25.65	0.04
982B	39 - 4	15 - 17	380.45	10.4292	0.911	26.28	0.02
982B	40 - 1	15 - 17	385.65	10.5575	0.909	26.20	0.01
982B	40 - 2	15 - 17	387.15	10.5950	0.911	26.29	0.01
982B	41 - 1	15 - 17	395.25	10.8009	0.935	26.99	0.03
982B	41 - 2	15 - 17	396.75	10.8397	0.904	26.05	0.02
982B	41 - 3	15 - 17	398.25	10.8788	0.927	26.75	0.02
982B	41 - 5	15 - 17	401.25	10.9576	0.922	26.59	0.01
982B	42 - 2	15 - 17	406.35	11.0937	0.934	26.98	0.01
982B	42 - 3	15 - 17	407.85	11.1342	0.860	24.73	0.02
982B	42 - 4	15 - 17	409.35	11.1750	0.929	26.81	0.03
982B	42 - 5	15 - 17	410.85	11.2161	0.873	25.11	0.01

Appendix B Alkenone Indices from ODP Sites 883, 884, 887, 907, 982, 1088

Core	Section	Interval (cm)	MCD (m)	Age(Ma)	UK'37	SST (°C) M	[C37] total (nmol/g)
1088B	6 - 5	84 - 85	50.35	5.2757	0.693	19.67	0.24
1088B	6 - 5	97 - 98	50.48	5.2886	0.656	18.55	0.14
1088B	6 - 5	120 - 121	50.71	5.3114	0.650	18.36	0.49
1088B	6 - 5	138 - 139	50.89	5.3292	0.649	18.33	0.14
1088B	6 - 6	4 - 6	51.05	5.3455	0.661	18.70	0.18
1088B	6 - 6	18 - 20	51.19	5.3593	0.649	18.33	0.28
1088B	6 - 6	28 - 29	51.29	5.3687	0.608	17.09	0.41
1088B	6 - 6	52 - 54	51.53	5.3928	0.751	21.42	0.02
1088B	6 - 6	64 - 66	51.65	5.4046	0.624	17.58	0.27
1088B	6 - 6	76 - 77	51.77	5.4159	0.642	18.12	0.17
1088B	6 - 6	100 - 102	52.01	5.4400	0.698	19.82	0.05
1088B	6 - 6	126 - 128	52.27	5.4654	0.688	19.52	0.10
1088B	6 - 6	148 - 150	52.49	5.4870	0.698	19.82	0.06
1088B	7 - 1	32 - 34	53.33	5.5687	0.546	15.21	0.15
1088B	7 - 1	43 - 45	53.44	5.5794	0.292	7.52	0.16
1088B	7 - 1	56 - 58	53.57	5.5920	0.525	14.58	0.30
1088B	7 - 1	68 - 70	53.69	5.6036	0.513	14.21	0.39
1088B	7 - 1	80 - 82	53.81	5.6152	0.336	8.85	0.39
1088B	7 - 1	92 - 94	53.93	5.6268	0.548	15.27	0.15
1088B	7 - 1	104 - 106	54.05	5.6384	0.543	15.12	0.27
1088B	7 - 1	128 - 130	54.29	5.6615	0.506	14.00	0.46
1088B	7 - 1	139 - 141	54.40	5.6721	0.534	14.85	0.38
1088B	7 - 2	8 - 10	54.59	5.6904	0.510	14.12	0.43
1088B	7 - 2	20 - 22	54.71	5.7019	0.568	15.88	0.28
1088B	7 - 2	44 - 46	54.95	5.7249	0.536	14.91	0.74
1088B	7 - 2	56 - 58	55.07	5.7364	0.461	12.64	0.63
1088B	7 - 2	68 - 70	55.19	5.7479	0.502	13.88	0.68
1088B	7 - 2	80 - 82	55.31	5.7594	0.533	14.82	0.46
1088B	7 - 2	116 - 118	55.67	5.7937	0.454	12.42	0.43
1088B	7 - 2	127 - 129	55.78	5.8042	0.545	15.18	0.46
1088B	7 - 3	8 - 10	56.09	5.8336	0.527	14.64	0.40
1088B	7 - 3	20 - 22	56.21	5.8450	0.556	15.52	0.37
1088B	7 - 3	44 - 46	56.45	5.8677	0.497	13.73	0.40
1088B	7 - 3	56 - 57	56.57	5.8786	0.542	15.09	0.33
1088B	7 - 3	68 - 70	56.69	5.8904	0.543	15.12	0.35
1088B	7 - 3	80 - 82	56.81	5.9017	0.575	16.09	0.34
1088B	7 - 3	92 - 94	56.93	5.9130	0.501	13.85	0.71
1088B	7 - 3	116 - 118	57.17	5.9356	0.508	14.06	0.41
1088B	7 - 3	128 - 130	57.29	5.9468	0.519	14.39	0.29
1088B	7 - 3	140 - 141	57.41	5.9576	0.553	15.42	0.23
1088B	7 - 4	8 - 10	57.59	5.9750	0.578	16.18	0.18
1088B	7 - 4	20 - 22	57.71	5.9862	0.547	15.24	0.16
1088B	7 - 4	44 - 45	57.95	6.0082	0.542	15.09	0.36
1088B	7 - 4	56 - 58	58.07	6.0198	0.493	13.61	0.49
1088B	7 - 4	68 - 70	58.19	6.0310	0.517	14.33	0.64
1088B	7 - 4	80 - 82	58.31	6.0422	0.519	14.39	0.42
1088B	7 - 4	92 - 94	58.43	6.0533	0.545	15.18	0.35
1088B	7 - 4	116 - 118	58.67	6.0756	0.540	15.03	0.28
1088B	7 - 4	128 - 129	58.79	6.0862	0.563	15.73	0.36
1088B	7 - 4	136 - 138	58.87	6.0941	0.536	14.91	0.21

Appendix B Alkenone Indices from ODP Sites 883, 884, 887, 907, 982, 1088

Core	Section	Interval (cm)	MCD (m)	Age(Ma)	UK'37	SST (°C) M	[C37] total (nmol/g)
1088B	7 - 5	8 - 10	59.09	6.1144	0.533	14.82	0.33
1088B	7 - 5	20 - 21	59.21	6.1251	0.585	16.39	0.18
1088B	7 - 5	44 - 45	59.45	6.1472	0.508	14.06	0.35
1088B	7 - 5	56 - 58	59.57	6.1587	0.538	14.97	0.24
1088B	7 - 5	66 - 67	59.67	6.1674	0.583	16.33	0.27
1088B	7 - 5	80 - 81	59.81	6.1802	0.581	16.27	0.36
1088B	7 - 5	92 - 93	59.93	6.1912	0.562	15.70	0.28
1088B	7 - 5	101.5 - 102.5	60.02	6.1999	0.561	15.67	0.30
1088B	7 - 5	128 - 129	60.29	6.2242	0.547	15.24	0.26
1088B	7 - 5	142 - 143	60.43	6.2369	0.582	16.30	0.22
1088B	7 - 6	8 - 10	60.59	6.2520	0.594	16.67	0.31
1088B	7 - 6	20 - 22	60.71	6.2629	0.585	16.39	0.26
1088B	7 - 6	29 - 31	60.80	6.2711	0.573	16.03	0.23
1088B	7 - 6	50 - 52	61.01	6.2901	0.576	16.12	0.29
1088B	7 - 6	70 - 72	61.21	6.3082	0.571	15.97	0.25
1088B	7 - 6	80 - 82	61.31	6.3173	0.593	16.64	0.37
1088B	7 - 6	92 - 94	61.43	6.3281	0.590	16.55	0.31
1088B	7 - 6	104 - 106	61.55	6.3390	0.590	16.55	0.28
1088B	7 - 6	116 - 118	61.67	6.3498	0.584	16.36	0.24
1088B	7 - 6	140 - 142	61.91	6.3714	0.593	16.64	0.33
1088B	8 - 1	24 - 26	62.75	6.4465	0.600	16.85	0.74
1088B	8 - 1	36 - 38	62.87	6.4572	0.547	15.24	0.53
1088B	8 - 1	47 - 49	62.98	6.4670	0.615	17.30	0.19
1088B	8 - 1	60 - 62	63.11	6.4785	0.596	16.73	0.22
1088B	8 - 1	72 - 74	63.23	6.4892	0.638	18.00	0.17
1088B	8 - 1	84 - 86	63.35	6.4998	0.591	16.58	0.17
1088B	8 - 1	108 - 110	63.59	6.5210	0.525	14.58	0.17
1088B	8 - 1	120 - 122	63.71	6.5316	0.620	17.45	0.15
1088B	8 - 1	132 - 134	63.83	6.5422	0.592	16.61	0.39
1088B	8 - 1	144 - 146	63.95	6.5527	0.557	15.55	0.17
1088B	8 - 2	9.5 - 11.5	64.11	6.5664	0.633	17.85	0.24
1088B	8 - 2	22 - 24	64.23	6.5773	0.599	16.82	0.19
1088B	8 - 2	46 - 48	64.47	6.5984	0.631	17.79	0.26
1088B	8 - 2	58 - 60	64.59	6.6089	0.619	17.42	0.31
1088B	8 - 2	70 - 72	64.71	6.6193	0.633	17.85	0.27
1088B	8 - 2	82 - 84	64.83	6.6298	0.645	18.21	0.30
1088B	8 - 2	94 - 96	64.95	6.6403	0.619	17.42	0.32
1088B	8 - 2	118 - 120	65.19	6.6611	0.592	16.61	0.40
1088B	8 - 2	130 - 132	65.31	6.6715	0.628	17.70	0.27
1088B	8 - 2	142 - 144	65.43	6.6819	0.605	17.00	0.23
1088B	8 - 3	10 - 12	65.61	6.6975	0.623	17.55	0.22
1088B	8 - 3	22 - 24	65.73	6.7079	0.660	18.67	0.24
1088B	8 - 3	46 - 48	65.97	6.7285	0.637	17.97	0.25
1088B	8 - 3	58 - 60	66.09	6.7389	0.579	16.21	0.20
1088B	8 - 3	70 - 72	66.21	6.7492	0.669	18.94	0.14
1088B	8 - 3	82 - 84	66.33	6.7595	0.635	17.91	0.31
1088B	8 - 3	94 - 96	66.45	6.7698	0.584	16.36	0.28
1088B	8 - 3	118 - 120	66.69	6.7903	0.734	20.91	0.19
1088B	8 - 3	130 - 132	66.81	6.8005	0.720	20.48	0.23
1088B	8 - 3	142 - 144	66.93	6.8107	0.672	19.03	0.23

Appendix B Alkenone Indices from ODP Sites 883, 884, 887, 907, 982, 1088

Core	Section	Interval (cm)	MCD (m)	Age(Ma)	UK'37	SST (°C) M	[C37] total (nmol/g)
1088B	8 - 4	10 - 12	67.11	6.8260	0.679	19.24	0.14
1088B	8 - 4	22 - 24	67.23	6.8362	0.661	18.70	0.09
1088B	8 - 4	46 - 48	67.47	6.8566	0.705	20.03	0.12
1088B	8 - 4	58 - 60	67.59	6.8667	0.686	19.45	0.10
1088B	8 - 4	70 - 72	67.71	6.8769	0.646	18.24	0.16
1088B	8 - 4	82 - 84	67.83	6.8870	0.692	19.64	0.10
1088B	8 - 4	92 - 94	67.93	6.8954	0.667	18.88	0.12
1088B	8 - 4	118 - 120	68.19	6.9173	0.702	19.94	0.16
1088B	8 - 4	130 - 132	68.31	6.9273	0.681	19.30	0.14
1088B	8 - 4	140 - 142	68.41	6.9357	0.668	18.91	0.15
1088B	8 - 5	10 - 12	68.61	6.9524	0.662	18.73	0.13
1088B	8 - 5	22 - 24	68.73	6.9624	0.653	18.45	0.23
1088B	8 - 5	46 - 48	68.97	6.9824	0.610	17.15	0.19
1088B	8 - 5	58 - 60	69.09	6.9924	0.634	17.88	0.28
1088B	8 - 5	70 - 72	69.21	7.0023	0.681	19.30	0.13
1088B	8 - 5	82 - 84	69.33	7.0123	0.685	19.42	0.12
1088B	8 - 5	94 - 96	69.45	7.0222	0.649	18.33	0.21
1088B	8 - 5	118 - 120	69.69	7.0420	0.617	17.36	0.13
1088B	8 - 5	128 - 130	69.79	7.0503	0.696	19.76	0.06
1088B	8 - 5	139 - 141	69.90	7.0593	0.684	19.39	0.06
1088B	8 - 6	10 - 12	70.11	7.0766	0.681	19.30	0.08
1088B	8 - 6	28.5 - 30.5	70.30	7.0917	0.604	16.97	0.15
1088B	8 - 6	46 - 48	70.47	7.1060	0.692	19.64	0.09
1088B	8 - 6	58 - 60	70.59	7.1158	0.603	16.94	0.22
1088B	8 - 6	70 - 72	70.71	7.1256	0.653	18.45	0.17
1088B	8 - 6	83 - 85	70.84	7.1362	0.657	18.58	0.15
1088B	8 - 6	94 - 96	70.95	7.1451	0.634	17.88	0.13
1088B	8 - 6	106 - 108	71.07	7.1549	0.663	18.76	0.07
1088B	8 - 6	130 - 132	71.31	7.1743	0.691	19.61	0.09
1088B	9 - 1	20 - 22	72.21	7.2466	0.610	17.15	0.15
1088B	9 - 1	32 - 34	72.33	7.2562	0.628	17.70	0.11
1088B	9 - 1	44 - 46	72.45	7.2658	0.684	19.39	0.09
1088B	9 - 1	56 - 58	72.57	7.2753	0.708	20.12	0.09
1088B	9 - 1	68 - 70	72.69	7.2849	0.650	18.36	0.12
1088B	9 - 1	80 - 82	72.81	7.2944	0.653	18.45	0.15
1088B	9 - 1	92 - 94	72.93	7.3039	0.665	18.82	0.08
1088B	9 - 1	104 - 106	73.05	7.3134	0.702	19.94	0.11
1088B	9 - 1	116 - 118	73.17	7.3229	0.657	18.58	0.16
1088B	9 - 1	130 - 132	73.31	7.3339	0.744	21.21	0.05
1088B	9 - 2	54 - 56	74.05	7.3919	0.741	21.12	0.09
1088B	9 - 2	84 - 86	74.35	7.4153	0.710	20.18	0.15
1088B	9 - 2	121 - 123	74.72	7.4440	0.661	18.70	0.22
1088B	9 - 3	64 - 66	75.65	7.5155	0.767	21.91	0.05
1088B	9 - 4	94 - 96	77.45	7.6512	0.693	19.67	0.22
1088B	9 - 4	130 - 132	77.81	7.6780	0.744	21.21	0.04
1088B	9 - 5	91 - 93	78.92	7.7596	0.771	22.03	0.04

APPENDIX C

ALKENONE INDICES FROM IODP SITE U1387

Appendix C Alkenone Indices from IODP Site U1387

Core	Section	Interval (cm)	mbsf (m)	Age(Ma)	UK'37	SST (°C) M	[C37] total (nmol/g)
1387C	19 - R	4 - 47	457.98	2.6840	0.892	25.68	4.11
1387C	19 - R	4 - 68	458.19	2.6860	0.892	25.71	3.89
1387C	19 - R	4 - 88	458.39	2.6890	0.883	25.42	3.47
1387C	20 - R	1 - 40	463.00	2.6960	0.905	26.10	0.45
1387C	20 - R	1 - 60	463.20	2.7000	0.901	25.98	1.15
1387C	20 - R	1 - 78	463.38	2.7000	0.901	25.97	3.64
1387C	20 - R	1 - 95	463.55	2.7020	0.907	26.16	3.81
1387C	20 - R	1 - 120	463.80	2.7050	0.910	26.24	3.03
1387C	20 - R	1 - 140	464.00	2.7080	0.915	26.38	2.68
1387C	20 - R	2 - 2	464.13	2.7090	0.917	26.46	4.12
1387C	20 - R	2 - 23	464.34	2.7096	0.910	26.24	4.56
1387C	20 - R	2 - 45	464.56	2.7120	0.913	26.32	4.09
1387C	20 - R	2 - 65	464.76	2.7120	0.913	26.33	3.36
1387C	20 - R	2 - 86	464.97	2.7150	0.913	26.33	3.53
1387C	20 - R	2 - 104	465.15	2.7160	0.921	26.58	2.93
1387C	20 - R	2 - 123	465.34	2.7165	0.924	26.67	2.38
1387C	20 - R	2 - 141	465.52	2.7180	0.916	26.42	1.29
1387C	20 - R	3 - 10	465.70	2.7200	0.911	26.28	0.68
1387C	20 - R	3 - 28	465.88	2.7250	0.922	26.62	3.58
1387C	20 - R	3 - 57	466.17	2.7280	0.925	26.70	3.07
1387C	20 - R	3 - 70	466.30	2.7310	0.929	26.83	2.70
1387C	20 - R	3 - 110	466.70	2.7340	0.925	26.69	2.15
1387C	20 - R	3 - 128	466.88	2.7380	0.928	26.78	1.45
1387C	20 - R	4 - 10	467.21	2.7490	0.924	26.67	1.33
1387C	20 - R	4 - 30	467.41	2.7500	0.911	26.26	0.80
1387C	20 - R	4 - 53	467.64	2.7540	0.931	26.87	3.91
1387C	20 - R	4 - 70	467.81	2.7580	0.932	26.91	3.37
1387C	20 - R	4 - 90	468.01	2.7600	0.928	26.79	3.70
1387C	20 - R	4 - 110	468.21	2.7660	0.939	27.12	3.17
1387C	20 - R	4 - 130	468.41	2.7670	0.936	27.04	2.13
1387C	20 - R	4 - 148	468.59	2.7690	0.929	26.82	1.52
1387C	20 - R	5 - 10	468.70	2.7700	0.930	26.86	1.21
1387C	20 - R	5 - 30	468.90	2.7720	0.926	26.74	1.27
1387C	20 - R	5 - 50	469.10	2.7740	0.926	26.71	1.09
1387C	20 - R	5 - 68	469.28	2.7750	0.914	26.36	1.14
1387C	20 - R	5 - 110	469.70	2.7790	0.932	26.90	3.18
1387C	20 - R	5 - 130	469.90	2.7810	0.923	26.64	2.81
1387C	20 - R	6 - 10	470.21	2.7840	0.923	26.65	3.29
1387C	20 - R	6 - 30	470.41	2.7860	0.909	26.22	3.05
1387C	20 - R	6 - 50	470.61	2.7880	0.904	26.06	1.67
1387C	20 - R	6 - 70	470.81	2.7900	0.892	25.68	2.38
1387C	20 - R	6 - 90	471.01	2.7910	0.884	25.46	0.86
1387C	20 - R	6 - 110	471.21	2.7930	0.892	25.68	0.84
1387C	20 - R	6 - 148	471.59	2.7970	0.954	27.59	3.38
1387C	20 - R	7 - 10	471.70	2.7980	0.952	27.51	3.43
1387C	20 - R	7 - 48	472.08	2.8010	0.955	27.61	2.65
1387C	20 - R	7 - 68	472.28	2.8030	0.949	27.42	2.75
1387C	21 - R	1 - 8	472.28	2.8030	0.943	27.25	2.63
1387C	21 - R	1 - 48	472.68	2.8070	0.938	27.09	0.91
1387C	21 - R	1 - 68	472.89	2.8090	0.937	27.06	0.90

Appendix C Alkenone Indices from IODP Site U1387

Core	Section	Interval (cm)	mbsf (m)	Age(Ma)	UK'37	SST (°C) PW	SST (°C) M	[C37] total (nmol/g)
1387C	21 - R	1 - 86	473.06	2.8100	0.916	25.81	26.44	0.97
1387C	21 - R	1 - 126	473.46	2.8140	0.905	25.48	26.10	0.52
1387C	21 - R	1 - 148	473.68	2.8360	0.942	26.43	27.08	1.47
1387C	21 - R	2 - 10	473.81	2.8370	0.944	26.60	27.26	1.56
1387C	21 - R	2 - 30	474.01	2.8390	0.937	26.43	27.08	1.48
1387C	21 - R	2 - 50	474.21	2.8410	0.934	26.33	26.98	1.35
1387C	21 - R	2 - 70	474.40	2.8430	0.923	25.99	26.62	1.43
1387C	21 - R	2 - 90	474.61	2.8450	0.928	26.13	26.77	1.08
1387C	21 - R	2 - 110	474.81	2.8460	0.932	26.28	26.92	0.86
1387C	21 - R	2 - 130	475.01	2.8480	0.920	25.91	26.54	1.02
1387C	21 - R	2 - 148	475.19	2.8500	0.928	26.16	26.80	0.94
1387C	21 - R	3 - 10	475.30	2.8510	0.926	26.09	26.73	0.97
1387C	21 - R	3 - 30	475.51	2.8530	0.898	25.27	25.88	3.57
1387C	21 - R	3 - 50	475.70	2.8550	0.927	26.11	26.75	0.97
1387C	21 - R	3 - 68	475.88	2.8560	0.932	26.27	26.91	1.08
1387C	21 - R	3 - 110	476.30	2.8730	0.930	26.21	26.85	0.65
1387C	21 - R	3 - 130	476.50	2.8750	0.924	25.98	26.62	1.14
1387C	21 - R	3 - 148	476.68	2.8770	0.926	26.08	26.71	1.38
1387C	21 - R	4 - 10	476.81	2.8780	0.930	26.19	26.83	1.53
1387C	21 - R	4 - 30	477.01	2.8800	0.931	26.23	26.87	1.51
1387C	21 - R	4 - 52	477.23	2.8820	0.923	25.99	26.63	1.51
1387C	21 - R	4 - 67	477.38	2.8830	0.929	26.19	26.83	1.51
1387C	21 - R	4 - 90	477.61	2.8850	0.930	26.20	26.85	1.18
1387C	21 - R	4 - 110	477.81	2.8870	0.926	26.07	26.71	1.28
1387C	21 - R	4 - 130	478.01	2.8890	0.924	26.04	26.68	1.34
1387C	21 - R	4 - 148	478.19	2.8900	0.926	26.08	26.72	1.21
1387C	21 - R	5 - 10	478.30	2.9010	0.916	25.78	26.41	1.19
1387C	21 - R	5 - 30	478.50	2.9015	0.918	25.87	26.50	1.44
1387C	21 - R	5 - 50	478.70	2.9020	0.918	25.86	26.49	1.27
1387C	21 - R	5 - 90	478.90	2.9025	0.907	25.52	26.14	1.22
1387C	21 - R	5 - 70	478.91	2.9028	0.915	25.78	26.41	1.27
1387C	21 - R	1 - 28	479.28	2.9040	0.940	26.49	27.14	3.73
1387C	21 - R	CC - 7	479.28	2.9060	0.933	26.31	26.95	2.38
1387C	22 - R	1 - 51	482.31	2.9080	0.910	25.61	26.24	1.43
1387C	22 - R	1 - 71	482.51	2.9100	0.908	25.56	26.18	1.27
1387C	22 - R	1 - 91	482.71	2.9130	0.897	25.24	25.85	0.95
1387C	22 - R	1 - 113	482.93	2.9240	0.935	26.34	26.99	4.12
1387C	22 - R	1 - 136	483.16	2.9260	0.935	26.36	27.00	3.79
1387C	22 - R	2 - 10	483.40	2.9380	0.930	26.22	26.86	2.76
1387C	22 - R	2 - 30	483.60	2.9440	0.926	26.10	26.74	4.21
1387C	22 - R	2 - 50	483.80	2.9460	0.920	25.92	26.55	5.24
1387C	22 - R	2 - 69	483.99	2.9480	0.921	25.95	26.58	2.12
1387C	22 - R	2 - 110	484.40	2.9520	0.930	26.20	26.84	2.59
1387C	22 - R	2 - 130	484.60	2.9530	0.934	26.34	26.98	2.87
1387C	22 - R	3 - 35	485.15	2.9520	0.921	25.93	26.57	1.88
1387C	22 - R	3 - 56	485.36	2.9540	0.913	25.71	26.34	1.53
1387C	22 - R	3 - 76	485.56	2.9560	0.915	25.76	26.39	1.26
1387C	22 - R	3 - 94	485.74	2.9580	0.918	25.85	26.48	1.43
1387C	22 - R	3 - 112	485.92	2.9600	0.915	25.75	26.38	1.06
1387C	22 - R	3 - 133	486.13	2.9610	0.919	25.89	26.52	1.85

Appendix C Alkenone Indices from IODP Site U1387

Core	Section	Interval (cm)	mbsf (m)	Age(Ma)	UK'37	SST (°C) M	[C37] total (nmol/g)
1387C	22 - R	4 - 10	486.40	2.9640	0.921	26.58	1.60
1387C	22 - R	4 - 28	486.58	2.9660	0.919	26.51	5.16
1387C	22 - R	4 - 50	486.80	2.9680	0.929	26.81	3.01
1387C	22 - R	4 - 72	487.02	2.9700	0.909	26.22	4.34
1387C	22 - R	4 - 91	487.21	2.9710	0.916	26.43	5.29
1387C	22 - R	4 - 132	487.62	2.9690	0.904	26.06	4.60
1387C	22 - R	5 - 1	487.81	2.9710	0.908	26.19	2.30
1387C	22 - R	5 - 21	488.01	2.9730	0.899	25.90	1.62
1387C	22 - R	5 - 37	488.17	2.9740	0.890	25.62	1.38
1387C	22 - R	5 - 58	488.39	2.9760	0.889	25.59	1.15
1387C	22 - R	2 - 69	488.49	2.9770	0.917	26.45	2.19
1387C	22 - R	5 - 78	488.58	2.9780	0.873	25.11	0.46
1387C	22 - R	5 - 99	488.79	2.9800	0.903	26.03	0.65
1387C	22 - R	6 - 8	489.08	2.9830	0.869	24.99	0.59
1387C	22 - R	6 - 30	489.30	2.9850	0.883	25.41	1.03
1387C	22 - R	6 - 50	489.50	2.9870	0.894	25.75	1.46
1387C	23 - R	1 - 18	491.58	3.0160	0.916	26.43	4.44
1387C	23 - R	1 - 38	491.79	3.0180	0.927	26.75	0.83
1387C	23 - R	1 - 58	491.98	3.0190	0.905	26.08	2.57
1387C	23 - R	1 - 78	492.19	3.0210	0.900	25.95	4.23
1387C	23 - R	1 - 96	492.36	3.0230	0.905	26.08	1.67
1387C	23 - R	1 - 118	492.58	3.0250	0.890	25.62	1.10
1387C	23 - R	1 - 138	492.78	3.0270	0.885	25.47	0.87
1387C	23 - R	2 - 10	493.00	3.0290	0.878	25.27	0.60
1387C	23 - R	2 - 30	493.20	3.0310	0.906	26.11	0.52
1387C	23 - R	2 - 50	493.40	3.0320	0.941	27.19	3.72
1387C	23 - R	2 - 69	493.59	3.0340	0.935	27.00	3.51
1387C	23 - R	2 - 90	493.81	3.0360	0.939	27.14	2.24
1387C	23 - R	2 - 110	494.00	3.0380	0.931	26.88	2.98
1387C	23 - R	2 - 130	494.20	3.0460	0.924	26.66	1.98
1387C	23 - R	2 - 148	494.39	3.0470	0.910	26.25	1.31
1387C	23 - R	3 - 19	494.59	3.0570	0.932	26.91	3.23
1387C	23 - R	3 - 36	494.76	3.0590	0.939	27.13	2.88
1387C	23 - R	3 - 58	494.99	3.0610	0.934	26.96	3.71
1387C	23 - R	3 - 80	495.20	3.0630	0.937	27.07	2.00
1387C	23 - R	3 - 101	495.41	3.0650	0.939	27.11	1.47
1387C	23 - R	3 - 120	495.60	3.0670	0.929	26.82	0.73
1387C	23 - R	3 - 140	495.80	3.0680	0.924	26.66	0.80
1387C	23 - R	4 - 15	496.05	3.0710	0.911	26.26	0.89
1387C	23 - R	4 - 42	496.32	3.0730	0.931	26.89	1.29
1387C	23 - R	4 - 62	496.52	3.0740	0.942	27.20	4.16
1387C	23 - R	4 - 84	496.74	3.0750	0.945	27.30	3.52
1387C	23 - R	4 - 104	496.94	3.0760	0.935	27.00	3.28
1387C	23 - R	4 - 124	497.14	3.0770	0.934	26.95	3.96
1387C	23 - R	5 - 14	497.54	3.0790	0.937	27.06	3.65
1387C	23 - R	5 - 32	497.72	3.0800	0.930	26.83	4.59
1387C	23 - R	5 - 54	497.94	3.0850	0.930	26.85	2.82
1387C	23 - R	5 - 71	498.12	3.0860	0.932	26.92	3.74
1387C	23 - R	5 - 92	498.32	3.0910	0.927	26.76	3.69
1387C	23 - R	5 - 112	498.52	3.0930	0.925	26.71	3.86

Appendix C Alkenone Indices from IODP Site U1387

Core	Section	Interval (cm)	mbsf (m)	Age(Ma)	UK'37	SST (°C) PW	SST (°C) M	[C37] total (nmol/g)
1387C	23 - R	5 - 132	498.72	3.0940	0.920	25.91	26.54	1.39
1387C	23 - R	6 - 2	498.92	3.0950	0.905	25.47	26.09	1.15
1387C	23 - R	6 - 22	499.12	3.1070	0.909	25.57	26.20	0.97
1387C	23 - R	6 - 42	499.32	3.1090	0.906	25.50	26.12	0.93
1387C	23 - R	6 - 62	499.52	3.1110	0.906	25.48	26.11	0.79
1387C	24 - R	1 - 3	501.03	3.1170	0.890	25.02	25.62	0.85
1387C	24 - R	1 - 27	501.27	3.1190	0.894	25.16	25.77	0.44
1387C	24 - R	1 - 49	501.49	3.1210	0.893	25.20	25.81	0.50
1387C	24 - R	1 - 66	501.67	3.1220	0.903	25.41	26.03	0.66
1387C	24 - R	1 - 87	501.87	3.1240	0.918	25.86	26.49	1.06
1387C	24 - R	1 - 108	502.08	3.1260	0.922	25.97	26.61	1.48
1387C	24 - R	1 - 128	502.28	3.1280	0.925	26.07	26.71	4.25
1387C	24 - R	1 - 145	502.45	3.1300	0.924	26.03	26.66	5.31
1387C	24 - R	2 - 16	502.66	3.1320	0.926	26.08	26.72	5.29
1387C	24 - R	2 - 36	502.86	3.1330	0.929	26.19	26.83	5.63
1387C	24 - R	2 - 56	503.06	3.1350	0.929	26.17	26.81	5.03
1387C	24 - R	2 - 73	503.23	3.1370	0.932	26.25	26.90	4.67
1387C	24 - R	2 - 93	503.43	3.1390	0.932	26.25	26.90	3.39
1387C	24 - R	2 - 113	503.64	3.1410	0.915	25.77	26.40	1.33
1387C	24 - R	2 - 131	503.81	3.1420	0.921	25.95	26.58	0.96
1387C	24 - R	3 - 1	504.01	3.1440	0.918	25.84	26.47	0.83
1387C	24 - R	3 - 21	504.21	3.1460	0.938	26.45	27.10	4.44
1387C	24 - R	3 - 41	504.41	3.1480	0.949	26.78	27.44	3.75
1387C	24 - R	3 - 63	504.64	3.1500	0.949	26.76	27.42	2.03
1387C	24 - R	3 - 86	504.86	3.1520	0.944	26.63	27.28	3.94
1387C	24 - R	3 - 106	505.06	3.1540	0.941	26.52	27.17	3.63
1387C	24 - R	3 - 126	505.26	3.1550	0.942	26.56	27.21	3.32
1387C	24 - R	4 - 15	505.65	3.1590	0.935	26.34	26.99	3.20
1387C	24 - R	4 - 35	505.85	3.1610	0.936	26.39	27.03	1.27
1387C	24 - R	4 - 55	506.05	3.1630	0.925	26.07	26.71	0.70
1387C	24 - R	4 - 75	506.25	3.1750	0.939	26.48	27.13	4.54
1387C	24 - R	4 - 93	506.43	3.1760	0.938	26.45	27.10	4.41
1387C	24 - R	4 - 113	506.64	3.1780	0.936	26.39	27.04	4.20
1387C	24 - R	4 - 134	506.84	3.1790	0.939	26.47	27.12	3.98
1387C	24 - R	5 - 12	507.12	3.1800	0.938	26.45	27.10	4.09
1387C	24 - R	5 - 32	507.32	3.1820	0.939	26.47	27.12	1.43
1387C	24 - R	5 - 52	507.53	3.1835	0.930	26.11	26.75	1.25
1387C	24 - R	5 - 70	507.70	3.1880	0.920	25.91	26.54	0.79
1387C	24 - R	5 - 90	507.90	3.1935	0.937	26.42	27.07	2.59
1387C	24 - R	5 - 108	508.08	3.1960	0.911	25.64	26.27	1.16
1387C	24 - R	5 - 128	508.28	3.1970	0.904	25.45	26.07	0.90
1387C	24 - R	5 - 145	508.46	3.1980	0.899	25.29	25.90	0.73
1387C	24 - R	6 - 13	508.63	3.1985	0.946	26.66	27.32	3.38
1387C	24 - R	6 - 32	508.82	3.1995	0.945	26.64	27.29	3.58
1387C	24 - R	6 - 52	509.03	3.2000	0.943	26.58	27.23	3.87
1387C	24 - R	6 - 69	509.19	3.2020	0.940	26.51	27.16	3.62
1387C	24 - R	6 - 89	509.39	3.2030	0.940	26.49	27.14	2.87
1387C	24 - R	6 - 109	509.59	3.2050	0.943	26.59	27.24	1.63
1387C	24 - R	6 - 129	509.79	3.2070	0.944	26.62	27.27	1.49
1387C	24 - R	CC - 8	509.99	3.2090	0.930	26.22	26.86	1.42

Appendix C Alkenone Indices from IODP Site U1387

Core	Section	Interval (cm)	mbsf (m)	Age(Ma)	UK'37	SST (°C) M	[C37] total (nmol/g)
1387C	25 - R	1 - 8	510.68	3.2150	0.937	27.06	0.94
1387C	25 - R	1 - 28	510.88	3.2170	0.939	27.13	1.31
1387C	25 - R	1 - 48	511.08	3.2190	0.933	26.94	1.32
1387C	25 - R	1 - 68	511.29	3.2210	0.939	27.11	1.27
1387C	25 - R	1 - 88	511.48	3.2230	0.937	27.05	1.48
1387C	25 - R	1 - 109	511.69	3.2250	0.933	26.93	1.73
1387C	25 - R	1 - 129	511.89	3.2260	0.934	26.97	1.35
1387C	25 - R	1 - 148	512.09	3.2280	0.925	26.71	1.23
1387C	25 - R	2 - 18	512.28	3.2300	0.933	26.94	1.26
1387C	25 - R	2 - 38	512.48	3.2320	0.933	26.94	1.35
1387C	25 - R	2 - 58	512.68	3.2340	0.932	26.92	1.16
1387C	25 - R	2 - 78	512.88	3.2360	0.934	26.98	0.97
1387C	25 - R	2 - 98	513.08	3.2370	0.931	26.89	0.83
1387C	25 - R	2 - 118	513.29	3.2390	0.930	26.85	1.00
1387C	25 - R	2 - 138	513.48	3.2410	0.941	27.18	1.79
1387C	25 - R	3 - 22	513.82	3.2440	0.951	27.48	4.81
1387C	25 - R	3 - 42	514.02	3.2460	0.949	27.43	3.81
1387C	25 - R	3 - 62	514.23	3.2515	0.857	24.63	4.40
1387C	25 - R	3 - 85	514.45	3.2535	0.939	27.13	4.88
1387C	25 - R	3 - 102	514.62	3.2545	0.944	27.26	4.53
1387C	25 - R	3 - 122	514.82	3.2555	0.942	27.23	4.06
1387C	25 - R	4 - 12	515.22	3.2570	0.930	26.85	1.47
1387C	25 - R	4 - 33	515.43	3.2590	0.931	26.89	1.12
1387C	25 - R	4 - 53	515.63	3.2610	0.933	26.93	0.81
1387C	25 - R	4 - 73	515.83	3.2630	0.920	26.55	0.85
1387C	25 - R	4 - 93	516.04	3.2650	0.943	27.24	2.72
1387C	25 - R	4 - 113	516.23	3.2660	0.940	27.17	4.11
1387C	25 - R	4 - 133	516.43	3.2690	0.942	27.21	3.06
1387C	25 - R	5 - 3	516.63	3.2760	0.947	27.35	0.60
1387C	25 - R	5 - 23	516.83	3.2760	0.943	27.25	4.01
1387C	25 - R	5 - 43	517.03	3.2810	0.941	27.18	3.52
1387C	25 - R	5 - 63	517.24	3.2820	0.949	27.43	5.57
1387C	25 - R	5 - 83	517.43	3.2830	0.942	27.22	3.66
1387C	25 - R	5 - 103	517.63	3.2840	0.933	26.95	3.81
1387C	25 - R	5 - 123	517.83	3.2850	0.940	27.15	3.60
1387C	25 - R	5 - 143	518.04	3.2860	0.935	27.01	1.92
1387C	25 - R	6 - 3	518.13	3.2870	0.941	27.18	3.32
1387C	25 - R	6 - 25	518.35	3.2870	0.937	27.07	3.15
1387C	25 - R	6 - 43	518.53	3.2890	0.940	27.15	1.86
1387C	25 - R	6 - 63	518.74	3.2900	0.926	26.73	0.82
1387C	25 - R	6 - 84	518.94	3.2910	0.929	26.83	0.81
1387C	25 - R	6 - 102	519.12	3.2930	0.922	26.61	0.85
1387C	25 - R	6 - 112	519.23	3.2940	0.916	26.43	0.65
1387C	25 - R	6 - 131	519.41	3.3010	0.936	27.02	3.30
1387C	25 - R	7 - 3	519.43	3.3010	0.942	27.22	2.41
1387C	25 - R	7 - 24	519.64	3.3060	0.931	26.88	3.38
1387C	25 - R	7 - 64	520.04	3.3100	0.921	26.59	1.28
1387C	25 - R	7 - 43	520.04	3.3100	0.925	26.71	3.07
1387C	26 - R	1 - 63	520.54	3.3180	0.941	27.20	3.90
1387C	26 - R	3 - 63	523.54	3.3330	0.924	26.66	1.17

Appendix C Alkenone Indices from IODP Site U1387

Core	Section	Interval (cm)	mbsf (m)	Age(Ma)	UK'37	SST (°C) PW	SST (°C) M	[C37] total (nmol/g)
1387C	26 - R	4 - 63	525.04	3.3440	0.939	26.47	27.12	4.50
1387C	27 - R	1 - 63	530.14	3.3990	0.905	25.48	26.10	1.72
1387C	27 - R	3 - 63	533.14	3.3990	0.938	26.45	27.10	0.71
1387C	27 - R	5 - 63	536.14	3.3990	0.962	27.15	27.82	2.40
1387C	27 - R	7 - 55	539.06	3.4810	0.957	27.01	27.68	2.89
1387C	28 - R	1 - 62	539.73	3.4880	0.955	26.94	27.60	1.43
1387C	28 - R	1 - 123	540.34	3.4930	0.934	26.32	26.97	1.11
1387C	28 - R	3 - 8	542.19	3.5100	0.968	27.33	28.01	3.30
1387C	28 - R	5 - 15	545.26	3.5380	0.933	26.29	26.94	0.88
1387C	29 - R	1 - 0	548.71	3.5700	0.908	25.55	26.17	2.53
1387C	29 - R	1 - 61	549.32	3.5760	0.954	26.91	27.58	0.69
1387C	29 - R	1 - 116	549.87	3.5810	0.957	27.00	27.66	2.53
1387C	29 - R	2 - 4	550.24	3.5840	0.957	26.99	27.66	2.08
1387C	29 - R	2 - 62	550.62	3.5880	0.938	26.44	27.09	0.63
1387C	29 - R	3 - 14	551.84	3.5990	0.969	27.36	28.04	1.16
1387C	29 - R	3 - 54	552.25	3.6030	0.958	27.03	27.70	4.26
1387C	29 - R	3 - 79	552.49	3.6050	0.966	27.26	27.94	1.87
1387C	29 - R	4 - 69	553.90	3.6180	0.955	26.95	27.62	2.05
1387C	29 - R	5 - 18	554.88	3.6270	0.930	26.20	26.85	0.80
1387C	29 - R	5 - 59	555.30	3.6310	0.952	26.84	27.51	4.56
1387C	29 - R	6 - 8	556.29	3.6400	0.946	26.66	27.32	1.53
1387C	29 - R	6 - 68	556.89	3.6450	0.950	26.80	27.46	0.98
1387C	29 - R	7 - 6	557.77	3.6540	0.950	26.78	27.44	3.36
1387C	29 - R	7 - 46	558.17	3.6570	0.951	26.83	27.49	4.19
1387C	29 - R	7 - 66	558.37	3.6590	0.953	26.90	27.56	2.91
1387C	30 - R	1 - 62	558.93	3.6640	0.960	27.09	27.76	3.67
1387C	30 - R	1 - 122	559.53	3.6700	0.947	26.70	27.36	1.86
1387C	30 - R	2 - 102	560.83	3.6820	0.955	26.95	27.62	2.69
1387C	30 - R	3 - 22	561.53	3.6880	0.961	27.12	27.79	3.39
1387C	30 - R	3 - 82	562.13	3.6940	0.956	26.96	27.62	0.79
1387C	30 - R	3 - 122	562.42	3.6960	0.965	27.24	27.92	0.98
1387C	30 - R	3 - 142	562.73	3.6990	0.956	26.98	27.65	1.15
1387C	30 - R	4 - 62	563.43	3.7060	0.960	27.07	27.74	1.38
1387C	30 - R	4 - 82	563.62	3.7070	0.957	27.01	27.68	1.21
1387C	30 - R	4 - 122	564.02	3.7110	0.958	27.03	27.70	1.43
1387C	30 - R	5 - 62	564.63	3.7170	0.954	26.91	27.57	0.46
1387C	31 - R	1 - 42	568.32	3.7510	0.949	26.75	27.41	0.93
1387C	31 - R	2 - 42	568.32	3.7510	0.958	27.02	27.69	3.49
1387C	31 - R	1 - 62	568.53	3.7530	0.942	26.56	27.21	1.13
1387C	31 - R	1 - 82	568.72	3.7540	0.934	26.31	26.96	0.90
1387C	31 - R	2 - 42	569.82	3.7640	0.957	27.00	27.67	3.49
1387C	31 - R	2 - 62	570.03	3.7660	0.929	26.18	26.83	2.05
1387C	31 - R	2 - 82	570.22	3.7680	0.953	26.88	27.55	3.56
1387C	31 - R	3 - 42	571.32	3.7780	0.943	26.58	27.23	1.11
1387C	31 - R	3 - 62	571.53	3.7800	0.941	26.54	27.19	0.48
1387C	31 - R	3 - 82	571.72	3.7820	0.941	26.52	27.17	0.76
1387C	31 - R	4 - 42	572.83	3.7920	0.953	26.89	27.55	1.32
1387C	31 - R	4 - 60	573.01	3.7940	0.937	26.41	27.06	0.96
1387C	31 - R	4 - 82	573.23	3.7960	0.954	26.91	27.57	0.91
1387C	32 - R	1 - 22	577.73	3.8370	0.952	26.85	27.52	1.17

Appendix C Alkenone Indices from IODP Site U1387

Core	Section	Interval (cm)	mbsf (m)	Age(Ma)	UK'37	SST (°C) M	[C37] total (nmol/g)
1387C	32 - R	1 - 62	578.13	3.8410	0.947	27.38	0.90
1387C	32 - R	1 - 102	578.52	3.8440	0.954	27.57	1.25
1387C	32 - R	1 - 142	578.92	3.8480	0.953	27.55	1.43
1387C	32 - R	2 - 25	579.25	3.8510	0.957	27.67	1.28
1387C	32 - R	2 - 62	579.63	3.8550	0.959	27.74	1.33
1387C	32 - R	2 - 102	580.03	3.8580	0.961	27.80	1.32
1387C	32 - R	2 - 142	580.43	3.8620	0.948	27.40	1.13
1387C	32 - R	3 - 62	581.13	3.8680	0.964	27.87	2.83
1387C	32 - R	3 - 142	581.93	3.8760	0.957	27.68	0.86
1387C	32 - R	4 - 22	582.22	3.8790	0.948	27.39	0.69
1387C	32 - R	4 - 102	583.03	3.8860	0.957	27.68	2.26
1387C	32 - R	5 - 22	583.73	3.8920	0.954	27.58	3.08
1387C	32 - R	5 - 62	584.13	3.8960	0.954	27.57	1.56
1387C	32 - R	5 - 102	584.53	3.9000	0.944	27.27	0.51
1387C	32 - R	5 - 142	584.93	3.9030	0.956	27.64	2.47
1387C	32 - R	6 - 22	585.22	3.9060	0.948	27.39	2.84
1387C	32 - R	6 - 62	585.63	3.9100	0.945	27.31	1.95
1387C	32 - R	6 - 102	586.03	3.9140	0.931	26.87	0.74
1387C	33 - R	1 - 42	587.53	3.9270	0.928	26.78	0.78
1387C	33 - R	1 - 62	587.73	3.9290	0.949	27.44	1.87
1387C	33 - R	1 - 82	587.93	3.9310	0.955	27.60	2.86
1387C	33 - R	1 - 102	588.13	3.9330	0.957	27.66	3.27
1387C	33 - R	1 - 142	588.53	3.9370	0.958	27.70	3.09
1387C	33 - R	2 - 22	588.82	3.9390	0.916	26.42	2.31
1387C	33 - R	2 - 42	589.03	3.9410	0.954	27.56	3.15
1387C	33 - R	2 - 82	589.42	3.9450	0.889	25.61	2.45
1387C	33 - R	2 - 102	589.63	3.9470	0.959	27.73	1.76
1387C	33 - R	2 - 122	589.83	3.9490	0.953	27.55	0.99
1387C	33 - R	2 - 142	590.03	3.9500	0.952	27.52	1.09
1387C	33 - R	3 - 62	590.73	3.9570	0.956	27.63	2.23
1387C	33 - R	3 - 82	590.93	3.9590	0.954	27.58	2.04
1387C	33 - R	3 - 102	591.13	3.9600	0.963	27.85	2.07
1387C	33 - R	3 - 142	591.53	3.9640	0.964	27.87	1.64
1387C	33 - R	4 - 42	592.03	3.9690	0.952	27.53	2.09
1387C	33 - R	4 - 82	592.43	3.9720	0.947	27.35	2.17
1387C	33 - R	4 - 102	592.63	3.9770	0.950	27.47	1.58
1387C	33 - R	4 - 142	593.03	3.9810	0.941	27.19	0.70
1387C	33 - R	5 - 62	593.73	3.9870	0.962	27.83	3.09
1387C	33 - R	5 - 82	593.93	3.9890	0.963	27.84	3.23
1387C	33 - R	5 - 102	594.13	3.9910	0.966	27.93	2.55
1387C	33 - R	5 - 142	594.53	3.9950	0.964	27.87	4.03
1387C	33 - R	6 - 22	594.83	3.9980	0.958	27.71	4.15
1387C	33 - R	6 - 42	595.03	3.9990	0.962	27.83	3.78
1387C	33 - R	6 - 82	595.43	4.0030	0.962	27.82	3.82
1387C	33 - R	7 - 2	596.13	4.0090	0.988	28.61	3.14
1387C	34 - R	1 - 2	596.73	4.0150	0.976	28.24	3.82
1387C	34 - R	1 - 82	597.53	4.0220	0.975	28.19	3.63
1387C	34 - R	2 - 2	598.23	4.0290	0.976	28.24	0.90
1387C	34 - R	2 - 42	598.63	4.0320	0.974	28.19	3.34
1387C	34 - R	2 - 122	599.43	4.0400	0.981	28.40	2.01

Appendix C Alkenone Indices from IODP Site U1387

Core	Section	Interval (cm)	mbsf (m)	Age(Ma)	UK'37	SST (°C) PW	SST (°C) M	[C37] total (nmol/g)
1387C	35 - R	3 - 105	610.36	4.1400	0.977	27.58	28.26	3.29
1387C	35 - R	5 - 85	613.16	4.1660	0.977	27.58	28.27	5.81
1387C	36 - R	3 - 85	619.76	4.2270	0.963	27.18	27.85	1.00
1387C	38 - R	5 - 2	629.13	4.3130	0.960	27.09	27.76	2.69
1387C	38 - R	5 - 20	629.31	4.3150	0.971	27.43	28.10	1.15
1387C	38 - R	5 - 70	629.81	4.3190	0.955	26.94	27.60	0.33
1387C	38 - R	5 - 88	629.99	4.3210	0.963	27.19	27.86	0.63
1387C	37 - R	4 - 115	631.16	4.3320	0.920	25.92	26.55	0.68
1387C	38 - R	5 - 125	642.36	4.4350	0.953	26.88	27.54	0.82
1387C	39 - R	2 - 120	647.41	4.4810	0.971	27.42	28.10	1.03
1387C	39 - R	2 - 148	647.69	4.4840	0.960	27.09	27.76	0.77
1387C	39 - R	4 - 95	650.16	4.5070	0.946	26.68	27.34	0.49
1387C	40 - R	1 - 13	654.44	4.5460	0.939	26.67	27.33	0.24
1387C	40 - R	2 - 63	656.44	4.5640	0.954	26.92	27.58	0.51
1387C	40 - R	3 - 133	658.64	4.5850	0.967	27.30	27.97	0.75
1387C	40 - R	4 - 83	659.64	4.5940	0.967	27.31	27.98	0.95
1387C	40 - R	5 - 93	661.24	4.6090	0.978	27.60	28.29	1.00
1387C	40 - R	6 - 23	662.04	4.6160	0.973	27.48	28.16	0.54
1387C	41 - R	1 - 103	664.94	4.6430	0.945	26.64	27.29	0.82
1387C	42 - R	1 - 53	674.04	4.7260	0.950	26.78	27.44	0.71
1387C	42 - R	2 - 143	676.44	4.7480	0.960	27.09	27.76	0.64
1387C	42 - R	4 - 43	678.44	4.7670	0.953	26.88	27.54	0.77
1387C	42 - R	5 - 33	679.84	4.7800	0.940	26.49	27.14	0.44
1387C	42 - R	6 - 83	681.84	4.7980	0.942	26.56	27.21	0.55
1387C	43 - R	1 - 42	683.63	4.8140	0.975	27.53	28.21	0.96
1387C	43 - R	2 - 73	685.44	4.8310	0.982	27.73	28.42	2.86
1387C	44 - R	1 - 3	692.94	4.9000	0.970	27.39	28.07	0.15
1387C	44 - R	1 - 23	693.14	4.9020	0.970	27.39	28.07	0.40
1387C	46 - R	CC - 1	712.02	5.0760	0.938	26.43	27.08	0.01
1387C	47 - R	1 - 43	722.04	5.1680	0.952	26.86	27.52	0.57
1387C	48 - R	1 - 95	732.16	5.2610	0.967	27.29	27.97	0.80
1387C	48 - R	2 - 95	733.66	5.2750	0.971	27.41	28.09	2.25
1387C	48 - R	3 - 65	734.86	5.2860	0.972	27.44	28.12	0.54
1387C	48 - R	4 - 95	736.66	5.3020	0.961	27.11	27.78	0.43
1387C	48 - R	5 - 45	737.66	5.3120	0.967	27.31	27.98	0.50
1387C	49 - R	1 - 35	741.16	5.3440	0.967	27.30	27.98	0.89
1387C	49 - R	3 - 35	744.16	5.3710	0.959	27.07	27.73	0.47
1387C	49 - R	4 - 64	745.95	5.3880	0.970	27.37	28.05	0.58
1387C	49 - R	5 - 95	747.76	5.4040	0.978	27.60	28.29	1.89
1387C	50 - R	1 - 47	750.88	5.4330	0.973	27.47	28.15	0.47
1387C	50 - R	1 - 91	751.32	5.4370	0.962	27.14	27.81	0.44
1387C	50 - R	2 - 9	752.00	5.4440	0.958	27.02	27.69	0.47
1387C	50 - R	2 - 54	752.45	5.4480	0.960	27.08	27.75	0.28
1387C	51 - R	1 - 62	760.63	5.5230	0.946	26.68	27.33	0.62
1387C	51 - R	2 - 82	762.03	5.5360	0.977	27.60	28.28	2.60
1387C	51 - R	3 - 22	762.85	5.5430	0.965	27.24	27.91	2.57
1387C	51 - R	3 - 102	763.65	5.5510	0.965	27.25	27.92	2.88
1387C	51 - R	3 - 122	763.85	5.5530	0.967	27.30	27.97	1.17
1387C	51 - R	5 - 62	765.58	5.5680	0.943	26.58	27.23	1.07
1387C	52 - R	1 - 62	770.23	5.6110	0.974	27.51	28.19	0.84

Appendix C Alkenone Indices from IODP Site U1387

Core	Section	Interval (cm)	mbsf (m)	Age(Ma)	UK'37	SST (°C) M	[C37] total (nmol/g)
1387C	52 - R	2 - 2	771.13	5.6190	0.971	28.09	0.52
1387C	52 - R	2 - 82	771.93	5.6270	0.971	28.11	1.74
1387C	52 - R	2 - 102	772.13	5.6290	0.967	27.96	1.71
1387C	52 - R	3 - 42	772.13	5.6290	0.971	28.10	1.72
1387C	52 - R	3 - 82	772.53	5.6320	0.973	28.16	0.51
1387C	53 - R	1 - 62	779.83	5.7000	0.957	27.67	0.60
1387C	53 - R	1 - 102	780.23	5.7030	0.967	27.98	0.84
1387C	53 - R	3 - 42	782.43	5.7230	0.956	27.62	0.62
1387C	53 - R	3 - 64	782.65	5.7250	0.960	27.76	0.62
1387C	53 - R	5 - 62	785.33	5.7500	0.970	28.07	0.67
1387C	53 - R	6 - 48	786.49	5.7610	0.973	28.16	1.15
1387C	54 - R	1 - 62	789.43	5.7880	0.959	27.73	0.49
1387C	54 - R	1 - 102	789.83	5.7920	0.960	27.75	0.57
1387C	54 - R	2 - 22	790.53	5.7980	0.959	27.73	0.44
1387C	54 - R	2 - 62	790.93	5.8020	0.967	27.97	0.45
1387C	54 - R	2 - 122	791.53	5.8070	0.962	27.81	0.56
1387C	54 - R	3 - 82	792.58	5.8170	0.964	27.86	0.51
1387C	55 - R	1 - 22	798.63	5.8720	0.972	28.11	0.85
1387C	55 - R	1 - 62	799.03	5.8760	0.969	28.04	0.88
1387C	55 - R	3 - 22	801.63	5.9000	0.964	27.89	0.58
1387C	55 - R	3 - 122	802.63	5.9090	0.962	27.83	0.51
1387C	55 - R	3 - 142	802.83	5.9110	0.960	27.76	0.43
1387C	55 - R	5 - 62	805.03	5.9310	0.957	27.67	0.78
1387C	56 - R	1 - 42	808.43	5.9630	0.957	27.67	0.68
1387C	56 - R	1 - 62	808.63	5.9640	0.966	27.93	0.69
1387C	56 - R	2 - 102	810.53	5.9820	0.944	27.27	0.65
1387C	56 - R	3 - 57	811.58	5.9920	0.958	27.69	0.70
1387C	56 - R	5 - 62	814.63	6.0200	0.960	27.76	0.61
1387C	56 - R	7 - 22	816.63	6.0380	0.963	27.86	0.70
1387C	57 - R	1 - 62	818.23	6.0530	0.971	28.09	0.64
1387C	57 - R	3 - 62	821.28	6.0810	0.963	27.86	0.47
1387C	57 - R	4 - 62	822.75	6.0940	0.967	27.97	0.40
1387C	57 - R	6 - 2	823.65	6.1030	0.971	28.10	0.60
1387C	57 - R	5 - 15	823.78	6.1040	0.981	28.39	0.37
1387C	57 - R	6 - 22	823.85	6.1050	0.961	27.80	0.59
1387C	58 - R	1 - 62	827.23	6.1360	0.971	28.09	0.56
1387C	58 - R	2 - 2	828.93	6.1510	0.964	27.89	0.39
1387C	58 - R	3 - 22	830.43	6.1650	0.962	27.83	0.31
1387C	58 - R	3 - 122	830.63	6.1670	0.971	28.08	0.39
1387C	58 - R	5 - 22	833.83	6.1960	0.939	27.12	0.37
1387C	58 - R	5 - 62	833.83	6.1960	0.950	27.47	0.40